frontiers | Research Topics

Flow, mass transport and ecological process in land-freshwater-marine ecosystems on Earth

Edited by
Weijie Wang, Senlin Zhu and Guotao Cui

Coordinated by
Huilin Wang and Qingchuan Chou

Published in
Frontiers in Marine Science
Frontiers in Environmental Science

ISSN 1664-8714
ISBN 978-2-8325-4035-0
DOI 10.3389/978-2-8325-4035-0

About Frontiers

Frontiers is more than just an open access publisher of scholarly articles: it is a pioneering approach to the world of academia, radically improving the way scholarly research is managed. The grand vision of Frontiers is a world where all people have an equal opportunity to seek, share and generate knowledge. Frontiers provides immediate and permanent online open access to all its publications, but this alone is not enough to realize our grand goals.

Frontiers journal series

The Frontiers journal series is a multi-tier and interdisciplinary set of open-access, online journals, promising a paradigm shift from the current review, selection and dissemination processes in academic publishing. All Frontiers journals are driven by researchers for researchers; therefore, they constitute a service to the scholarly community. At the same time, the *Frontiers journal series* operates on a revolutionary invention, the tiered publishing system, initially addressing specific communities of scholars, and gradually climbing up to broader public understanding, thus serving the interests of the lay society, too.

Dedication to quality

Each Frontiers article is a landmark of the highest quality, thanks to genuinely collaborative interactions between authors and review editors, who include some of the world's best academicians. Research must be certified by peers before entering a stream of knowledge that may eventually reach the public - and shape society; therefore, Frontiers only applies the most rigorous and unbiased reviews. Frontiers revolutionizes research publishing by freely delivering the most outstanding research, evaluated with no bias from both the academic and social point of view. By applying the most advanced information technologies, Frontiers is catapulting scholarly publishing into a new generation.

What are Frontiers Research Topics?

Frontiers Research Topics are very popular trademarks of the *Frontiers journals series*: they are collections of at least ten articles, all centered on a particular subject. With their unique mix of varied contributions from Original Research to Review Articles, Frontiers Research Topics unify the most influential researchers, the latest key findings and historical advances in a hot research area.

Find out more on how to host your own Frontiers Research Topic or contribute to one as an author by contacting the Frontiers editorial office: frontiersin.org/about/contact

Flow, mass transport and ecological process in land-freshwater-marine ecosystems on Earth

Topic editors

Weijie Wang — China Institute of Water Resources and Hydropower Research, China

Senlin Zhu — Yangzhou University, China

Guotao Cui — University of California, Merced, United States

Topic Coordinators

Huilin Wang — South China Agricultural University, China

Qingchuan Chou — Institute of Hydrobiology, Chinese Academy of Sciences (CAS), China

Citation

Wang, W., Zhu, S., Cui, G., Wang, H., Chou, Q., eds. (2023). *Flow, mass transport and ecological process in land-freshwater-marine ecosystems on Earth*. Lausanne: Frontiers Media SA. doi: 10.3389/978-2-8325-4035-0

Table of contents

frontiers | Frontiers in Marine Science

TYPE Editorial
PUBLISHED 18 December 2023
DOI 10.3389/fmars.2023.1324983

OPEN ACCESS

EDITED AND REVIEWED BY
Heliana Teixeira,
University of Aveiro, Portugal

*CORRESPONDENCE
Weijie Wang
wjwang@whu.edu.cn

RECEIVED 20 October 2023
ACCEPTED 11 December 2023
PUBLISHED 18 December 2023

CITATION
Wang W, Zhu S, Cui G, Chou Q and Wang H (2023) Editorial: Flow, mass transport and ecological process in land-freshwater-marine ecosystems on earth.
Front. Mar. Sci. 10:1324983.
doi: 10.3389/fmars.2023.1324983

Editorial: Flow, mass transport and ecological process in land-freshwater-marine ecosystems on earth

Weijie Wang[1]*, Senlin Zhu[2], Guotao Cui[3], Qingchuan Chou[4] and Huilin Wang[5]

[1]State Key Laboratory of Simulation and Regulation of Water Cycle in River Basin, China Institute of Water Resources and Hydropower Research, Beijing, China, [2]College of Hydraulic Science and Engineering, Yangzhou University, Yangzhou, China, [3]Carbon-Water Research Station in Karst Regions of Northern Guangdong, School of Geography and Planning, Sun Yat-sen University, Guangzhou, China, [4]State Key Laboratory of Freshwater Ecology and Biotechnology, Institute of Hydrobiology, Chinese Academy of Sciences, Wuhan, China, [5]College of Water Conservancy and Civil Engineering, South China Agricultural University, Guangzhou, China

KEYWORDS

hydrodynamics, mixing, ecology, land ecosystem, freshwater ecosystem, marine ecosystem

Editorial on the Research Topic
Flow, mass transport and ecological process in land-freshwater-marine ecosystems on earth

Water is the most basic material circulating between land, freshwater, and marine environments; exerts important ecological functions; and provides significant economic products. Flow, mass transport, and ecological processes are critical determinants of flow-organism interactions in ecosystems at multiple scales and have very important impacts on the structure and function of aquatic ecosystems. Therefore, studies are needed to evaluate the mechanism analysis, process dynamic simulation, and optimal regulation of ecosystems at different scales. Particularly, ongoing climate warming and human activities have altered flow-organism interactions in different regions, including in land, freshwater, and marine ecosystems. It remains necessary to improve the understanding of the flow, mass transport, and ecological processes in land freshwater marine ecosystems on Earth.

This Research Topic aims to explore in-depth flow, mass transport, and ecological processes and their impacts on land-freshwater-marine ecosystems based on recent studies involving numerical modelling, on-site observations, lab experiments, and literature review. We hope that this Research Topic will provide a scientific basis for optimising the design and practice of different ecosystems in the context of climate change.

The Research Topic "Flow, Mass Transport and Ecological Process in Land-Freshwater-Marine Ecosystems on Earth" has brought together several articles reporting on new advances in this field.

In the opening paper of the Research Topic, "*The Effects of Accelerated Sea-Level Rise on Tidal Dynamics*", Li et al. use a long-term data series, from 1952 to 2020, to

describe significant spatiotemporal variability of the tidal dynamics of the Pearl River Estuary, showing how coastal geomorphology, river discharge, and sea level together influenced the estuarine hydrodynamics.

Overall, net estuary fluxes under complex conditions have not been extensively evaluated by the scientific community. In the contribution, "*Analysis of the Influence of the Rubber Dam and Sea Ice Cover on Seawater Flux and Salinity Processes*" by Hu et al., the net inlet water inflow into the sea from 2017 to 2020 were calculated and evaluated based on field monitoring data of the water level, velocity, and salinity at the Liao River Estuary. The results provide an effective method and technical support for measuring seawater flux in other rivers.

Different heights of aquatic vegetation in natural rivers affect the hydrodynamic conditions of water flow, as shown in the study titled, "*Flow Characteristics of Double-Layered Rigid Vegetation Flow*". Wang et al. constructed a semi-analytical longitudinal flow velocity model in open-channel flows with double-layered rigid vegetation. The results of this model, verified with experimental data, provide a reference for environmental management and restoration of ecological rivers.

However, the role of polytrophic diversity in maintaining aquatic ecosystem versatility remains unclear. Xu et al. in "*Links Between the Species Richness and Ecosystem Functioning*", constructed a species addition experiment involving a diversity gradient to examine the relationship between biodiversity and ecosystem function within and across trophic levels. The results showed that the relationship between ecosystem species richness and ecosystem function at each trophic level was jointly regulated by the environment and time.

The simplified configurations of aquatic vegetation used in previous studies may mask or amplify the complex flow velocity and turbulent motion properties of submerged vegetation. The contribution "*Numerical and Analytical Methods to Study the Interaction Between Submerged Vegetation and Freshwater*" by Zhao et al. proposes an adjustment coefficient of the Karman constant to describe the complex vegetation morphology. The authors also discuss an improved mixed layer thickness formula for foliated vegetation and an expression for the Manning coefficient based on the analytical solution model of multi-layer flow velocity, providing a theoretical basis for vegetation ecological restoration.

Hydrodynamic analysis of the interaction between submerged vegetation and water flow has attracted considerable attention. The contribution "*Vertical Distribution of Water Flow Velocity in Submerged Vegetation*" by Zhang et al. proposes an analytical model for classifying water flow vertically into uniform, mixing, and logarithmic layers. The results showed that the longitudinal velocity of the model fitted well with measured values. Furthermore, the theoretical model can be applied to more complex velocity distribution cases.

However, the relationship between other commonly addressed ecological factors and macrophyte communities remains a challenge for management. In the contribution, "*Seasonal Variation and Nutrient Response Analysis on Macrophyte Community Diversity*" by Tian et al., the authors studied the composition of aquatic plant communities in lakes across different seasons and trophic states, showing that seasonal variation and nutrients jointly regulated the macrophyte community structure in lakes. These results can contribute to the management and restoration of eutrophic lakes.

Low spatial resolution limits the application of remote sensing images for conveying the surface water environment. As described in the contribution "*Super-Resolution Reconstruction of Sea Surface Pollutant Diffusion Images*", Duan et al. constructed a thermal infrared imaging dataset of thermal emission from cooling water of coastal power plants and used efficient sub-pixel convolutional neural network and enhanced super-resolution generative adversarial network models to reconstruct high-resolution remote sensing images. The two super-resolution models based on deep learning show application potential for improving water pollution detection.

Dams and large reservoirs are the main sources of suspended sediments in rivers. The contribution "*Fine Sediment and Water Retention in the Nile Damming*" by Herut et al. shows that fragmentation of the Nile River resulted in almost complete retention of fine sediments, leading to marine oligotrophication. Dissolved nutrients decreased because of anthropogenic sediment and water retention. This study provides a reference for analysing the ecological responses of other fragmented rivers worldwide.

Top-down approaches have also potential to manage the trophic state of aquatic ecosystems as shown by the study "*Phytoplankton Control Studies by Stocking Filter-Feeding Fish*" by Zhang et al., where monitoring data of filter-feeding fish stocked annually for ten years (2010–2020) were analysed in a typical subtropical highland reservoir in southwest China. The results showed that filter-feeding fish contributed significantly to reductions in the phytoplankton and zooplankton biomass. Despite further research is needed, this suggests that the optimal intensity of filter-feeding fish placement can help control phytoplankton.

The Research Topic compiled in this research theme improves the understanding of studies of flow, mass transport, and ecological processes in land-freshwater-marine ecosystems on Earth from multiple perspectives and provides a good example of the integration of multidisciplinary approaches.

Author contributions

WW: Writing – original draft, Writing – review & editing. SZ: Writing – review & editing. GC: Writing – review & editing. QC: Writing – review & editing. HW: Writing – review & editing.

Funding

The author(s) declare financial support was received for the research, authorship, and/or publication of this article. The authors acknowledge the support of the Beijing Natural Science Foundation (8232052), National Natural Science Foundation of China (12202150, 51809286), and Talent Program of the China Institute of Water Resources and Hydropower Research (WE0199A052021).

Conflict of interest

The authors declare that the research was conducted in the absence of any commercial or financial relationships that could be construed as a potential conflict of interest.

Publisher's note

frontiers | Frontiers in Environmental Science

TYPE Original Research
PUBLISHED 12 January 2023
DOI 10.3389/fenvs.2022.1094572

OPEN ACCESS

EDITED BY
Weijie Wang,
China Institute of Water Resources and Hydropower Research, China

REVIEWED BY
Bin Chen,
Beijing Normal University, China
Bohan Wang,
Peking University, China
Jinlan Guo,
Macau University of Science and Technology, Macao, SAR China

*CORRESPONDENCE
Ping Wang,
wangp@bjfu.edu.cn
Yonggang Zhang,
zygang3116@bjfu.edu.cn

SPECIALTY SECTION
This article was submitted to Freshwater Science,
a section of the journal
Frontiers in Environmental Science

RECEIVED 10 November 2022
ACCEPTED 27 December 2022
PUBLISHED 12 January 2023

CITATION
Wang Q, Zhang Y, Wang P, Feng T and Bai Y (2023), Longitudinal velocity profile of flows in open channel with double-layered rigid vegetation.
Front. Environ. Sci. 10:1094572.
doi: 10.3389/fenvs.2022.1094572

Longitudinal velocity profile of flows in open channel with double-layered rigid vegetation

Qitong Wang, Yonggang Zhang*, Ping Wang*, Tianjiao Feng and Yang Bai

School of Soil and Water Conservation, Beijing Forestry University, Beijing, China

Aquatic vegetation of different heights is widely scattered in natural rivers and is conducive to their environmental function while affecting the flow hydrodynamic conditions. A semi-analytical velocity model is constructed and used to study the longitudinal velocity profile in open channel flow through double-layered rigid vegetation. The double-layered vegetation flow is separated into three zones according to the velocity profile: 1) nearly uniform distributed velocity zone 1A in the lower region of the short vegetation layer, 2) a mixing layer zone B, 3) uniform distributed velocity zone 2A in the upper region of the tall vegetation layer. Two force equilibrium equations about the gravity-driving and vegetation drag are solved to obtain the uniform velocity distribution equations in zone 1A and 2A. The velocity of zone 1A and B is further modeled as a linear superposition of two concepts: the uniform velocity distribution term of zone 1A and a hyperbolic tangent profile. Meanwhile, longitudinal velocity and the lateral vorticity profiles of open channel flow through double-layered rigid vegetation are studied by laboratory flume tests of different vegetation arrangements exposed to two water depths and three slopes. The experimental results show that the longitudinal velocity increases with the slope increase. The verification of the velocity model is based on the instantaneous velocity measured by Acoustic Doppler Velocimetry (ADV), which shows acceptable agreement, indicating that the model can give a reference to the longitudinal velocity of multi-layered vegetation flow in some cases. The effects of wake vortices and boundary friction on the model are further explored in the discussions. The results presented in this study could contribute to the management of aquatic vegetation configurations and the restoration of freshwater ecology.

KEYWORDS

double-layered vegetation, flow characteristics, longitudinal velocity profile, velocity model, mixing layer

1 Introduction

Aquatic vegetation is widely distributed in the riffles and shallow water areas of rivers, forming a more complex hydrodynamic system than the bare channel. Vegetation increases the flow resistance, raises the water level, reduces the flow capacity, alters the local flow dynamic characteristics and sediment sorting process, and thus influences the erosion and geomorphic evolution of the river (Yang et al., 2015; Huai et al., 2019; Li et al., 2020). Meanwhile, vegetation is also beneficial to the freshwater ecosystem. For example, aquatic plants can enhance the water quality by absorbing or degrading some harmful substances and can shelter the aquatic microorganisms and fish in the river (Xu and Nepf, 2020; 2021; Huai et al., 2021). Sometimes, vegetation increases the transparency of the water by reducing the flow velocity

and enhancing the deposition of suspended sediment (Liu and Nepf, 2016). Vegetation roots can consolidate the riverbed soil and improve the bank stability to prevent excessive flow erosion (Qu, 2014). Since the appropriate arrangement of vegetation impacts the ecological process on land-freshwater ecosystems, the bioremediation technology of planting vegetation in river channels has been widely applied (Zhang, 2014). Analyzing the hydrodynamic characteristics and establishing accurate flow velocity models provide a scientific basis for water environment management and restoration of rivers and streams (Wang et al., 2021). Therefore, it is of great practical significance to study the hydrodynamic structure within the vegetation, which helps predict the flood hazards and restore the freshwater ecosystem.

Vegetated flow is generally divided into single-layered or double-layered vegetation flow, where the aquatic vegetation is emergent or submerged (Huai et al., 2021). Numerous studies have revealed the hydrodynamic characteristics of open channel flow with single-layered vegetation by investigating the vegetation flexibility, density, leaf area, and stem diameter (Velasco et al., 2003; Cheng, 2013; Zhang et al., 2020). The study on vegetation drag coefficient also extends from individual plants to vegetation arrays and from rigid vegetation to flexible vegetation (Tang et al., 2007; Chen et al., 2013). Redefining some parameters in vegetated flow compared to the bare bed is utility to quantify the flow characteristics. For example, a new model of the friction factor f in the vegetated flow concerned about the vegetation turbulence is more reasonable compared with the Darcy-Weisbach formula (Wang et al., 2019a), where the friction factor f is vital in the bulk velocity prediction of the flow with rigid or flexible vegetation (Wang et al., 2020).

In rivers, flexible vegetation accounts for much aquatic vegetation, so the flow through flexible vegetation has been widely concerned in recent years. Flexible vegetation will bend and deform under the influence of water flow, meanwhile, the deformation of vegetation affects the flow characteristics, resulting in a complex turbulence structure and redistribution of flow velocity (Kubrak et al., 2008; Zhang and Lai, 2015; Zhang et al., 2020). The flow structure is more complicated when consider the geometry of the plant shape (Wang et al., 2019b), and it is usually using rigid cylinders to represent the aquatic plants with fewer leaves in numerous studies (Huai et al., 2021), the study here also simulates the vegetation with rigid material.

In the flow through single-layered submerged vegetation, the vertical profile of longitudinal velocity no longer follows the law of logarithmic distribution from the bed to the free water surface, but can be divided into two layers, i.e., the vegetation layer and the free-water layer, or divided into three layers by adding a mixing layer between the vegetation layer and the free-water layer (Zhang, 2014). The longitudinal velocity through the flexible vegetation conforms to the "C" distribution while conforming to the "J" distribution above the vegetation layer (Fan et al., 2020). For the emergent canopy, the vegetation-bed-flow coherent structures affect the near-bed flow region, which is so called the effective bottom boundary, causing the flow velocity to increase from the bed, reach a peak, and decline to a constant value above this layer (Tseng et al., 2021). In addition to flow through the vegetation of uniform arrangements, the flow characteristic in a channel partially covered with vegetation array or fully covered with compound vegetation patterns has been studied. Zhang et al. (2021) derived the theoretical solutions of longitudinal velocity from the momentum model of a two-zone vortex structure in a channel partially covered with vegetation. Li et al. (2022) explored the characteristics of open channel flows with two layout patterns of rigid-flexible and flexible-rigid vegetation.

However, the vegetation in natural rivers often shows different heights. Both submerged and emergent vegetation are widely distributed in floodplains or shallow water (Zhao et al., 2015). Numerous experimental, numerical, and analytical researches on the hydrodynamic structure of double-layered vegetation flow were conducted. When both vegetation layers are submerged, according to the longitudinal velocity profile, the double-layered vegetation flow is separated into a short vegetation layer, a tall vegetation layer, and a free-water zone (Huai et al., 2014). Each vegetation layer is divided into an upper vegetation zone and a lower vegetation zone, in which the velocity of lower vegetation zones is constant and increases in upper vegetation zones and free-water zone (Liu et al., 2010; Huai et al., 2014; Zhao, 2017; Wang Z. et al., 2019; Rahimi et al., 2020; Tang et al., 2021). Under different vegetation arrangements, densities, vegetation height, and flow depths, the velocity, turbulence intensity, the flow resistance, and the vorticity of double-layered vegetation flows were found more complex than single-layered vegetation flow (Liu et al., 2010; Wang Z. et al., 2019; Rahimi et al., 2020). Therefore, considering the effect of the double-layered vegetation, an analytical model of the longitudinal velocity was proposed basing on the momentum balance equation (Huai et al., 2014), and the hydraulic radius formula and Manning coefficient formula were modified (Tang et al., 2021).

Above all, it is more common that the aquatic vegetation has two or more different heights in natural rivers. Most studies of double-layered rigid vegetation flow focused on the vertical or longitudinal distribution of flow velocity, Reynolds stress, and turbulence intensity. Only a few studies are concerned about using a formula to describe the flow velocity profile under different vegetation arrangements and slopes, and this is also initial to understand the characteristics of flow with multiple-layered vegetation. This paper aims to study the flow characteristics of the double-layered rigid vegetation flow with different water depths, slopes, and vegetation densities. By subdividing the flow into distinct zones, listing the force balance equations, and using the superposition method to describe the momentum transport of the mixing layer, a longitudinal velocity model of the open-channel flows with double-layered rigid vegetation is proposed and verified by the experimental data. The laboratory flume tests use Acoustic Doppler Velocimetry (ADV) to collect three-dimensional velocity. The results can provide guidance for vegetation arrangements in channels, the construction of ecological rivers, and support river environment management and restoration.

2 Theoretical analysis

The steady and uniform open-channel flow with double-layered rigid vegetation composed of short and tall cylindrical stems with the height of h_1 and h_2 is generally separated into two cases in previous studies according to the water depth H, i.e., $H > h_2$ or $h_1 < H < h_2$. In this paper, we only study the case of $h_1 < H < h_2$. Using layer 1 and layer 2 to respectively denote the short and tall vegetation layer, Huai et al. (2014) suggested that in the case of $h_1 < H < h_2$, the flow can be separated into three zones according to the longitudinal velocity profile, i.e., lower zone of layer 1 marked as zone 1A ($z < h_1$-h_u), mixing layer zone marked as zone B at the upper region of layer 1 (h_1-$h_u < z < h_1$), and tall vegetation layer marked as zone 2A ($h_1 < z < H$),

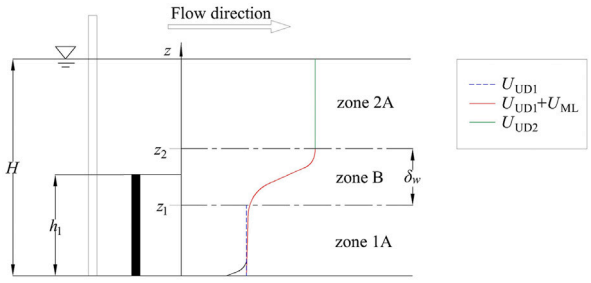

FIGURE 1
Conceptual model for flows with double-layered rigid vegetation.

where h_u is the height of zone B and the upper edge of zone B coincides the top of layer 1. While the mean velocities in zone 1A and zone 2A are nearly constant, it significantly increases in zone B.

According to the study of mixing layer in the submerged vegetation (Nikora et al., 2013), the mean velocity can be obtained by a (quasi-)linear superposition of individual mechanisms acting in the double-layered vegetated flow at zone 1A and zone B, taking two concepts into account, i.e., (1) a uniform velocity distribution within zone 1A with a constant value (U_{UD1}), and (2) a mixing layer concept generated by the Kelvin-Helmholtz instability (U_{ML}). Besides, the velocity of zone 2A is expressed as a constant velocity profile (U_{UD2}) in brief. The conceptual velocity model for flows with double-layered rigid vegetation is outlined in Figure 1. Assuming the upper inflection point (marked z_2) of zone B is slightly above the canopy of the short vegetation layer, and our experimental results will verify this assumption. The lower inflection point of the mixing layer zone in the short vegetation layer is marked as z_1, $\delta_w = z_2 - z_1$ is the height of the mixing layer.

For a unit canopy volume in vegetated flow, the vegetation drag can be calculated as (Huai et al., 2014):

$$F_d = \frac{1}{2}\rho C_D m D u^2, \tag{1}$$

where ρ (kg·m^{-3}) is the water density, C_D is the vegetation drag coefficient, m is the number of stems per bed area, D (m) is the diameter of the vegetation stem, and u (m·s^{-1}) is the mean velocity of the flow.

The force equation of a small length-scale dx along the streamwise direction in zone 1A can be expressed as a balance of the gravity-driving term, vegetation drag term, bed friction term, and the sidewall friction term:

$$\rho g i (1-\lambda_1) W z_1 dx = \frac{1}{2}\rho C_D m_1 D U_{UD1}{}^2 W z_1 dx + \tau_{bed}(1-\lambda_1) W dx + 2 z_1 \tau_{wall} dx. \tag{2}$$

Meanwhile, the force balance equation in zone 2A can be expressed as:

$$\rho g i (1-\lambda_2) W (H-z_2) dx = \frac{1}{2}\rho C_D m_2 D U_{UD2}{}^2 W (H-z_2) dx + 2(H-z_2)\tau_{wall} dx. \tag{3}$$

where the gravity-driving term on the left side of the Eqs 2, 3 considers the existence of the vegetation, g (m·s^{-2}) is the gravity acceleration, i is the energy slope equaling to the bed slope J in open-channel flow, W (m) is the flume width, m_1 (plant·m^{-2}) is the density of the short vegetation layer (including the short stems and the tall stems embedded in layer 1), m_2 (plant·m^{-2}) is the density of the tall vegetation layer (only the tall stems in layer 2), U_{UD1} (m·s^{-1}) is the uniform velocity in zone 1A, U_{UD2} (m·s^{-1}) is the uniform velocity in zone 2A, $\lambda_1 = \frac{m_1 D^2 \pi}{4}$; $\lambda_2 = \frac{m_2 D^2 \pi}{4}$ are the solid volume fractions of the cylinders in the short and tall vegetation layers, respectively. Darcy-Weisbach formula $\tau_{bed} = \frac{1}{8}\rho U^2 f_{bed}$ (kg·m^{-1}·s^{-2}) and $\tau_{wall} = \frac{1}{8}\rho U^2 f_{wall}$ (kg·m^{-1}·s^{-2}) represents the shear stress produced by the bed and sidewalls, using the roughness parameter f_{bed}: and f_{wall} to calculate, respectively (Wang et al., 2015).

Among the several terms in Eqs 2, 3, the bed friction $[\tau_{bed}(1-\lambda_1)Wdx]$ and the sidewall friction $[2z_1\tau_{wall}dx]$, $[2(H-z_2)\tau_{wall}dx]$ are negligible since they are significantly lower than the vegetation drag, and the impact of the boundary stress terms is later discussed in Section 6.2. Then Eqs 2, 3 can be simplified as momentum equations:

$$\rho g i (1-\lambda_1) - \frac{1}{2}\rho C_D m_1 D U_{UD1}{}^2 = 0, \tag{4}$$

$$\rho g i (1-\lambda_2) - \frac{1}{2}\rho C_D m_2 D U_{UD2}{}^2 = 0. \tag{5}$$

The uniform distributed velocity term within the layer 1 can be expressed as:

$$U_{UD1} = \left(\frac{g i (1-\lambda_1)}{0.5 D C_D m_1}\right)^{1/2} \tag{6}$$

The velocity profiles in zone 2A can be expressed as:

$$U_{2A} = U_{UD2} = \left(\frac{g i (1-\lambda_2)}{0.5 D C_D m_2}\right)^{1/2}. \tag{7}$$

The vegetation density significantly differs between the short and tall vegetation layers. The vegetation drag in zone 1A is more significant than that in zone 2A due to its large density, leading to a prominent velocity gradient in zone B, which derives the generation of Kelvin-Helmholtz vortices there (Liu et al., 2010). Therefore, the Reynolds stress should be considered in the momentum equation. Assuming the mixing layer velocity term U_{ML} is a hyperbolic tangent profile:

$$U_{ML} = (U_{z_2} - U_{UD1}) \cdot \left[1 + \tanh\left(\frac{z - z_2}{\delta_w}\right)\right]. \tag{8}$$

where U_{z_2} is the velocity at the inflection point z_2, equaling to U_{UD2}. And then, the velocity in zone 1A and zone B can be expressed as the superposition of the uniform distribution of the zone 1A and the hyperbolic tangent profile term:

$$U_{1A,B} = U_{UD1} + U_{ML} = \left(\frac{g i (1-\lambda_1)}{0.5 D C_D m_1}\right)^{1/2} + \left[\left(\frac{g i (1-\lambda_2)}{0.5 D C_D m_2}\right)^{1/2} - \left(\frac{g i (1-\lambda_1)}{0.5 D C_D m_1}\right)^{1/2}\right] \cdot \left[1 + \tanh\left(\frac{z - z_2}{\delta_w}\right)\right]. \tag{9}$$

3 Experiments

3.1 Experimental settings

The experiments were conducted in a recirculating, free-surface flow flume at the Hydraulics Laboratory of the School of Soil and Water Conservation at Beijing Forestry University. The flume was

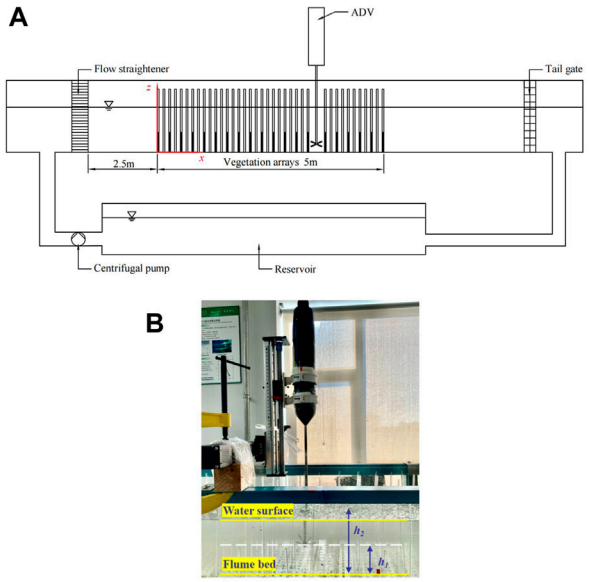

FIGURE 2
Experimental arrangement: **(A)** Sketch of the laboratory recirculating flume setup, the black part of the vegetation section represents the short cylinder; **(B)** A photo of the experiment for run XHS1, where short cylinders (h_1) are submerged and tall cylinders (h_2) are emergent.

12.4 m long (L), .3 m wide (W), and .25 m deep (H_0). The electromagnetic flowmeter system controlled the discharge. At the same time, a honeycomb-shaped straightener at the inlet and an adjustable weir gate at the end of the flume were used to set a stable and uniform flow.

The vegetation was simulated with plastic cylinders of .006 m diameter (D), and the cylinders representing short vegetation and tall vegetation were .07 m (h_1) and .18 m (h_2), respectively. The cylinders were embedded in five 1 m long, .3 m wide, and .5 cm thick plexiglass plates. The vegetation section was 5-m-long, and the leading edge was 2.5 m from the flume inlet (see Figure 2A). A Cartesian coordinate is established with the frontal edge of the vegetation section as the origin. The x, y, and z coordinates denote streamwise, lateral, and vertical directions, respectively. The preliminary experiment of double-layered vegetation flow was conducted, the velocities at x = 0, .5, 1.3, 2.5, 3.6, and 4.5 m were measured, and the results showed that the longitudinal velocity at x = 3.6 m and x = 4.5 m had high consistency which means the flow behind x = 3.6 m is fully developed. Therefore, the velocity was measured at x = 4.0 m, representing the velocity of the fully developed region. Several cylinders were removed in order to measure the velocity using ADV. A side-view image of the double-layer model plants and velocity measurements for run XHS1 are shown in Figure 2B.

3.2 Experimental conditions

The specific parameters of each run are given in Table 1. The experiments include two vegetation arrangements marked as X and Y, with different density ratios $\alpha = m_1/m_2$. The water depth was set as a higher submergence state H = 14.00 cm (HS), and a lower submergence state H = 12.80 cm (LS), under which condition the short vegetation layer was submerged and the tall vegetation layer was emergent. The numbers 1-3 denoted three different slopes J, .001, .002, and .003. According to the Reynolds number $Re=(U_mR)/\nu$ and the Froude number $F_r=U_m/\sqrt{gH}$, the experimental flow is turbulent and subcritical flow, where $U_m = Q/WH$ is the average velocity over the section, $R=(H-\lambda_1 h_1-\lambda_2 H)/(m_1 h_1 D + m_2 HD)$ is the hydraulic radius of the half-submerged double-layered vegetation flow without consideration of the impact of the bed and walls (Tang et al., 2021), H is the water depth, Q is the flow discharge, g = 9.81 ms^{-2} is the acceleration of the gravity, $\nu = 1.01 \times 10^{-6}$ m^{2}s^{-1} is the kinematic viscosity of the water (based on the kinematic viscosity of the water under 101.325 kPa and 20°C).

3.3 Data collection and processing

Nortek Acoustic Doppler Velocimetry (ADV) was used to measure the instantaneous velocities. The ADV has one transmitting probe and four receiving probes. The transmitting probe in the center emits acoustic signals, and then receiving probes receive the acoustic frequency changes caused by the reflection or scattering of moving particles in the water to collect the data of the sampling body 5 cm in front of the probe. After the signal is processed by the system, the instantaneous velocity, signal intensity, signal-to-noise ratio (SNR), and correlation (COR) of each measuring point can be converted into a text file for output. The ADV cannot accurately measure the range of 2–3 cm below the water surface, for the upper signal-receiving probe will be emergent. The data acquisition frequency was 200 Hz, the sample volume was 5.5 mm^3, and the sampling time was 40 s. Before the experiment, the ADV was fixed on a support. The tracer particles used in the experiment are hollow plexiglass beads of 20 μm diameter, and the density is .9 gcm^{-3}. Figure 3 shows that there were three measuring locations in runs X representing behind the tall cylinder (BT), free stream behind the tall and short cylinders' gap (BTS) and the short cylinder (BS), and one more for runs Y: Free stream behind two short cylinders' gap (BSS). The measurement was done from the bed (z = .005 m) towards the free water surface with an increment of .005 m at each measuring location.

Python processed the experimental data. The longitudinal, lateral, and vertical instantaneous velocities with a signal-to-noise ratio (SNR) greater than 15 and correlation (COR) greater than 70% are regarded as valid data, and the time-average velocity of x, y, and z direction $\bar{u}$, $\bar{v}$, and $\bar{w}$ are obtained by time averaging the instantaneous velocities. The time-average longitudinal velocity of each measuring location was averaged horizontally to obtain the mean longitudinal velocity of the measuring cross-section.

4 Results

4.1 Longitudinal velocity profiles at different measurement locations

Figure 4 shows the longitudinal velocities at different locations of runs X and Y, and the black dotted line indicates the height of short vegetation h_1 = .07 m. The longitudinal velocity profile can be roughly divided into three zones, as mentioned above. Zone 1A is from the bed to z = .055 m ($0 < z \leq .79h_1$), which is called the constant velocity zone, the velocity almost stays constant or has an insignificant increasing tendency. Zone B is from z = .055 m to z = .07–.08 m ($.79h_1 < z \leq$

TABLE 1 Experimental parameters of each run.

Run	m_1 (plant·m^{-2})	m_2 (plant·m^{-2})	α	J	H (m)	Q (10^{-3} m^{3}s^{-1})	U_m (m·s^{-1})	Re	F_r
XHS1	778	389	2	.001	.140	6.27	.149	30908.14	.127
XHS2	778	389	2	.002	.140	6.62	.158	34642.01	.134
XHS3	778	389	2	.003	.140	7.00	.167	32152.77	.142
XLS1	778	389	2	.001	.128	5.05	.132	31274.52	.117
XLS2	778	389	2	.002	.128	5.97	.155	26128.08	.139
XLS3	778	389	2	.003	.128	6.60	.172	34045.68	.153
YHS1	778	259	3	.001	.140	3.23	.077	19249.61	.066
YLS1	778	259	3	.001	.128	2.80	.073	17259.13	.065

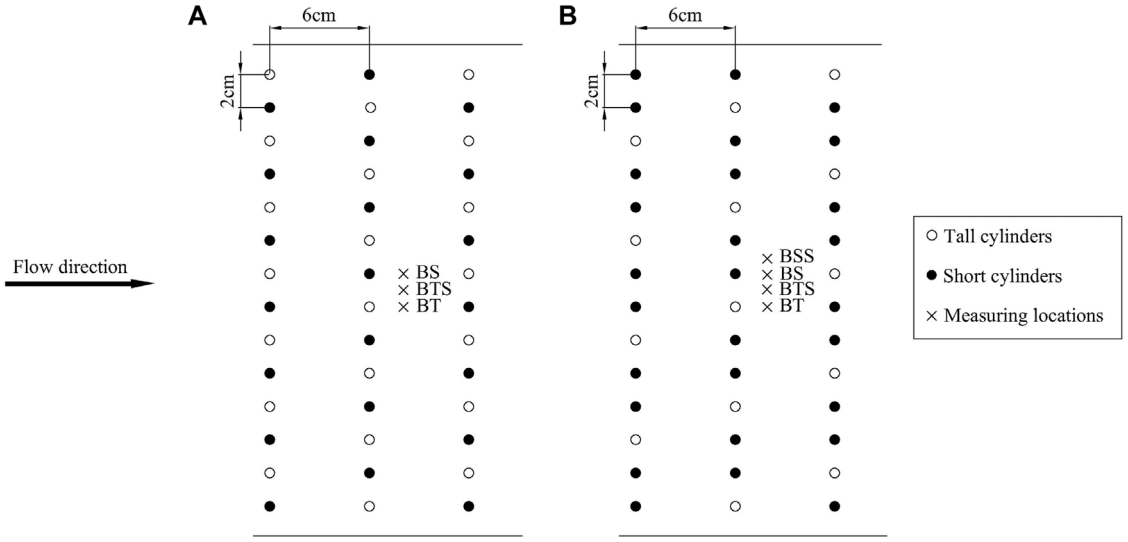

FIGURE 3
The arrangement of vegetation and measuring locations of **(A)** runs X and **(B)** runs Y. Black and white circles representing short and tall cylinders respectively, and the crosses represent measurement locations.

$1.14h_1$). The velocity reaches the maximum at the top of the short vegetation or a slightly higher place and basically remains constant at zone 2A ($1.14h_1 < z \leq 1.71h_1$). The zoning of the longitudinal velocity profile is almost the same as the previous experimental results (Liu et al., 2010; Huai et al., 2014; Tang et al., 2021).

Figure 4 shows that, except for run XHS2, the longitudinal velocity at location BT in runs X is the largest, and the one at location BTS is the smallest. The velocity at location BT in run XHS2 ranges between the value of location BS and location BTS, which is different from the regularities of the other runs, probably due to the error caused by an experimental operation, such as the slight deviation of the measurement location. Furthermore, in runs XHS1, XLS2, and XLS3, the velocities at locations BT and BTS have a percentage variance of 5%–18%. This is most likely due to the fact that the increasing of velocity component caused by the wake vortices after stem, based on the velocity model of linear superposition (Nikora et al., 2013). In runs Y, the velocity profiles at different locations are similar, and the velocity curve is not as smooth as that of runs X, especially the measured data of run YLS1, possibly due to the more complex arrangement of the vegetation cylinders of runs Y, leading to the frequent fluctuation of the velocity.

4.2 Mean longitudinal velocity of each run

Figure 5 displays the dimensionless mean longitudinal velocity of the measuring cross-section in each run. Every dimensionless velocity shows consistent distribution characteristic of "constant-increasing-constant" in vertical. For runs X, the velocity in zone 1A (u_{1A}) have a magnitude of .69–.83U_m and the velocity in zone 2A u_{2A} = .97–1.17U_m. For runs Y, the velocity in zone 1A u_{1A} = .59–.76U_m, and the velocity in zone 2A u_{2A} = 1.04–1.35U_m. The density ratio α of the double-layer vegetation under the same water depth and slope condition dictates the magnitude of the constant velocity within it. Here, the discharge Q is also an important factor affecting the velocity within the upper layer.

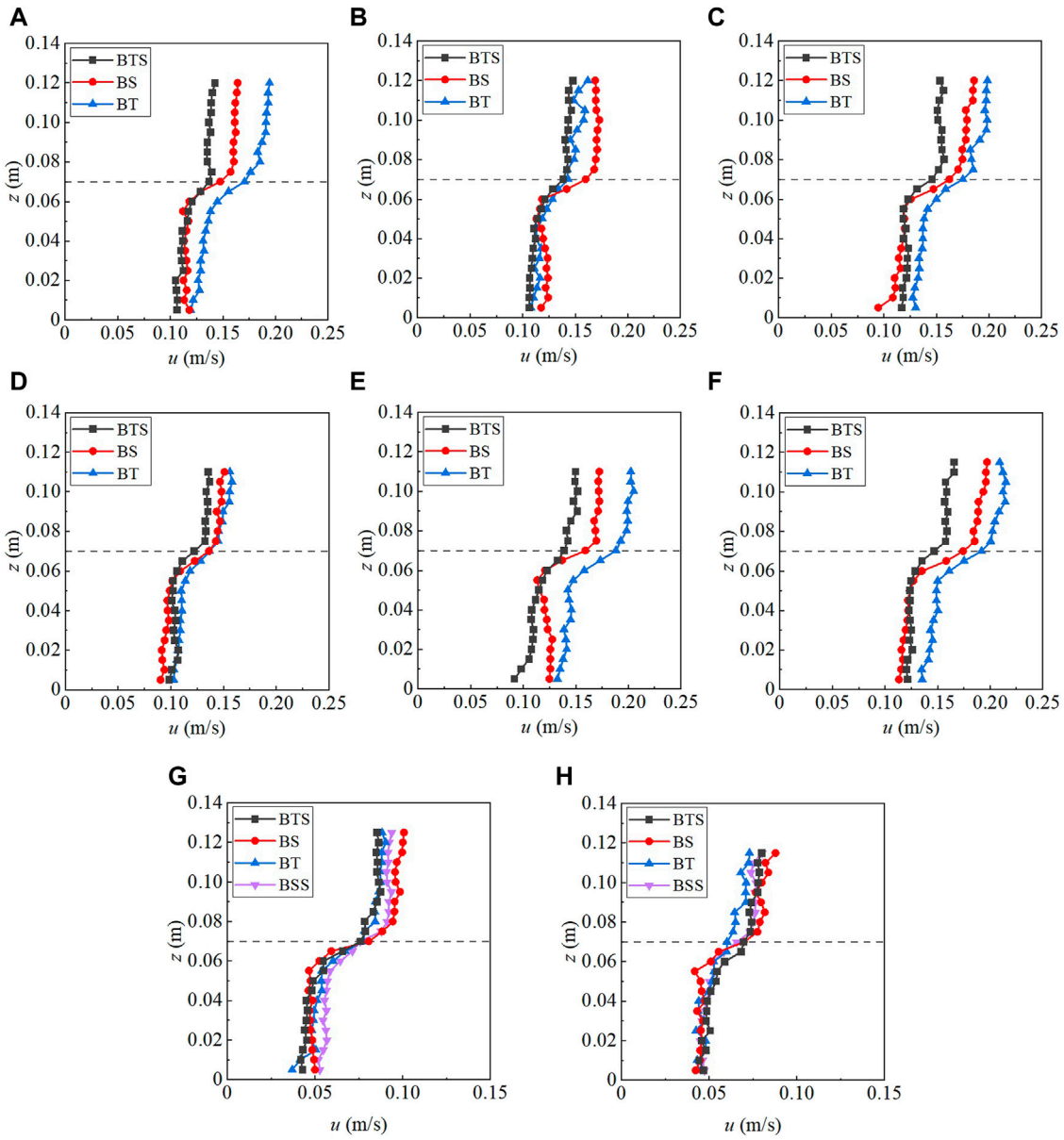

FIGURE 4
Vertical profiles of longitudinal velocity at different measurement locations for runs X and runs Y, **(A–C)** present results for runs XHS1 to XHS3, **(D–F)** present results for runs XLS1 to XLS3, **(G,H)** present results for runs YHS1 and YLS1, respectively. The black dotted line represents the height of the short cylinders.

We define that the ratio of the mean velocity in zone 2A to the mean velocity in zone 1A $\beta = \overline{u_{2A}}/\overline{u_{1A}}$, where $\overline{u_{2A}}$ and $\overline{u_{1A}}$ is the mean experimental velocity of zone 2A and zone 1A, respectively. The α of runs Y is greater than runs X, leading to a more significant difference between the vegetation resistance and velocity distribution in zones 1A and 2A, and β of runs Y is 1.59–1.80. Table 1 shows that the velocity increases with the channel slope under the condition of the same vegetation arrangement and water depth. It can also be concluded from Figure 5 that the slope does not have much effect on the velocity ratio between zones 2A and 1A, the β of runs XHS and XLS are similar as the slope changes.

4.3 Lateral vorticity

The inflection point of the velocity profile in vegetated flows can be characterized by the lateral vorticity, and it can be calculated as the following equation (Singh et al., 2019):

$$\omega = \frac{\partial w}{\partial x} - \frac{\partial u}{\partial z}, \tag{10}$$

where the fluctuation of the vertical velocity $\partial w/\partial x$ is much weaker than the streamwise fluctuation $\partial u/\partial z$, so the term $\partial w/\partial x$ is neglected in the present calculation. The lateral vorticity profile is shown in

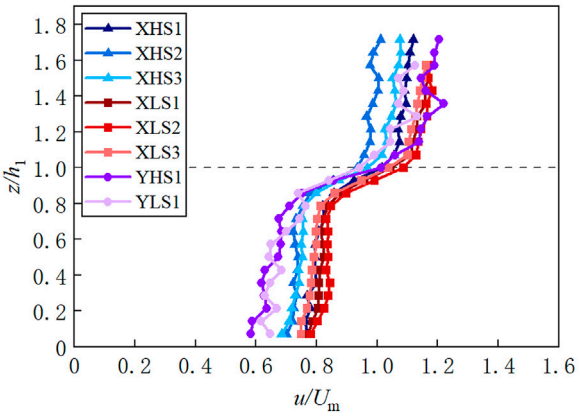

FIGURE 5
Vertical profile of the dimensionless mean longitudinal velocity for each run. The black dotted line represents the height of the short cylinders.

Figure 6. In Figures6A–G, the lateral vorticity basically stays constant, being about zero in the lower zone of the short vegetation layer and upper zone of the tall vegetation layer, and there is a spike at the junction of short and tall vegetation layer. It shows that the momentum exchange in zone B is distinctly larger than in zones 1A and 2A. The results are similar to the lateral vorticity profiles of single-layered rigid vegetation flow found in Liu et al. (2008), and double-layered vegetation flow of Liu et al. (2010) and Singh et al. (2019). The vorticity distribution perfectly corresponds to the velocity distribution in Figure 4. The lateral vorticity profiles of run YLS1 show a strong fluctuation in zones 1A and 2A, and there is an exceptional value in run XHS2 at z = .115 m, possibly due to the experimental error at some measurement points.

5 Application of the velocity model

5.1 Velocity model validation and error analysis

The application of the velocity model should base on the determination of the two parameters: The length scale of the mixing layer zone B (δ_w) and the vegetation drag coefficient (C_D).

For simplicity, the deflection points of the mixing layer are determined using the method in Truong et al. (2019), which is used to define the edge of the penetration length in the vegetated zone and non-vegetated zone. The deflection points z_1 and z_2 are defined as the streamwise velocity $u_{z_1} = (1 + 5\%) \cdot \overline{u_{1A}}$ and $u_{z_2} = (1 - 5\%) \cdot \overline{u_{2A}}$, respectively.

The drag coefficient is calculated using the measurement data in zone 1A:

$$C_D = \frac{gi(1-\lambda_1)}{\frac{1}{2}Dm_1\overline{u_{1A}}^2}. \tag{11}$$

In runs X, the velocity model almost agrees well with the experimental data (Figures 7A–F), but underestimates or overestimates the velocity of zone 2A in runs Y (Figures 7G, H).

Moreover, in order to intuitively present the deviation of the predicted velocity from the measured velocity, the relative error (*RE*) is defined as follow:

$$RE = \frac{|U_{mod} - u_{mea}|}{u_{mea}}. \tag{12}$$

where U_{mod} is the predicted velocity of the model, and u_{mea} is the measured velocity. Figure 8 shows the *RE* at each measuring point of runs X along the water depth. The *RE* are relatively small in general, indicating that the model is a good reflection of the flow velocity profile. However, the *RE* in the near-bed 1 cm zone, zone B and zone 2A are larger than those in zone 1A, because the constant velocity model in zone 1A cannot catch the influence of boundary conditions precisely, and the entire velocity model is dependence on the C_D and δ_w determined by the measurement data in zone 1A, leading to a higher *RE* in zone B and 2A.

It is mentioned in Section 4.2 that the slope does not contribute to β, and the velocity model of zone 2A applied here denotes that the uniform velocity term difference between zone 2A and zone 1A is only related to the density of two vegetation layers, i.e., $U_{UD2}/U_{UD1} = \sqrt{\alpha(1-\lambda_1/1-\lambda_2)}$, the calculated values of runs X and runs Y are 1.406 and 1.715 respectively, while the β of runs X is 1.35–1.44, and 1.59–1.80 of runs Y. Therefore, it shows a small deviation in the modeling of the velocity in zone 2A. The model application results also verify that the longitudinal velocity in double-layered rigid vegetation flow follows a hyperbolic tangent distribution in the mixing layer as the distribution in single-layered submerged flexible vegetation flow, which may extend to the prediction of the mixing layer velocity in multi-layered vegetation flow; for instance, the velocity in a mixing layer can be expressed as the linear superposition of a uniform velocity in the lower layer and a hyperbolic tangent profile.

5.2 Relationship between C_D and the U_{UD1} term

The C_D of this paper was estimated from the flow condition in zone 1A, and the dependence of the C_D on the stem Reynolds number of zone 1A $Re_{UD1}=(U_{UD1}D)/\nu$ for runs X is illustrated in Figure 9. It shows that C_D decreases as the Re_{UD1} increases and has an increasing tendency to a growing slope *J*. This trend is probably due to the vortices penetrating deeper into the vegetation, and the gravitational component of the water along the slope direction is more significant with an increased slope, creating a more considerable vegetation drag. The results are consistent with the experimental data of single-layered submerged vegetation flow published in Nikora et al. (2013).

6 Discussion

6.1 Edge of the mixing layer

This study is concerned with the influence of vegetation on the gravity-driving term compared with the velocity model proposed by Huai et al. (2014). The upper inflection point z_2 of the mixing layer is found above the top of the short vegetation canopy, while this point appears at the height of short vegetation in

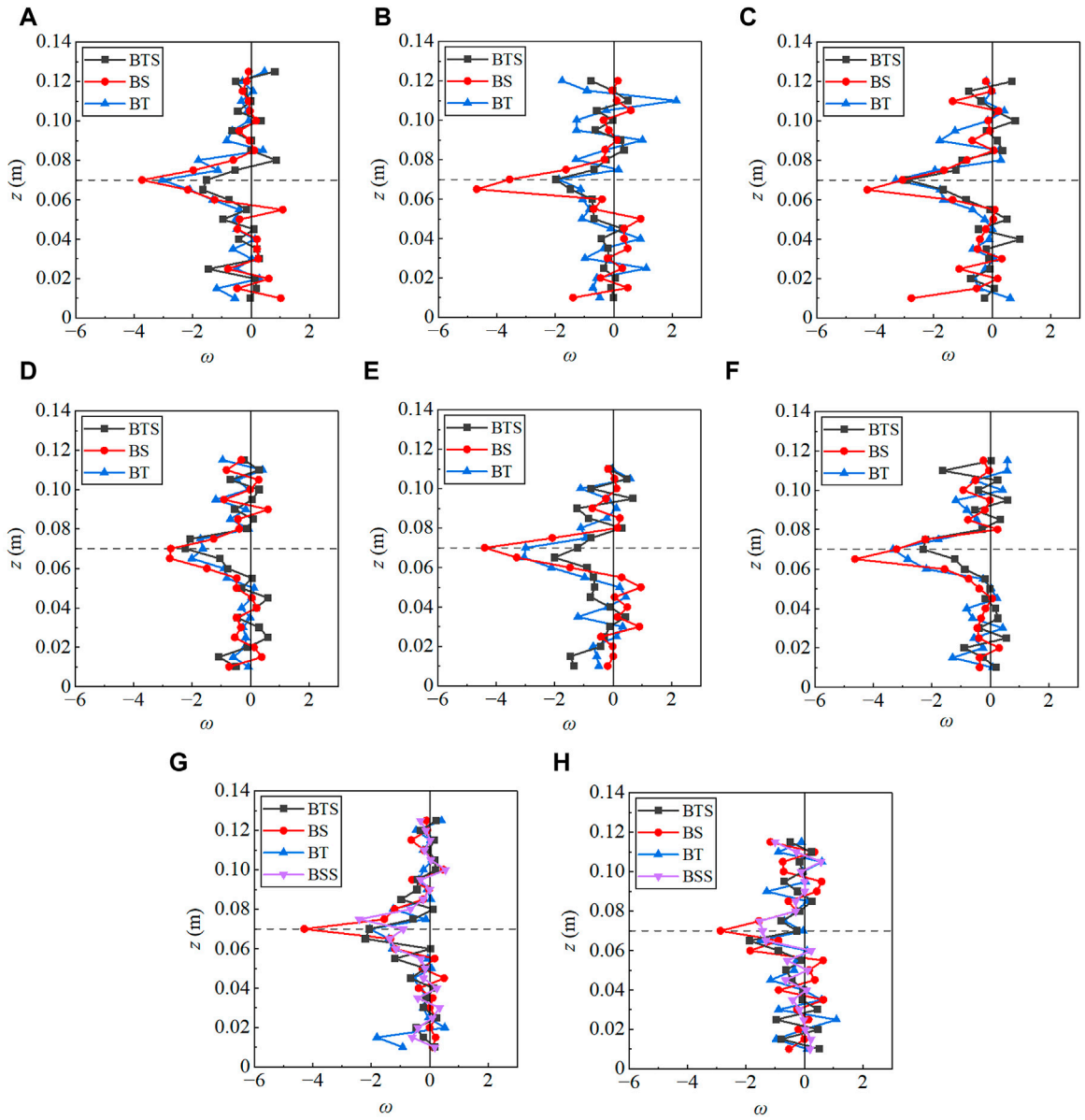

FIGURE 6
Lateral vorticity profile of different measurement locations, **(A–C)** present results for runs XHS1 to XHS3, **(D–F)** present results for runs XLS1 to XLS3, **(G,H)** present results for runs YHS1 and YLS1, respectively. The black dotted line represents the height of the short cylinders.

study of Huai et al. (2014). It is learned that the penetration length scale will change in different situations. The dense vegetation density (m_1 = 778 plant·m^{-2}) in this study may cause larger scale coherent vortices and thus penetrate to the tall vegetation layer, compared with the sparse vegetation density (m_1 = 117 plant·m^{-2}) in Huai et al. (2014); Figure 6 shows that the lateral vorticity reaches a peak at the height of short vegetation and decreases to zero near z = .075–.08 m, verifying the existence of the large-scale Kelvin-Helmholtz vortices. Moreover, according to Figures 4E, 8A in the study of Anjum and Tanaka (2020), the Reynolds stress turbulence model of double-layered vegetation flow indicates that the mixing region affected by the vertical coherent vortices contains the zone in short vegetation layer and tall vegetation layer, it is reasonable to assume that the upper inflection point of the mixing layer lies above the short vegetation canopy.

6.2 Impact of the boundary friction

A slightly increasing tendency of the velocity in zone 1A (Figure 5), indicates the insignificant effect of the near-bed boundary friction. Recall from Eq. 2, the bed shear stress friction $[\tau_{bed}(1-\lambda_1)Wdx]$ was compared against the vegetation drag $[\frac{1}{2}\rho C_D m_1 D U_{\mathrm{UD1}}{}^2 W(z_2-\delta_w)dx]$ in zone 1A, which is given as:

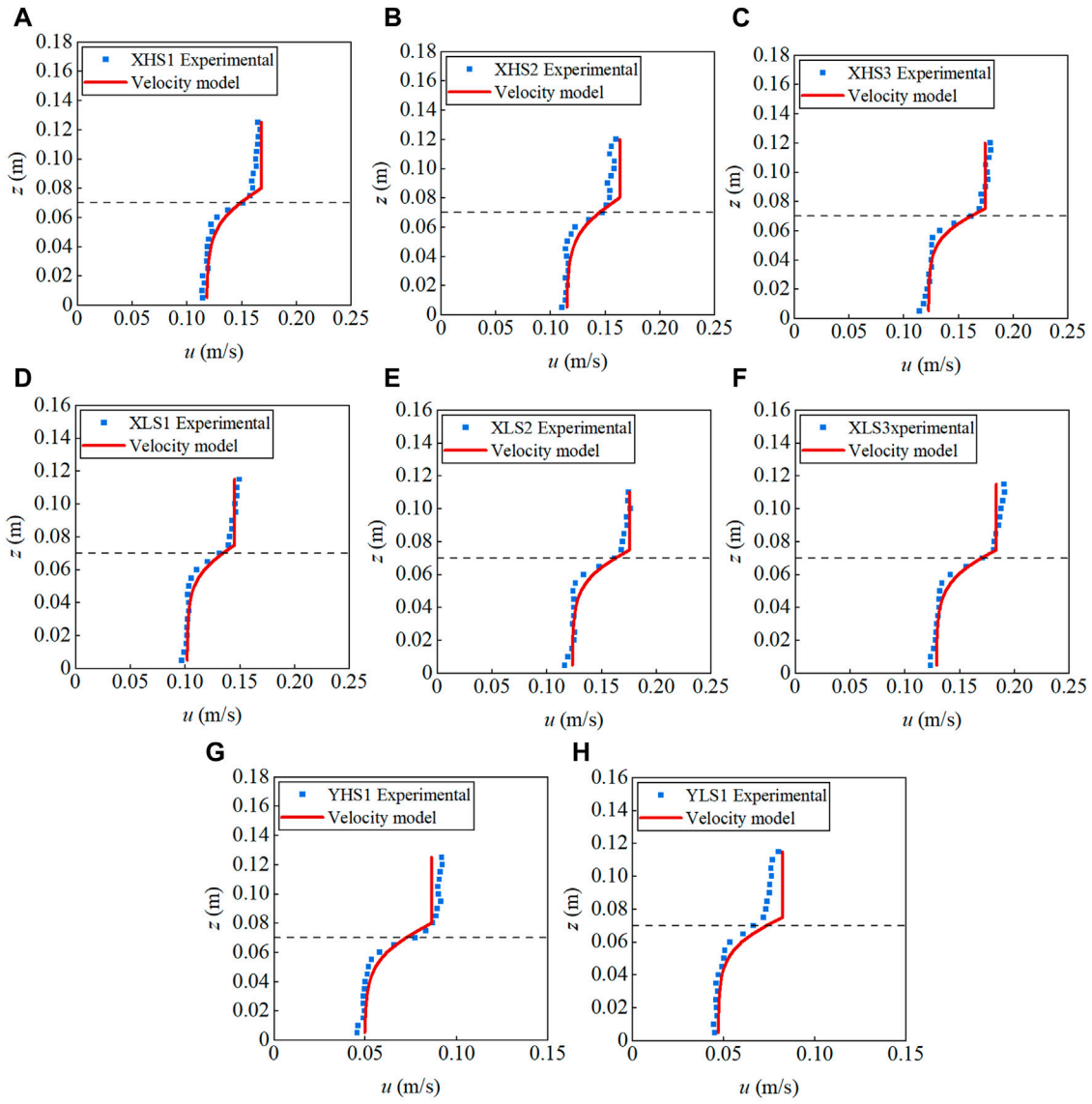

FIGURE 7
The velocity profile of the experimental data and predicted model for runs X and runs Y, the black dotted line represents the height of the short cylinders. **(A-F)** present results for runs X, and **(G, H)** present results for runs Y.

$$\frac{\tau_{bed}(1-\lambda_1)Wdx}{\frac{1}{2}\rho C_D m_1 D U_{UD1}{}^2 W z_1 dx} = \frac{f_{bed}(1-\lambda_1)}{4C_D m_1 D z_1}. \tag{13}$$

For run YHS1, the $\lambda_1 = 0.022$, $C_D = 1.68$, $z_1 = 0.055$m, and the $f_{bed} = 0.01 - 0.05$ of the plexiglass plate was estimated by a Moody chart roughness height $k_s = 0.0025$mm (Zhang et al., 2020). Substituting the maximum value of the roughness parameter $f_{bed} = .05$ into Eq. 13 and yields a result of 2.80%. It means that compared with the vegetation drag the near-bed boundary friction is negligible in the momentum balance equation by comparing with the vegetation drag. Similarly, according to Eqs 2, 3, the sidewall friction term $[2z_1\tau_{wall}dx]$ and $[2(H-z_2)\tau_{wall}dx]$ were compared with the vegetation drag in zone 1A and zone 2A, respectively, as the following equations:

$$\frac{2z_1\tau_{wall}dx}{\frac{1}{2}\rho C_D m_1 D U_{UD1}{}^2 W z_1 dx} = \frac{f_{wall}}{2C_D m_1 DW}, \tag{14}$$

$$\frac{2(H-z_2)\tau_{wall}dx}{\frac{1}{2}\rho C_D m_2 D U_{UD2}{}^2 W (H-z_2) dx} = \frac{f_{wall}}{2C_D m_2 DW}. \tag{15}$$

For run YHS1, $f_{wall} = 0.05$ is selected to calculate Eqs 14, 15, and gets results of 1.06% and 3.19%, respectively. Even if the roughness conditions f_{bed} and f_{wall} being taken as the maximum value .05 in the sparsest vegetation arrangement run, the bed friction and sidewall friction reveal a small proportion relative to vegetation drag. Therefore, it is reasonable to assume that the boundary friction is negligible for all runs.

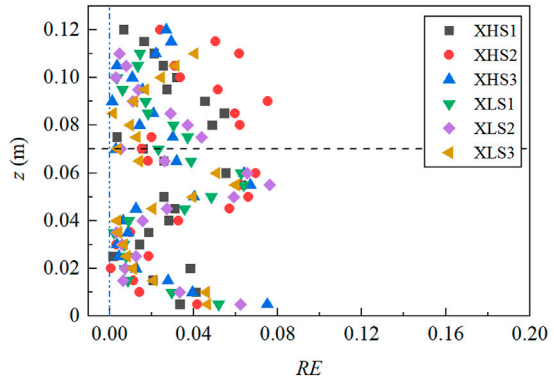

FIGURE 8
Relative error between the analytical model and the experimental velocity of runs X. The black dotted line represents the height of the short cylinders.

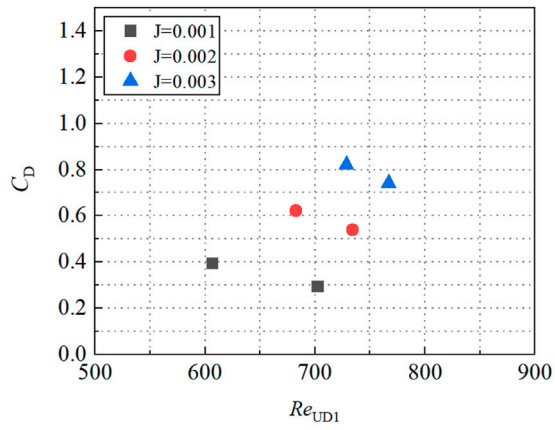

FIGURE 9
Dependence of the C_D on the Reynolds number of zone 1A for runs X.

6.3 The effect of the wake vortices

Eqs 6, 7 predict that the velocity is constant in zone 1A and zone 2A, but measured velocity has an increasing trend in zone 2A in Figure 7 and the model needs to be further improved. The velocity increasing is likely put down to the wake vortices generated by the cylinders, which are limited by the tall cylinders but not totally eliminated compared with the single-layered vegetation flow. In submerged vegetation flow, the wake region effect term can be approximately presented as a trigonometric function (Nikora et al., 2013):

$$U_{WF} = u_{*m}\frac{2\Pi}{\kappa}\sin^2\left(\frac{\pi z}{2H}\right). \quad (16)$$

where u_{*m} is the shear velocity and is usually expressed as a formula of the maximum values of Reynolds stress which is usually found at the top of the vegetation layer (Järvelä, 2005; Nepf, 2012) i.e., $u_{*m} = \sqrt{-(\overline{u'w'})_{max}}$, and the u_{*m} applied here is calculated using the Reynolds stress at the short vegetation height, κ = .40 is the Von Kármán constant, Π is Coles's wake strength parameter and was suggested equal to .2 in uniform flows (Nezu and Rodi, 1986).

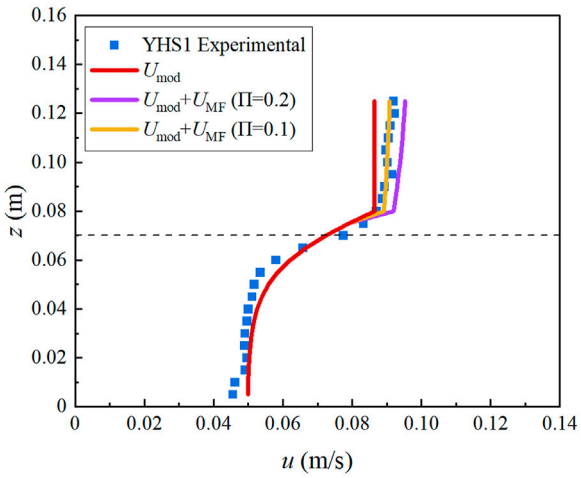

FIGURE 10
The effect of wake term to the velocity model of run YHS1. The black dotted line represents the height of the short vegetation.

For the density of tall vegetation layer is sparser of Y arrangement than X, the increasing tendency of the velocity at zone 2A is more significant of runs YHS1 and YLS1, and the wake region effect is discussed of run YHS1. As shown in Figure 10, considering the wake term in the flow velocity model indeed can better reflect the experimental velocity characteristic in zone 2A. The Coles's wake strength parameter changes from .2 to a value of .1, which means the resistance of the tall vegetation can significantly reduce the Coles's wake strength parameter. The applicability of the wake parameter value to the velocity model of double-layered vegetation needs to be further explored.

7 Conclusion

Through flume experiments using ADV, the flow characteristics of uniform flow with double-layered rigid vegetation are studied, including the longitudinal velocity and lateral vorticity profiles. The proposed model combined the mixing layer concepts in Nikora et al. (2013) and the force balance equations have an acceptable agreement with the experimental data.

(1) In the double-layered vegetation flow, the longitudinal velocity roughly follows a "constant-increasing-constant" distribution vertically. The upper inflection point of the mixing layer zone is found above the height of the short vegetation canopy. When the water depth and vegetation density are the same, the longitudinal velocity has positive tendency with the increasing slope.
(2) It is verified that the velocity profile in zone 2A can be obtained by solving the momentum equation of the balance between the vegetation drag and potential gradient. The velocity in zone 1A and zone B can be predicted by the superposition of the concepts of a uniform velocity distribution in zone 1A (U_{UD1}) and a hyperbolic tangent profile (U_{ML}) as the profile in single-layered submerged flexible vegetation flow.
(3) The effects of wake vortices and boundary friction on the velocity model are further explored.

It is worth noting that taking the influence of the vegetation on the gravity-driving term into consideration when solving the force balance equation can describe the velocity profile more precisely. And the velocity model of multi-layered vegetation flow should be further studied based on the research about double-layered vegetation flow in the future.

Data availability statement

The original contributions presented in the study are included in the article/Supplementary Material, further inquiries can be directed to the corresponding authors.

Author contributions

QW, YZ, and PW designed the research. QW, YZ, and TF conducted the experiment. QW wrote the paper. YZ, PW, TF and YB reviewed the paper. All authors read and approved the submitted version.

Funding

The National Natural Science Foundation of China (52179056).

Conflict of interest

The authors declare that the research was conducted in the absence of any commercial or financial relationships that could be construed as a potential conflict of interest.

Publisher's note

All claims expressed in this article are solely those of the authors and do not necessarily represent those of their affiliated organizations, or those of the publisher, the editors and the reviewers. Any product that may be evaluated in this article, or claim that may be made by its manufacturer, is not guaranteed or endorsed by the publisher.

References

Anjum, N., and Tanaka, N. (2020). Investigating the turbulent flow behaviour through partially distributed discontinuous rigid vegetation in an open channel. *River Res. Appl.* 36 (8), 1701–1716. doi:10.1002/rra.3671

Chen, Z. B., Jiang, C. B., and Nepf, H. M. (2013). Flow adjustment at the leading edge of a submerged aquatic canopy. *Water Resour. Res.* 49, 5537–5551. doi:10.1002/wrcr.20403

Cheng, N. S. (2013). Calculation of drag coefficient for arrays of emergent circular cylinders with pseudofluid model. *J. Hydraulic Eng.* 139 (6), 602–611. doi:10.1061/(asce)hy.1943-7900.0000722

Fan, X. J., Lei, P., Wang, C., and Liu, G. Y. (2020). Influence of flexible submerged vegetation on flow characteristics under different arrangement patterns. *J. Huazhong Univ. Sci. Technol. Nat. Sci. Ed.* 48 (3), 127–132.

Huai, W. X., Li, S., Katul, G. G., Liu, M. Y., and Yang, Z. H. (2021). Flow dynamics and sediment transport in vegetated rivers: A review. *J. Hydrodynamics* 33 (3), 400–420. doi:10.1007/s42241-021-0043-7

Huai, W. X., Wang, W. J., Hu, Y., Zeng, Y. H., and Yang, Z. H. (2014). Analytical model of the mean velocity distribution in an open channel with double-layered rigid vegetation. *Adv. Water Resour.* 69, 106–113. doi:10.1016/j.advwatres.2014.04.001

Huai, W. X., Yang, L., Wang, W. J., Guo, Y., Wang, T., and Cheng, Y. (2019). Predicting the vertical low suspended sediment concentration in vegetated flow using a random displacement model. *J. Hydrology* 578, 124101. doi:10.1016/j.jhydrol.2019.124101

Järvelä, J. (2005). Effect of submerged flexible vegetation on flow structure and resistance. *J. Hydrology* 307, 233–241. doi:10.1016/j.jhydrol.2004.10.013

Kubrak, E., Kubrak, J., and Rowinski, P. M. (2008). Vertical velocity distributions through and above submerged, flexible vegetation. *Hydrological Sci. J.* 53 (4), 905–920. doi:10.1623/hysj.53.4.905

Li, D., Yang, Z. H., Zhu, Z. T., Guo, M., Gao, W., and Sun, Z. H. (2020). Estimating the distribution of suspended sediment concentration in submerged vegetation flow based on gravitational theory. *J. Hydrology* 587, 124921. doi:10.1016/j.jhydrol.2020.124921

Li, L., Shi, X., and Li, J. T. (2022). Experimental study on vegetation flow characteristics under rigid-flexible and flexible-rigid patterns. *China Rural Water Hydropower* 64 (10), 67–73. doi:10.12396/znsd.212119

Liu, C., and Nepf, H. (2016). Sediment deposition within and around a finite patch of model vegetation over a range of channel velocity. *Water Resour. Res.* 52, 600–612. doi:10.1002/2015wr018249

Liu, D., Diplas, P., Fairbanks, J. D., and Hodges, C. C. (2008). An experimental study of flow through rigid vegetation. *J. Geophys. Res.* 113, 4015. doi:10.1029/2008jf001042

Liu, D., Diplas, P., Hodges, C. C., and Fairbanks, J. D. (2010). Hydrodynamics of flow through double layer rigid vegetation. *Geomorphology* 116 (4), 286–296. doi:10.1016/j.geomorph.2009.11.024

Nepf, H. (2012). Hydrodynamics of vegetated channels. *J. Hydraulic Res.* 50 (3), 262–279. doi:10.1080/00221686.2012.696559

Nezu, I., and Rodi, W. (1986). Open-channel flow measurements with a laser Doppler anemometer. *J. Hydraulic Eng.* 112 (5), 335–355. doi:10.1061/(asce)0733-9429(1986)112:5(335)

Nikora, N., Nikora, V., and O'Donoghue, T. (2013). Velocity profiles in vegetated open-channel flows: Combined effects of multiple mechanisms. *J. Hydraulic Eng.* 139, 1021–1032. doi:10.1061/(asce)hy.1943-7900.0000779

Qu, G. (2014). "Experimental study on water and sediment transport in open channel flow with vegetation,". Doctoral dissertation (Wuhan, China: Wuhan University).

Rahimi, H. R., Tang, X., and Singh, P. (2020). Experimental and numerical study on impact of double layer vegetation in open channel flows. *J. Hydrologic Eng.* 25 (2), 4019064. doi:10.1061/(asce)he.1943-5584.0001865

Singh, P., Rahimi, H. R., and Tang, X. (2019). Parameterization of the modeling variables in velocity analytical solutions of open-channel flows with double-layered vegetation. *Environ. Fluid Mech.* 19, 765–784. doi:10.1007/s10652-018-09656-8

Tang, H. W., Yan, J., and Lu, S. Q. (2007). Advances in research on flows with vegetation in river management. *Adv. Water Sci.* 18 (5), 785–792. doi:10.3321/j.issn:1001-6791.2007.05.024

Tang, X. N., Rahimi, H., Guan, Y. T., and Wang, Y. X. (2021). Hydraulic characteristics of open-channel flow with partially-placed double layer rigid vegetation. *Environ. Fluid Mech.* 21 (2), 317–342. doi:10.1007/s10652-020-09775-1

Truong, S. H., Uijttewaal, W. S. J., and Stive, M. J. F. (2019). Exchange processes induced by large horizontal coherent structures in floodplain vegetated channels. *Water Resour. Res.* 55, 2014–2032. doi:10.1029/2018wr022954

Tseng, C. Y., and Tinoco, R. O. (2021). A two-layer turbulence-based model to predict suspended sediment concentration in flows with aquatic vegetation. *Geophys. Res. Lett.* 48 (3), 91255. doi:10.1029/2020gl091255

Velasco, D., Bateman, A., Redondo, J. M., and Demedina, V. (2003). An open channel flow experimental and theoretical study of resistance and turbulent characterization over flexible vegetated linings. *Flow Turbul. Combust.* 70 (4), 69–88. doi:10.1023/b:appl.0000004932.81261.40

Wang, P., and Cirpka, O. A. (2021). Surface transient storage under low-flow conditions in streams with rough bathymetry. *Water Resour. Res.* 57 (12), 29899. doi:10.1029/2021wr029899

Wang, W. J., Cui, X. Y., Dong, F., Peng, W. Q., Han, Z., Huang, A. P., et al. (2020). Predictions of bulk velocity for open channel flow through submerged vegetation. *J. Hydrodyn.* 32 (4), 795–799. doi:10.1007/s42241-020-0040-2

Wang, W. J., Huai, W. X., Li, S. L., Wang, P., Wang, Y. F., and Zhang, J. (2019b). Analytical solutions of velocity profile in flow through submerged vegetation with variable frontal width. *J. Hydrology* 578, 124088. doi:10.1016/j.jhydrol.2019.124088

Wang, W. J., Huai, W. X., Thompson, S., and Katul, G. G. (2015). Steady nonuniform shallow flow within emergent vegetation. *Water Resour. Res.* 51 (12), 10047–10064. doi:10.1002/2015wr017658

Wang, W. J., Peng, W. Q., Huai, W. X., Katul, G. G., Liu, X. B., Qu, D., et al. (2019a). Friction factor for turbulent open channel flow covered by vegetation. *Sci. Rep.* 9, 5178. doi:10.1038/s41598-019-41477-7

Wang, Z., Li, G. B., He, X. Q., Liu, Y., and Wang, Z. K. (2019c). Water flow resistance characteristics of double-layer vegetation in different submerged states. *Water Supply* 19 (8), 2435–2442. doi:10.2166/ws.2019.125

Xu, Y., and Nepf, H. M. (2020). Measured and predicted turbulent kinetic energy inflow through emergent vegetation with real plant morphology. *Water Resour. Res.* 56, 27892. doi:10.1029/2020wr027892

Xu, Y., and Nepf, H. M. (2021). Suspended sediment concentration profile in a *Typha Latifolia* Canopy. *Water Resour. Res.* 57, 29902. doi:10.1029/2021wr029902

Yang, J. Q., Kerger, F., and Nepf, H. M. (2015). Estimation of the bed shear stress in vegetated and bare channels with smooth beds. *Water Resour. Res.* 51, 3647–3663. doi:10.1002/2014wr016042

Zhang, J., Wang, W., Shi, H. R., Wang, W. J., Li, Z. B., and Xia, Z. H. (2021). Two-zone analysis of velocity profiles in a compound channel with partial artificial vegetation cover. *J. Hydrology* 596. doi:10.1016/j.jhydrol.2021.126147126147

Zhang, Y. G., Wang, P., Cheng, J. H., Wang, W. J., Zeng, L., and Wang, B. (2020). Drag coefficient of emergent flexible vegetation in steady nonuniform flow. *Water Resour. Res.* 56 (8), 1–16. doi:10.1029/2020wr027613

Zhang, Y. H., and Lai, X. J. (2015). Impact of Vallisneria natans on flow structure. *Adv. Water Sci.* 26 (1), 99–106. doi:10.14042/j.cnki.32.1309.2015.01.013

Zhang, Y. H. (2014). Research progress in effect of vegetation on flow and sediment transport. *Wetl. Sci.* 12 (5), 669–676. doi:10.13248/j.cnki.wetlandsci.2014.05.020

Zhao, F., Huai, W. X., Hu, Y., and Wang, W. J. (2015). Characteristic study of open-channel flow through double layer rigid vegetation. *J. Huazhong Univ. Sci. Technol. Nat. Sci. Ed.* 43 (01), 85–90. doi:10.13245/j.hust.150118

Zhao, F. (2017). "Research on hydraulic characteristics of open channel flows with rigid vegetation,". Doctoral dissertation (WuhanWuhan, China: Wuhan University).

frontiers | Frontiers in Marine Science

TYPE Original Research
PUBLISHED 24 January 2023
DOI 10.3389/fmars.2023.1065100

OPEN ACCESS

EDITED BY
Weijie Wang,
China Institute of Water Resources and Hydropower Research, China

REVIEWED BY
Lili Wang,
Agro-Environmental Protection Institute (CAAS), China
Laibin Huang,
University of California, Davis, United States
Bowen Zhang,
Ball State University, United States

*CORRESPONDENCE
Baoshan Cui
cuibs@bnu.edu.cn
Ze Ren
renzedyk@gmail.com

†These authors have contributed equally to this work

SPECIALTY SECTION
This article was submitted to Marine Ecosystem Ecology, a section of the journal Frontiers in Marine Science

RECEIVED 09 October 2022
ACCEPTED 09 January 2023
PUBLISHED 24 January 2023

CITATION
Li X, Cai Y, Liu Z, Mo X, Zhang L, Zhang C, Cui B and Ren Z (2023) Impacts of river discharge, coastal geomorphology, and regional sea level rise on tidal dynamics in Pearl River Estuary.
Front. Mar. Sci. 10:1065100.
doi: 10.3389/fmars.2023.1065100

Impacts of river discharge, coastal geomorphology, and regional sea level rise on tidal dynamics in Pearl River Estuary

Xia Li[1,2,3†], Yanzi Cai[2,4†], Zezheng Liu[2,4], Xiaobiao Mo[5], Li Zhang[3,6,7], Cheng Zhang[1,8], Baoshan Cui[2,4*] and Ze Ren[1,2*]

[1]Research and Development Center for Watershed Environmental Eco-Engineering, Beijing Normal University, Zhuhai, China, [2]State Key Laboratory of Water Environment Simulation, School of Environment, Beijing Normal University, Beijing, China, [3]Southern Ocean Science and Engineering Guangdong Laboratory (Guangzhou), Guangzhou, China, [4]School of Environment, Beijing Normal University, Beijing, China, [5]Faculty of Arts and Sciences, Beijing Normal University, Zhuhai, China, [6]South China Sea Institute of Oceanology, Chinese Academy of Sciences (CAS), Guangzhou, China, [7]University of Chinese Academy of Sciences, Beijing, China, [8]School of Engineering Technology, Beijing Normal University, Zhuhai, China

Introduction: Recently, accelerated sea-level rise (SLR) has raised major concerns on estuarine management and restoration because it modifies estuarine hydrodynamics, such as tidal inundation extent and amplitude, tidal current asymmetry, flood frequency, etc. Understanding underlying processes which regulate estuarine tidal dynamics is critical for mitigating potential impacts on the coastal population and development.

Methods: We selected the Pearl River Estuary (PRE), an estuary with a higher regional SLR compared to the global SLR as the study area. To identify the effects of regional SLR on tidal dynamics, we analyzed long-term records of four tidal variables from 19 gauge stations between 1952 and 2020, including annual highest tidal levels (AHTLs), annual lowest tidal levels (ALTLs), annual mean tidal ranges (AMTRs), and annual mean tidal levels (AMTLs).

Results: Results suggested that variability in tidal variables was site-specific. The AMTRs decreased gradually from offshore regions to the upper reaches of rivers with a maximum at the mouth of the estuary. In contrast, the magnitudes of the AHTLs, AMTLs, and ALTLs decreased when approaching the coastline. Distance to the coastline had the highest correlations with the AHTLs, ALTLs, and AMTLs, followed by river width and river depth. The local SLR was responsible for the temporal variability in AHTLs, ALTLs, and AMTLs at the estuarine mouth with correlation coefficients from 0.43 to 0.85 ($P < 0.001$) but showed low correlations with these three tidal variables at the upper reaches of rivers ($P > 0.001$). Instead, the tidal variables were highly correlated with river discharge at the upper reaches of rivers, especially for the AHTLs (correlation coefficient = 0.83, $P < 0.0001$).

Conclusions: Our study demonstrated that the tidal dynamics demonstrate significant spatial-temporal variability. Geomorphology, river discharge, and sea levels have jointly affected estuarine hydrodynamics.

KEYWORDS

tidal dynamics, climate change, estuarine hydrology, temporal trends, spatial variability

1 Introduction

Estuaries are transition zones from rivers to the ocean and provide irreplaceable services such as natural habitat, recreation, navigation, and energy generation. Recently, concerns have been mounting around the vulnerability of estuaries to oceanic sea-level rise (SLR) (Khojasteh et al., 2020). Rising water levels in estuaries can potentially elevate proportions of inundation in surrounding low-lying lands, leading to severe flooding, intensification of storm surge, coastal erosion, and soil salinization (FitzGerald et al., 2008; Haigh et al., 2010; Burgos et al., 2018; Khojasteh et al., 2020; Khojasteh et al., 2021b). According to the Sixth Assessment Report (AR6) of the Intergovernmental Panel on Climate Change (IPCC), the global sea level could rise by 0.63-1.01 m under higher greenhouse gas (GHG) emission scenarios by 2100 and may even exceed 2 m due to a possible melt of the Antarctic and Greenland Ice Sheet (Bamber et al., 2019; Horton et al., 2020; Masson-Delmotte et al., 2021). Moreover, increased anthropogenic pressures from urbanization, land reclamation, and agricultural development reduce streamflow, change estuarine hydrological patterns, and threaten ecological integrity and environmental services (Zhang et al., 2010; Gao et al., 2014; Ma et al., 2019; Xie et al., 2020).

Tides (e.g., tidal range, prism, current) are key components of estuarine hydrology. In most estuaries, the gravitational effects of the Moon and Sun on the ocean are the dominant forces that cause water vertical or horizontal movements. These movements are usually referred to as tides. Dynamics in tides reflect the joint impacts of coastal processes and anthropogenic pressures on salt-fresh water mixture, circulation, sedimentation, nutrient transport, and primary productivity (Dieckmann et al., 1987; Mao et al., 2004; Bouillon et al., 2007; Liu et al., 2021a). For example, high tide is often associated with flooding and tidal asymmetry, which causes traffic problems and damage to low-lying infrastructure (Dronkers, 1986; Cherqui et al., 2015; Nabangchang et al., 2015; Fant et al., 2021). Tidal range and current have been identified as the predominant factors controlling the transport of suspended particulate matters, ultimately changing subsidence dynamics and primary productivity distributions in flat tidal zones (Dieckmann et al., 1987; Fitzgerald, 1996; Raw et al., 2019; Wang et al., 2021). Moreover, an enlarged tidal range would significantly influence water quality due to increased hydraulic gradient and saltwater intrusion (Vandenbohede and Lebbe, 2006). Therefore, an improved understanding of tidal variability will be beneficial for better environment assessments and management in coastal areas.

Geometry (e.g., length, width, depth, and shapes of the estuary) and energy drivers (e.g., river discharges, waves) are the main external drivers causing the spatial and temporal variability in tidal dynamics due to their impacts on friction, stratification, reflection, and resonance processes (Mao et al., 2004; Haigh et al., 2020; Khojasteh et al., 2021b; Khojasteh et al., 2021a; Talke et al., 2021). Channel shapes impact the tides through controlling concentrations of energy fluxing to estuaries. In converging (upstream narrowing) estuaries, the tide- and wave-driver energy funneled from sea to estuaries has been considered as the main factor determining tidal range (Van Rijn, 2011). Bathymetric characteristics of an estuary, as another geometric driver, also influence tides because the tidal levels may increase with decreased depth under a constant energy flux (Van Rijn, 2011). The additional source of energy, such as upland flows, tends to reduce the tidal range in upstream areas (Godin, 1999; Horrevoets et al., 2004). Climate change in conjunction with intensifying human activities, has further complicated the coastal hydrodynamics, such as tidal amplitude changes in response to sea level rises (SLRs) and tidal velocity decreases due to human-induced siltation (Wolanski et al., 2001; Pelling et al., 2013a; Pelling et al., 2013b). Since estuarine hydrodynamics have been receiving increasing attention (Moftakhari et al., 2017; Khojasteh et al., 2021b; Talke et al., 2021), a comprehensive understanding of river discharge, coastal geomorphology, and their combined impacts on tidal variability is essential and can provide a necessary basis for evaluating SLR influences on estuaries in the context of environmental changes.

The Pearl River Estuary (PRE) is located at the northern margin of the South China Sea, with tides propagating from the Pacific Ocean. According to the SOA, (2020) the estuary suffers from an extremely high regional SLR. The global average rate of SLR was about 3.3 mm yr^{-1} between 1993 and 2020, but PRE experienced an increased rate of 3.9 mm yr^{-1} in SLR during the same period. Although the higher regional SLR in PRE has enhanced the surface elevation of peak storm surge and typhoon intensity (Yin et al., 2017; Zhang et al., 2017; Jian et al., 2021), it did not significantly increase the submerged area in PRE, as was predicted by Li et al. (Li et al., 1993). Instead, intensified human activities, such as dam construction and reclamation, have led to changes in upstream discharge, accelerated losses of the shoals and waterways, alterations in inundation area distributions, and landward migration of coastlines (Chen et al., 2005; Li and Damen, 2010; Shao et al., 2020; Liu et al., 2021b). Tidal changes in our study area have never been systemically analyzed, posing challenges to climate change mitigation and environmental risk management. The long-term and spatially-explicit study can help us better understand the tidal changes under regional SLR, which is urgent for flood control and coastal ecosystem management in the Pearl River Bay area. Therefore, our study aims to investigate the long-term tide variability under climate change and human disturbances. The objectives of this study are to 1) investigate spatial and temporal variability in tides in PRE and 2) explore to which extent the SLR dominates the tidal dynamics.

2 Study area

As the second largest estuary in China, the PRE is located along the coast of Guangdong Province, with a longitude of 113°E-115°E and a latitude of 21°N-23°N. The mean annual rainfall ranges from 1600 to 2300 mm, and the mean annual temperature ranges from 14 to 22 °C. Tides propagate from offshore to the estuary, resulting in a mean tidal range from 1.0 to 1.7m. The Pearl River, including three main branches - West River, North River, and East River, flows into the South China Sea through PRE. The annual average freshwater discharge of Pearl River is 10,000 m^3 s^{-1}, with a maximum of 20,000 m^3 s^{-1} in the wet seasons and a minimum of 3,600 m^3 s^{-1} in the dry seasons (Zhang et al., 2008). In total, the Pearl River delivers 350×10^9 m^3 of freshwater and 85×10^6 tons of sediment loads to PRE per year.

The PRE is subject to intensive human interventions and climate change. Anthropogenic activities have caused sustainable changes in

ecology, environments, and hydrology. From 1990 to 2015, construction land increased about two times (Liu et al., 2019). Accelerated urbanization resulted in landscape fragmentation (Hu et al., 2021), notorious pollution (Wang and Hao, 2020), hydrological connectivity changes (Shao et al., 2020), and discharge reduction (Horrevoets et al., 2004; Liu et al., 2022), leading to the irreversible structural and functional deterioration of the estuarine ecosystem (Zhang et al., 2010).

3 Methods and materials

3.1 Data collection

We collected annual highest tidal levels (AHTLs), annual lowest tidal levels (ALTLs), annual mean tidal ranges (AMTRs), and annual mean tidal levels (AMTLs) from 19 gauge stations in the PRE area to explore the hydrodynamics of the estuary (Figure 1). The AHTL group refers to the largest tidal level over a year at a station, caused by storm surges (Talke and Jay, 2020). On the contrary, the ALTL is the lowest tidal level at a station over a year. The AMTL is the mean daily tidal level obtained by averaging the daily high mean tidal level and low mean tidal level. The tidal range is defined as the differences between the high mean tidal level and the low mean tidal level per day, and the AMTR is the annual averaged value of tidal ranges. The start times of the gauge observations vary with stations with the earliest observations being in 1951. Besides tidal levels, we also collected streamflow data of the Pearl River from Makou, Sanshui, and Bolou stations. We digitalized all the above data from the Hydrological Yearbooks of the People's Republic of China.

Geomorphological variables, such as distances of hydrological stations to the estuary (DTE), distances to the coastline (DTC), river channel width (RW), and water depth (WD), were derived from multiple sources (Table 1). The DTE is defined as the distance of a station to the estuary. This variable was digitalized from the Hydrological Yearbooks of the People's Republic of China. Based on the locations and DTE, we renamed the stations using the abbreviations of main branches plus the ranking of stations according to the DTE values from the lowest to the highest. The river channel width was an averaged width over a 400 - 500 m waterway around a station based on the high-resolution basemap imagery in the ArcMap software package. We derived the river depth (WD) through ETOPO1 Global Relief Model (https://www.ngdc.noaa.gov/mgg/global/global.html). The river depth is the average water depth within a 400 - 500 m buffer zone around each station. We also quantified DTC values since tidal dynamics are closely related to the travel paths of ocean waves. The coastline of PRE was derived from the Coastline Extractor program, the GEODAS-NG (GEOphysical DAta System - Next Generation) software developed by NOAA/National Geophysical Data center (https://www.ngdc.noaa.gov/mgg/geodas/trackline.html). We used the "Point Distance" command in ArcGIS 10.3 to measure the distance of each station to the closest coastline (DTC). The rates of sea-level changes were collected from the SOA, (2020) and tidal gauge records from the study of Church and White (Church and White, 2006).

3.2 Statistical analyses

To better understand the factors causing the spatial variability of tidal variables, we performed the Spearman's rank correlation to test relationships between the selected variables and geomorphological features, river discharge, and SLR. Spearman's rank correlation is a nonparametric technique and evaluating the degree of correlation of two independent variables through the ranks of the data (Gauthier, 2001). The nonparametric characteristics of Spearman's rank correlation can limit the impacts of non-normal distribution on data analysis. We further conducted clustering analysis to understand mechanisms regulating spatial patters of the tides. The *K*-mean cluster with Elbow Method was applied to classify the 19 stations into several groups based on the four tidal variables' similarity (mean values). We then calculated long-term trends of tidal variables in each cluster using linear regression and tested the statistical significance of the regression slopes for trend detections. We used the *P-values* (statistical significance) of 0.05 to test whether trends and correlations were statistically significant.

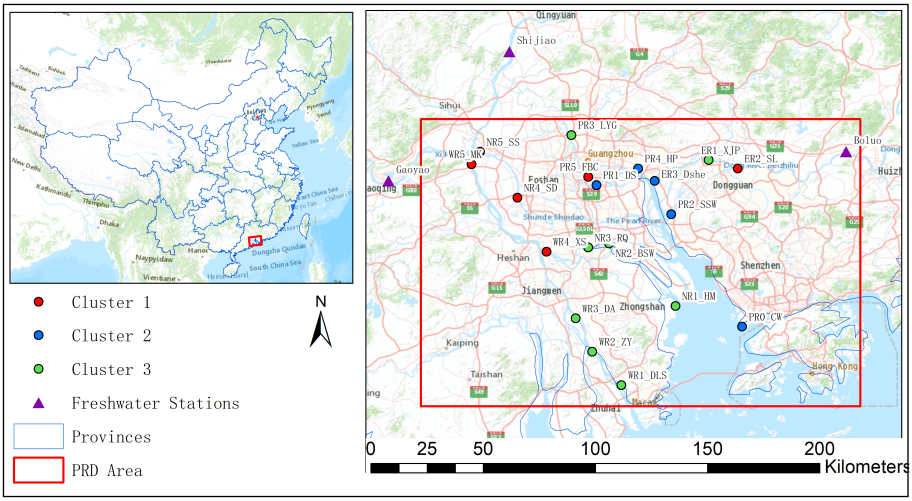

FIGURE 1
Location of Pearl River Estuary (PRE) and the selected stations (Stations of different clusters were grouped in the Results).

TABLE 1 The morphological characteristics at hydrological stations.

River	Station	ID	DTE (km)	DTC (km)	RW (m)	WD (m)
West River	MaKou	WR5_MK	129	58.14	670	3.25
	XianSha	WR4_XS	61	30.76	667	-1.5
	Da'ao	WR3_DA	42	14.85	563	-5
	ZhuYin	WR2_ZY	25	0.05	700	-2.75
	DengLongShan	WR1_DLS	5.2	0	1821	-1.25
North River	SanShui	NR5_SS	116	55.09	632	7
	SanDuo	NR4_SD	65	41.72	406	1.25
	RongQi	NR3_RQ	41	17.96	394	3
	BanShaWei	NR2_BSW	33	11.84	841	-1.75
	HengMen	NR1_HM	4.8	-3.57	1863	-2
East River	DaSheng	ER3_DShe	2	23.05	809	-1
	ShiLong	ER2_SL	1	28.45	457	3. 5
	XinJiaPu	ER1_XJP	1	21.42	611	-1
Pearl River	GuangZhouFuBiaoChang	PR5_FBC	69	11.23	630	1.75
	HuangPu	PR4_HP	45	1.20	2470	-1
	LaoYaGang	PR3_LYG	21	21.91	244	-4.33
	SiShengWei	PR2_SSW	2	0.02	1303	-1.5
	DaShi	PR1_DS	0.4	9.79	419	1.33
Near Shore	ChiWan	PR0_CW	0	-0.07	771	-2

DTC is the distance of hydrological stations to the coastline. DTE is the distance of hydrological stations to the estuary. RW is the river channel width and WD is the water depth.

In addition, the Complex Morlet wavelet (CMW) transform was applied to detect periodical changes in each cluster. It is a complex sine wave localized by a real-valued Gaussian window. The CMW is useful in extracting time-frequency characteristics of non-stationary vibration signals, such as tidal dynamics (Flinchem and Jay, 2000; Lopes and Tenreiro Machado, 2017). The time domain and frequency domain of CMW can be defined as follows:

$$\Psi_{CMW}(t) = \pi^{-\frac{1}{4}}\left(e^{iw_0 t} - e^{-\frac{1}{2}w_0^2}\right)e^{-\frac{1}{2}t^2} \quad (1)$$

where t is the time; i is the imaginary operator; w_0 is the non-dimensional frequency. In this study, w_0 is set to 6.0 to satisfy the wavelet admissibility condition. The transform coefficient $\Psi_{CMW}(t)$ represents the signal strength (local wavelet spectra) of time scales. The real parts of transform coefficients extract intensify (amplitude) and phase information of time scales, showing the periodic distribution of the signal in the time domain. The global wavelet power spectra V (a) of clusters were also calculated to identify the dominant periodic components:

$$V(a) = \frac{1}{n}\sum_{j=1}^{n}\Psi^2(a, x_j) \quad (2)$$

where n is the length of the time series. Therefore, higher values of the wavelet variance at a given scale suggest more times of peaks and greater intensified values of the time series signal. All statistical analyses were carried out using R version 4.1.0.

4 Results

4.1 Spatial variability of tidal dynamics

Tidal variables presented substantial spatial variability in the PRE. The AHTLs, ALTLs, and AMTLs increased with the increasing distances from coastlines, but the AMTRs decreased from near-shore regions to upper reaches (Table 2). AHTLs and ALTLs in the lower reaches of PRE were less than those in the higher reaches, while tidal ranges were higher for stations located closer to river inlets of the estuary (Table 2). For stations (WR5_MK and NR5_SS) located along the West and North rivers, the AHTLs were the highest, with values of more than 6.90 m. Extremely high inter-annual fluctuations of AHTLs were also found at the mentioned upstream stations (WR5_MK and NR5_SS), as indicated by the largest SD values than at the other stations. AHTLs tend to be smaller at the mouth of the PRE. Similar statistical characteristics with the highest tidal levels and SD values at the upper-reach stations and lowest tidal levels and SD values at the lower-reaches stations were observed for ALTLs and AMTLs. The annual mean tidal ranges (AMTRs) showed relatively low values at the upper reaches and high values at the lower reaches, suggesting increasing deviations between the daily high and low tidal levels for stations closer to the coastline. The near-shore station PR0_CW exhibited the highest AMTR of 1.36 m, which was about 3.8 times the lowest AMTR value observed at WR5_MK in the upstream region of the West River (Figure 1).

10.3389/fmars.2023.1065100

TABLE 2 Mean values and standard deviations (SDs) of the tidal currents and tidal ranges at 20 hydrological stations in PRE.

	AHTL(m)		ALTL(m)		AMTL(m)		AMTR(m)	
	Mean	SD	Mean	SD	Mean	SD	Mean	SD
West River								
WR5_MK	6.93	1.61	-0.32	0.18	0.83	0.17	0.36	0.11
WR4_XS	4.09	0.91	-0.55	0.10	0.72	0.20	0.51	0.08
WR3_DA	2.45	0.48	-0.73	0.10	0.34	0.10	0.63	0.10
WR2_ZY	1.95	0.28	-0.82	0.10	0.24	0.07	0.72	0.10
WR1_DLS	1.75	0.38	-1.02	0.09	0.06	0.04	0.87	0.05
North River								
NR5_SS	6.99	1.62	-0.34	0.20	0.81	0.18	0.37	0.14
NR4_SD	4.76	1.16	-0.55	0.09	0.77	0.17	0.81	0.10
NR3_RQ	2.65	0.52	-0.86	0.11	0.43	0.11	0.88	0.07
NR2_BSW	2.31	0.35	-1.01	0.09	0.29	0.09	1.03	0.09
NR1_HM	1.94	0.35	-1.04	0.08	0.13	0.07	1.11	0.07
East River								
ER3_DShe	1.99	0.29	-1.66	0.24	-0.04	0.05	1.61	0.06
ER2_SL	4.55	1.47	-0.18	0.41	0.79	0.31	0.49	0.26
ER1_XJP	3.09	0.85	-0.72	0.34	0.48	0.20	0.97	0.30
Mouth of the PRE								
PR5_FBC	3.44	0.28	-0.06	0.08	1.38	0.06	1.42	0.05
PR4_HP	2.03	0.29	-1.70	0.08	-0.05	0.04	1.64	0.05
PR3_LYG	2.16	0.31	-1.07	0.10	0.22	0.07	1.11	0.05
PR2_SSW	2.29	0.33	-1.41	0.12	0.26	0.05	1.62	0.06
PR1_DS	2.22	0.28	-1.45	0.09	0.08	0.05	1.51	0.06
Nearshore								
PR0_CW	1.57	0.28	-1.89	0.10	-0.24	0.05	1.36	0.03

AHTL, annual highest tidal level; ALTL, annual lowest tidal level; AMTL, annual mean tidal level; AMTR, annual mean tidal range.

To better understand factors leading to the differences in the mean and SD values of tidal dynamic variables at different stations, we quantified controls of geomorphological variables on tidal levels through Spearman's Rank Correlation (Table 3). The DTC significantly influenced all tidal variables, as suggested by the highest correlation coefficients with tidal variables among all factors. DTE and WD controls on tides were similar to DTC, but the correlation coefficients were smaller. RW demonstrated significantly negative correlations with AHTLs and AMTLs (Table 3).

TABLE 3 Correlations between geomorphological variables and tidal level variables.

	AHTL	ALTL	AMTL	AMTR
DTE	0.589	0.571	0.600	-0.455
DTC	0.830	0.608	0.672	-0.623
RW	-0.511	–	-0.465	–
WD	0.646	0.475	0.538	–

Red, orange, and yellow cells suggest positive correlations with P values less than 0.001, 0.005, and 0.05, respectively; Dark blue, blue, and light blue cells suggest negative correlations with *P* values less than 0.001, 0.005, and 0.05, respectively.
DTC, distance of hydrological stations to the coastline; DTE, distance of hydrological stations to the estuary; RW, river width; WD, water depth; AHTL, annual highest tidal level; ALTL, annual lowest tidal level; AMTL, annual mean tidal level; AMTR, annual mean tidal range.

Since the variables showed significant variability in mean and SD values, we tried the k-mean cluster analysis to sort all 19 stations into clusters based on AHTLs, ALTLs, AMTLs, and AMTRs. After exploring the optimal number of clusters, we grouped the stations into three clusters, which present strong spatial patterns (Figure 2). The first cluster are stations in the upper reaches of the rivers, including WR5_MK, WR4_XS, NR5_SS, NR4_SD, ER2_SL, and PR5_FBC; cluster 2 are stations in the mouth of PRE, including ER3_Dshe, PR4_HP, PR2_SSW, PR1_DS, and PR0_CW; and cluster 3 are stations in middle and lower reaches of the rivers, including WR3_DA, WR2_ZY, WR1_DLS, NR3_RQ, NR2_BSW, NR1_HM, ER1_XJP, and PR3_LYG.

We obtained different temporal variability and trends at different clusters (Table 4). For AHTLs, the highest value of 5.23 m was found in Cluster 1, which was more than two times higher than that in Clusters 2 (2.02 m) and 3 (2.29 m). A significant downward trend (slope -0.044, $P< 0.0001$) was observed in Cluster 1. The decreasing rate of 0.044 m/yr was the highest trend value in all clusters. Although the mean values of AHTLs were both around 2 m in Clusters 2 and 3, the trends in the annual time series were different from each other. The mean values of AHTLs in Cluster 2 showed a significant upward trend (slope 0.0074, $P< 0.001$) with the lowest variability (lowest SD value, 0.38 m). In contrast, the mean values of AHTLs in Cluster 3 did not show any significant trend, and the variability among stations was higher (0.63 m) than that in Cluster 2. Similarly, we also found the highest mean values of ALTLs (-0.34 m) and AMTLs (0.86 m) in Cluster 1 and the lowest values of ALTLs (-1.63 m) and AMTLs (0.0007 m) in Cluster 2. The mean values of these two tides were significantly decreased with time in Cluster 1 (ALTL: slope -0.0081, $P< 0.0001$; AMTL: slope -0.0091, $P< 0.0001$) and increased with time in Cluster 3 (ALTLs: slope 0.0034, $P< 0.0001$; AMTLs: slope 0.0022, $P< 0.0001$). As for AMTRs, we found upward trends in all clusters, but the increased rates varied with clusters. The mean value of AMTRs was 0.59 m, the lowest in Cluster 1, but experienced the highest increase with the rate of 0.0067 m/yr. The mean value of AMTRs was the highest in Cluster 2 (1.55 m) with the lowest increasing rate of 0.0016 m/yr.

4.2 Temporal variability of tidal variables

In addition to magnitudes and trends, periodic patterns in different clusters were also compared to further understand long-term changes in tidal levels. Most tidal variables showed high

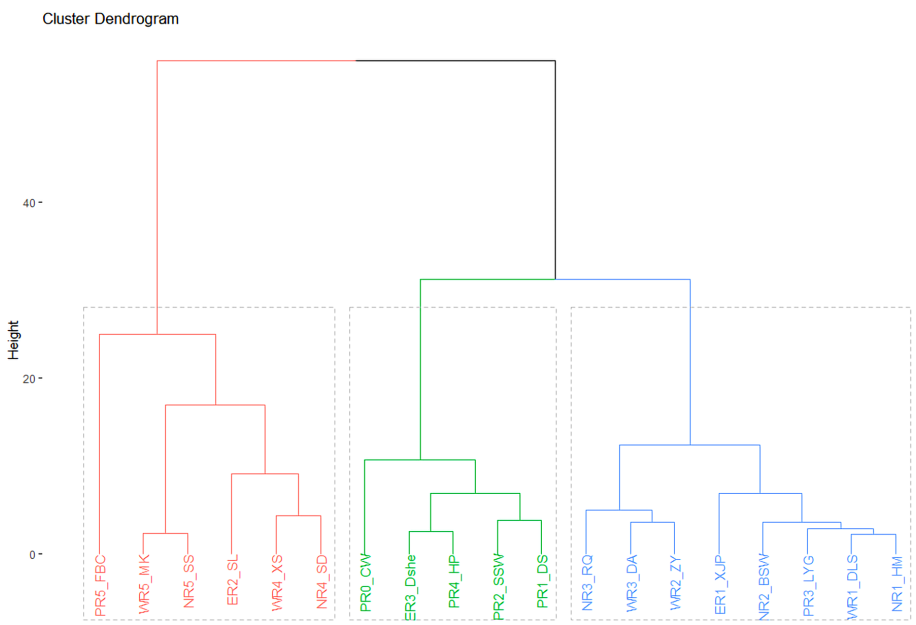

FIGURE 2
K-mean cluster diagram of the hydrological stations based on standardized tidal variables in the PRE, China.

TABLE 4 Mean, Standard Deviations (SDs), and the temporal trends of four tidal variables in different clusters.

Clusters	AHTL		ALTL		AMTL		AMTR	
	Mean (SD), m	Trends	Mean (SD), m	Trends	Mean (SD), m	Trends	Mean (SD), m	Trends
Cluster 1	5.23 (1.86)	-0.044 ***	-0.34 (0.27)	-0.0081 ***	0.86 (0.28)	-0.0091 ***	0.59 (0.36)	0.0067 ***
Cluster 2	2.02 (0.38)	0.0074 **	-1.63 (0.22)	0.0034 ***	0.0007 (0.17)	0.0022 ***	1.55 (0.12)	0.0016 ***
Cluster 3	2.29 (0.63)	–	-0.92 (0.20)	-0.0036 ***	0.29 (0.16)	–	0.95 (0.21)	0.0059 ***

AHTL, annual highest tidal level; ALTL, annual lowest tidal level; AMTL, annual mean tidal level; AMTR, annual mean tidal range. ** is $P < 0.001$, *** is $P < 0.0001$.

10.3389/fmars.2023.1065100

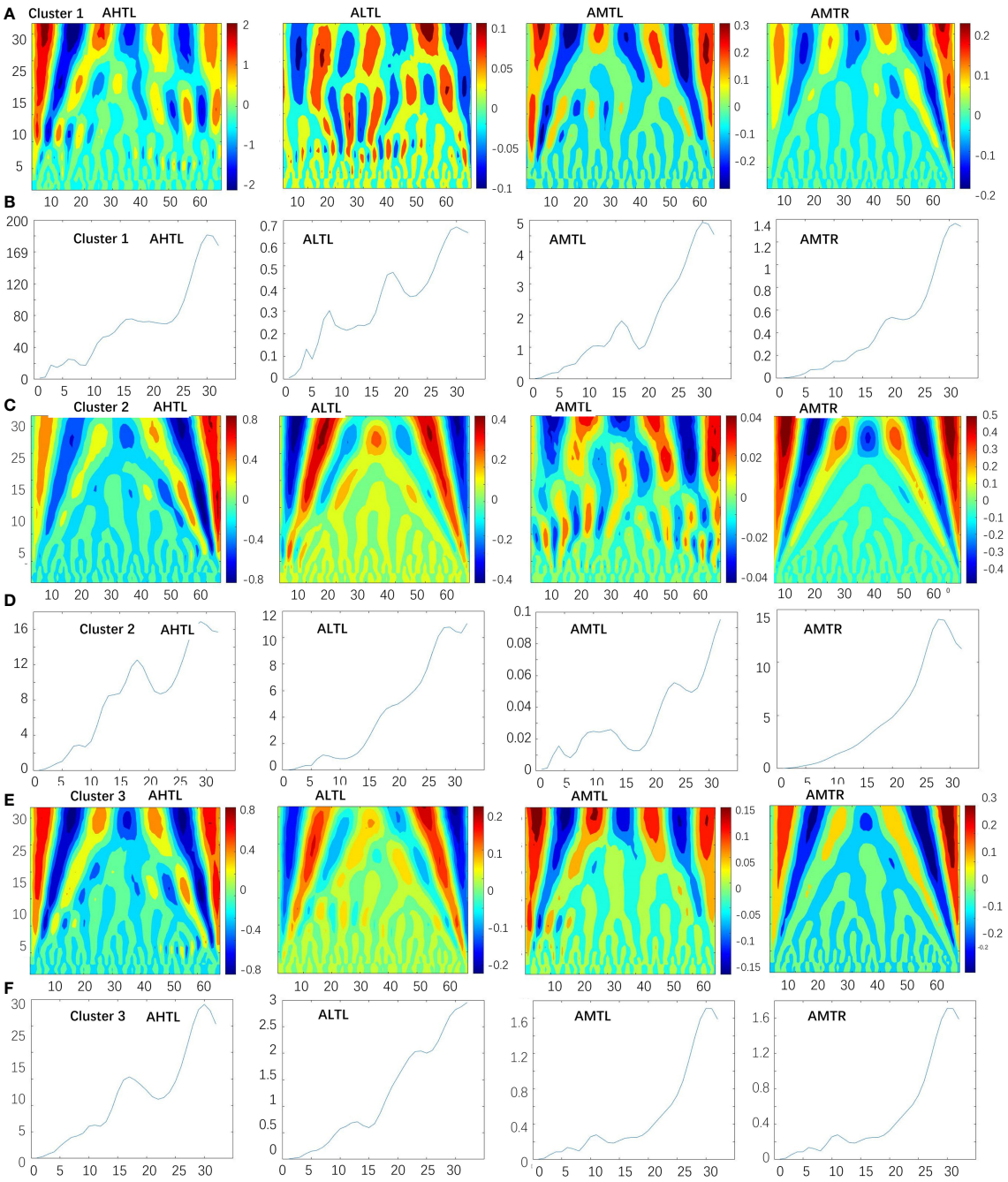

FIGURE 3
The local and global power wavelet spectrum of the tidal variables in PRE. **(A, B)** are the local and global power wavelet spectrum of AHTLs, ALTLs, AMTLs, and AMTRs in Cluster 1; **(C, D)** are the local and global power wavelet spectrum of AHTLs, ALTLs, AMTLs, and AMTRs in Cluster 2; **(E, F)** are the local and global power wavelet spectrum of AHTLs, ALTLs, AMTLs, and AMTRs in Cluster 3.

proportions of long-period components of 30 years, in which relatively stable tidal cycles were observed and oscillated over the whole studied years (Figure 3). For AHTLs, a shift was observed from a 12-year period component to 6- year and 16-year period components in Cluster 1. A shift to a shorter year-period component was also found for AHTLs in Cluster 3 (middle and lower reaches), while slight changes were found in the periodic analyses in Cluster 2 (mouth of the PRE). For ALTLs and AMTRs, evident periodic pattern shifts were found in Cluster 1, but relative symmetric patterns were observed in Cluster 2. The short-period component shifts in AMTLs occurred after 50 years and 20 years in Clusters 1 and 3, respectively. High proportions of 10- and 25-year periodic components were observed in local and global wavelet spectra in AMTLs in Cluster 2.

Since there were significant differences in tidal level variables among different periods, we further tested the primary energy drivers influencing tidal dynamics. The sea level has gradually increased in the recent 80 years. The mean SLR between 1950 and 2020 was about 2.6 mm yr^{-1}, with an accelerated increased rate of 3.4 mm yr^{-1} in recent decades between 1980 and 2020 (Figure 4). The increased sea

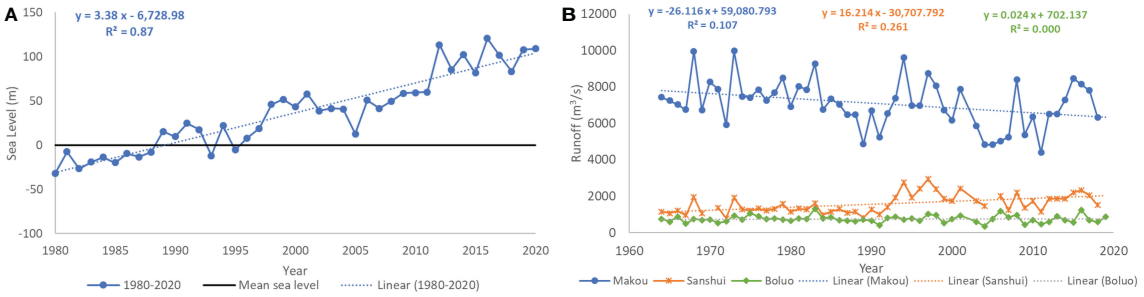

FIGURE 4
Time series of **(A)** sea level and **(B)** runoff. Sea level data was collection from Church and White (2006) and the SOA, (2020). Zero in 4 **(A)** represents the 1961–2020 averages for the sea level data.

level would directly influence the temporal variability of AHTLs, ALTLs, AMTLs, and AMTRs. Generally, the mean AMTRs in Clusters 1 and 3 enlarged with the increased SLR, in which the correlation coefficients were larger than 0.87 ($P< 0.0001$, Table 5). However, no statistically significant SLR control on AMTR ($P > 0.05$) was found in Cluster 2. For the other three tidal level variables, the sea level changes showed stronger impacts on the mean values of AHTLs and ALTLs in the uppers (Cluster 1) and mouth of the estuary (Cluster 2) (AHTLs in Cluster 1: r = -0.55, $P< 0.0001$, ALTLs in Cluster 1: r = -0.64, $P< 0.0001$; AHTLs in Cluster 2: r = 0.43, $P< 0.001$, ALTLs in Cluster 2: r = 0.57, $P< 0.0001$) than in the middle and lower reaches of rivers (AHTLs in Cluster 3: r = -0.30, $P< 0.05$, ALTLs in Cluster 3: r = -0.38, $P< 0.05$). In Cluster 1 (located in the upper reaches of rivers), significantly negative relationships were found between SLR and the mean AHTLs, ALTLs, and AMTLs. While in Cluster 2 (located at the mouth of PRE), mean AHTLs, ALTLs, and AMTLs showed similar upward trends as the SLR. In Cluster 3, mean ALTLs and AMTLs showed negative correlations with SLR, but no significant correlation was observed between mean AHTLs and SLR.

We further tested how SLR correlated with different tidal dynamic variables for each station (Table 5). The results showed high consistency with SLR controls on mean tidal dynamic variables for Clusters 1 and 2. Negative correlations between SLR and AHTLs, ALTLs, and AMTLs were observed for Cluster 1 stations. In contrast, positive correlations between SLR and AHTLs, ALTLs, and AMTLs were observed at the mouth of the estuary (Cluster 2). However, large inconsistencies were observed for stations of Cluster 3. Specifically, both positive and negative correlations between SLR and tidal dynamic variables were found for stations of this cluster.

Besides SLR, we also analyzed the correlations between runoff and tidal variables to investigate the river discharge controls on tides (Table 5). For the river discharge time series data, only the river discharge collected from the Makou station in the West River showed a slightly downward trend (Figure 4B, $R^2 = 0.11$ $P< 0.05$). Significantly increased river discharge with time in the North Rivers was recorded at the Sanshui station (Figure 4B, $R^2 = 0.26$, $P< 0.0001$). We found no significant decreasing or increasing trend for the river discharge collected from the Bolou station in the East River ($P > 0.05$). When relating the river discharge data with tides, we discovered that the river discharge changes were highly correlated with the AHTLs, ALTLs, AMTLs, and AMTRs in Clusters 1 and 3. Significantly high correlation coefficients were observed between the river discharge and mean values of AHTLs (r = -0.50, $P< 0.0001$), ALTLs (r = -0.52, $P< 0.0001$), and AMTLs (r = -0.83, $P< 0.0001$) in Cluster 3, in which insignificant or weak SLR effects were found. However, for the stations at the mouth of the estuary (Cluster 2), river discharge only had weak controls on mean values of tidal ranges (r = 0.34, $P< 0.05$) and no impacts on other variables ($P > 0.05$). Specifically, not all stations of the same cluster showed similar correlations with river discharge. The larger volume of river discharge led to higher AHTLs, ALTLs, and AMTLs across most stations in Clusters 1 and 3. Effects of river discharge on AMTRs varied with the main flow path changes. Negative correlations were found between the river discharge of the Makou station and AMTRs in the West River, and between the river discharge of the Sanshui station and AMTRs. No correlations or weak positive correlations were found between river discharge and AMTRs for most stations of the East River and the mouth of PRE.

5 Discussion

5.1 Geomorphological impacts on tidal dynamics

Although the tide is an astronomical force-caused phenomenon, it can be influenced by geomorphological variability, river discharge, and climate change (Hoitink and Jay, 2016; Burgos et al., 2018; Sulaiman et al., 2021). When the tidal wave propagates up the river, the crest and trough of the wave also move up progressively. Such a progressive wave can be significantly influenced by river width and depth. The increased amplitude of tides would be expected if river width/depth decreased since the same amount of water is passing from a larger cross-section to a smaller cross-section (Hinton, 1996; Talke et al., 2021). The tidal amplification due to the gradual decline of the estuarine width is called funneling; and the tidal amplification caused by the gradual decline of the estuarine depth is called shoaling. Van Rijn (2011) further clarified that the funneling and shoaling phenomena could be explained by the concept of tidal wave energy flux. The squared tidal range would negatively linearly correlate with the width if there was no energy loss and no reflection at the head. Our study did not find significant correlations between AMTRs and RWs or between AMTRs and squared RWs (r = 0.365, $P > 0.05$). Instead, positivity correlations were found between water depth and AHTLs, ALTLs, as well as AMTLs. The insignificant RW effects and

TABLE 5 Correlations between tidal level variables and sea level rise (SLR) and river discharge.

		Cluster 1					Cluster 2						Cluster 3							
		PR5_FBC	WR5_MK	NR5_SS	ER2_SL	WR4_XS	NR4_SD	Mean	PR0_CW	ER3_Dshe	PR4_HP	PR2_SSW	PR1_DS	Mean	NR3_RQ	WR3_DA	WR2_ZY	ER1_XJP	NR2_BSW	PR3_LYG	WR1_DLS	NR1_HM	Mean
SLR																							
	AHTL		-0.339	-0.340	-0.577	-0.313	-0.266	-0.546	0.296	0.464	0.326	0.460	0.265	0.426				-0.496			0.307	0.467	
	ALTL	-0.278	-0.529	-0.643	-0.704	-0.529		-0.639	0.522	0.865	0.370	0.549	0.490	0.569	0.512	-0.712	-0.456	-0.769	0.337	0.246	-0.351	0.273	-0.305
	AMTL	-0.399	-0.238		-0.676	-0.579	-0.242	-0.247	0.786	0.778	0.867	0.897	0.645	0.851	-0.271	-0.517	-0.460	-0.747	-0.248		0.807		-0.385
	AMTR	0.805	0.630	0.721	0.688	0.770	0.895	0.919	-0.398		0.280		0.768		0.449	0.810	0.793	0.888	0.433	0.663	0.858		0.878
River discharge																							
	AHTL	0.411	0.590	0.559	0.440	0.581	0.622	0.582					0.404		0.580	0.395		0.376	0.542	0.433			0.495
	ALTL		0.507	-0.383		0.428	0.420	0.325							0.365	0.498	0.446	0.327	0.429		0.417		0.522
	AMTL	0.511	0.488	0.333		0.748	0.679	0.507							0.845	0.739	0.762	0.416	0.850	0.679	0.620	0.441	0.830
	AMTR		-0.460	-0.497		-0.585	-0.362		0.412			0.391		0.335	-0.430	-0.455	-0.539		-0.349		-0.335		-0.310

colors red, orange, and yellow suggest positive correlations with P values less than 0.0001, 0.001 and 0.05, respectively; colors dark blue, blue, and light blue suggest negative correlations with P values less than 0.0001, 0.001 and 0.05, respectively.

significant WD effects on tidal levels can be explained by the bottom friction that increased energy dissipates as the WD decreases (Hinton, 1996; Huess and Andersen, 2001; Yu et al., 2017).

Furthermore, decreasing tidal ranges over the DTC were observed due to the tidal wave reflection. This may be related to the impacts of waterway lengths that the DTC reflects. During the tide transformation, the wave propagation is reflected back from a sudden decrease in width or close end, combined with the incident wave, forming a standing tide wave (Van Rijn, 2011; Díez-Minguito et al., 2012). The waterway length along its travel can significantly influence this standing tidal wave because of the energy loss (Davies and Woodroffe, 2010). If the waterway is long enough, the tidal range will decrease when moving up along river waterways. The reason is that the reflected wave may coincide with the incident wave, and the two waves can cancel out parts of the wave energy (Khojasteh et al., 2020; Khojasteh et al., 2021a; Khojasteh et al., 2022). In the PRE, the tidal limits could reach as far as hydrological stations Gaoyao, Shijiao, and Boluo stations in the West River, North River, and East River, respectively (Figure 1), which are located further up from the 19 selected stations for tide analysis (Zhang et al., 2010). The long waterway length may be responsible for the negative relationship between tidal ranges and DTC values. Similar attenuation effects caused by the waterway length were also observed in the study of Khojasteh et al. (2020), which analytically demonstrated decreased tidal ranges along with waterway lengths less than 100 km.

5.2 Energy driving forces on tidal dynamics

The astronomical forces lead to variations in tides, including daily cycles induced by the rotation of the Earth, fortnightly cycles caused by the rotation of the Moon, semi-annual cycles caused by the annual revolution of the Earth around the Sun, as well as 4.4-, 8.8-, and 18.6-year cycles induced from the orbital inclination between the Moon and the Earth (Khojasteh et al., 2021b). However, previous studies also reported inter-annual cycle changes in estuaries during the 20th and 21st centuries due to external forces, such as river discharge changes and sea-level rise (Houston and Dean, 2011; Ezer and Atkinson, 2014; Lee et al., 2017; Thompson et al., 2021). Increases in river discharge and sea-level rise would enlarge water volume in the head of PRE, causing a reduction in bed friction and increases in minor flood, which can lead to high recurrent high-tide flooding in the coastal areas (Pelling et al., 2013a; Ezer and Atkinson, 2014; Thompson et al., 2021). Our study also found similar decreases in tidal inter-annual cycles over the past 70 years. Specifically, AHTLs changed from around a 10-year to around a 6-year cycle at the rivers' upper and middle reaches, suggesting an increase in the frequency of high tidal level periods. Similarly, higher proportions in ALTL's longer-term cycles in recent decades suggested decreased frequencies in extremely low tidal events, which may also be explained by the friction reduction due to river discharge changes and sea-level rise (Pelling et al., 2013a).

River discharge from upper reaches has been reported as other main forces influencing estuarine hydrodynamics (Horrevoets et al., 2004; Hoitink and Jay, 2016; Talke et al., 2021). The flow volume is determined by surface runoff and groundwater discharge, which can be amplified or reduced due to natural processes (e.g., precipitation

and evapotranspiration) or anthropogenic activities (e.g., damming and urbanization). In the PRE region, surprisingly, as an estuary suffered from intensive human activities, only a slightly decreasing trend in discharge was observed in one branch of the Pearl River (Zhang et al., 2008). However, we still found changes in circular periods as well as decreases in tidal heights in the upper and middle reaches, where the river discharge significantly affected the tidal variables. One possible explanation is the joint effects of river discharge and SLR. Due to the bottom friction, river inflow interacts with tides and distorts tidal hydrodynamics. During high tide periods, the river current and the tidal current are in the opposite direction, leading to an asymmetric effect that causes tidal distortions and increases high tidal frequency, inducing a sharply increased tidal level (Ensing et al., 2015; Thompson et al., 2021). SLR further changes estuarine tidal energy and alters the circular patterns at different locations (Khojasteh et al., 2021b). River flow attenuates tidal ranges due to the increased low tidal levels when the ebb is larger than the increased high tidal levels during a flood (Horrevoets et al., 2004). Therefore, positive correlations were found between inflows and AHTLs, ALTLs, and AMTLs, while negative correlations were observed between inflows and AMTRs at the upper and middle reaches of the rivers. However, the river flow impacts decreased due to the increased SLR and the widening of river channels when approaching the mouth of the estuary (Davies and Woodroffe, 2010; Khojasteh et al., 2020).

The SLR significantly influenced tidal dynamics. The AHTLs, ALTLs, AMTLs, and AMTRs have been reported to increase with SLR, which possible because the increasing volumes of exchange water in and out of the PRE (Khojasteh et al., 2021b; Khojasteh et al., 2022). However, the controls of SLR decreased with the DTC. At the upper reaches, increasing energy losses of tides due to the bottom friction may loosen the SLR controls (Khojasteh et al., 2022). Furthermore, interactions of the SLR with other factors pose even complex influences on estuarine tidal dynamics (Ensing et al., 2015; Palmer et al., 2019). Khojasteh et al. (2020) suggested that tidal responses to SLR would perform differently between restricted and unrestricted estuaries. The friction loss and head loss led to the initial attenuation of tides, causing a reduction of tidal range at locations close to the mouth of the estuary (Hanslow et al., 2018; Kumbier et al., 2018). Therefore, the amplification of the tidal range under SLR enlarged with increased longitudinal distance (Ensing et al., 2015). Our study also observed increased SLR controls and enlarged upward trends of AMTRs. In addition to the interactions between geomorphology and SLR, decreased river discharges can offset or even exceed controls of SLR at the upper reaches (Horrevoets et al., 2004). Coastal recession would also interact with SLR, perturbating the natural period of oscillation of the tides and increasingly causing a reduction in tidal range (Pickering et al., 2017).

6 Implications from tidal changes

The latest Intergovernmental Panel on Climate Change (IPCC) Sixth Assessment Reports emphasized that the interactions between SRL and tidal changes can lead to extreme water level changes (Masson-Delmotte et al., 2021). A number of studies have suggested that an allowance should be considered in studying the SLR impacts due to the SLR effect on surge elevations and tidal levels (Greenberg et al., 2012; Pickering et al., 2012; Pelling and Mattias Green, 2013; Pelling et al., 2013a; Pelling et al., 2013b; Schuerch et al., 2018). For example, the Dutch Delta committee applied a 10% allowance for the SLR imposed effect on the storm surge and tides (Vellinga et al., 2009). In this study, the AHTL changes exceed 10% of the SLR at 7 of the 19 stations between 1950 and 2019 (See Table S1). They are WR1_DLS, NR1_HM, ER3_Dashe, PR4_HP, PR2_SSW, PR1_DS, and PR0_CW. The results suggest the extremely high tidal levels in the coastline and the main Pearl River have exceeded the allowance for normal variations and should be considered specially in PRE management.

Our results have demonstrated that levels and amplitudes of tides would be significantly affected by runoff discharge and geomorphology, and the responses get even more complicated due to climate change-induced SLR. The combined effects caused significant differences in tidal dynamics over time and space. We found significant upward trends in AHTLs, ALTLs, and AMTLs at stations close to the coastline (Cluster 2). The elevated tidal levels, especially the AMTLs would be one of the problems causing major concerns since it would lead to more instances of nuisance flooding (Chaumillon et al., 2017; Moftakhari et al., 2017; Burgos et al., 2018). At stations upstream reaches, the extremely high decrease rate in mean values of AHTLs suggests a decreased possibility of being threatened by storm surge. However, we also found decreases in the circular patterns, which led to a reduction in the durations of wet-dry periods and an increase in the frequencies of high and dry seasons. The acceleration in the wet-dry circle but the lower in the highest tides would influence the hydrological regimes in the upper reaches of the PRE, and ultimately impact the environment and ecology of the coast and threaten human health (Mao et al., 2004; Zhang et al., 2010; Liu et al., 2018). Therefore, it is of considerable importance to include tidal level and circular pattern dynamics analysis in coastal hydrodynamic studies to better assess possible risks due to climate change and anthropogenic disturbances. This investigation is expected to benefit efficient coastal habitat protection and contribute to achieving sustainable development goals.

7 Further studies

Our analysis is based on long-term observations and widely used statistical methods. It demonstrated that the spatial and temporal changes occurred, and the change characteristics varied between the mouth and the upper reaches of PRE. This time series analysis of tides is the basis for understanding tidal hydrodynamics of this region in recent decades and would provide valuable information on coastal habitat and ecology protection. Further studies, such as how changes in tides influenced sediment and nutrient transport in PRE, how changes in tides influenced the vegetation composition and fishery in PRE, and how changes in tides increase/decrease the risk of flooding in PRE, can be developed based on this study.

Data availability statement

The tidal dataset was collected from the Hydrological Yearbooks of the People's Republic of China, which is not a publicly accessible dataset. However, part of the data can be sent individually by request to the corresponding authors. Requests to access these datasets should be directed to XL, lixiabnu@bnu.edu.cn.

Author contributions

XL is the primary author who analyzed the datasets, generated results, and wrote the draft. YC is the author who contributed equally to this work and is mainly responsible for data collection, analysis, and result interpretation. ZL provided critical technique support. XM and LZ contributed to the data collection. CZ helped interpret the results. BC was responsible for the overall design of the work and provided constructive suggestions in the discussion section. ZR contributed to the manuscript review and editing and provided comments for the data analyses. All authors provided comments and suggestions for the manuscript revision. All authors contributed to the article and approved the submitted version.

Funding

This study was funded by the Key Project of National Natural Science Foundation of China (U1901212), the National Natural Science Foundation of China (42206170), the Key Special Project for Introduced Talents Team of Southern Marine Science and Engineering Guangdong Laboratory (Guangzhou) (GML2019ZD0402), the GuangDong Basic and Applied Basic Research Foundation (2021A1515110830), the Shandong key research and development program (2021CXGC011201), and the National key research and development program (2021YFC3101701).

Conflict of interest

The authors declare that the research was conducted in the absence of any commercial or financial relationships that could be construed as a potential conflict of interest.

Publisher's note

All claims expressed in this article are solely those of the authors and do not necessarily represent those of their affiliated organizations, or those of the publisher, the editors and the reviewers. Any product that may be evaluated in this article, or claim that may be made by its manufacturer, is not guaranteed or endorsed by the publisher.

Supplementary material

The Supplementary Material for this article can be found online at: https://www.frontiersin.org/articles/10.3389/fmars.2023.1065100/full#supplementary-material

References

Bamber, J. L., Oppenheimer, M., Kopp, R. E., Aspinall, W. P., and Cooke, R. M. (2019). Ice sheet contributions to future sea-level rise from structured expert judgment. *Proc. Natl. Acad. Sci. U. S. A.* 166, 11195–11200. doi: 10.1073/pnas.1817205116

Bouillon, S., Middelburg, J. J., Dehairs, F., Borges, A. V., Abril, G., Flindt, M. R., et al. (2007). Importance of intertidal intertidal sediment processes and porewater exchange on the water column biogeochemistry in a pristine mangrove creek (Ras dege, Tanzania). *Biogeosciences* 4, 311–322. doi: 10.5194/bg-4-311-2007

Burgos, A. G., Hamlington, B. D., Thompson, P. R., and Ray, R. D. (2018). Future nuisance flooding in Norfolk, VA, from astronomical tides and annual to decadal internal climate variability. *Geophys. Res. Lett.* 45, 12,432–12,439. doi: 10.1029/2018GL079572

Chaumillon, E., Bertin, X., Fortunato, A. B., Bajo, M., Schneider, J. L., Dezileau, L., et al. (2017). Storm-induced marine flooding: Lessons from a multidisciplinary approach. *Earth-Science Rev.* 165, 151–184. doi: 10.1016/j.earscirev.2016.12.005

Chen, S., Chen, L. F., Liu, Q. H., Li, X., and Tan, Q. (2005). Remote sensing and GIS-based integrated analysis of coastal changes and their environmental impacts in lingding bay, pearl river estuary, south China. *Ocean Coast. Manage.* 48, 65–83. doi: 10.1016/j.ocecoaman.2004.11.004

Cherqui, F., Belmeziti, A., Granger, D., Sourdril, A., and Le Gauffre, P. (2015). Assessing urban potential flooding risk and identifying effective risk-reduction measures. *Sci. Total Environ.* 514, 418–425. doi: 10.1016/j.scitotenv.2015.02.027

Church, J. A., and White, N. J. (2006). A 20th century acceleration in global sea-level rise. *Geophys. Res. Lett.* 33, 94–97. doi: 10.1029/2005GL024826

Davies, G., and Woodroffe, C. D. (2010). Tidal estuary width convergence: Theory and form in north Australian estuaries. *Earth Surf. Process. Landforms* 35, 737–749. doi: 10.1002/esp.1864

Dieckmann, R., Osterthun, M., and Partenscky, H. W. (1987). Influence of water-level elevation and tidal range on the sedimentation in a German tidal flat area. *Prog. Oceanogr.* 18, 151–166. doi: 10.1016/0079-6611(87)90031-0

Díez-Minguito, M., Baquerizo, A., Ortega-Sánchez, M., Ruiz, I., and Losada, M. A. (2012). Tidal wave reflection from the closure dam in the guadalquivir estuary (Sw Spain). *Coast. Eng. Proc.* 1, 58. doi: 10.9753/icce.v33.currents.58

Dronkers, J. (1986). Tidal asymmetry and estuarine morphology. *Netherlands J. Sea Res.* 20, 117–131. doi: 10.1016/0077-7579(86)90036-0

Ensing, E., de Swart, H. E., and Schuttelaars, H. M. (2015). Sensitivity of tidal motion in well-mixed estuaries to cross-sectional shape, deepening, and sea level rise: An analytical study. *Ocean Dyn.* 65, 933–950. doi: 10.1007/s10236-015-0844-8

Ezer, T., and Atkinson, L. P. (2014). Accelerated flooding along the U.S. East coast: On the impact of sea-level rise, tides, storms, the gulf stream, and the north Atlantic oscillations. *Earth's Futur.* 2, 362–382. doi: 10.1002/2014ef000252

Fant, C., Jacobs, J. M., Chinowsky, P., Sweet, W., Weiss, N., Sias, J. E., et al. (2021). Mere nuisance or growing threat? the physical and economic impact of high tide flooding on US road networks. *J. Infrastruct. Syst.* 27, 04021044. doi: 10.1061/(asce)is.1943-555x.0000652

Fitzgerald, D. M. (1996). Geomorphic variability and morphologic and sedimentologic controls on tidal inlets. *J. Coast. Res.* 23, 47–71.

FitzGerald, D. M., Fenster, M. S., Argow, B. A., and Buynevich, I. V. (2008). Coastal impacts due to sea-level rise. *Annu. Rev. Earth Planet. Sci.* 36, 601–647. doi: 10.1146/annurev.earth.35.031306.140139

Flinchem, E. P., and Jay, D. A. (2000). An introduction to wavelet transform tidal analysis methods. *Estuar. Coast. Shelf Sci.* 51, 177–200. doi: 10.1006/ecss.2000.0586

Gao, G. D., Wang, X. H., and Bao, X. W. (2014). Land reclamation and its impact on tidal dynamics in jiaozhou bay, qingdao, China. *Estuar. Coast. Shelf Sci.* 151, 285–294. doi: 10.1016/j.ecss.2014.07.017

Gauthier, T. D. (2001). Detecting trends using spearman's rank correlation coefficient. *Environ. Forensics* 2, 359–362. doi: 10.1006/enfo.2001.0061

Godin, G. (1999). The propagation of tides up rivers with special considerations on the upper saint Lawrence river. *Estuar. Coast. Shelf Sci.* 48, 307–324. doi: 10.1006/ecss.1998.0422

Greenberg, D. A., Blanchard, W., Smith, B., and Barrow, E. (2012). Climate change, mean sea level and high tides in the bay of fundy. *Atmos. - Ocean* 50, 261–276. doi: 10.1080/07055900.2012.668670

Haigh, I. D., Nicholls, R., and Wells, N. (2010). A comparison of the main methods for estimating probabilities of extreme still water levels. *Coast. Eng.* 57, 838–849. doi: 10.1016/j.coastaleng.2010.04.002

Haigh, I. D., Pickering, M. D., Green, J. A. M., Arbic, B. K., Arns, A., Dangendorf, S., et al. (2020). The tides they are a-changin': A comprehensive review of past and future

nonastronomical changes in tides, their driving mechanisms, and future implications. *Rev. Geophys.* 58, 1–39. doi: 10.1029/2018RG000636

Hanslow, D. J., Morris, B. D., Foulsham, E., and Kinsela, M. A. (2018). A regional scale approach to assessing current and potential future exposure to tidal inundation in different types of estuaries. *Sci. Rep.* 8, 1–13. doi: 10.1038/s41598-018-25410-y

Hinton, A. C. (1996). Tides in the northeast Atlantic: Considerations for modelling water depth changes. *Quat. Sci. Rev.* 15, 873–894. doi: 10.1016/S0277-3791(96)00061-3

Hoitink, A. J. F., and Jay, D. A. (2016). Tidal river dynamics: Implications for deltas. *Rev. Geophys.* 54, 240–272. doi: 10.1002/2015RG000507

Horrevoets, A. C., Savenije, H. H. G., Schuurman, J. N., and Graas, S. (2004). The influence of river discharge on tidal damping in alluvial estuaries. *J. Hydrol.* 294, 213–228. doi: 10.1016/j.jhydrol.2004.02.012

Horton, B. P., Khan, N. S., Cahill, N., Lee, J. S. H., Shaw, T. A., Garner, A. J., et al. (2020). Estimating global mean sea-level rise and its uncertainties by 2100 and 2300 from an expert survey. *NPJ Cnlimate Atmos. Sci.* 3, 18. doi: 10.1038/s41612-020-0121-5

Houston, J. R., and Dean, R. G. (2011). Sea-Level acceleration based on U.S. tide gauges and extensions of previous global-gauge analyses. *J. Coast. Res.* 27, 409–417. doi: 10.2112/JCOASTRES-D-10-00157.1

Huess, V., and Andersen, O. B. (2001). Seasonal variation in the main tidal constituent from altimetry. *Geophys. Res. Lett.* 28, 567–570. doi: 10.1029/2000GL011921

Hu, P., Li, F., Sun, X., Liu, Y., Chen, X. , and Hu, D. (2021). Assessment of land-use/cover changes and its ecological effect in rapidly urbanized areas-taking pearl river delta urban agglomeration as a case. *Sustainability* 13, 5075. doi: 10.3390/su13095075

Jian, W., Lo, E. Y. M., and Pan, T. C. (2021). Probabilistic storm surge hazard using a steady-state surge model for the pearl river delta region, China. *Sci. Total Environ.* 801, 149606. doi: 10.1016/j.scitotenv.2021.149606

Khojasteh, D., Chen, S., Felder, S., Heimhuber, V., and Glamore, W. (2021a). Estuarine tidal range dynamics under rising sea levels. *PloS One* 16, 1–25. doi: 10.1371/journal.pone.0257538

Khojasteh, D., Glamore, W., Heimhuber, V., and Felder, S. (2021b). Sea Level rise impacts on estuarine dynamics: A review. *Sci. Total Environ.* 780, 146470. doi: 10.1016/j.scitotenv.2021.146470

Khojasteh, D., Hottinger, S., Felder, S., De Cesare, G., Heimhuber, V., Hanslow, D. J., et al. (2020). Estuarine tidal response to sea level rise: The significance of entrance restriction. *Estuar. Coast. Shelf Sci.* 244, 106941. doi: 10.1016/j.ecss.2020.106941

Khojasteh, D., Lewis, M., Tavakoli, S., Farzadkhoo, M., Felder, S., Iglesias, G., et al. (2022). Sea Level rise will change estuarine tidal energy: A review. *Renew. Sustain. Energy Rev.* 156, 111855. doi: 10.1016/j.rser.2021.111855

Kumbier, K., Carvalho, R. C., and Woodroffe, C. D. (2018). Modelling hydrodynamic impacts of sea-level rise on wave-dominated Australian estuaries with differing geomorphology. *J. Mar. Sci. Eng.* 6, 66. doi: 10.3390/jmse6020066

Lee, S. B., Li, M., and Zhang, F. (2017). Impact of sea level rise on tidal range in Chesapeake and Delaware bays. *J. Geophys. Res. Ocean.* 122, 3917–3938. doi: 10.1038/175238c0

Li, X., and Damen, M. C. J. (2010). Coastline change detection with satellite remote sensing for environmental management of the pearl river estuary, China. *J. Mar. Syst.* 82, S54–S61. doi: 10.1016/j.jmarsys.2010.02.005

Li, P., Fang, G., and Huang, G. (1993). Impacts of sea level rising on the economic development of zhujiang delta and countermeasures. *Acta Geogr. Sin.* 48, 527–534. doi: 10.11821/xb199306006

Liu, Z., Fagherazzi, S., and Cui, B. (2021a). Success of coastal wetlands restoration is driven by sediment availability. *Commun. Earth Environ.* 2, 1–9. doi: 10.1038/s43247-021-00117-7

Liu, Z., Fagherazzi, S., Li, J., and Cui, B. (2021b). Mismatch between watershed effects and local efforts constrains the success of coastal salt marsh vegetation restoration. *J. Clean. Prod.* 292, 126103. doi: 10.1016/j.jclepro.2021.126103

Liu, Z., Fagherazzi, S., Liu, X., Shao, D., Miao, C., and Cai, Y. (2022). Long-term variations in water discharge and sediment load of the pearl river Estuary : Implications for sustainable development of the greater bay area 9, 983517. doi: 10.3389/fmars.2022.983517

Liu, H., Gao, C., and Wang, G. (2018). Understand the resilience and regime shift of the wetland ecosystem after human disturbances. *Sci. Total Environ.* 643, 1031–1040. doi: 10.1016/J.SCITOTENV.2018.06.276

Liu, W., Zhan, J., Zhao, F., Yan, H., Zhang, F., and Wei, X. (2019). Impacts of urbanization-induced land-use changes on ecosystem services: A case study of the pearl river delta metropolitan region, China. *Ecol. Indic.* 98, 228–238. doi: 10.1016/j.ecolind.2018.10.054

Lopes, A. M., and Tenreiro Machado, J. A. (2017). Tidal analysis using time-frequency signal processing and information clustering. *Entropy* 19, 29–33. doi: 10.3390/e19080390

Ma, C., Ai, B., Zhao, J., Xu, X., and Huang, W. (2019). Change detection of mangrove forests in coastal guangdong during the past three decades based on remote sensing data. *Remote Sens.* 11, 921. doi: 10.3390/rs11080921

Mao, Q., Shi, P., Yin, K., Gan, J., and Qi, Y. (2004). Tides and tidal currents in the pearl river estuary. *Cont. Shelf Res.* 24, 1797–1808. doi: 10.1016/j.csr.2004.06.008

Masson-Delmotte, V., Zhai, P., Pirani, A., Connors, S., Péan, C., Berger, S., et al. (2021) IPCC: Climate change 2021: the physical science basis. Available at: https://www.ipcc.ch/report/ar6/wg1/.

Moftakhari, H. R., AghaKouchak, A., Sanders, B. F., and Matthew, R. A. (2017). Cumulative hazard: The case of nuisance flooding. *Earth's Futur.* 5, 214–223. doi: 10.1002/2016EF000494

Nabangchang, O., Allaire, M., Leangcharoen, P., Jarungrattanapong, R., and Whittington, D. (2015). Economic costs incurred by households in the 2011 GreaterBangkok flood. *Water Resour. Res.* 51, 58–77. doi: 10.1002/2013WR014979.Reply

Palmer, K., Watson, C., and Fischer, A. (2019). Non-linear interactions between sea-level rise, tides, and geomorphic change in the Tamar estuary, Australia. *Estuar. Coast. Shelf Sci.* 225, 106247. doi: 10.1016/j.ecss.2019.106247

Pelling, H. E., and Mattias Green, J. A. (2013). Sea Level rise and tidal power plants in the gulf of Maine. *J. Geophys. Res. Ocean.* 118, 2863–2873. doi: 10.1002/jgrc.20221

Pelling, H. E., Mattias Green, J. A., and Ward, S. L. (2013a). Modelling tides and sea-level rise: To flood or not to flood. *Ocean Model.* 63, 21–29. doi: 10.1016/j.ocemod.2012.12.004

Pelling, H. E., Uehara, K., and Green, J. A. M. (2013b). The impact of rapid coastline changes and sea level rise on the tides in the bohai Sea, China. *J. Geophys. Res. Ocean.* 118, 3462–3472. doi: 10.1002/jgrc.20258

Pickering, M. D., Horsburgh, K. J., Blundell, J. R., Hirschi, J. J. M., Nicholls, R. J., Verlaan, M., et al. (2017). The impact of future sea-level rise on the global tides. *Cont. Shelf Res.* 142, 50–68. doi: 10.1016/j.csr.2017.02.004

Pickering, M. D., Wells, N. C., Horsburgh, K. J., and Green, J. A. M. (2012). The impact of future sea-level rise on the European shelf tides. *Cont. Shelf Res.* 35, 1–15. doi: 10.1016/j.csr.2011.11.011

Raw, J. L., Godbold, J. A., van Niekerk, L., and Adams, J. B. (2019). Drivers of mangrove distribution at the high-energy, wave-dominated, southern African range limit. *Estuar. Coast. Shelf Sci.* 226, 106296. doi: 10.1016/j.ecss.2019.106296

Schuerch, M., Spencer, T., Temmerman, S., Kirwan, M. L., Wolff, C., Lincke, D., et al. (2018). Future response of global coastal wetlands to sea-level rise. *Nature* 561, 231–234. doi: 10.1038/s41586-018-0476-5

Shao, X., Fang, Y., and Cui, B. (2020). A model to evaluate spatiotemporal variations of hydrological connectivity on a basin-scale complex river network with intensive human activity. *Sci. Total Environ.* 723, 138051. doi: 10.1016/j.scitotenv.2020.138051

SOA (State Oceanic Administration People's Republic of China). (2020). Bulletin of Chinese sea level rise 2020. Available at: http://gi.mnr.gov.cn/202104/t20210426_2630186.html.

Sulaiman, Z. A., Viparelli, E., Torres, R., Yankovsky, A., and Grego, J. (2021). The influence of tides on coastal plain channel geomorphology: Altamaha river, Georgia, USA. *J. Geophys. Res. Earth Surf.* 126, 1–17. doi: 10.1029/2020JF005839

Talke, S. A., Familkhalili, R., and Jay, D. A. (2021). The influence of channel deepening on tides, river discharge effects, and storm surge. *J. Geophys. Res. Ocean.* 126, 1–24. doi: 10.1029/2020JC016328

Talke, S. A., and Jay, D. A. (2020). Changing tides: The role of natural and anthropogenic factors. *Ann. Rev. Mar. Sci.* 12, 121–151. doi: 10.1146/annurev-marine-010419-010727

Thompson, P. R., Widlansky, M. J., Hamlington, B. D., Merrifield, M. A., Marra, J. J., Mitchum, G. T., et al. (2021). Rapid increases and extreme months in projections of united states high-tide flooding. *Nat. Clim. Change* 11, 584–590. doi: 10.1038/s41558-021-01077-8

Vandenbohede, A., and Lebbe, L. (2006). Occurrence of salt water above fresh water in dynamic equilibrium in a coastal groundwater flow system near de panne, Belgium. *Hydrogeol. J.* 14, 462–472. doi: 10.1007/s10040-005-0446-5

Van Rijn, L. C. (2011). Analytical and numerical analysis of tides and salinities in estuaries; part I: Tidal wave propagation in convergent estuaries. *Ocean Dyn.* 61, 1719–1741. doi: 10.1007/s10236-011-0453-0

Vellinga, P., Katsman, C., Sterl, A., Beersma, J. J., Hazeleger, W., Church, J., et al. (2009). Exploring high-end climate change scenarios for flood protection of the Netherlands. *KNMI Sci. Rep. WR-2009-05 KNMI/Alterra Netherlands.*

Wang, F., and Hao, R. J. (2020). Environmental pollution in pearl river delta, China: Status and potential effects. *J. Environ. Inf. Lett.* 3, 110–123. doi: 10.3808/jeil.202000033

Wang, F., Sanders, C. J., Santos, I. R., Tang, J., Schuerch, M., Kirwan, M. L., et al. (2021). Global blue carbon accumulation in tidal wetlands increases with climate change. *Natl. Sci. Rev.* 8, nwaa296. doi: 10.1093/nsr/nwaa296

Wolanski, E., Moore, K., Spagnol, S., D'Adamo, N., and Pattiaratchi, C. (2001). Rapid, human-induced siltation of the macro-tidal ord river estuary, Western Australia. *Estuar. Coast. Shelf Sci.* 53, 717–732. doi: 10.1006/ecss.2001.0799

Xie, C., Cui, B., Xie, T., Yu, S., Liu, Z., Chen, C., et al. (2020). Hydrological connectivity dynamics of tidal flat systems impacted by severe reclamation in the yellow river delta. *Sci. Total Environ.* 739, 139860. doi: 10.1016/j.scitotenv.2020.139860

Yin, K., Xu, S., Huang, W., and Xie, Y. (2017). Effects of sea level rise and typhoon intensity on storm surge and waves in pearl river estuary. *Ocean Eng.* 136, 80–93. doi: 10.1016/j.oceaneng.2017.03.016

Yu, H., Yu, H., Wang, L., Kuang, L., Wang, H., Ding, Y., et al. (2017). Tidal propagation and dissipation in the Taiwan strait. *Cont. Shelf Res.* 136, 57–73. doi: 10.1016/j.csr.2016.12.006

Zhang, W., Cao, Y., Zhu, Y., Wu, Y., Ji, X., He, Y., et al. (2017). Flood frequency analysis for alterations of extreme maximum water levels in the pearl river delta. *Ocean Eng.* 129, 117–132. doi: 10.1016/j.oceaneng.2016.11.013

Zhang, S., Lu, X. X., Higgitt, D. L., Chen, C. T. A., Han, J., and Sun, H. (2008). Recent changes of water discharge and sediment load in the zhujiang (Pearl river) basin, China. *Glob. Planet. Change* 60, 365–380. doi: 10.1016/j.gloplacha.2007.04.003

Zhang, W., Ruan, X., Zheng, J., Zhu, Y., and Wu, H. (2010). Long-term change in tidal dynamics and its cause in the pearl river delta, China. *Geomorphology* 120, 209–223. doi: 10.1016/j.geomorph.2010.03.031

frontiers | Frontiers in Marine Science

TYPE Original Research
PUBLISHED 20 April 2023
DOI 10.3389/fmars.2023.1125705

OPEN ACCESS

EDITED BY
Stelios Katsanevakis,
University of the Aegean, Greece

REVIEWED BY
Yongjiu Cai,
Nanjing Institute of Geography and Limnology, Chinese Academy of Sciences (CAS), China
Chunhua Liu,
Wuhan University, China

*CORRESPONDENCE
Zhongqiang Li
lizhq@hubu.edu.cn
Lifei Wei
weilifei2508@163.com

SPECIALTY SECTION
This article was submitted to Marine Ecosystem Ecology, a section of the journal Frontiers in Marine Science

RECEIVED 16 December 2022
ACCEPTED 29 March 2023
PUBLISHED 20 April 2023

CITATION
Xu Z, Yang H, Mao H, Peng Q, Yang S, Chou Q, Yang Y, Li Z and Wei L (2023) Environment and time drive the links between the species richness and ecosystem multifunctionality from multitrophic freshwater mesocosms. *Front. Mar. Sci.* 10:1125705. doi: 10.3389/fmars.2023.1125705

Environment and time drive the links between the species richness and ecosystem multifunctionality from multitrophic freshwater mesocosms

Zhiyan Xu[1], Hui Yang[1], Hongzhi Mao[1], Qiutong Peng[1], Shiwen Yang[1], Qingchuan Chou[2], Yujing Yang[1], Zhongqiang Li[1]* and Lifei Wei[1]*

[1]Hubei Key Laboratory of Regional Development and Environmental Response, Faculty of Resource and Environment, Hubei University, Wuhan, China, [2]Institute of Hydrobiology, Chinese Academy of Sciences (CAS), Wuhan, China

Understanding the link between biodiversity and ecosystem functioning is imperative for ecosystem-based management. The role of multitrophic diversity in sustaining multifunctionality remains unclear, especially in highly diverse aquatic ecosystems. We performed a species-addition experiment consisting of one, two, three, and five species in simulated multitrophic ecosystems to evaluate biodiversity and ecosystem functioning relationships within and across trophic levels. Our results showed that there are positive species richness–productivity relationships within and across trophic levels. We found significant negative correlations between species richness and the cumulative variation of total phosphorus, and between species richness and ecosystem multifunctionality across trophic levels. Also, we found that the relationships between ecosystem multifunctionality and species richness within and across the trophic levels are mediated by a combination of environmental factors, including water temperature, dissolved oxygen, pH, irradiance, and time, rather than by species richness. Our results imply that species richness–ecosystem functioning relationships vary for different ecological functions; the individual ecosystem functions selected and the way multifunctionality calculated are critical when examining links between biodiversity and ecosystem multifunctionality. Our study highlights that multitrophic richness, such as for consumers, is crucial for driving ecosystem multifunctionality. Furthermore, our study implies that management practices for restoring the diversity of aquatic macrophytes in wetlands should consider not only macrophyte richness but also different functional groups and life-forms.

KEYWORDS

ecosystem functioning, multitrophic richness, freshwater ecosystem, temporal stability, multifunctionality

1 Introduction

Biodiversity–ecosystem function (BEF) relationships are a common focus in ecological research programs (Jaillard et al., 2014; van der Plas, 2019). The detrimental effects of human-induced biodiversity loss on ecosystem functions (EFs) have received extensive attention (Jaillard et al., 2014; Schuldt et al., 2018). Early BEF relationship research mostly focused on the relationship between species richness and individual EFs, particularly for productivity and biomass, and revealed that biodiversity–productivity relationships increase monotonically (Zavaleta et al., 2010; Jaillard et al., 2014; Slade et al., 2017). However, other studies have identified other types of biodiversity–productivity relationships, including positive hump-shaped, negative U-shaped, monotonically decreasing, and no apparent relationship (Mittelbach et al., 2001; Hooper et al., 2005; Duffy, 2009; Jaillard et al., 2014). Other researchers concluded that biodiversity effects on EFs seem to be consistent across different groups of organisms, among trophic levels, and across various ecosystems (Cardinale et al., 2012). These inconsistent results therefore suggest that biodiversity–productivity relationships vary depending on the ecosystem (Jaillard et al., 2014).

Most evidence for BEF relationships is from terrestrial systems, like grasslands, forests, and agricultural ecosystems (Bai et al., 2007; Messmer et al., 2014; Gagic et al., 2015; Brooker et al., 2021), whereas freshwater ecosystems have received less attention (Yasuhara et al., 2016). Some studies showed ambivalent evidence of whether BEF relationships attained from terrestrial ecosystems can be extrapolated to aquatic realms (Vaughn, 2010; Duncan et al., 2015; Gamfeldt et al., 2015; Strong et al., 2015; Daam et al., 2019). Freshwater ecosystems are among the most threatened ecosystems in the world (Scheffer, 2004; Davidson et al., 2013; Zhang et al., 2019), therefore, there is an urgent need for assessing BEF relationships in freshwater ecosystems to determine whether they follow the general significance and direction of BEF relationships (Duncan et al., 2015).

Some studies have examined the links between biodiversity and ecosystem functioning (EF) in the freshwater realm, such as the links between macrophyte species richness and biomass and water quality (Engelhardt and Ritchie, 2001; Zhang et al., 2019; Hu et al., 2022), as well as links between benthic macroinvertebrates, the microbial community, and nutrient cycling (Cao et al., 2018; Zhang et al., 2021). These studies showed that the shapes of BEF relationships vary based on the taxonomic group considered, the nature of multi-trophic diversity interactions, and the type of biodiversity indicators selected (Daam et al., 2019). Like previous BEF research in terrestrial ecosystems, studies on BEF in freshwater ecosystems has focused on single trophic levels and individual EFs, but studies indicate that biodiversity affects multiple EFs simultaneously (Jing et al., 2015; Lefcheck et al., 2015; Zhang et al., 2021). Thus, considering an individual EF may underestimate the importance of biodiversity (Lefcheck et al., 2015; Garland et al., 2021), ignore the synergies or trade-offs between different EFs (Hector and Bagchi, 2007; Fu and Yu, 2016), and mask that the functional role of any trophic group may depend on the diversity of others (Jing et al., 2015).

Ecosystems are composed of multiple trophic levels and multitrophic communities are especially important in maintaining multiple EFs (Brose and Hillebrand, 2016; Wang and Brose, 2017; Anujan et al., 2021). Studies of single trophic levels are insufficient to understand the functional consequences of biodiversity decline (Gamfeldt et al., 2015; Lefcheck et al., 2015) because different trophic groups may have complementary (Eisenhauer et al., 2013; Ebeling et al., 2018) or opposite effects on EFs (Duffy et al., 2007). Additionally, some recent studies have shown that the strength of biodiversity effects on EFs can increase over time (Xu et al., 2021). Understanding how biodiversity affects ecosystem multifunctionality (EMF) requires analysis of the diversity within (horizontal diversity) and across trophic levels (vertical diversity) over time (Duffy et al., 2007; Xu et al., 2021). Compared with terrestrial and marine ecosystems, quantitative information about the effect of multitrophic levels and time on biodiversity–ecosystem multifunctionality (BEMF) relationships are largely lacking for freshwater ecosystems (Duffy et al., 2007; Daam et al., 2019). There is thus an urgent need for strengthening this research on BEMF relationships in freshwater ecosystems to fill current research gaps (Guy-Haim et al., 2018).

Due to human activities and global changes, the biodiversity crisis of freshwater ecosystems is deepening, affecting ecosystem services (Zhang et al., 2019). Increasing evidence has shown that freshwater biodiversity loss can cause serious impacts on EFs and may threaten human welfare (Scheffer et al., 2001; Jackson et al., 2016; Xu et al., 2016; Janssen et al., 2021; Losapio et al., 2021). Assessing BEMF relationships within and across trophic levels can allow prediction of the impacts of biodiversity change on the provisioning of ecosystem services (Duncan et al., 2015). We constructed a species-addition microcosm experiment with a diversity gradient (one, two, or three macrophyte species, and three macrophyte species with two aquatic animals) to investigate if (1) the effects of species richness on individual EF and EMF differed significantly among, within, and across trophic levels and, (2) there was a positive diversity–ecosystem stability relationship within and across trophic levels over time.

2 Materials and methods

2.1 Materials and experimental set-up

Three common submerged macrophytes and two common aquatic animals, *Hydrilla verticillata*, *Vallisneria natans*, *Potamogeton maackianus*, *Cyprinus carpio*, and *Cipangopaludina cahayensis* were chosen to evaluate the effects of species diversity within and across trophic levels on EMF. *H.verticillata*, *V. natans*, and *P. maackianus* are common macrophytes in the middle-lower reach of the Yangtze River, and they often can grow together and form a stable aquatic plant community. They were collected from Shahu Lake, a eutrophic lake near Hubei University, the proximity facilitating transport. The plants were then washed with running tap water to remove particles and other adjacent organisms. *Cyprinus carpio* that were 7.78 ± 0.80 cm (n = 24) in length and 4.93 ± 1.95 g (n = 24) in weight, and *Cipangopaludina cahayensis*

were 5.68 ± 0.40 g (n = 12) in weight, were brought from Chongqing Yongchuan Yuxi aquaculture base. The protocols involving animals were reviewed and approved by the Animal Ethics and Welfare Committee of Hubei University. Before the experiment, the three macrophytes and the two aquatic animals were cultivated in aquariums with tap water in the greenhouse; the temperature varied from 12.5 °C to 30.4 °C and the average temperature was 23.1 ± 6.1 °C during the experiment.

A species-addition experiment, consisting of twelve 110 L polyethylene buckets (diameter = 0.4 m, height = 0.65 m), was carried out from August 20 to November 20, 2021. The buckets were placed in the experimental greenhouse of Hubei University and filled with tap water which had total nitrogen (TN) and total phosphorus (TP) concentrations of 1.8 and 0.02 mg/L, respectively, and a water depth of 47 cm. The buckets were randomly divided into four treatments, each replicated three times, including *H. verticillata* monoculture (Mon), *H. verticillata* + *V. natans* mixed culture (Mix_{two}), *H. verticillata* + *V. natans* + *P. maackianus* mixed culture (Mix_{three}), and *H. verticillata* + *V. natans* + *P. maackianus* + *C. carpio* + *C. cahayensis* mixed culture (Mix_{five}). During the experiment, the water temperature varied from 10.7 °C to 28.6 °C, the average water temperature was 21.3 ± 6.0 °C, and the pH of the water varied from 8.3 to 9.9.

Before the experiment, *H. verticillata*, *V. natans*, and *P. maackianus* were washed thoroughly with tap water followed by deionized water, and the lateral branches or stolons of the plants were removed. Then, complete clean plants of *V. natans* (10 *cm* length) and apices of *H. verticillata and P. maackianus* cut at 10 cm below the top were prepared and planted in small plastic pots (length 18 cm and width 12 cm), which were filled with 5 cm fine sand. Fourteen plants were planted in each plastic pot. The density of *H. verticillata* was 14 in monoculture, the densities of *H. verticillata* and *V. natans* were eight and six in Mix_{two}, and the densities of *H. verticillata*, *V. natans*, and *P. maackianus* were eight, three, and three in Mix_{three} in each pot, respectively. In total, 168 young seedlings of similar size were transplanted into 12 small plastic pots, which included three *H. verticillata* monoculture pots, three *H. verticillata* + *V. natans* mixed culture pots, and six *H. verticillata* + *V. natans* + *P. maackianus* mixed culture pots. Then, 12 small plastic pots were placed randomly into the 12 polyethylene buckets. At the same time, three polyethylene buckets of the *H. verticillata* + *V. natans* + *P. maackianus* mixed cultures and two *C. carpio* and three *C. cahayensis* were randomly added to each polyethylene bucket. We used a line to lift and lower the pots, which allowed gentle and nondestructive sampling. During the experiment, deionized water was replenished every 2 days to compensate for evaporation losses and assure that the water levels were similar in all 12 polyethylene buckets. Also, dead *C. carpio* were replaced with live ones of approximately similar size.

2.2 Sampling and chemical analyses

At the beginning of the experiment, the height/length and fresh weight of all 168 macrophytes were measured with a ruler and an analysis balance. Macrophytes were measured on days 14, 28, 42, 56, and 70 after the start of the experiment. This was done by pulling up the tray on which the plant pots were standing, making handling and measuring easy and non-destructive. The height and length of each branch were measured with a ruler. After each measurement (except the last time), we put the macrophytes back into the corresponding polyethylene bucket. At the end of the experiment, all macrophytes were harvested and weighed, and the biomass of phytoplankton in the water column was proxied by total chlorophyll. Chlorophyll content was measured according to the method described by Jampeetong and Brix (2009). Filamentous macroalgae growing on the macrophytes or at the water surface were collected by hand, and epiphyton growing on the bucket wall and on the sand surface was collected by brush and then weighed.

The macrophyte biomasses of different sampling times were estimated by the fitted linear relationship between plant height and biomass using the data of height and biomass measured at the beginning of the experiment and at 70 days. The linear fitting equations for the three tested macrophytes were as follows:

$$H.\ verticillata: y = 3.10 + 0.015x$$

$$V.\ natans: y = 1.19 + 0.018x$$

$$P.\ maackianu: y = 0.16 + 0.013x$$

where x is the plant height in cm and y is the plant biomass in g.

The water temperature, dissolved oxygen content and pH, total nitrogen (TN), and total phosphorus (TP) concentration of each polyethylene bucket were measured at the beginning of the experiment and on days 14, 28, 42, 56, and 70. The water temperature, dissolved oxygen content, and pH of the water bodies were measured at 30 cm depth between 10:30 and 12:00 using a YSI (YSI 6600V2). The irradiance was measured by an illuminance meter (MODEL ZDS-10W-2D). TP content was measured using a colorimeter, an AutoAnalyzer (Bran+Luebbe GmbH, Inc., Germany), following sulfuric acid/hydrogen peroxide digestion and the ammonium molybdate ascorbic acid method. TN content was measured using an IL-500N nitrogen analyzer (Hach Company, Loveland, USA). During the experiment, different volumes of NH_4CL and KH_2PO_4 were added every 14 days to maintain 1.8 mg/L TN and 0.02 mg/L TP concentration in the water column in each bucket.

2.3 Statistical analysis

Three ecological functions, including total net primary productivity (the total biomass of macrophyte, phytoplankton, filamentous macroalgae, and epiphyton) and cumulative variation of TN and TP, at the end of the experiment in each polyethylene bucket, were used to quantify EMF.

The cumulative variation of TN and TP was calculated as:

$$C_{TN} = \sum_{i=1}^{n}(C_0 - C_i)$$

where $C_{TN(TP)}$ represents the cumulative variation of TN or TP, C_i represents the TN or TP content of the water measured at different sampling periods, and C_0 represents the value of the TN or TP content at the beginning of the experiment.

According to Maestre et al. (2012), we used the mean value method to quantify EMF because it simply and intuitively reflects the ability of communities to maintain EMF (Jing et al., 2015). We calculated the average of standardized data of the total net primary productivity and TN and TP cumulative variation. The multifunctionality index (*M*) for each polyethylene bucket was the average of the three evaluated functions *M* can be calculated according to the method used by Xu et al. (2016):

$$M = \frac{1}{F}\sum_{i=1}^{F} g(r_i(f_i))$$

where *F* represents the number of functions being measured, f_i represents the measures of function *i*, r_i represents a mathematical function that converts f_i to a positive value, and *g* represents standardizing of all index values (the top 5% of the measured values of each function are averaged as the maximum value of the function, and the ratio of each measured value to the maximum value is calculated).

The mean value method cannot distinguish between one function being provided at a high level and another being provided at a low level vs. two functions being provided at an intermediate level (Byrnes et al., 2014). As such, we calculated MF_t using 20%, 30%, 40%, 50%, 60%, and 70% of our threshold values. Thus, we supplemented the mean value method with a threshold analysis method for further analysis of the relationship between species richness and EMF.

Community temporal stability of macrophyte productivity was calculated for each treatment using the ratio of μ to σ:

$$St = \frac{\mu}{\sigma}$$

where μ represents mean net macrophyte primary productivity and σ represents net macrophyte primary productivity standard deviation.

Before statistical analysis, all data were tested for normality and were subjected to Levene's tests. Non-normal data were transformed (log10) to obtain normality. Repeated-measures ANOVA was used to test the effects of species richness, time, and their interaction on the total primary productivity, $C_{TN(TP)}$, and temporal stability of macrophyte productivity. A one-way ANOVA was applied to determine the statistical significance ($P< 0.05$) of the differences in the total primary productivity and the productivity of macrophytes, filamentous macroalgae and epiphyton, and phytoplankton at the end of the experiment, as well as $C_{TN(TP)}$, EMF, and temporal stability of macrophyte productivity among different treatments. The relationships between species richness and individual EFs, EMF, and temporal stability of macrophyte productivity were evaluated using simple OLS regressions within and across trophic levels. Variation partitioning analysis was used to analyze the degree of explanation of three indicator systems (environmental factors including water temperature, dissolved oxygen, pH, irradiance, time, and species richness) for the variation in EMF within and across trophic levels.

All the statistical analyses were performed with SPSS 20.0 for Windows (IBM Inc., Chicago, IL, USA) and R version 4.2.1 (https://www.r-project.org/), and figures were generated in Origin 2021 for Windows (OriginLab, Inc., USA).

3 Results

3.1 Effects of experimental treatments on individual EFs, EMF, and temporal stability of macrophyte productivity

For the three tested individual EFs (total primary productivity and the cumulative variation of TN and TP) and the temporal stability of macrophyte productivity, repeated-measures ANOVA showed that experimental treatments only significantly influenced total primary productivity ($P< 0.001$, Table 1, Figure 1). Time significantly influenced total primary productivity and the cumulative variation of TN (Table 1, Figure 2). The interactions of experimental treatments and time affect the three tested individual EFs (Table 1).

The response patterns of the total primary productivity and the macrophyte productivity for experimental treatments were similar. At the end of the experiment, the highest total primary productivity and macrophyte productivity both occurred in the Mix_{two} treatment, but significant differences in total primary productivity and macrophyte productivity were only found between the Mon

TABLE 1 Results from the repeated-measures ANOVA testing the effects of experimental treatments, time, and their interaction on the total primary productivity, the cumulative variation of TN and TP, and temporal stability of macrophyte productivity.

Effects	Total primary productivity (g)		The cumulative variation of TN (mg)		The cumulative variation of TP (mg)		Temporal stability of macrophyte productivity	
	F	*P*	*F*	*P*	*F*	*P*	*F*	*P*
Experimental treatments (*E*)	17.10	<0.001	2.81	0.11	3.38	0.08	1.53	0.28
Time (*T*)	81.41	<0.001	123.37	<0.001	2.21	0.07	1.40	0.24
E × *T*	3.36	<0.01	4.74	<0.001	3.27	<0.01	0.87	0.60

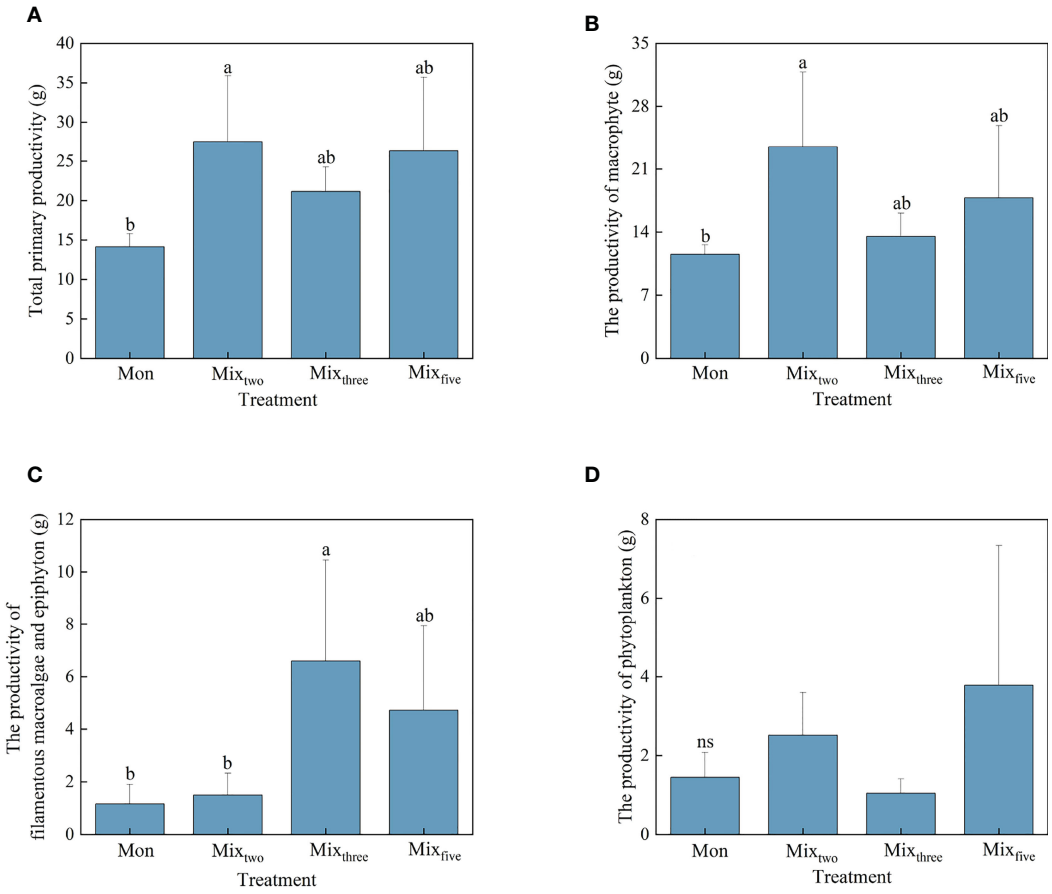

FIGURE 1
The total primary productivity **(A)** and the productivity of macrophyte **(B)**, filamentous macroalgae and epiphyton **(C)**, and phytoplankton **(D)** under different treatments at the end of the experiment. Bars represent mean values ± *SD* (*n* = 3), and different letters indicate significant differences ($P< 0.05$) between the treatments. (Mon: *H. verticillata* monoculture, Mix$_{two}$: *H. verticillata* + V. natans mixed culture, Mix$_{three}$: *H. verticillata* + *V. natans* + *P. maackianus* mixed culture, and Mix$_{five}$: *H. verticillata* + *V. natans* + *P. maackianus* + *C. carpio* + *C. cahayensis* mixed culture).

and Mix$_{two}$ treatments ($P< 0.05$, Figures 1A, B). For other primary producers, the productivity of phytoplankton showed no significant difference among the four experimental treatments, and the productivity of filamentous macroalgae and epiphyton under the Mix$_{three}$ treatment was significantly higher than Mon and Mix$_{two}$ treatments ($P< 0.05$, Figures 1C, D).

For the cumulative variation of TN and TP, the values of the two tested individual EFs in the Mix$_{five}$ treatment were significantly lower than that under other experimental treatments at the end of the experiment ($P< 0.05$). However, no significant differences were found in the amount of cumulative variation of the two aforementioned individual EFs among the three experimental treatments within a trophic level (Figures 2A, B). For the temporal stability of macrophyte productivity, there was no significant difference among the four experimental treatments (Figure 2C).

A one-way ANOVA showed that trophic complexity had a significant effect on EMF ($P< 0.05$, Figure 3). At the end of the experiment, the value of EMF across trophic levels was significantly lower than that within a trophic level ($P< 0.05$), while there was no significant difference among different macrophyte species richness treatments within a trophic level (Figure 3).

3.2 Relationship between species richness and individual EFs, EMF, and temporal stability of macrophyte productivity

For individual EFs, simple OLS regression analyses showed that species richness positively correlated with the total primary productivity within and across the trophic levels (Figure 4A). Across the trophic levels, there was a significant negative relationship between species richness and the cumulative variation of TP and EMF ($P< 0.05$, Figures 4C, D). However, there were no significant correlations between species richness and the cumulative variation of TN and temporal stability of macrophyte productivity within and across the trophic levels (Figures 4B–E).

A threshold analysis showed that species richness positively affected the number of functions exceeding the threshold at values of 40% and 50%, and the relationships between species richness and the number of functions became flatter at higher and lower threshold values of 70% and 30%, respectively. By contrast, when the threshold value was 20%, species richness negatively affected the number of functions exceeded (Figure 5).

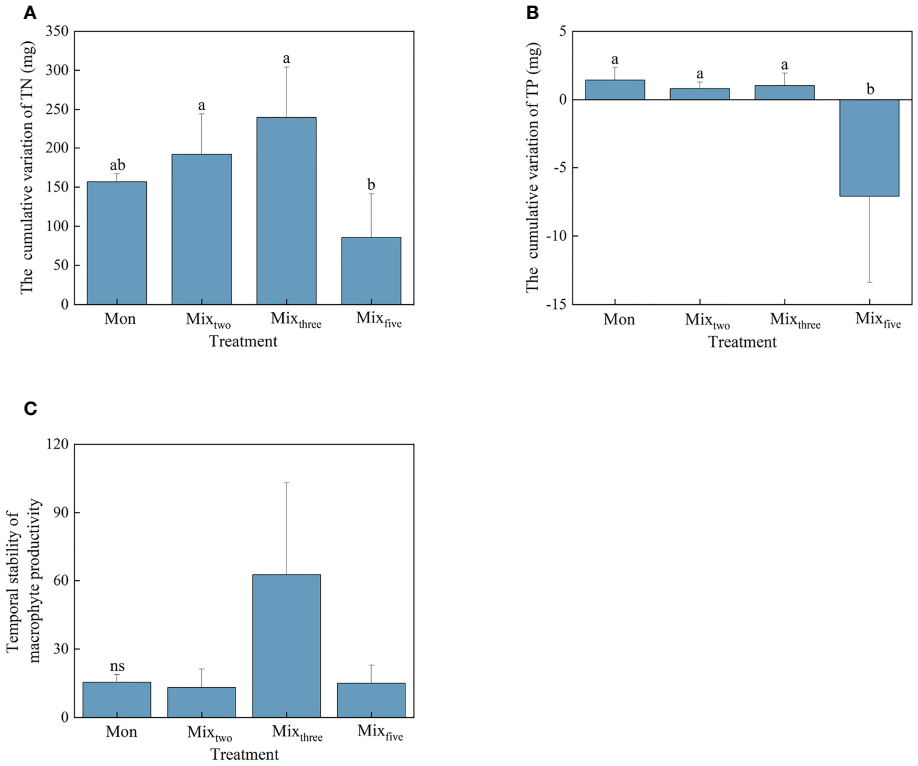

FIGURE 2
The cumulative variation of TN **(A)** and TP **(B)** and the temporal stability of macrophyte productivity **(C)** under different treatments at the end of the experiment. Bars represent mean values ± *SD* (*n* = 3), and different letters indicate significant differences (*P*< 0.05) between the treatments.

3.3 Estimation of the relative contribution of the driving factors of EMF

Variation partitioning analyses showed that the number of variances of EMF explained by environmental factors, time, and species richness were similar among, within, and across the trophic levels, and the total explanations for EMF within and across trophic levels both were 99.60%, although the independent effects of the three driving factors were weak (Figure 6). Variation partitioning showed that the shared effects of environmental factors and time accounted for a high percentage, with their combined effects for EMF within and across trophic levels 94.10% and 89.00%, respectively (Figure 6). Furthermore, our results showed that time has the strongest independent effects on EMF within and across trophic levels among the three tested factors.

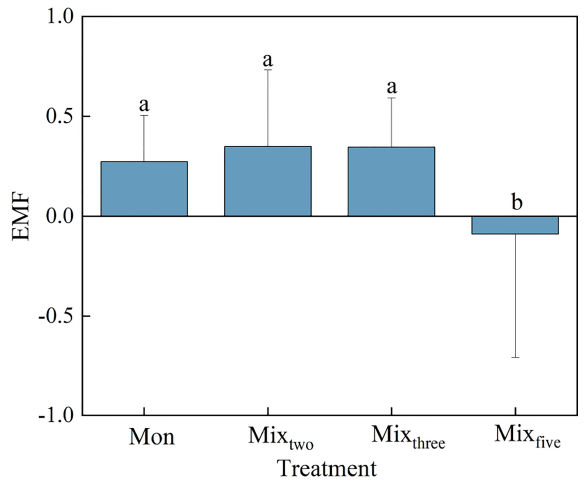

FIGURE 3
The EMF in different treatments at the end of the experiment. Bars represent mean values ± *SD* (*n* = 3), and different letters indicate significant differences (*P*< 0.05) between the treatments.

4 Discussion

4.1 Individual EFs within and across trophic levels

For individual EFs, as found in several other studies (Tilman et al., 1997; Engelhardt and Ritchie, 2001; Isbell et al., 2011; Chang et al., 2022), we showed that species richness–productivity relationships are positive both within and across trophic species diversity levels. Previous studies showed that the two main mechanisms responsible for the positive species richness–productivity relationship are the niche complementarity effect hypothesis and the selection effect hypothesis (Loreau and Hector, 2001). In this study, our results indicated that positive richness–productivity relationships may be largely due to the selection effect. Some studies demonstrated that higher productivity from greater

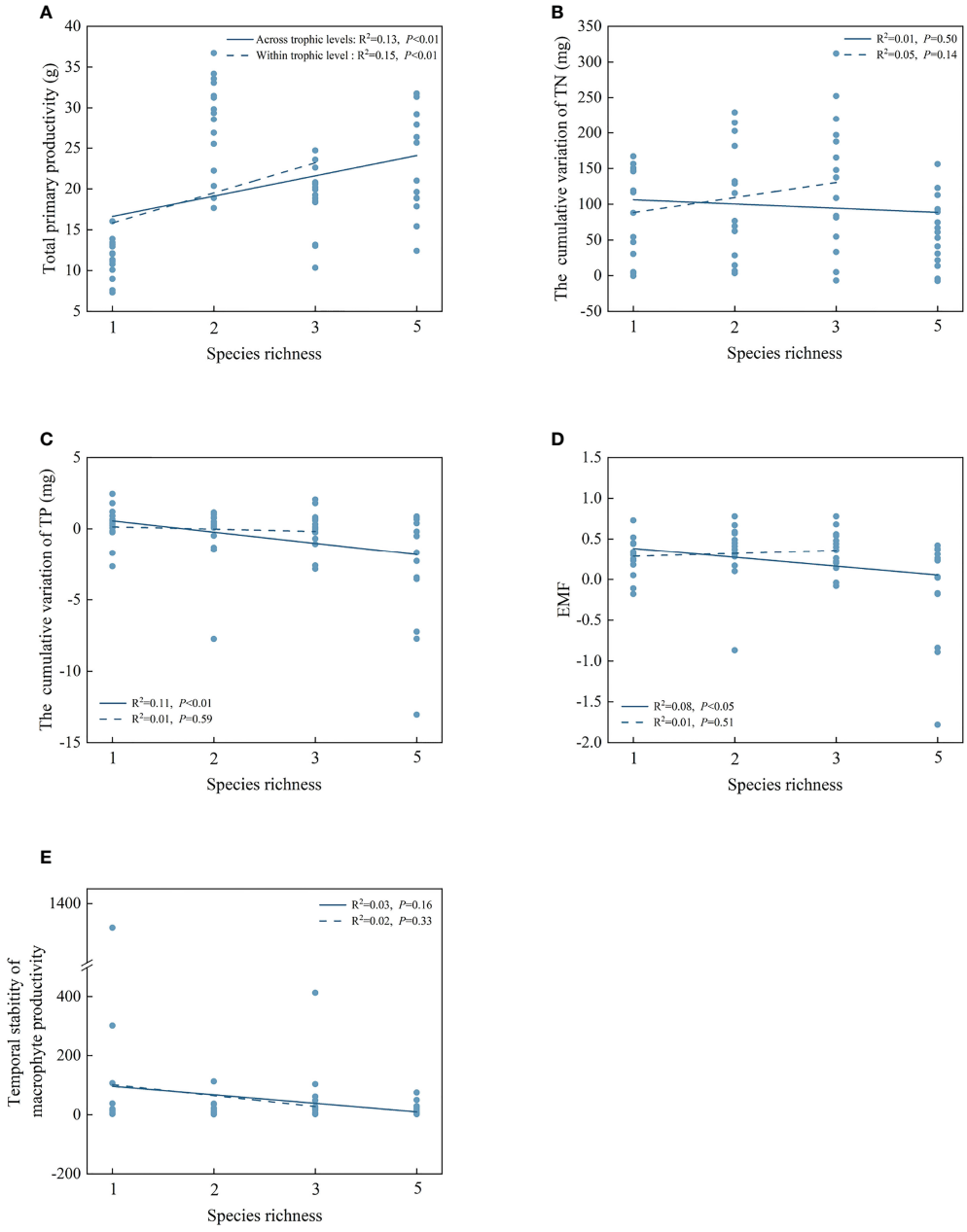

FIGURE 4
The correlations of species richness on total primary productivity **(A)**, the cumulative variation of TN **(B)**, the cumulative variation of TP **(C)**, EMF **(D)**, and temporal stability of macrophyte productivity **(E)** within and across trophic levels.

species richness sometimes arises from the greater chance that superior competitors with high productivity are present in species mixtures (Tilman et al., 1997; Engelhardt and Ritchie, 2001). Our results indicated that *H. verticillata* became dominant due to environmental selection and competition and provided higher productivity within a community. Similar life-forms of submerged macrophyte species involved in our study may reduce the niche complementarity effect on system productivity. This may be because complementarity among submerged macrophyte species, especially for species of a similar type, might be rather weak, resulting in species diversity having no significant effect on vegetative production (Zhang et al., 2019). Thus, it is important to note that the types of species used in such experiments may lead to different outcomes (Zhang et al., 2019). Besides macrophyte productivity, our results showed that there were higher filamentous macroalgae and epiphyton productivity in communities with greater species richness. The most plausible explanation may be through a niche complementarity effect because various macrophytes can access different and more overall resources (Vanderstukken et al., 2011; Zhang et al., 2019). Therefore, our results suggest that the underlying mechanisms of species richness–productivity relationships were primary producer taxonomic group-specific.

Different from the positive correlation between species richness and productivity, our findings showed that species richness did not

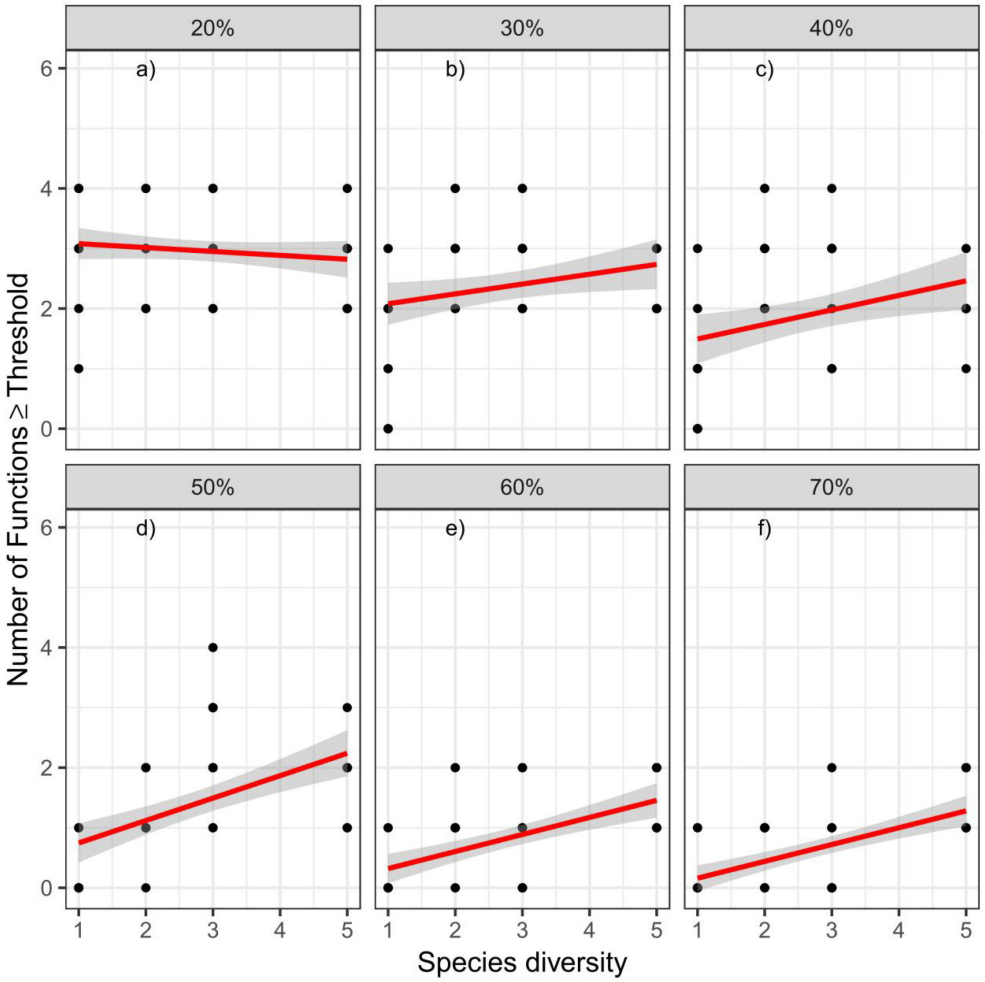

FIGURE 5
The relationships between species richness and multifunctionality. Panels show the relationships for six different thresholds (20%, 30%, 40%, 50%, 60%, and 70%).

significantly relate to the cumulative variation of TN and TP within a trophic level. Previous studies demonstrated that BEF relationships for different EFs are not always congruent, and there are many different BEF relationships with positive, negative, nonlinear, and non-significant correlations (Mittelbach et al., 2001; Hooper et al., 2005; Duffy, 2009; Jaillard et al., 2014; Brose and Hillebrand, 2016). The observed non-significant correlations between species richness and the cumulative variation of TN and TP can be explained by other important processes besides nutrient uptake by plants and algae, including nutrient recycling by microorganisms or nutrients retained by sediment or surface structures, playing vital roles in nitrogen and phosphorus removal (Engelhardt and Ritchie, 2001; Zhang et al., 2019). We found a significant negative relationship between species richness and the cumulative variation of TP across trophic levels, but there were no significant correlations between species richness and the cumulative variation of TN. The main reason may be due to the different removal mechanisms of TN and TP in the water column, e.g., TN loss is mainly *via* denitrification by microorganisms; however, TP loss is mainly by plant absorption (Kyambadde et al., 2004; Paerl et al., 2011; Ma et al., 2017; Xing et al., 2020). Another reason may be that consumer excretion and decomposition of dead bodies release nutrients to the water column, resulting in increased phosphorus concentrations in the water column (Northcote, 1988). Our results further suggest that consumers play an important role in the EFs of freshwater systems (Duffy, 2002; Thébault and Loreau, 2003; Duffy et al., 2005) and that multitrophic species diversity has a greater impact on EMF than macrophyte diversity (Lefcheck et al., 2015).

4.2 EMF and temporal stability of macrophyte productivity within and across trophic levels

Quite different from most research results that biodiversity enhances EMF (Hector and Bagchi, 2007; Lefcheck et al., 2015; Perkins et al., 2015; Moi et al., 2021), our results showed a significant negative correlation between species richness and EMF across trophic levels. Early research about the relationship between biodiversity and

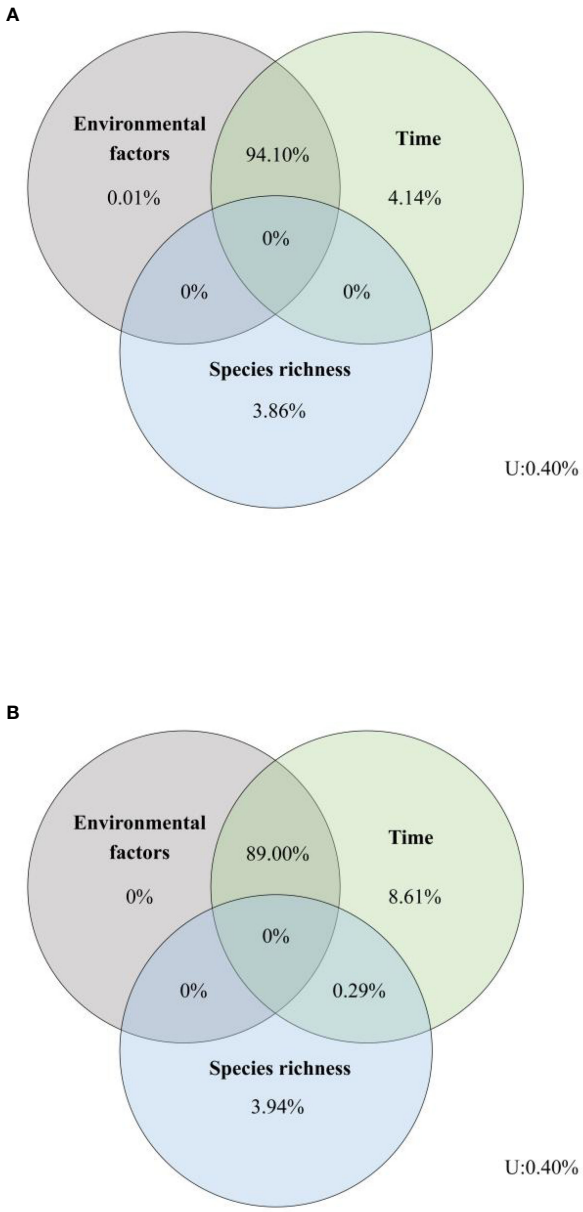

FIGURE 6
Relative effects of environmental factors, time, and species richness on EMF **(A)** within a trophic level, **(B)** across trophic levels. U, unexplained.

EF showed similar negative species richness–EMF relationships and suggested that greater diversity caused by poor competitors results in reduced productivity (Loreau, 1998; Lasky et al., 2014). In our study, the negative species richness–EMF relationships were not due to primary productivity because there were non-significant differences in total primary productivity. Two reasons account for this phenomenon. First, it may be due to selected individual EFs and the functions used to calculate EMF (Edlinger et al., 2020; Garland et al., 2021; Jing and He, 2021), because different individual EFs would influence EMF through different trade-offs or synergies (Zavaleta et al., 2010; Byrnes et al., 2014). Second, the average approach used to calculate EMF in our study may affect the objective weight and general weight of the three selected individual EFs, which can lead to higher contribution rates of TN and TP cumulative variation for EMF (Byrnes et al., 2014). The effects of nutrients released *via* consumer excretion and the decomposition of dead bodies may be additive (or synergistic). Thus, our results emphasize the importance of selecting individual EFs, as well as the fact that the calculation of EMF can result in different outcomes for BEMF relationships.

Increased diversity facilitates the temporal stability of community productivity (Cottingham et al., 2001; Valone and Hoffman, 2003; Tilman et al., 2006). Although we hypothesized that there were positive diversity–ecosystem stability relationships within and across trophic levels, the lack of consistent differences in temporal stability of productivity among the four experimental treatments did not support this hypothesis. In agreement with some other studies

(Jiang and Pu, 2009; Sasaki and Lauenroth, 2011; Ma et al., 2017), our results also showed that increased macrophyte species richness does not affect the temporal stability of macrophyte productivity within a trophic level. The most probable explanation is that productivity was controlled by dominant macrophyte species, rather than species richness, which results in no effect of species richness on macrophyte productivity (Sasaki and Lauenroth, 2011; Ma et al., 2017). Another possible reason may be lower species richness and lower trophic level complexity, as the relationship between species richness and temporal stability of community productivity was critically dependent (Jiang and Pu, 2009). Our study uses low species richness and fewer trophic levels and, therefore, almost certainly underestimates the levels of diversity needed for EMF.

4.3 Effect of species richness, time and environmental factors on EMF

Our results showed that the links between EMF and biodiversity within and across trophic levels are mediated by the combination of environmental factors and time, more so than by species richness. Many studies have proved that environmental factors and time can affect the interactions between the various elements of an ecosystem which results in effects on the EMF (Bai et al., 2022). Changing environmental factors can affect EF both directly *via* altering rates of ecosystem processes (Spaak et al., 2017) and indirectly *via* altering species dynamics and interactions (Dornelas et al., 2014; Blowes et al., 2019); environmental factors could also interact with biodiversity in regulating EF (Eisenhauer et al., 2019; Benkwitt et al., 2020). For example, individual responses to environmental variations cause changes in population abundance, generating interactions between populations, which in turn affect community structure and composition that extend to entire ecosystems (Hofmann and Todgham, 2010). Some studies indicated the effects of environmental factors on EMF may change over time (Tilman et al., 2001; Xu et al., 2021; Guo et al., 2022; Hong et al., 2022), and the response rate of EF to environmental change depends on the resilience of ecosystem functions over time (Wu et al., 2018; Qu et al., 2019). Long-term experiments are revealing that the slope of the BEF relationship can vary with environmental context across sites and through time (Isbell et al., 2011; Qiu and Cardinale, 2020). Thus, some researchers strongly emphasize that the dimension of time should be taken into consideration in experiments and observational studies which can predict whether, when, and to what extent ecosystems will be affected by altered conditions (Edlinger et al., 2020).

We found a weak influence of species richness on EMF within and across trophic levels. This also may be due to selected individual EFs and the diversity of the taxonomic group considered. In our study, we only took macrophytes, snails, and fish as representatives for biodiversity. Other groups of organisms, such as microbes, can drive many ecosystem processes, especially nutrient cycling, but our study does not directly address the functional role played by these and other important groups. Obviously, our results underestimated the effects of some organisms on EMF, especially for microbes which can significantly influence the nitrogen cycle in our study. Therefore, our results further highlight the significance of selecting individual EFs and considering the diversity of the taxonomic groups for BEMF relationship research (Vaughn, 2010; Zhang et al., 2019).

5 Conclusion

In this study, we examined how biodiversity affects the individual EFs and EMF within and across trophic levels over time in freshwater ecosystems. Although our study used low levels of species richness and fewer trophic levels, we found the following: 1) positive diversity–productivity relationships within and across trophic levels, 2) significant negative correlations between species richness and the cumulative variation of TP and EMF across trophic levels, and 3) the links between EMF and biodiversity within and across the trophic levels are mediated by the combination of environmental factors and time, rather than by species richness. Together with other research, these results indicate that BEF relationships for different EFs are not always the same, and multitrophic species diversity has a greater impact on EF than plant diversity.

Beyond experimental limitations, our study provides important insights and implications for the conservation and management of shallow lakes. Species richness of multiple trophic groups, such as consumers and primary producers, are crucial moderators of EMF. Similar submerged macrophyte species involved in this study may have influenced the experimental outcomes because individual species with unique traits can be as important to ecosystem function as high species richness. Furthermore, species within functional groups are not necessarily ecological equivalents. The composition of aquatic plant functional groups is directly related to community productivity (Fu et al., 2014; 2019). Some studies have shown that differences in ecosystem function among different life forms due to plant phylogeny or plant adaptations to the environment, and the complex interactions between species of different functional groups in natural ecosystems can have significant effects on the structure and function of ecosystems (Thébault and Loreau, 2003; Ives et al., 2005). Thus, our results imply that management practices that restore the diversity of aquatic macrophytes in wetlands should consider not only species diversity but also different functional groups and life forms. Future research should study these relationships between different functional groups and life forms in the context of global change to more comprehensively study the functional dynamics of freshwater ecosystems to achieve better predictive power for conservation and restoration initiatives.

Data availability statement

The raw data supporting the conclusions of this article will be made available by the authors, without undue reservation.

Ethics statement

The studies involving animals were reviewed and approved by Animal Ethics and Welfare Committee of Hubei University.

Author contributions

ZL and ZX designed the study. ZX, HY, HM, QP and SY conducted the experiment. ZX, QC, YY, and LW performed chemical analyses and statistical analyses. ZX wrote the paper, and other co-authors reviewed the paper. All authors contributed to the article and approved the submitted version.

Funding

The study was financed by National Natural Science Foundation of China (32271612), the Key Project of the National Natural Science Foundation of Hubei Province (2020CFA005), and the Young and Middle-aged Science & Technology Innovation Team Project of Hubei Provincial Department of Education (T201701).

Conflict of interest

The authors declare that the research was conducted in the absence of any commercial or financial relationships that could be construed as a potential conflict of interest.

Publisher's note

References

Anujan, K., Heipern, S. A., Prager, C. M., Weeks, B. C., and Naeem, S. (2021). Trophic complexity alters the diversity multifunctionality relationship in experimental grassland mesocosms. *Ecol. Evolution.* 11, 6471–6479. doi: 10.1002/ece3.7498

Bai, Y., Wu, J., Pan, Q., Huang, J., Wang, Q., Li, F., et al. (2007). Positive linear relationship between productivity and diversity: Evidence from the Eurasian steppe. *J. Appl. Ecol.* 44, 1023–1034. doi: 10.1111/j.1365-2664.2007.01351.x

Bai, X. H., Zhao, W. W., and Yin, C. C. (2022). Change process and interaction mechanism of ecosystem services from the perspective of regime shift. *Acta Ecologica Sin.* 42 (15), 6054–6065. doi: 10.5846/stxb202103280808

Benkwitt, C. E., Wilson, S. K., and Graham, N. A. (2020). Biodiversity increases ecosystem functions despite multiple stressors on coral reefs. *Nat. Ecol. Evol.* 4 (7), 919–926. doi: 10.1038/s41559-020-1203-9

Blowes, S. A., Supp, S. R., Antão, L. H., Bates, A., Bruelheide, H., Chase, J. M. , et al. (2019). The geography of biodiversity change in marine and terrestrial assemblages. *Science* 366 (6463), 339–345. doi: 10.1126/science.aaw1620

Brooker, R. W., George, T. S., Homulle, Z., Karley, A. J., Newton, A. C., Pakeman, R. J., et al. (2021). Facilitation and biodiversity-ecosystem function relationships in crop production systems and their role in sustainable farming. *J. Ecol.* 109 (5), 2054–2067. doi: 10.1111/1365-2745.13592

Brose, U., and Hillebrand, H. (2016). Biodiversity and ecosystem functioning in dynamic landscapes. *Philos. Trans. R. Soc. Lond. B. Biol. Sci.* 371 (1694), 20150267. doi: 10.1098/rstb.2015.0267

Byrnes, J. E., Gamfeldt, L., Isbell, F., Lefcheck, J. S., Griffin, J. N., Hector, A., et al. (2014). Investigating the relationship between biodiversity and ecosystem multifunctionality: challenges and solutions. *Methods Ecol. Evol.* 5 (2), 111–124. doi: 10.1111/2041-210X.12143

Cao, X., Chai, L., Jiang, D., Wang, J., Liu, Y., and Huang, Y. (2018). Loss of biodiversity alters ecosystem function in freshwater streams: potential evidence from benthic macroinvertebrates. *Ecosphere* 9 (10), e02445. doi: 10.1002/ecs2.2445

Cardinale, B. J., Duffy, J. E., Gonzalez, A., Hooper, D. U., Perrings, C., Venail, P., et al. (2012). Biodiversity loss and its impact on humanity. *Nature* 486 (7401), 59–67. doi: 10.1038/nature11148

Chang, C. W., Miki, T., Ye, H., Souissi, S., Adrian, R., Anneville, O., et al. (2022). Causal networks of phytoplankton diversity and biomass are modulated by environmental context. *Nat. Commun.* 13 (1), 1140. doi: 10.1038/s41467-022-28761-3

Cottingham, K. L., Brown, B. L., and Lennon, J. T. (2001). Biodiversity may regulate the temporal variability of ecological systems. *Ecol. Lett.* 4 (1), 72–85. doi: 10.1046/j.1461-0248.2001.00189.x

Daam, M. A., Teixeira, H., Lillebø, A. I., and Nogueira, A. J. A. (2019). Establishing causal links between aquatic biodiversity and ecosystem functioning: Status and research needs. *Sci. Total Environ.* 656, 1145–1156. doi: 10.1016/j.scitotenv.2018.11.413

Davidson, T. A., Reid, M. A., Sayer, C. D., and Chilcott, S. (2013). Palaeolimnological records of shallow lake biodiversity change: exploring the merits of single versus multi-proxy approaches. *J. Paleolimnology* 49, 431–446. doi: 10.1007/s10933-013-9696-8

Dornelas, M., Gotelli, N. J., McGill, B., Shimadzu, H., Moyes, F., Sievers, C., et al. (2014). Assemblage time series reveal biodiversity change but not systematic loss. *Science* 344 (6181), 296–299. doi: 10.1126/science.1248484

Duffy, J. E. (2002). Biodiversity and ecosystem function: the consumer connection. *Oikos* 99 (2), 201–219. doi: 10.1034/j.1600-0706.2002.990201.x

Duffy, J. E. (2009). Why biodiversity is important to the functioning of real-world ecosystems. *Front. Ecol. Environ.* 7 (8), 437–444. doi: 10.1890/070195

Duffy, J. E., Cardinale, B. J., France, K. E., McIntyre, P. B., Thébault, E., and Loreau, M. (2007). The functional role of biodiversity in ecosystems: incorporating trophic complexity. *Ecol. Lett.* 10 (6), 522–538. doi: 10.1111/j.1461-0248.2007.01037.x

Duffy, J. E., Paul Richardson, J., and France, K. E. (2005). Ecosystem consequences of diversity depend on food chain length in estuarine vegetation. *Ecol. Lett.* 8 (3), 301–309. doi: 10.1111/j.1461-0248.2005.00725.x

Duncan, C., Thompson, J. R., and Pettorelli, N. (2015). The quest for a mechanistic understanding of biodiversity-ecosystem services relationships. *Proc. R. Soc. B: Biol. Sci.* 282 (1817), 20151348. doi: 10.1098/rspb.2015.1348

Ebeling, A., Rzanny, M., Lange, M., Eisenhauer, N., Hertzog, L. R., Meyer, S. T., et al. (2018). Plant diversity induces shifts in the functional structure and diversity across trophic levels. *Oikos* 127 (2), 208–219. doi: 10.1111/oik.04210

Edlinger, A., Saghaï, A., Herzog, C., Degrune, F., and Garland, G. (2020). Towards a multidimensional view of biodiversity and ecosystem functioning in a changing world. *New Phytol.* 228, 820–822. doi: 10.1111/nph.16881

Eisenhauer, N., Dobies, T., Cesarz, S., Hobbie, S. E., Meyer, R. J., Worm, K., et al. (2013). Plant diversity effects on soil food webs are stronger than those of elevated CO_2 and n deposition in a long-term grassland experiment. *Proc. Natl. Acad. Sci.* 110 (17), 6889–6894. doi: 10.1073/pnas.1217382110

Eisenhauer, N., Schielzeth, H., Barnes, A. D., Barry, K., Brose, U., Bruelheide, H., et al. (2019). A multitrophic perspective on biodiversity–ecosystem functioning research. *Adv. Ecol. Res.* 61, 1–48. doi: 10.1016/bs.aecr.2019.06.001

Engelhardt, K. A., and Ritchie, M. E. (2001). Effects of macrophyte species richness on wetland ecosystem functioning and services. *Nature* 411 (6838), 687–689. doi: 10.1038/35079573

Fu, H., Yuan, G., Li, W., Ge, D., Zou, D., and Huang, Z. (2019). Environmental effects on community productivity of aquatic macrophytes are mediated by species and functional composition. *Ecohydrology* 12 (8), e2147. doi: 10.1002/eco.2147

Fu, H., Zhong, J., Yuan, G., Ni, L., Xie, P., and Cao, T. (2014). Functional traits composition predict macrophytes community productivity along a water depth gradient in a freshwater lake. *Ecol. Evol.* 4 (9), 1516–1523. doi: 10.1002/ece3.1022

Fu, B. J., and Yu, D. D. (2016). Trade-off analyses and synthetic integrated method of multiple ecosystem services. *Resour. Sci.* 38 (1), 1–9. doi: 10.18402/resci.2016.01.01

Gagic, V., Bartomeus, I., Jonsson, T., Taylor, A., Winqvist, C., Fischer, C., et al. (2015). Functional identity and diversity of animals predict ecosystem functioning better than species-based indices. *Proc. R. Soc. B: Biol. Sci.* 282 (1801), 20142620. doi: 10.1098/rspb.2014.2620

Gamfeldt, L., Lefcheck, J. S., Byrnes, J. E., Cardinale, B. J., Duffy, J. E., and Griffin, J. N. (2015). Marine biodiversity and ecosystem functioning: what's known and what's next? *Oikos* 124 (3), 252–265. doi: 10.1111/oik.01549

Garland, G., Banerjee, S., Edlinger, A., Miranda Oliveira, E., Herzog, C., Wittwer, R., et al. (2021). A closer look at the functions behind ecosystem multifunctionality: A review. *J. Ecol.* 109 (2), 600–613. doi: 10.1111/1365-2745.13511

Guo, C., Zhu, M., Xu, H., Zhang, Y., Qin, B., Zhu, G., et al. (2022). Spatiotemporal dependency of resource use efficiency on phytoplankton diversity in lake taihu. *Limnology Oceanography* 67 (4), 830–842. doi: 10.1002/lno.12038

Guy-Haim, T., Lyons, D. A., Kotta, J., Ojaveer, H., Queirós, A. M., Chatzinikolaou, E., et al. (2018). Diverse effects of invasive ecosystem engineers on marine biodiversity and ecosystem functions: A global review and meta-analysis. *Global Change Biol.* 24 (3), 906–924. doi: 10.1111/gcb.14007

Hector, A., and Bagchi, R. (2007). Biodiversity and ecosystem multifunctionality. *Nature* 448 (7150), 188–190. doi: 10.1038/nature05947

Hofmann, G. E., and Todgham, A. E. (2010). Living in the now: physiological mechanisms to tolerate a rapidly changing environment. *Annu. Rev. Physiol.* 72, 127–145. doi: 10.1146/annurev-physiol-021909-135900

Hong, P., Schmid, B., De Laender, F., Eisenhauer, N., Zhang, X., Chen, H., et al. (2022). Biodiversity promotes ecosystem functioning despite environmental change. *Ecol. Lett.* 25 (2), 555–569. doi: 10.1111/ele.13936

Hooper, D. U., Chapin, F. S. III, Ewel, J. J., Hector, A., Inchausti, P., Lavorel, S., et al. (2005). Effects of biodiversity on ecosystem functioning: a consensus of current knowledge. *Ecol. Monogr.* 75 (1), 3–35. doi: 10.1890/04-0922

Hu, A., Li, Y., Yang, Y., Peng, Q., and Li, Z. (2022). Effects of different growth form submerged macrophyte assemblages on biomass accumulation and water purification. *Lake Sci.* 34 (5), 1484–1492. doi: 10.18307/2022.0527

Isbell, F., Calcagno, V., Hector, A., Connolly, J., Harpole, W. S., Reich, P. B., et al. (2011). High plant diversity is needed to maintain ecosystem services. *Nature* 477 (7363), 199–202. doi: 10.1038/nature10282

Ives, A. R., Cardinale, B. J., and Snyder, W. E. (2005). A synthesis of subdisciplines: predator-prey interactions, and biodiversity and ecosystem functioning. *Ecol. Lett.* 8 (1), 102–116. doi: 10.1111/j.1461-0248.2004.00698.x

Jackson, M. C., Weyl, O. L. F., Altermatt, F., Durance, I., Friberg, N., Dumbrell, A. J., et al. (2016). "Recommendations for the next generation of global freshwater biological monitoring tools," in *Advances in ecological research*, vol. 55 . Eds. A. J. Dumbrell, R. L. Kordas and G. Woodward (Academic Press), 615–636. doi: 10.1016/bs.aecr.2016.08.008

Jaillard, B., Rapaport, A., Harmand, J., Brauman, A., and Nunan, N. (2014). Community assembly effects shape the biodiversity-ecosystem functioning relationships. *Funct. Ecol.* 28 (6), 1523–1533. doi: 10.1111/1365-2435.12267

Jampeetong, A., and Brix, H. (2009). Effects of NaCl salinity on growth, morphology, photosynthesis and proline accumulation of salvinia natans. *Aquat. Bot.* 91 (3), 181–186. doi: 10.1016/j.aquabot.2009.05.003

Janssen, A. B. G., Hilt, S., Kosten, S., de Klein, J. J., Paerl, H. W., and Van de Waal, D. B. (2021). Shifting states, shifting services: Linking regime shifts to changes in ecosystem services of shallow lakes. *Freshw. Biol.* 66, 1–12. doi: 10.1111/fwb.13582

Jiang, L., and Pu, Z. (2009). Different effects of species diversity on temporal stability in single-trophic and multitrophic communities. *Am. Nat.* 174 (5), 651–659. doi: 10.1086/605961

Jing, X., Sanders, N. J., Shi, Y., Chu, H., Classen, A. T., Zhao, K., et al. (2015). The links between ecosystem multifunctionality and above-and belowground biodiversity are mediated by climate. *Nat. Commun.* 6 (1), 8159. doi: 10.1038/ncomms9159

Jing, X., and He, J. (2021). Relationship between biodiversity, ecosystem multifunctionality and multiserviceability: literature overview and research advances. *Chin. J. Plant Ecology.* 45 (10), 1094–1111. doi: 10.17521/cjpe.2020.0154

Kyambadde, J., Kansiime, F., Gumaelius, L., and Dalhammar, G. (2004). A comparative study of cyperus papyrus and miscanthidium violaceum-based constructed wetlands for wastewater treatment in a tropical climate. *Water Res.* 38 (2), 475–485. doi: 10.1016/j.watres.2003.10.008

Lasky, J. R., Uriarte, M., Boukili, V. K., Erickson, D. L., John Kress, W., and Chazdon, R. L. (2014). The relationship between tree biodiversity and biomass dynamics changes with tropical forest succession. *Ecol. Lett.* 17 (9), 1158–1167. doi: 10.1111/ele.12322

Lefcheck, J. S., Byrnes, J. E., Isbell, F., Gamfeldt, L., Griffin, J. N., Eisenhauer, N., et al. (2015). Biodiversity enhances ecosystem multifunctionality across trophic levels and habitats. *Nat. Commun.* 6 (1), 1–7. doi: 10.1038/ncomms7936

Loreau, M. (1998). Ecosystem development explained by competition within and between material cycles. *Proc. R. Soc. London. Ser. B: Biol. Sci.* 265 (1390), 33–38. doi: 10.1098/rspb.1998.0260

Loreau, M., and Hector, A. (2001). Partitioning selection and complementarity in biodiversity experiments. *Nature* 412 (6842), 72–76. doi: 10.1038/35083573

Losapio, G., Schmid, B., Bascompte, J., Michalet, R., Cerretti, P., Germann, C., et al. (2021). An experimental approach to assessing the impact of ecosystem engineers on biodiversity and ecosystem functions. *Ecology* 102 (2), e03243. doi: 10.1002/ecy.3243

Ma, Z., Liu, H., Mi, Z., Zhang, Z., Wang, Y., Xu, W., et al. (2017). Climate warming reduces the temporal stability of plant community biomass production. *Nat. Commun.* 8 (1), 15378. doi: 10.1038/ncomms15378

Maestre, F. T., Quero, J. L., Gotelli, N. J., Escudero, A., Ochoa, V., Delgado-Baquerizo, M., et al. (2012). Plant species richness and ecosystem multifunctionality in global drylands. *Science* 335 (6065), 214–218. doi: 10.1126/science.1215442

Messmer, V., Blowes, S. A., Jones, G. P., and Munday, P. L. (2014). Experimental evaluation of diversity-productivity relationships in a coral reef fish assemblage. *Oecologia* 176, 237–249. doi: 10.1007/s00442-014-2992-9

Mittelbach, G. G., Steiner, C. F., Scheiner, S. M., Gross, K. L., Reynolds, H. L., Waide, R. B., et al. (2001). What is the observed relationship between species richness and productivity? *Ecology* 82 (9), 2381–2396. doi: 10.1890/0012-9658(2001)082[2381:WITORB]2.0.CO;2

Moi, D. A., Romero, G. Q., Antiqueira, P. A., Mormul, R. P., Teixeira de Mello, F., and Bonecker, C. C. (2021). Multitrophic richness enhances ecosystem multifunctionality of tropical shallow lakes. *Funct. Ecol.* 35 (4), 942–954. doi: 10.1111/1365-2435.13758

Northcote, T. G. (1988). Fish in the structure and function of freshwater ecosystems: a "top-down" view. *Can. J. Fisheries Aquat. Sci.* 45 (2), 361–379. doi: 10.1139/f88-044

Paerl, H. W., Xu, H., McCarthy, M. J., Zhu, G., Qin, B., Li, Y., et al. (2011). Controlling harmful cyanobacterial blooms in a hyper-eutrophic lake (Lake Taihu, China): the need for a dual nutrient (N & P) management strategy. *Water Res.* 45 (5), 1973–1983. doi: 10.1016/j.watres.2010.09.018

Perkins, D. M., Bailey, R. A., Dossena, M., Gamfeldt, L., Reiss, J., Trimmer, M., et al. (2015). Higher biodiversity is required to sustain multiple ecosystem processes across temperature regimes. *Global Change Biol.* 21 (1), 396–406. doi: 10.1111/gcb.12688

Qiu, J., and Cardinale, B. J. (2020). Scaling up biodiversity-ecosystem function relationships across space and over time. *Ecology* 101 (11), e03166. doi: 10.1002/ecy.3166

Qu, Y., Wu, N., Guse, B., Makarevičiūtė, K., Sun, X., and Fohrer, N. (2019). Riverine phytoplankton functional groups response to multiple stressors variously depending on hydrological periods. *Ecol. Indic.* 101, 41–49. doi: 10.1016/j.ecolind.2018.12.049

Sasaki, T., and Lauenroth, W. K. (2011). Dominant species, rather than diversity, regulates temporal stability of plant communities. *Oecologia* 166 (3), 761–768. doi: 10.1007/s00442-011-1916-1

Scheffer, M. (2004). "The story of some shallow lakes," in *Ecology of shallow lakes*. Eds. D. L. DeAngelis and B. F. J. Manly (Dordrecht, the Netherlands: Kluwer Academic Publishers), 1–19.

Scheffer, M., Carpenter, S., Foley, J. A., Folke, C., and Walker, B. (2001). Catastrophic shifts in ecosystems. *Nature* 413 (6856), 591–596. doi: 10.1038/35098000

Schuldt, A., Assmann, T., Brezzi, M., Buscot, F., Eichenberg, D., Gutknecht, J., et al. (2018). Biodiversity across trophic levels drives multifunctionality in highly diverse forests. *Nat. Commun.* 9 (1), 2989. doi: 10.1038/s41467-018-05421-z

Slade, E. M., Kirwan, L., Bell, T., Philipson, C. D., Lewis, O. T., and Roslin, T. (2017). The importance of species identity and interactions for multifunctionality depends on how ecosystem functions are valued. *Ecology* 98 (10), 2626–2639. doi: 10.1002/ecy.1954

Spaak, J. W., Baert, J. M., Baird, D. J., Eisenhauer, N., Maltby, L., Pomati, F., et al. (2017). Shifts of community composition and population density substantially affect ecosystem function despite invariant richness. *Ecol. Lett.* 20 (10), 1315–1324. doi: 10.1111/ele.12828

Strong, J. A., Andonegi, E., Bizsel, K. C., Danovaro, R., Elliott, M., Franco, A., et al. (2015). Marine biodiversity and ecosystem function relationships: the potential for practical monitoring applications. *Estuarine Coast. Shelf Sci.* 161, 46–64. doi: 10.1016/j.ecss.2015.04.008

Thébault, E., and Loreau, M. (2003). Food-web constraints on biodiversity–ecosystem functioning relationships. *Proc. Natl. Acad. Sci.* 100 (25), 14949–14954. doi: 10.1073/pnas.2434847100

Tilman, D., Lehman, C. L., and Thomson, K. T. (1997). Plant diversity and ecosystem productivity: theoretical considerations. *Proc. Natl. Acad. Sci.* 94 (5), 1857–1861. doi: 10.1073/pnas.94.5.1857

Tilman, D., Reich, P. B., and Knops, J. M. (2006). Biodiversity and ecosystem stability in a decade-long grassland experiment. *Nature* 441 (7093), 629–632. doi: 10.1038/nature04742

Tilman, D., Reich, P. B., Knops, J., Wedin, D., Mielke, T., and Lehman, C. (2001). Diversity and productivity in a long-term grassland experiment. *Science* 294 (5543), 843–845. doi: 10.1126/science.1060391

Valone, T. J., and Hoffman, C. D. (2003). A mechanistic examination of diversity-stability relationships in annual plant communities. *Oikos* 103 (3), 519–527. doi: 10.1034/j.1600-0706.2003.12279.x

van der Plas, F. (2019). Biodiversity and ecosystem functioning in naturally assembled communities. *Biol. Rev.* 94 (4), 1220–1245. doi: 10.1111/brv.12499

Vanderstukken, M., Mazzeo, N., Van Colen, W., Declerck, S. A., and Muylaert, K. (2011). Biological control of phytoplankton by the subtropical submerged macrophytes Egeria densa and Potamogeton illinoensis: a mesocosm study. *Freshw. Biol.* 56 (9), 1837–1849. doi: 10.1111/j.1365-2427.2011.02624.x

Vaughn, C. C. (2010). Biodiversity losses and ecosystem function in freshwaters: emerging conclusions and research directions. *BioScience* 60 (1), 25–35. doi: 10.1525/bio.2010.60.1.7

Wang, S., and Brose, U. (2017). Biodiversity and ecosystem functioning in food webs: the vertical diversity hypothesis. *Ecol. Lett.* 21, 9–20. doi: 10.1111/ele.12865Wu

Wu, N., Qu, Y., Guse, B., Makarevičiūtė, K., To, S., Riis, T., et al. (2018). Hydrological and environmental variables outperform spatial factors in structuring species, trait composition, and beta diversity of pelagic algae. *Ecol. Evol.* 8 (5), 2947–2961. doi: 10.1002/ece3.3903

Xing, P., Li, B., Han, Y., Gu, Q., and Wan, H. (2020). Responses of freshwater ecosystems to global change: research progress and outlook. *Chin. J. Plant Ecol.* 44 (5), 565–574. doi: 10.17521/cjpe.2020.0009

Xu, W., Jing, X., Ma, Z., and He, J. S. (2016). A review on the measurement of ecosystem multifunctionality. *Biodiversity Sci.* 24 (1), 72–84. doi: 10.17520/biods.2015170

Xu, Q., Yang, X., Yan, Y., Wang, S., Loreau, M., and Jiang, L. (2021). Consistently positive effect of species diversity on ecosystem, but not population, temporal stability. *Ecol. Lett.* 24 (10), 2256–2266. doi: 10.1111/ele.13777

Yasuhara, M., Doi, H., Wei, C. L., Danovaro, R., and Myhre, S. E. (2016). Biodiversity-ecosystem functioning relationships in long-term time series and palaeoecological records: deep sea as a test bed. *Philos. Trans. R. Soc. B: Biol. Sci.* 371 (1694), 20150282. doi: 10.1098/rstb.2015.0282

Zavaleta, E. S., Pasari, J. R., Hulvey, K. B., and Tilman, G. D. (2010). Sustaining multiple ecosystem functions in grassland communities requires higher biodiversity. *Proc. Natl. Acad. Sci.* 107 (4), 1443–1446. doi: 10.1073/pnas.0906829107

Zhang, Q., Liu, Y. P., Luo, F. L., Dong, B. C., and Yu, F. H. (2019). Does species richness affect the growth and water quality of submerged macrophyte assemblages? *Aquat. Bot.* 153, 51–57. doi: 10.1016/j.aquabot.2018.11.006

Zhang, W., Chen, R., Meng, F., Yuan, H., Geng, M., Cheng, L., et al. (2021). Ecosystem functioning is linked to microbial evenness and community composition along depth gradient in a semiarid lake. *Ecol. Indic.* 132, 108314. doi: 10.1016/j.ecolind.2021.108314

frontiers | Frontiers in Marine Science

TYPE Original Research
PUBLISHED 05 May 2023
DOI 10.3389/fmars.2023.1154150

OPEN ACCESS

EDITED BY
Weijie Wang,
China Institute of Water Resources and Hydropower Research, China

REVIEWED BY
Zhipeng Zang,
Tianjin University, China
Meng Xia,
University of Maryland Eastern Shore, United States
Chunyan Li,
Louisiana State University, United States

*CORRESPONDENCE
Mingliang Zhang
zhmliang_mail@126.com

RECEIVED 30 January 2023
ACCEPTED 21 April 2023
PUBLISHED 05 May 2023

CITATION
Hu Z, Guo K, Yang Y and Zhang M (2023) Field survey and analysis of water flux and salinity gradients considering the effects of sea ice coverage and rubber dam: a case study of the Liao River Estuary, China. *Front. Mar. Sci.* 10:1154150. doi: 10.3389/fmars.2023.1154150

Field survey and analysis of water flux and salinity gradients considering the effects of sea ice coverage and rubber dam: a case study of the Liao River Estuary, China

Zhanming Hu[1], Kaiyuan Guo[2], Yongjun Yang[1] and Mingliang Zhang[2,3]*

[1]Marine Dynamics Department, National Marine Environmental Monitoring Center, Dalian, China, [2]College of Ocean Science and Environment, Dalian Ocean University, Dalian, China, [3]Technology Innovation Center for Coastal Ecological Environment and Disaster Protection, Liaoning, Dalian, China

Predicting net river fluxes is important to promote good water quality, maritime transport, and water exchange in estuaries. However, few studies have observed and evaluated net water fluxes to estuaries under complex conditions. This study used advanced survey techniques to obtain high-frequency monitoring data of cross-sectional current velocity, water level, and salinity in the Liao River Estuary (LRE) from 2017 to 2020. The net water flux into the sea was computed based on field data and the impacts of the rubber dam and sea ice cover on water flux and salinity processes were analyzed in the study region. In the Liao River Station (LRS), the fluctuations of water level and discharge were not obvious in winter due to the sea ice cover. There were significant seasonal and inter-annual changes in water fluxes due to variability in river discharge and tidal oscillations. The results also showed that the net water flux into the sea from the LRS was positive in wet season, and greater during ebb tides than flood tides. The net water fluxes in the normal and dry seasons were mostly negative due to the influence of tides, indicating that the annual runoff from the Liao River fluctuated greatly throughout the year. The water flux in the LRS was more suitable for representing water flux into the sea than the Liujianfang Hydrometric Station (LHS) in the LRE. The impacts of the rubber dam and Panshan Sluice on water fluxes to the sea were both significant. Lower salinity in the study area coincided mostly with height water fluxes to the sea and periods when the rubber dam was raised. This study results provide us new insights to measure the water flux into sea under the condition of ice cover in the tidal reach of estuary and the method can be used for water flux observation for other estuaries.

KEYWORDS

discharge, water level, net water flux, salinity variation, rubber dam, sea ice

Introduction

Estuaries are transition regions between freshwater and marine systems, subjected to both terrestrial and oceanic processes from the upstream river and tide from the open sea (de Pablo et al., 2022). The saline water bodies of estuaries are diluted by inflowing freshwater, and studies have shown that water quality, water temperature, biogeochemical processes, and species abundances in estuaries are sensitive to changes in freshwater input (Bartsch et al., 2014; Zamparas and Zacharias, 2014; Priya et al., 2016; Onabule et al., 2020; Chin et al., 2022). Furthermore, freshwater inputs from rivers determine the estuarine salinity gradients which are critical to the growth and development of many salt-marsh plants in estuarine tidal flats (Sheldon et al., 2017; Chen et al., 2022). These influences are especially critical in shallow bays with weak connections to the ocean, or in estuaries affected or transformed by manmade structures and human activities. Thus the fluxes of freshwater into the sea are especially important for understanding the coupling between river discharge and marine ecosystem processes in coastal and estuarine regions.

The fluxes in freshwater inflow in estuaries vary in time and space and are influenced by a suite of factors. For example, freshwater flux can be significantly impacted by high river discharge from upstream rivers (Ji and Zhang, 2019) as well as by tidal current intensity and tidal range (Mou et al., 2022), which were observed to dominate the water exchange processes in partially-mixed and bar-built estuaries (Lemagie and Lerczak, 2015). In addition to river and tidal forcings, estuarine depth and human influences can also influence water flux exchange mechanisms (Chin et al., 2022). This wide variety of influencing factors makes the evaluation about freshwater flux in estuaries critical to further understanding estuarine processes. In general, quantifying freshwater fluxes along estuarine cross sections can be achieved using a variety of methods. In terms of spatial and temporal measurements, Acoustic Doppler Current Profilers (ADCPs) are advanced tools capable of measuring different water body parameters, and have become standard in measurement methods (Lane et al., 1997; Sakho et al., 2019; Zhu et al., 2021; Li and Boswell, 2022). Straightforward volume calculations can be used to determine water fluxes, where the detailed intertidal bathymetry, tidal current, and accurate tidal water level data based on field surveys are required to obtain a complete coverage of tidally affected areas over tidal timescales (Fukamachi et al., 2010; Li et al., 2018; Shin et al., 2022). For example, shipboard ADCPs measurements can be used to provide vertical profiles of velocities and to compute tidally varying discharges in estuarine channels and regions (Dinehart and Burau, 2005; Chen et al., 2021; Zhu et al., 2022). The data from bottom-mounted ADCPs can be used to describe seasonal and spatial variation in current structure, such as volume transport, which was calculated across the Jeju Strait and Portsmouth Harbour (Onabule et al., 2020). However, under-ice discharge must also be considered when estimating the fresh water flux into open-sea, but the measurement water flow for ice-affected sites are generally qualified as poor. To overcome this obstacle, one possible field approach is to moor an ADCP at the sea bottom and river bed to analyze the impacts of ice cover on near-bed flow characteristics in rivers (Fulton et al., 2018; Lotsari et al., 2022) and estimate vertical and temporal variability in total suspended particulate matter (Ha et al., 2015).

Salinity intrusion is a growing problem and may adversely affect drinking-water supplies and aquatic environments in tidal estuaries around the world, as well as coastal agriculture, which may experience yield reductions due to salinity increases during sea water inundation (Kaniewski et al., 2016). Freshwater inputs in estuaries influence the net downstream transport of water within the estuaries, therefore the regulation of freshwater inflows has become the primary means of maintaining preferable estuarine salinity gradients in many coastal management strategies. Some hydraulic structures, such as dams and weirs, have been built at estuary mouths to limit tidal influences and protect water supplies for irrigation and domestic usage from the intrusion of salt water (Kennish, 2001; Sin and Lee, 2020; Figueroa et al., 2022), but their effects on estuarine environments are not well understood. Previous field surveys have observed water flux and salinity transport behaviors in estuaries operating with sluice gates (Kwak et al., 2023; Liu et al., 2023), and significant variations in the water flux and salinity gradient were observed in the water body of the study region due to the combined effects of sluices and open sea tides. To understand the effects of estuarine dams on estuarine environments, a series of related studies have been reported in the literature (Lavín and Sánchez, 1999; Van Proosdij et al., 2009), where the characteristics of salinity gradients and estuarine circulation were analyzed in the presence of estuarine dams. Other studies focusing primarily on the dam-controlled freshwater fluxes using extensive field hydrodynamics data and numerical models of tidal currents in shallow estuaries showed that estuarine environments were significantly influenced by river discharge, tidal range, wind and dams (Kim et al., 2006; Xia et al., 2011; Kang et al., 2017; Prasad et al., 2018; Ahn et al., 2020). Similarly, after dam construction, series of ship-borne surveys using ADCPs and CTD instruments were used to investigate the role of the dam-induced horizontal salinity gradient in stratification and sediment dynamics, which helped to understand the response of estuarine systems to seasonal and tidal controls (Figueroa et al., 2020; Figueroa et al., 2022). However, literature reporting field surveys of water flux to the sea and salinity variation in tidal reaches with estuarine dams and ice cover are relatively rare, therefore the effects of estuarine dams and ice cover on river fluxes into the sea and salinity in the tidal reach are not well understood.

Predicting net river fluxes into the sea is central to maintaining good water quality, maritime transport, and agricultural production in estuarine regions, especially in areas affected by estuarine dams. To expand our knowledge about how the net water flux into sea and salinity variations are influenced by estuarine dams and ice cover, a long term field survey was conducted to observe water levels and tidal currents in an estuary with an estuarine rubber dam from 2017 to 2020, followed by an evaluation of the salinity and water inflow fluxes into the Liao River Estuary (LRE) over broad regions of the Liao River. This paper is organized as follows. Firstly, we describe the field survey methods using representative points to monitor the flow current and water level in the transition region between river into sea using the H-ADCP instrument. The method is then

validated by comparing the monitoring data to the data of an ADCP navigation survey from the marine environment. Secondly, we compare water surface level and discharge in the surveyed cross-section with an estuarine dam based on high resolution observation level data. Thirdly, we calculate the monthly and annual water fluxes into the LRE and analyze the uncertainty. Finally, we investigate the response of river flux and salinity to the operation of a rubber dam. This method provides technological support that will facilitate the monitoring of water fluxes and pollution fluxes from rivers to sea.

Material and methods

Study area

The Liao River Estuary is located in the northernmost part of Liaodong Bay near Panjin City in Liaoning Province, China and covers a total area of 360 km^2 (Figure 1A). The LRE is affected by saline water from Liaodong Bay and runoff from the Liao River, Daliao River, and Daling River, of which Liao River is the largest. Of the eight major river systems in China the Liao River has the highest latitude, and the tidal reach is restricted by ice for about three months every year. Tides adjacent to this study region are semi-diurnal, with two high and low tides every day, and a maximum tidal range of about 4.4 m. The study region has a complex geomorphology with numerous tidal trenches and tidal flats distributed alternately. The salt-marsh plants of the tidal flats are dominated by reeds and *Suaeda salsa*, which are responsible for the rare natural landscape known as the "pink beach" (Chen et al., 2022), this area is the largest reed wetland reserve in China. Because the land is fertile and water is sufficient, it is also an important rice production area in northern China.

The Liujianfang Hydrologic Station (LHS) is the main long-term, hydrologic station in the downstream area of the Liao River and has been providing measurements since it was built in 1964.The LHS is located in a non-tidal section of the Liao River about 74 km from the mouth of the Liao River Estuary (Figure 1A). For this study, data on the daily stream flow and evaporation from January 2015 to March 2020 were collected from the hydrologic yearbooks of the LHS. In order to meet the demand of industrial and agricultural water intake, the Panshan sluice tidal gate was built in 1968 (Figure 1B). Generally, the Panshan sluice is closed to store water during non-flood seasons and during low precipitation flood seasons. Furthermore, the Panjin Water Conservancy Bureau built a 200 m wide ecological rubber dam about 17 km downstream of Panshan sluice to alleviate severe water shortages and maintain the wetland landscape of Panjin City (Figure 1B). In 2017, the National Marine Environmental Monitoring Center set up a monitoring system (named the Liao River Station, LRS) in the tidal reach of Liao River near Dawa County, Panjin City, and completed a survey that monitored tidal current and water salinity (Figure 1B). The LRS is located 200 m upstream of the rubber dam in the Liao River, about 30 km away from the LRE.

Methods

Discharge into estuaries can determine the overall water quality of the estuary and maintain the balance of the ecosystem (Figueroa et al., 2022). The investigation and identification of freshwater input processes are important to understanding how salinity and freshwater transport change in the LRE, a part of which is the estimation of freshwater flux into the estuary. Some researchers developed a convenient way for water volume transport by establishing a correlation between the flow velocity from the bottom-mounted ADCP and an ADCP mounted to the auto-boat in a short period (Li et al., 2018; Weeks et al., 2018; Li and Boswell, 2022). In this study, we carried out a series of field surveys in the LRS, where the width of water surface is about 200 m. The investigation showed that this section of the LRS has complex topographic features and great variation in water depth, as shown in Figure 2. This estuary has long icy periods lasting nearly 3 months due to its high latitude, and the ice cover and effect of floating sea ice make it difficult to accurately assess river discharge. Compared to other observation methods using buoys, ships, and ropeways, submarine observation platforms have these advantages of *in-situ* placement, long-term continuity, good data stability, high reliability, and no influence of artificial measurement error, especially when considering the effect of sea ice cover in the

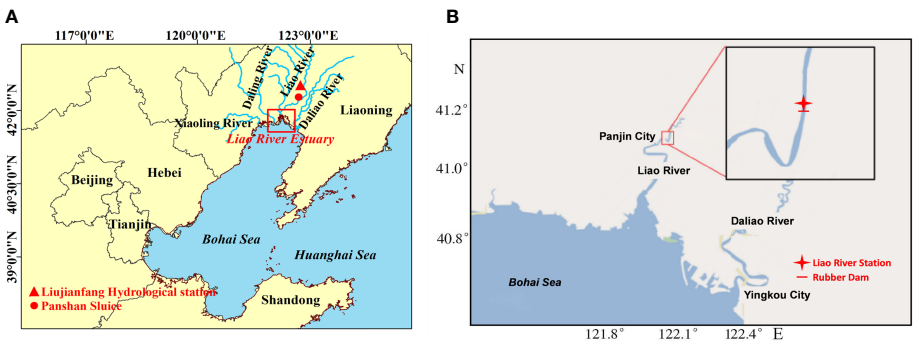

FIGURE 1
Maps of the study region illustrating the **(A)** geographical location of the Liao River Estuary and **(B)** the location of the monitoring station in Liao River.

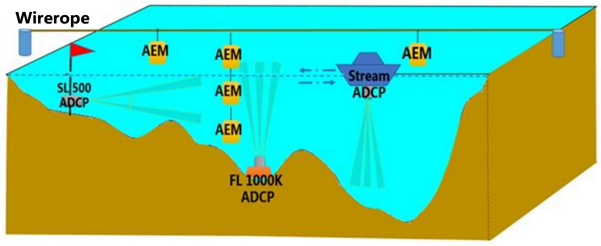

FIGURE 2
Sketch of monitoring instruments in the study area. A cable was secured across the river and used to fix the Infinity-EM AEM USB in the section for single-point flow monitoring during typical spring and spring tides.

winter season. Therefore, in this study we utilized submarine observation platforms to carry out the field survey. To survey the current velocity and evaluate the volume of water transported through the LHS in the LRE, the data for tidal current and water level in this section were prepared. In order to monitor the freshwater inflow flux into the LRE from the Liao River, China, the ADCP (Flowquest 1000k) instrument was installed on the submarine observation platform at the midline of the flow monitoring section, as presented in Figure 2. The maximum vertical profile range for FL1000k ADCP monitoring was 40 m, and the working group generally selects a profile range of 15 m based on the water depth of the monitoring section at Liao River Station. Flow velocity data was collected by the ADCP instrument in a 10 min burst mode over the observation period from January 1, 2017 to December, 31, 2020, where water levels were synchronously recorded at 10-min intervals. The other arrangements of ADCP were introduced for comparison and validation of tidal current in this study as shown in Figure 2. The SL 500 ADCP was moored at left bank to measure flow velocity for long-term monitoring of horizontal profile flow. The TRDI Stream ADCP was installed onboard the research vessel for mobile investigations for the flow velocity, direction and water depth in vertical profiles. The survey was conducted every 1 hour, each measurement took 10 minutes. The flow rate and cross-section area were measured, and then the depth - averaged velocity was calculated. The sampling setup of ship-borne navigation ADCP was as follows: sampling frequency was 1200K, unit length of D_c was 0.25m, the transducer entry depth of H_r was 0.1m, sampling time step was 1s, navigation ship speed V_b was 0.65m/s, magnetic declination angle was -6°. There was blind area in the top and bottom flow measurement, their thickness was generally between 7% - 10% of the water depth. The top and bottom flow rates were calculated by power function method ($y=x^b$) and power function exponent b = 1/6 (Software instructions). Water samples for salinity analyses were collected in the LHS and filtered immediately after collection with a vacuum pump into the workstation experimental platform. Salinity (psu) was measured in real time at ten minute intervals using the Multi-Parameter Water Quality Detector in the LHS. Before the field investigation, we needed to carry out a routine examination of the instrument including rationality test, range test and peak test etc. Furthermore, the measured unreasonable data needed to be eliminated before analysis.

Calculations of net water flux to estuary

The net water flux into the estuary was calculated from the five years of continuous water level and tidal current observation data from the ADCP instruments from 2017 to 2020. The mass conservation flux was used to calculate water fluxes by determining the product of mean velocity and cross-section area:

$$Q = V \cdot A \quad (1)$$

where Q is discharge of the cross section; V is averaged-velocity normal to the cross-section; and A is cross-sectional area of water.

Based on an application of mass conservation flux, the volume of water flux into the sea across the section area can be estimated as,

$$W_t = \int_0^T Q(t)dt = \int_{t_0}^{t_1} Q_i \, dt - \int_{t_1}^{t_2} Q_j dt \quad (2)$$

where W_t is the runoff flux into sea; t_0 is time of beginning of ebb tide; t_1 is duration of slack tide; t_2 is time of beginning of flood tide; t_3 is duration of slack tide; $Q_i$is the cross-section discharge in period of ebb tide; and Q_j is the cross-section discharge in the flood tide period.

Tidal current validation

The river discharge was calculated using the measured flow velocities and determined cross-sectional area of river channel (Costa et al., 2006). Weeks et al. (2018) also reported that the depth-averaged velocities from the bottom-mounted ADCP and the transport from USV ADCP were compared to follow each other. When an ADCP was moored on the seabed, the flow velocity could not be measured near the bottom or the surface. To fill in these gaps, daily average data were extrapolated based on the assumption that the velocities at the bottom and surface were the same as the index velocities at the nearest respective water depths (Ruhl and Simpson, 2005; Ganju et al., 2012). In this study, a complete record of cross-sectionally averaged velocity is computed using the correlation between index velocity (FL1000k ADCP) and tidal velocity from ADCP on board. The transducers of the ADCP were placed in water about 0.5 m below the surface. Continuous time-series indexes of water velocity and water level were obtained at the selected site using an ADCP mounted on the seabed in this study. Furthermore,

the cross-sectionally averaged velocity was collected using a ship-mounted ADCP for comparison with the velocity index. Using the shipboard ADCP, we collected data along 44 ADCP transects, successfully measuring channel area and geometry at different tidal levels, these transects also obtained cross-sectionally averaged velocities. The relationship between the cross-sectional mean velocity and the index-velocity from the near-bed ADCP was determined to calculate water flux in this study (Figure 3). In terms of site characterization, the quadratic relationship between the index velocity and the cross-sectionally averaged velocity was obtained to construct a continuous time-series from the index velocity. The correlation coefficient of the obtained relationship was 0.952, indicating there was a very strong correlation between the two sets of data. This suggested that the tidal water flux estimates derived from the index velocity method would closely agree with independent measurements based on changes in water depth and volume in the studied section.

Results

Variable observations in different periods

There LRE has a three-month ice period during the winter season, so we utilized the bottom-seated ADCPs placed on the seabed for measuring water level and tidal current in this study. Figure 4 shows the time series of water level and discharge in the LRS in different seasons. There was irregular fluctuation during one winter period (February 1–16, 2020) when the water level varied between 4.039 m and 4.91 m and the amplitude change in water level each day was small due to the effect of ice cover (Figure 4A). It could be seen that the water surface froze with a thickness of 30 cm during the full ice period, the ice and the coast were connected together. During the flood tide, there was no separation between the water body and the ice surface, and during the ebb tide, there was a separation between the ice surface and the water body. The discharge ranged between -35.68 m^3/s and 20.23 m^3/s between the flood tide and ebb tide periods, with the peak discharge of the flood tide being slightly larger than that of ebb tide, however, the

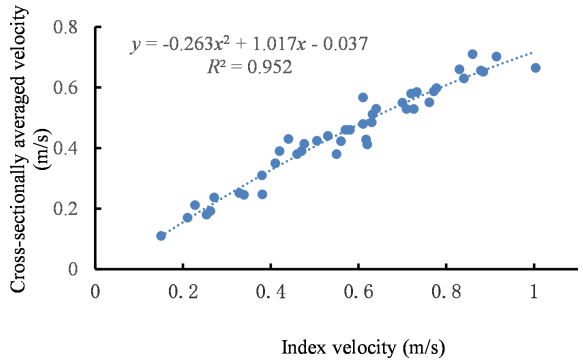

FIGURE 3
Calibration and validation of instruments in flow velocities for the field site.

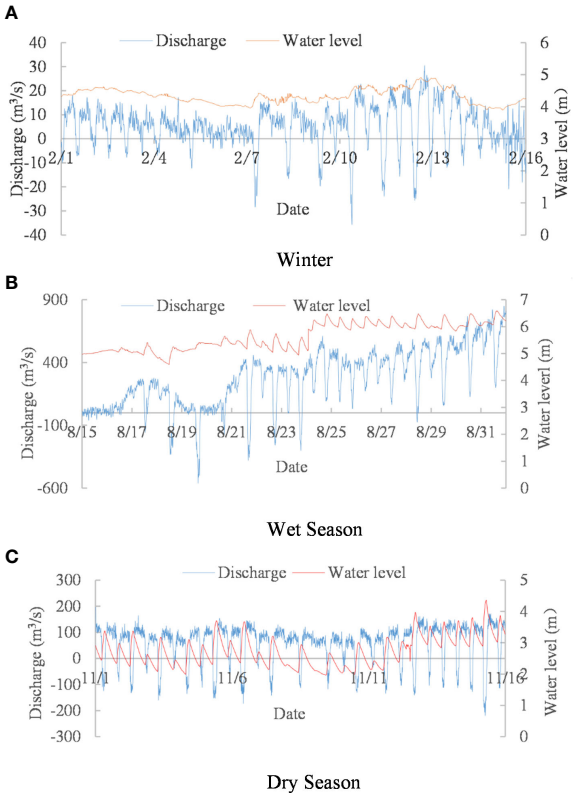

FIGURE 4
Variation in the observed discharge and water level of the Liao River Station. **(A)** Winter, **(B)** Wet Season and **(C)** Dry Season.

duration of peak discharge during the ebb tide was obviously longer than that of flood tide. The water discharge from the upstream LRS was always below 35 m^3/s during the periods when ice covered the entire river width. Figure 4B shows the observed discharge and water level in the LRS for the period from August 15th to August 31th, 2020. Before August 16th, the Liao River had relatively low runoff, and the amplitude of the tide was also small due to the neap tide period, so the changes of water level and discharge were relatively stable and were not obviously affected by upstream runoff nor the tidal cycle of the estuary. In mid-late August, 2020, the upper Panshan Sluice was gradually opened to release water due to the wet season, and the observed water levels changed gradually with a certain regularity, but still exhibited the characteristics of an irregular semi-diurnal tide due to the influence of the spring tide. The water levels varied between 4.971 m and 6.582 m in these periods, the peak discharge into sea during a flood tide was -561.2 m^3/s, which occurred at 16:00 on August 19th, and the peak discharge into the sea for an ebb tide period was 849.4 m^3/s, which occurred at 22:12 on August 31th, 2020. The peak value of discharge in the flood tide period was less than that of the ebb tide period, and the duration during the ebb tide was longer than that during flood tide. After the opening of the Panshan Sluice, the freshwater flux into sea was always positive, indicating that the freshwater continuously flowed into the LRE in the wet season, and a flood tide only appeared for about 20 minutes on August 28th, 2020 during spring tide associated with arrival of severe Typhoon

Bavi. There was only a brief upsurge in the whole month, and only for a few moments. Figure 4C gives the cross-sectional discharge and water level in the LRS from 1–16 November 2020, the water level ranged between 2.148 m and 4.362 m, the tidal discharges ranged from -254.4 m^3/s to 165.6 m^3/s during spring tides, and the peak discharge was larger during flood tide than during ebb tide. The rising tides and the falling tides lasted about 3 hours and 9 hours, respectively.

The long-term daily-salinity data from 2017 to 2020 in the LRS are shown in Figure 5. The salinity concentration ranged from 0.2 to 25 psu in this section of the LRS, showing lower values from September to May and significant fluctuation between May and September. The salinity peak in 2018 was the highest of the study period due to a lack of rainfall in the basin which led to low runoff from upstream rivers. Salt water intrusion generally started in May with the arrival of the dry season, but there were dramatic freshening events driven by the arrival of extreme spring tides. In 2017 and 2020, due to high precipitation in the basin, the salinity of the studied section was low. In summary, there were various significant trends in water salinity levels on both seasonal and inter-annual scales due to seasonal and annual variation in rainfall in this region. Through investigation and analysis, large areas of rice cultivation and growth occurred from May to August in Panjin region, a large amount of freshwater was intercepted, the amount of freshwater into the sea in this period was small, so the salinity had a relatively high value. In addition, if rainfall was sufficient in Liao River Basin and the river discharge was large in the Liao River, the upstream Panshan Sluice opened for a long time, and the salinity of the monitoring section would be low, vice versa.

Variability in monthly water flux into the LRE

Revealing the seasonal and inter-annual variability in river runoff into the LRE is critical to understanding the dynamic processes influencing freshwater and seawater exchange between the river and ocean. We performed a series of calculations based on the observed data over the entire study period to extract the monthly-mean water flux into the LRE; the water fluxes to the sea at the LHS and LRS from January to December 2020 are shown in Figure 6. The results indicated that the highest water flux to the sea occurred in September, 2020. This coincided with the wet season which occurred from August to October due to the long rainy season in the Liao River Basin. In contrast, the water fluxes during other periods were relatively small due to the low rainfall during the dry season. Furthermore, there was additional significant monthly variability in water flux in the LRS and the LHS due to the opening and closing of the upstream Panshan Sluice. In 2020, the annual runoff amounts from the LHS and LRS were about 35.27 billion m^3 and 19.78 billion m^3, respectively, with the LRS accounted for 56% of the annual runoff from the LHS into the sea. The water flux from the LRS to the sea from August to October was 15.01 billion m^3, representing 76% of the annual water flux. Therefore, the Liao River experiences obvious seasonal variability in river discharge due to uneven temporal of rainfall. The annual water fluxes in the two stations were different, and the water fluxes of the LHS were obviously larger than those of the LRS due to the water conservancy activities of farmland and industrial and domestic waters along the way.

Figure 7 shows the monthly changes in water fluxes in the LRS during the monitoring period from 2017 to 2020. The water flux into sea from the LRS was the largest in August of 2017 and 2019 and September of 2018 and 2020, and the monthly water fluxes in the LRS exhibited obvious differences among months. Taking 2019 as an example, the results showed that the water fluxes into the sea reached a four-year peak of 1.104 billion m^3 in August, 2019, however, the monthly water flux from the LRS was negative in certain other months. The maximum annual flux to the sea was highest in 2019, at 2.218 billion m^3, followed by 1.978 billion m^3 in 2020 and 0.058 billion m^3 in 2018.

Changes of variables due to the influence of the rubber dam

In order to effectively prevent the invasion of salinity and alleviate water shortages for industry and agriculture in the LRE, a rubber dam was installed in this tidal river. The rubber dam was bottomed to riverbed with a height of about 0.5 m when not inflated. It did not float on the water, but rose and dropped under

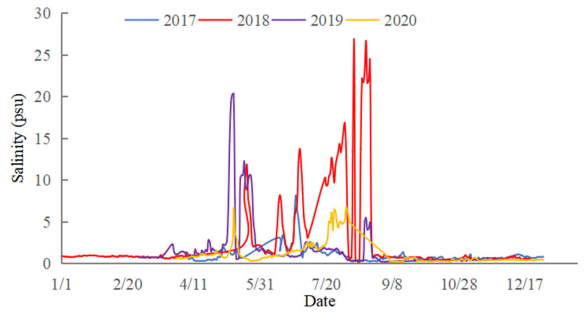

FIGURE 5
Measured daily salinity levels in the Liao River Station during 2017–2020.

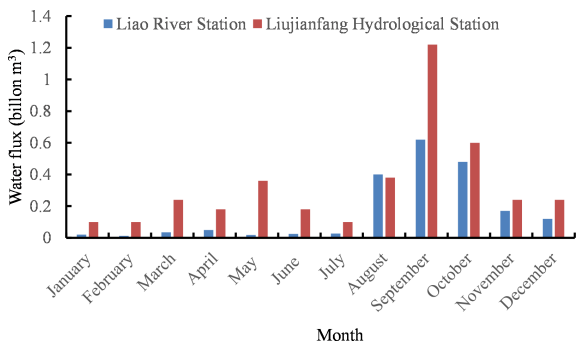

FIGURE 6
Monthly fluxes from the two selected stations in 2020 (billion m^3).

10.3389/fmars.2023.1154150

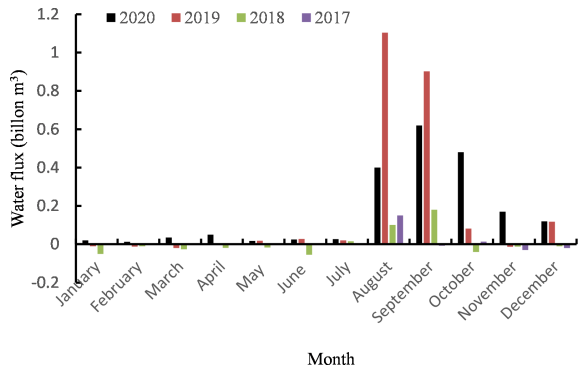

FIGURE 7
Monthly fluxes for different years at the Liao River Station (billion m^3).

manual control. Figure 8 shows the changes in the observed variables due to increasing and decreasing the rubber dam height in 2019. When the rubber dam was raised, the discharge and water level in this section changed slightly, however, the height of rubber dam was reduced to facilitate overflow during the flood season. There was high similarity in water level and discharge trends in terms of increasing and decreasing among the observation years, which showed that the discharge and water level were significantly affected by the height of the rubber dam (Figure 8A). The water level in the LRS showed a stepwise rising trend with increasing rubber dam height. This was because the two high tide levels of the LRE are different every day. The low-high tide is completely intercepted and prevented from infiltrating upstream when the tidal wave reaches the rubber dam, while the high-high tide level is higher than the elevation of rubber dam so the seawater can gradually flow upstream over the rubber dam. When the tide level gradually decreases to the height of the rubber dam crest, the seawater upstream of the dam will be prevented from returning downstream (Figure 8B). Therefore, the water flux into the LRE, water level, and salinity are affected, not only by the upstream runoff and downstream tidal current, but also by the artificial rubber dam.

Figure 9 shows the time series of the tide, discharge, and salinity in the LRS, where the tidal level is from the Laobeihekou station. In contrast to Liao River Station, the discharge and salinity exhibited obvious periodic characteristics associated with the tidal level, because the Laobeihekou station was located close to the open sea, and its rising and falling tides exhibited a phase difference with the upstream station of the LRS (Figure 9A). The salinity in the LRS exhibited clear variation with tidal fluctuations, with the maximum salinity reaching 14 psu during the observation period. The observed salinity remained relatively low in the wet season, during which time the salinity fluctuations caused by tidal effects were small, within the range of 0.2–1.0 psu (Figure 9B). The highest salinities occurred in the dry season, mainly due to the correlated water flux components and the amplitude of tides. It could be seen that the salinity of the water body was low and the change was small when the rubber dam was elevated, showing that the rubber dam prevented the invasion of saline water from the open sea. Generally, the water level at the monitored section remained basically unchanged until the high tide level surpasses the rubber dam height in the next tidal cycle.

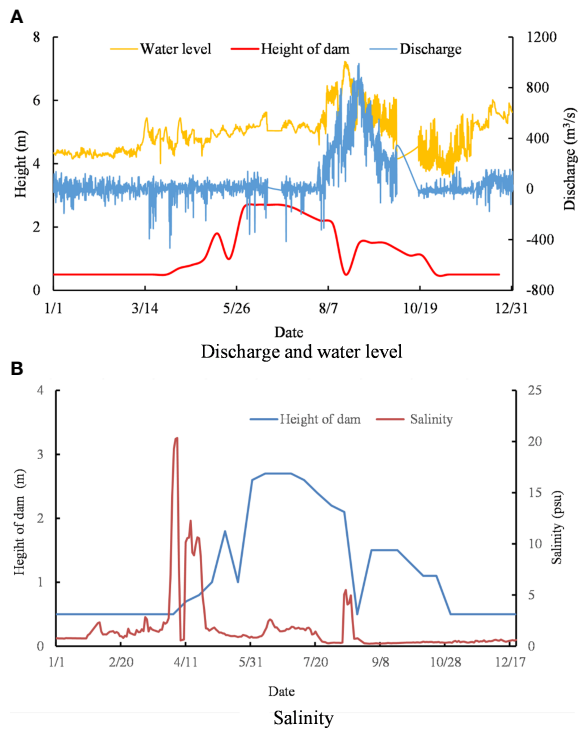

FIGURE 8
Change in discharge, water level, and salinity with variation in dam height in 2019. **(A)** Discharge and water level, **(B)** Salinity.

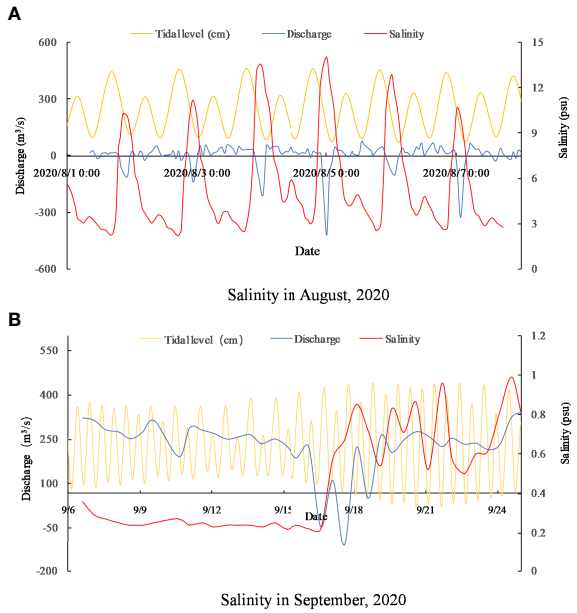

FIGURE 9
Time series of water level, water flux, and cross-sectionally averaged salinity in the LRS in 2020. **(A)** Salinity in August,2020, **(B)** Salinity in September, 2020.

Discussion

Factors impacting discharge and water level

With the introduction of uncertain fluctuation caused by the artificial influence of the sluice and dam in the study region, the hydrological processes and saline water transport in this tidal reach became more complex. The field survey of the upper tidal reach of the LRE revealed the relationships between the salinity and water flux in this estuary during different seasons. Except for 2020, the monthly fluxes into the sea in the other years from January to February were negative, and the water fluxes were far smaller than those during the non ice period. Therefore, ice cover had a certain impact on the water flux into the sea. The mainly reason was that the tidal velocity decreased significantly due to the limited water level rising and the friction force caused by the ice cover during flood tide. In winter, there was less upstream runoff, lower temperatures were prone to freezing, and therefore less water entered the sea. During the ice loading periods in winter, the Panshan Sluice was always closed to retain water, while the rubber dam located in the tidal reach of the Liao River was lowered completely. The water level at this cross-section of LRS remains basically unchanged because the seawater was blocked by the sea ice cover after reaching a certain water level. This phenomenon, where sea ice cover created a clear block against the tide and suppressed residual water level, has been observed elsewhere in western Laizhou Bay (Liu et al., 2022). Furthermore, in the Bohai Sea, sea ice also played a critical role in pollutant dispersion (Xiong et al., 2018) and tidal damping (Zhang et al., 2019). Therefore, the main factors affecting water level and discharge in the LRS in these periods included both downstream tidal current and sea ice coverage, and the flow pattern at the monitoring section presented reciprocating flow characteristics.

During the flood season, the Panshan Sluice was opened to release water, and the rubber dam was dropped completely as well. During this time the observed water levels showed obvious characteristics of irregular semi-diurnal tide, reflecting the two high tides and two low tides of each lunar day. The high tides lasted about 3 hours and the low tides lasted about 9 hours, and the daily fluctuations in the amplitude of water level and discharge were highly regular. The water level and discharge in the LRS were mainly affected by the upstream runoff and the downstream tide. This was similar the conclusions in the literature, which showed that the water levels in estuary regions were impacted by tide and upstream runoff (Palinkas et al., 2019; Lee et al., 2021). During the winter season, the rubber dam was dropped completely and the Panshan sluice gate was closed, so there was no water coming from the upper reaches and the water level was mainly affected by the downstream tidal current, which reflected the irregular semi-diurnal tide. Generally speaking, the LRS received much more freshwater runoff in the rainy season than the short rainy season or dry season when the high runoff was relatively low.

Factors controlling water flux to the sea

The water volume transported into sea was derived from the measured index velocity and tidal level, which has been shown to be a reliable method (Ganju et al., 2012; Weeks et al., 2018; Li and Boswell, 2022) and returned high accuracy in their studies. The results showed that there were apparent spring–neap cycles in the data-based water flux into sea in the LRS. The highest water flux into the sea occurred in September, 2020, which was in a wet season, and the maximum flood flux coincided with the transit of a typhoon associated with an extremely high tide flood period. The high flux was attributed to several factors that included the discharge from the upstream river, tide of the outside sea, height of the rubber dam, and the Panshan sluice operation. The LHS is the hydrologic station closest to the LRE, and it is located in the non-tidal reach, so it is possible to accurately estimate the runoff processes the LHS section. It is noteworthy that the LHS is about 80 km away from the LRE and the Panshan Sluice gate downstream of it controls river discharge for industry, irrigation, and domestic water intake. Therefore, the water flux into sea through the LRS has a certain time lag and difference in water volume compared to the LHS. The lag is greatly affected by the state of the Panshan Sluice, i.e., whether it is open and by how much, and the difference in total water volume represents the water intercepted for paddy irrigation and industrial water (Wang et al., 2017), only the remaining water not used for these purposes enters the LRE. Due to the release of water from the Panshan Sluice and the lowering of the rubber dam, the change trends in discharge into the sea from the LRS in September were basically consistent with the change trends of the observed discharge from the LHS in the upper reaches, as was demonstrated by the two obvious flow peaks and troughs in both locations (see Figure 6).

Due to the fact that Panshan Sluice was usually closed from January to July based on the gate controlling information from 2019, the river discharge from the LRS was less than 0.03 billion m^3 during this period, with the highest flux occurring in June at 0.028 billion m^3. The flood season begins in August in the Liao River basin, and the Panshan Sluice opened on August 23, 2019 due to heavy rainfall. The river discharge into sea increased to 1.104 billion m^3 in August, 2019. In mid-October, the Panshan Sluice began to close, and the monthly water flux to the sea from the LRS gradually decreased. These results showed that the water fluxes are significantly affected by the opening and closing of the Panshan Sluice, and that the amount of water entering into the LRE has a certain hysteresis and uncertainty. Similar observations have been made in related studies in a shallow microtidal estuary with an estuarine dam (Williams et al., 2015). The LHS is located in the upstream non-tidal reach, where the water flows through the LHS is larger than that of the LRS, only a portion of the water flows into the LRE through the monitored section of the LRS because of water interception, therefore, the water flux in the LRS is better suited to representing sea inflow flux than that the LHS in the LRE. Furthermore, there was significant inter-annual variability in the water flux to the Liao River Estuary. The main reasons were the serious droughts in 2017 and 2018 in this study region, with the

region average precipitation amounts of 543.6 and 586.1 mm in current year, respectively, which were obviously lower than the 687.2 mm in 2019 (see Table 1).

Effect of rubber dam on water input, water level, and salinity

A rubber dam was built between the estuary mouth and Liao River to establish the estuary's tidal limit in this study region. With the artificial manipulation of the rubber dam in the LRS, the complexity of the water level variation processes in tidal reach increased. During the rubber dam lowering period, the monitoring section was characterized by irregular semi-diurnal tides, which showed that the water flux to the LRE was significantly affected by the height of rubber dam. When the rubber dam was raised, the regularity of discharge change in the LRS decreased, while when the rubber dam was lowered, the discharge change showed a certain tidal regularity. According to the monitoring results, the water flux into the sea from the LRS was not only affected by the upstream water and downstream tide, but also by the artificial gate and rubber dam, resulting in a large seasonal and daily variation in discharge into the sea. Previous studies in the Geum and Oujiang estuaries showed that estuarine dams reduced the mean water level by about 10 cm after dam construction (Kim et al., 2006; Li and Liu, 2020), providing clear evidence that estuarine dams affect water fluxes.

It is of great importance to study the processes affecting the water level and salinity of tidal reaches to understand water fluxes into the sea. Here, salinity was greatly affected by runoff from the upstream river, which created a significant salinity gradient in the water body of the LRS. Furthermore, the obvious change in salinity along the Liao River revealed that the sluices and rubber dam effectively prevented seawater from infiltrating upstream, to a certain extent. However, these dams and gates also obviously blocked the hydrological connectivity, which may alter the ecological structure of the river and the estuary. It was also clear that the discharge affects the salinity distribution in the estuary, as was evident in the changes in salinity gradients in this estuary due to the operation of the rubber dam. So estuarine dams were reasoned to not only alter the timing of water fluxes to the sea, but also the water salinity (Shin et al., 2022) and water quality in the estuary (Jeong et al., 2014). Indeed, one study showed that the removal of the sluice gate, plus sea-level rise, allowed greater seawater influx and increased the regularity of monthly deep-water salinity fluctuations in Nakaumi Lagoon (Nomura et al., 2022). The data obtained in this study, on river discharge and salinity, were effectively used to determine salt variation mechanics within the main river, which helped to understand the effects of sluices and dams along with the relative importance of freshwater and tidal inputs.

TABLE 1 Yearly rainfall information.

Year	Region mean precipitation of the year (mm)	Equivalent total precipitation (billion m^3)	Deviation from multi-year mean (%)
2017	543.6	791.04	-19.8
2018	586.1	852.78	-13.6
2019	687.2	999.98	1.3
2020	748	1088.34	8.8

Conclusion

This study conducted a series of field surveys to measure flow velocity, direction, water depth, and salinity at the mouth section of the LRE from 2017–2020. About 200,000 sets of cross-sectional data were obtained in the LRS. The index velocity and cross-sectionally averaged velocity based on the ADCP data were compared over several tidal-cycle observations. An appropriate correlation was found so that a continuous record of discharge could be generated for further estimations of water fluxes in the estuary in combination with the velocity index methodology. In winter, the water flux into the sea was greatly affected by the ice cover, and the tidal level was suppressed by the ice cover, which reduced the tidal flux from the bay. The results showed that the annual water fluxes at the two stations (LRS and LHS) were quite different, and the water flux of the LHS was obviously greater than that of the LRS. A portion of the water flowing through the monitored section enters the LRE, but some of the water flowing through the LHS is stored by the Panshan Sluice to meet the needs of industry, agriculture, and landscape in the Liao River areas. The majority of the annual water flux to the estuary is concentrated in the flood season from August to October. It was concluded that the water flux into the sea measured in the LRS was representative of the sea-entering flux from the Liao River. The water flux to the estuary in the LRS was mainly controlled by the runoff from Liao River and the opening of the upstream Panshan Sluice. When the rubber dam was lowered, the water level at the monitored section was characterized by irregular semi-diurnal tides, and the duration of the rising and falling tides were quite different. The regulation by the rubber dam (i.e., raising or dropping) can impact the net freshwater flux to estuary as well, which changes water salinity gradient downstream. These results are helpful in clarifying the coupled influences of saline intrusion and sluice operation on the freshwater input and salinity characteristics in the LRE and will facilitate science-based management policies for water transfer in this basin. The comprehensive monitoring and analysis method for water flux into the sea proposed in this paper well reproduces the discharge changes in the Liao River, and this method will also provide a valuable reference for the measurement of water flux into the sea for other rivers. Furthermore, the Liao River discharges large amounts of pollutants (e.g., COD, ammonia nitrogen, phosphate, or heavy metals), but their fluxes into the LRE are also currently unknown. Based on the results of current study, future studies should focus on determining the total amount of pollutants discharged from Liao River into sea in each year to help establish total emission controls for various marine pollutants and determine the marine pollutant receiving capacity.

Data availability statement

The raw data supporting the conclusions of this article will be made available by the authors, without undue reservation.

Author contributions

ZH and MZ contributed to conception and design of the study. ZH contributed to data survey, methodology, writing - original draft. KG and YY organized the validation and data analysis. MZ: methodology, project administration, writing - review & editing. All authors contributed to the article and approved the submitted version.

Funding

This work was supported by the National Nature Science Foundation of China (Grant Number U21A20155, 51879028), Open Fund of State Key Laboratory of Coastal and Offshore Engineering of Dalian University of Technology, and Applied basic research plan project of Liaoning province (Grant Number 2023030048-JH2/1013).

Conflict of interest

The authors declare that the research was conducted in the absence of any commercial or financial relationships that could be construed as a potential conflict of interest.

Publisher's note

Supplementary material

The Supplementary Material for this article can be found online at: https://www.frontiersin.org/articles/10.3389/fmars.2023.1154150/full#supplementary-material

References

Ahn, J. M., Lee, K., and Lyu, S. (2020). Effect of changes in watershed runoff characteristics on salinity intrusion in estuary using EFDC. *KSCE J. Civ. Eng.* 24 (1), 87–98. doi: 10.1007/s12205-020-1306-5

Bartsch, S., Frei, S., Ruidisch, M., Shope, C. L., Peiffer, S., Kim, B., et al. (2014). River-aquifer exchange fluxes under monsoonal climate conditions. *J. Hydrol* 509, 601–614. doi: 10.1016/j.jhydrol.2013.12.005

Chen, Z. G., Pan, S., Zhou, F. N., Ban, Y., Li, M., and Li, D. J. (2021). A method for correcting discharge of boat-mounted ADCP measurements. *Flow Meas. Instrum.* 80, 101954. doi: 10.1016/j.flowmeasinst.2021.101954

Chen, X., Zhang, M. L., and Zhang, W. C. (2022). Landscape pattern changes and its drivers inferred from salt marsh plant variations in the coastal wetlands of the liao river estuary, China. *Ecol. Indic.* 145, 109719. doi: 10.1016/j.ecolind.2022.109719

Chin, T., Beecraft, L., and Wetz, M. S. (2022). Phytoplankton biomass and community composition in three Texas estuaries differing in freshwater inflow regime. *Estuar. Coast. Shelf Sci.* 277, 108059. doi: 10.1016/j.ecss.2022.108059

Costa, J. E., Cheng, R. T., Haeni, F. P., Melcher, N., Spicer, K. R., Hayes, E., et al. (2006). Use of radars to monitor stream discharge by noncontact methods. *Water Resour. Res.* 42, W07422. doi: 10.1029/2005WR004430

de Pablo, H., Sobrinho, J., Garaboa-Paz, D., Fonteles, C., Neves, R., and Gaspar, M. B. (2022). The influence of the river discharge on residence time, exposure time and integrated water fractions for the tagus estuary (Portugal). *Front. Mar. Sci.* 8. doi: 10.3389/fmars.2021.734814

Dinehart, R. L., and Burau, J. R. (2005). Repeated surveys by acoustic Doppler current profiler for flow and sediment dynamics in a tidal river. *J. Hydrol* 314, 1–21. doi: 10.1016/j.jhydrol.2005.03.019

Figueroa, S. M., Lee, G. H., Chang, J. W., Schieder, N. W., Kim, K., and Kim, S. Y. (2020). Evaluation of along-channel sediment flux gradients in an anthropocene estuary with an estuarine dam. *Mar. Geol.* 429, 106318. doi: 10.1016/j.margeo.2020.106318

Figueroa, S. M., Son, M., and Lee, G.-h. (2022). Effect of estuarine dam location and discharge interval on estuarine hydrodynamics, sediment dynamics, and morphodynamics. *Front. Mar. Sci.* 9. doi: 10.3389/fmars.2022.1035501

Fukamachi, Y., Ohshima, K. I., Ebuchi, N., Bando, T., Ono, K., and Sano, M. (2010). Volume transport in the soya strait during 2006–2008. *J. Oceanogr.* 66, 685–696. doi: 10.1007/s10872-010-0056-2

Fulton, J. W., Henneberg, M. F., Mills, T. J., Kohn, M. S., Epstein, B., Hittle, E. A., et al. (2018). Computing under-ice discharge: a proof-of-concept using hydroacoustics and the probability concept. *J. Hydrol* 562, 733–748. doi: 10.1016/j.jhydrol.2018.04.073

Ganju, N. K., Hayn, M., Chen, S. N., Howarth, R. W., Dickhudt, P. J., Aretxabaleta, A. L., et al. (2012). Tidal and groundwater fluxes to a shallow, microtidal estuary: constraining inputs through field observations and hydrodynamic modeling. *Estuar. Coasts* 35, 1285–1298. doi: 10.1007/s12237-012-9515-x

Ha, H. K., Kim, Y. H., Lee, H. J., Hwang, B., and Joo, H. M. (2015). Under-ice measurements of suspended particulate matters using ADCP and LISST-holo. *Ocean Sci. J.* 50, 97–108. doi: 10.1007/s12601-015-0008-2

Jeong, Y. H., Yang, J. S., and Park, K. (2014). Changes in water quality after the construction of an estuary dam in the geum river estuary dam system, Korea. *J. Coast. Res.* 30 (6), 1278–1286. doi: 10.2112/JCOASTRES-D-13-00081.1

Ji, X. M., and Zhang, W. (2019). Tidal influence on the discharge distribution over the pearl river delta, China. *Reg. Stud. Mar. Sci.* 31, 100791, 2352–4855. doi: 10.1016/j.rsma.2019.100791

Kang, X., Xia, M., Pitula, S. J., and Chigbu, P. (2017). Dynamics of water and salt exchange at Maryland coastal bays. *Estuar. Coast. Shelf Sci.* 189, 1–16. doi: 10.1016/j.ecss.2017.03.002

Kaniewski, D., Marriner, N., Morhange, C., Faivre, S., Otto, T., and Van Campo, E. (2016). Solar pacing of storm surges, coastal flooding and agricultural losses in the central Mediterranean. *Sci. Rep.* 6, 25197. doi: 10.1038/srep25197

Kennish, M. J. (2001). Coastal salt marsh system in the US: a review of anthropogenic impacts. *J. Coast. Res.* 17 (3), 731–748.

Kim, T. I., Choi, B. H., and Lee, S. W. (2006). Hydrodynamics and sedimentation induced by large-scale coastal developments in the keum river estuary, Korea. *Estuar. Coast. Shelf Sci.* 68 (3), 515–528. doi: 10.1016/j.ecss.2006.03.003

Kwak, D. H., Song, Y. S., Choi, Y. H., Kim, K. M., and Jeong, Y. H. (2023). Influence of sluice gate operation on salinity stratification and hypoxia development in a brackish estuary dam. *Reg. Stud. Mar. Sci.* 57, 102731. doi: 10.1016/j.rsma.2022.102731

Lane, A., Prandle, D., Harrison, A. J., Jones, P. D., and Jarvis, C. J. (1997). Measuring fluxes in tidal estuaries: sensitivity to instrumentation and associated data analyses. *Estuar. Coast. Shelf Sci.* 45 (4), 433–451. doi: 10.1006/ecss.1996.0220

Lavín, M. F., and Sánchez, S. (1999). On how the Colorado river affected the hydrography of the upper gulf of California. *Cont. Shelf Res.* 19, 1545–1560. doi: 10.1016/S0278-4343(99)00030-8

Lee, M., Yoo, Y., Joo, H., Kim, K. T., Kim, H. S., and Kim, S. (2021). Construction of rating curve at high water level considering rainfall effect in a tidal river. *J. Hydrol. Reg. Stud.* 37, 100907. doi: 10.1016/j.ejrh.2021.100907

Lemagie, E. P., and Lerczak, J. A. (2015). A comparison of bulk estuarine turnover timescales to particle tracking timescales using a model of the yaquina bay estuary. *Estuar. Coasts* 38, 1797–1814. doi: 10.1007/s12237-014-9915-1

Li, C. Y., and Boswell, K. M. (2022). Estimating water transport from short-term vessel-based and long-term bottom-mounted acoustic Doppler current profiler measurements in an Arctic lagoon connected to the Beaufort Sea. *Sensors* 22, 68. doi: 10.3390/s22010068

Li, Y., and Liu, J. (2020). Salt intrusion and its controls in the macro-tidal oujiang river estuary, China. *Ocean Dynam.* 70, 1409–1420. doi: 10.1007/s10236-020-01405-0

Li, C. Y., Weeks, E., Huang, W., and Milan, B. (2018). Weather induced transport through a tidal channel calibrated by an unmanned boat. *J. Atmos. Ocean. Tech.* 35 (2), 261–279. doi: 10.1175/JTECH-D-17-0130.1

Liu, Y., Hu, Y. C., Yu, C. X., Gao, Y. Q., Liu, Z. Y., Mostofa, K. M. G., et al. (2023). Spatiotemporal optical properties of dissolvedorganic matter in a sluice-controlled coastal plainriver with both salinityand trophic gradients. *J. Environ.Sci.* 129, 1–15. doi: 10.1016/j.jes.2022.09.031

Liu, S. Y., Liu, S. D., Li, G. X., Zhang, S. T., Xu, J. S., Zhang, L., et al. (2022). Impacts of sea ice on marine dynamics in western laizhou bay, bohai Sea. *Estuar. Coast. Shelf Sci.* 275, 107958. doi: 10.1016/j.ecss.2022.107958

Lotsari, E., Lintunen, K., Kasvi, E., Alho, P., Blåfield, L., and Part, A. (2022). The impacts of near-bed flow characteristics on river bed sediment transport under ice-covered conditions in 2016–2021. *J. Hydrol.* 615, 128610. doi: 10.1016/j.jhydrol.2022.128610

Mou, L., Niu, Q., and Xia, M. (2022). The roles of wind and baroclinic processes in the cross-isobath water exchange within the bohai Sea. *Estuar. Coast. Shelf Sci.* 274 (3), 107944. doi: 10.1016/j.ecss.2022.107944

Nomura, R., Tsujimoto, A., and Takata, H. (2022). Environmental impact of removal of a large-scale sluice gate on nakaumi lagoon and adjacent coastal waters, southwest Japan: evidence from long-term foraminiferal monitoring. *Mar. Environ. Res.* 182, 2022. doi: 10.1016/j.marenvres.2022.105767

Onabule, O. A., Mitchell, S. B., and Couceiro, F. (2020). The effects of freshwater flow and salinity on turbidity and dissolved oxygen in a shallow macrotidal estuary: a case study of Portsmouth harbour. *Ocean Coast. Manage.* 191:105179. doi: 10.1016/j.ocecoaman.2020.105179

Palinkas, C. M., Testa, J. M., Cornwell, J. C., Li, M., and Sanford, L. P. (2019). Influences of a river dam on delivery and fate of sediments and particulate nutrients to the adjacent estuary: case study of conowingo dam and Chesapeake bay. *Estuaries Coasts* 42 (8), 2072–2095. doi: 10.1007/s12237-019-00634-x

Prasad, K. V. S. R., Sridevi, T., and Sadhuram, Y. (2018). Influence of dam-controlled river discharge and tides on salinity intrusion in the godavari estuary, east coast of India. *J. Waterw. Port Coast.* (2018) 144(2):04017049. doi: 10.1061/(ASCE)WW.1943-5460.0000430

Priya, K. L., Jegathambal, P., and James, E. J. (2016). Salinity and suspended sediment transport in a shallow estuary on the east coast of India. *Reg. Stud. Mar. Sci.* 7, 88–99.doi:10.1016/j.rsma.2016.05.015. doi: 10.1016/j.rsma.2016.05.015

Ruhl, C. A., and Simpson, M. R. (2005). Computation of discharge using the index-velocity method in tidally affected areas. U.S. geological survey scientific investigations report 2005–5004. 1–31. doi: 10.3133/sir20055004

Sakho, I., Dussouillez, P., Delanghe, D., Hanot, B., Raccasi, G., Tal, M., et al. (2019). Suspended sediment flux at the Rhone river mouth (France) based on ADCP measurements during flood events. *Environ. Monit. Assess.* 191, 508. doi: 10.1007/s10661-019-7605-y

Sheldon, A. R., Dalal, R. C., Kirchhof, G., Kopittke, P. M., and Menzies, N. W. (2017). The effect of salinity on plant-available water. *Plant Soil* 418 (1), 477–491. doi: 10.1007/s11104-017-3309-7

Shin, H. R., Lee, J. H., Kim, C. H., Yoon, J. H., Hirose, N., Takikawa, T., et al. (2022). Long-term variation in volume transport of the tsushima warm current estimated from ADCP current measurement and sea level differences in the Korea/Tsushima strait. *J. Mar. Syst.* 232, 103750. doi: 10.1016/j.jmarsys.2022.103750

Sin, Y., and Lee, H. (2020). Changes in hydrology, water quality, and algal blooms in a freshwater system impounded with engineered structures in a temperate monsoon river estuary. *J. Hydrol.- Reg. Stud.* 32, 100744. doi: 10.1016/j.ejrh.2020.100744

Van Proosdij, D., Milligan, T., Bugden, G., and Butler, K. (2009). A tale of two macro tidal estuaries: differential morphodynamic response of the intertidal zone to causeway construction. *J. Coast. Res.* 56, 772–776.

Wang, Y., Zhou, L., Jia, Q. Y., and Yu, W. Y. (2017). Water use efficiency of a rice paddy field in liaohe delta, northeast China. *Agr. Water Manage.* 187, 222–231. doi: 10.1016/j.agwat.2017.03.029

Weeks, E., Robinson, M. E., and Li, C. Y. (2018). Quantifying cold front induced water transport of a Louisiana bay with *in-situ* observations using an unmanned boat. *Acta Oceanol. Sin.* 37 (11), 1–7. doi: 10.1007/s13131-018-1330-1

Williams, J., Lee, G., Shin, H. J., and Dellapenna, T. (2015). Mechanism for sediment convergence in the anthropogenically altered microtidal nakdong estuary, south Korea. *Mar. Geol.* 369, 79–90. doi: 10.1016/j.margeo.2015.08.004

Xia, M., Xie, L., Pietrafesa, L. J., and Whitney, M. M. (2011). The ideal response of a gulf of Mexico estuary plume to wind forcing: its connection with salt flux and a Lagrangian view. *J. Geophys. Res.* 116, C08035. doi: 10.1029/2010JC006689

Xiong, J., Wang, X. H., Wang, Y. P., Chen, J., Shi, B., Gao, J., et al. (2018). Reprint of mechanisms of maintaining high suspended sediment concentration over tide dominated offshore shoals in the southern yellow Sea. *Estuar. Coast. Shelf Sci.* 206:2–13. doi: 10.1016/j.ecss.2018.03.019

Zamparas, M., and Zacharias, I. (2014). Restoration of eutrophic freshwater by managing internal nutrient loads. a review. *Sci. Total Environ.* 496, 551–562. doi: 10.1016/j.scitotenv.2014.07.076

Zhang, N., Wang, J., Wu, Y. S., Wang, K. H., Zhang, Q. H., Wu, S. Q., et al. (2019). A modelling study of ice effect on tidal damping in the bohai Sea. *Ocean Eng.* 173, 748–760. doi: 10.1016/j.ecss.2018.03.019

Zhu, B. S., Yang, W., Jiang, C. F., Wang, T., and Wei, H. (2022).). observations of turbulent mixing and vertical diffusive salt flux in the changjiang diluted water. *J. Oceanol. Limnol.* 40 (4), 1349–1360. doi: 10.1007/s00343-021-1191-x

Zhu, Z. N., Zhu, X. H., Zhang, C., Chen, M., Zheng, H., Zhang, Z., et al. (2021). Monitoring of Yangtze river discharge at datong hydrometric station using acoustic tomography technology. *Front. Earth Sci.* 9. doi: 10.3389/feart.2021.723123

frontiers | Frontiers in Marine Science

TYPE Original Research
PUBLISHED 16 May 2023
DOI 10.3389/fmars.2023.1163456

OPEN ACCESS

EDITED BY
Guotao Cui,
University of California, Merced,
United States

REVIEWED BY
Anupal Baruah,
North Eastern Space Applications Centre (NESAC), India
Ruidi Bai,
Sichuan University, China

*CORRESPONDENCE
Huilin Wang
whl@scau.edu.cn
Wen Wang
wangwen1986@xaut.edu.cn

RECEIVED 10 February 2023
ACCEPTED 24 April 2023
PUBLISHED 16 May 2023

CITATION
Zhang J, Mi Z, Wang H, Wang W, Li Z and Guan M (2023) A multiple-fluids-mechanics-based model of velocity profiles in currents with submerged vegetation.
Front. Mar. Sci. 10:1163456.
doi: 10.3389/fmars.2023.1163456

A multiple-fluids-mechanics-based model of velocity profiles in currents with submerged vegetation

Jiao Zhang[1], Zhangyi Mi[1], Huilin Wang[2*], Wen Wang[1*], Zhanbin Li[1] and Muhong Guan[3]

[1]State Key Laboratory of Eco-Hydraulics in Northwest Arid Region, Xi'an University of Technology, Xi'an, China, [2]College of Water Conservancy and Civil Engineering, South China Agricultural University, Guangzhou, China, [3]AnHui Water Resources Development Co., Ltd., Anhui, China

Submerged aquatic vegetation can provide a habitat and food for marine and river organisms, and it has the ecological effect of purifying water by absorbing harmful substances. Therefore, it plays an important role in the maintenance, restoration, and improvement of marine and river ecosystems. Hydrodynamic problems caused by submerged vegetation have been a matter of wide concern. According to the distribution of submerged vegetation, the flow can be divided into three layers in the vertical direction: uniform, mixing, and logarithmic layers. This paper proposes an analytical model for the vertical distribution of longitudinal velocity in open-channel flows with submerged vegetation. A concept of velocity superimposition is applied in mixing and logarithmic layers. The velocity inside the vegetated layer can be solved by the balance between the drag force and bed gradient. The velocity difference between the vegetated layer and the free surface layer results in the formation of a mixing layer near the top of the vegetation. Flow at the junction between the vegetation and free surface layers is mainly controlled by the vortices in the mixing layer. The velocity in the mixing layer is commonly described by a hyperbolic tangent formula. The logarithmic distribution formula is applied to the free surface layer, where the velocity without effect arising from vortices is similar to the open-channel flow. The concept of the wake function is introduced to modify the distribution of velocity in the free surface layer. The longitudinal velocities from the theoretical model are compared to the measured velocities in the literature. The theoretical velocities agree well with the measured values in the flows with submerged vegetation, proving that the theoretical model proposed here can successfully predict the vertical distribution of velocity and has extensive adaptability.

KEYWORDS

submerged vegetation, velocity distribution, hydraulic resistance, vertical velocity profile, mixing layer, analytical solution

1 Introduction

Aquatic vegetation is widespread in natural rivers, coasts, and lakes, providing comfortable habitats and abundant food for organisms. This kind of vegetation changes the flow structure and reduces flow velocity and even forms hydraulic jumps because of the vegetation's resistance, leading to influence on the flow turbulence intensity, sediment, and nutrient transport in flow (Bai et al., 2022; Bai et al., 2022a, b; Shi et al., 1995; Nepf, 1999; Wu et al., 1999; Lou et al., 2022; Yang et al., 2022). Meanwhile, air entrainment takes place when the flow turbulence near the free surface is large enough. A vegetated waterway will promote the flow of energy dissipation and mixing between the water and air, which is of great help in the study of energy dissipation measures (Bai et al., 2022a; Wang et al., 2022). Therefore, it is important to better understand the flow characteristics of vegetated flow and its possible hydraulic impact (Huthoff et al., 2007).

The interaction between submerged vegetation and flow has awakened the broad interest of scholars. The resistance of vegetation to the flow causes a distinct velocity difference between the vegetated layer and upper flow, which causes a strong momentum exchange within the flow in the vegetated layer and the non-vegetated layer alike. This velocity difference is even more obvious especially in the case of large vegetation density. Previous researchers tended to divide the submerged-vegetated flow into several layers and then investigate the flow structure layer-by-layer (Stone and Shen, 2002; Sun and Shiono, 2009). For example, Klopstra et al. (1997) analyzed the vertical distribution of velocity in a flow with flexible submerged vegetation. They applied the Boussinesp concept to describe turbulent shear stresses in the vegetated layer and used the Prandtl mixing length concept in the free surface layer to obtain the logarithmic velocity profile. The velocity in the vegetated layer depends on factors such as slope, water depth, and vegetation characteristics (Yang and Choi, 2010). While in the free surface layer, the viscosity shear stress can also be omitted and only Reynolds shear stress need to be considered (Huai et al., 2009b). Yang et al. (2007) selected plastic grass, duck feathers, and plastic straws to simulate grass, shrubs, and trees, respectively. The distribution of velocity on a floodplain covered by different vegetation was measured. The difference in velocity distribution caused by different aquatic vegetation is mainly reflected in the position of the boundary layer (bottom and top of vegetation). Due to the bed resistance, the velocity near the bottom of the vegetation is low; however, due to the shear stress near the top of the vegetation, the velocity near the vegetation top is greater than that in the inner vegetated layer. The longitudinal velocity in the vegetated layer vertically conformed to an S-type distribution (White and Nepf, 2008; Kowalski and Torrilhon, 2017).

Many models have been proposed to describe the velocity distribution of vegetated flow. Cheng (2015) defined the friction coefficient with a new hydraulic radius and created a single-layer theoretical model for predicting velocity, which was compared with the proposed two-layer model (Stone and Shen, 2002; Baptist et al., 2007; Huthoff et al., 2007; Yang and Choi, 2010; Cheng, 2011). Most two-layer models divide the submerged vegetated flow into a vegetated layer and surface layer by using the top of vegetation as a boundary. The single-layer model was simpler than the two-layer model because it does not involve the calculation of the vegetation drag coefficient and hydrodynamic height of roughness. However, this single-layer model was not suitable for calculating velocity in channels without vegetation and channels with emergent vegetation. Righetti and Armanini (2002) solved the double-averaged (time and space) momentum equations based on the mixing length model and the assumption that turbulent shear stress was quasi-linear, and then they obtained the predicted velocities from the two-layer analytical solution. To explore the hydraulic characteristics of the vegetated and non-vegetated layers, Huai et al. (2009a) used three-dimensional ADV (Acoustic Doppler Velocimetry) to measure the longitudinal velocity with submerged flexible vegetation. They found that the upper part of the vegetated layer was mainly controlled by the K-H vortices while the lower part was mainly controlled by stem vortices caused by the vegetation. In addition, the turbulence intensity and the Reynolds stress reach their maximum near the top of the vegetation. Then, Huai et al. (2009b) proposed a new three-layer model (the inner vegetated layer, the outer vegetated layer, and the upper layer) to predict the vertical distribution of longitudinal velocity in open-channel flow with submerged rigid vegetation. For the upper non-vegetated layer, a modified mixing length theory was adopted. For the inner region near the channel boundary, the mixing length hypothesis is adopted to express the shear stress. And for the outer region within vegetation, shear stress can be simplified by Reynolds stress. The three-layer method can obtain more accurate results of the velocity in the vegetated layer. To obtain a satisfied predicted model of velocity in submerged vegetated flow, Nikora et al. (2013) proposed that the flow was vertically divided into five layers, i.e., the near-bed boundary layer, the uniform velocity layer, the mixing layer at the top of the vegetation, the logarithmic layer above the vegetation, and the wake layer. The near-bed boundary layer could be ignored in most vegetation flows (Nepf and Vivoni, 2000), and the formulas of velocity in other layers were proposed. In the uniform velocity layer, the velocity was related to vegetation resistance and bed slope. The velocity distribution in the mixing layer was complex and can be described by a hyperbolic tangent profile. In the area above the mixing layer, the velocity follows a logarithmic distribution, which should be corrected with the wake term. Shi et al. (2019) thought that the multi-layer method was complex, and people mainly focus on the cross-sectional average velocity of the section, so the traditional two-layer method was used in the flow with submerged rigid vegetation. The force balance equation was adopted in the vegetated layer, and a parameter similar to the Darcy-Weisbach parameter was proposed for the surface layer. This parameter was related to the other parameters through the GP algorithm to obtain a high-precision velocity formula. Different from the traditional layered method, Baruah et al. (2022) proposed a model which was developed by coupling the vegetation drag force with the modified form of two-dimensional shallow water equations. This method can be applied in complex flow scenarios for estimating the vertical distribution of longitudinal velocity in an open channel with submerged, flexible vegetation.

The open-channel flow was used to be divided into two separate layers, namely the submerged vegetation layer and the free surface

layer as in the literature (Hui et al., 2009; Ren and Feng, 2020; Zhang et al., 2021). These two layers were mutually independent and the interaction between them was ignored. In the presented article, we consider the complexity of flow structure in the vertical direction and divide the flow into three layers, which are the uniform velocity layer, mixing layer, and logarithmic layer. The mixing layers are formed near the vegetation top. The velocity in the mixing layer is more complex than those in the uniform vegetation layer and logarithmic layer. The purpose of this study is to predict the velocity by applying the superposition principle for the mixing and the logarithmic layers. To obtain the vertical velocity distribution, it is necessary to obtain the velocity additional term in each layer first. The inflection point occurs in the mixing layer according to the literature. The velocity at the inflection point still needs to be discussed. We introduce a corrected parameter β to obtain the predicted velocity at the inflection point and improve the formula for calculating the mixing layer's width. The model for predicting the velocity profile in the submerged vegetated channel is verified by the measured velocity data from previous studies. The presented paper is organized as follows: Section 2 introduces the methodology, namely the theoretical analysis, followed by a detailed description of model parameters in Section 3. Section 4 introduces the experimental setup and vegetation shape. In Section 5, the predicted and measured velocities are compared. Error analysis, parameter discussion, and model limitations are illustrated in Section 6. A summary of the main findings and conclusions is presented in Section 7.

2 Methodology

In terms of vegetation distribution, the flow structure is divided vertically by the submerged vegetation into two layers: the vegetated layer and the non-vegetated layer, as shown in Figure 1, where the deflected vegetation height is H_v and the water depth is H. The coordinates in the vegetated flow are defined as flow direction x, horizontal direction y, vertical direction z, and the corresponding velocity components are U, V, and W. The vertical distribution of longitudinal velocity is expressed as $U_{(z)}$, and U_i is the velocity at the inflection point z_i near the vegetation top. Due to the vegetation drag, the velocity difference between the vegetated and non-vegetated layers is distinct, leading to the K-H vortices appearing between the layers. Due to the presence of an inflection point in the velocity profile near the top of the vegetated layer (White and Nepf, 2008), the mixing layer is divided into two layers at the inflection point z_i. δ_o and δ_I are the inner and outer regions of the mixing layer respectively.

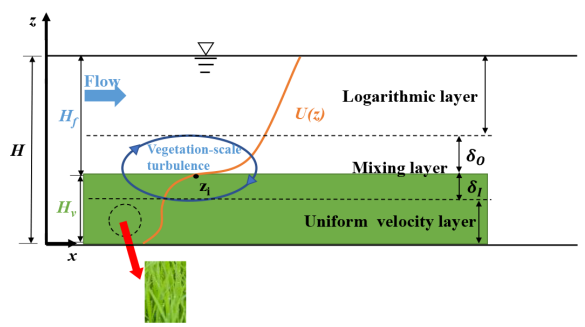

FIGURE 1
Side view of open channel flow with submerged flexible vegetation.

It is assumed that the velocity can be regarded as a (quasi-) linear superposition of individual mechanisms and the concept of velocity superposition is applied to the whole velocity profile (Nikora et al., 2013). The velocity profile can be divided into three layers. (1) In the uniform velocity layer, i.e., $0< z< z_i - \delta_I$, $U = U_v$, where U_v is a velocity in the uniform layer, which is not affected by vortices. (2) In the mixing layer, i.e., $z_i - \delta_I< z< z_i - \delta_o$, $U = U_v + U_m$, where U_m is a velocity additional term in the mixing layer. (3) In the logarithmic layer, i.e., $z_i - \delta_O< z< H$, $U = U_v + U_m + U_l + U_w$, where U_l is a velocity additional term in the logarithmic layer and U_w is the effect of wake term. The definitions of the specific velocities, i.e., U_v, U_m, U_l, U_w, are elaborated on below.

2.1 Uniform velocity layer

The velocity is set by a balance of vegetation drag and forcing in the inner layer of vegetation ($0< z< z_i - \delta_I$) without effect arising from vortices. The region from 0 to $z_i - \delta_I$ in the vertical direction is called the uniform velocity layer. The flow velocity in this layer with the effect of the vegetation drag force can be expressed as (Nepf, 2012):

$$U_v = \left(\frac{gS}{0.5C_Da}\right)^{0.5} \quad (1)$$

where g is the acceleration of gravity, S is the bed slope, C_D is the drag coefficient of vegetation, and a is the frontal vegetation area per unit volume. The change of the velocity in this layer mainly depends on the value of C_D and a. Bottom shear is ignored in the uniform velocity layer, and U_v is inversely proportional to the square root of the C_Da. In the case of cylindrical rigid vegetation, C_Da does not change with z in the vertical direction, so U_v remains unchanged. Because of the resistance of vegetation to flow, the velocity in the vegetated layer is always less than the velocity over a bare bed under the same depth and external forcing. According to the principle of momentum balance, Eq. (1) is applicable in both flexible and rigid vegetation.

2.2 Mixing layer

Due to the discontinuity of resistance at the vegetation top, a mixing layer caused by vortices is generated. The distance from the inflection point z_i to the lower boundary of the mixing layer is δ_I, and the distance from z_i to the upper boundary is δ_O (Figure 1). That is, the width of the mixing layer is $z_i - \delta_I< z< z_i + \delta_O$. The velocity term U_m is commonly described by a hyperbolic tangent profile (Raupach et al., 1996; Nepf, 2012; Nikora et al., 2013):

$$U_m = (U_i - U_v)[1 + tanh(\frac{z - z_i}{\delta_0})] \quad (2)$$

where U_i is the velocity at the inflection point z_i. $U_i - U_v = U_s$, where U_s is defined as the slip velocity (White and Nepf, 2008). The scale of the vortices gradually develops along the x direction after the flow enters the vegetated layer (Raupach et al., 1996). The flow enters the vegetated layer from the free surface layer in the z direction with the velocity $W< 0$, indicating the invasion of the vortices. To obtain the U_m, it is necessary to get the velocity U_i at the inflection point first. When the inflection point z_i is at the top of the vegetation, that is, when $z_i = \bar{z}$, the velocity U_i at the inflection point equals the average of the U_v and U_2, i.e., $U_i = (U_v + U_2)/2 = \bar{U}$. U_2 is the velocity within the water surface and $\bar{z}$ is the vertical coordinate of $\bar{U}$ (Nikora et al., 2013). However, for a large relative submergence degree, the width of the mixing layer is far less than that of the logarithmic layer, so $U_i \neq (U_v + U_2)/2$. The calculation process of U_i is described in detail at the end of the Section 2.

2.3 Logarithmic layer

Significant studies have been carried out on the distribution of turbulent velocity in natural rivers, and the logarithmic velocity distribution formula is widely used (Fu et al., 2013). The logarithmic formula is based on the semi-empirical theory with universality, where parameters are mainly constants and do not depend on the Reynolds number. The velocity distribution above the mixing layer is similar to the open-channel flow, which has a logarithmic shape based on previous experiments (Nepf and Vivoni, 2000; Nepf and Ghisalberti, 2008). The logarithmic term can be expressed as (Nikora et al., 2013), when $z_i - \delta_O < z < H$:

$$U_l = \frac{U_{*m}}{\kappa} ln\left(\frac{z - d}{z_0}\right) \quad (3)$$

$$z_0 = de^{-\kappa C} \quad (4)$$

where U_{*m} is shear velocity as a momentum transport scale, which is generally equal to the square root of the maximum Reynolds stress; κ (= 0.40) is the Von Kármán constant. The logarithmic formula is appropriate for the open channel flows without vegetation. Owing to the velocity in the vegetated layer not being equal to zero, the calculation starting plane for the logarithmic formula, i.e., a zero plane, should be raised. The zero-displacement height d is approximately equal to the height of submerged vegetation. $C = U_i/U_*$ is the ratio of velocity at the inflected point to the shear velocity. $U_* = \sqrt{gHS}$ is defined by Kouwen et al. (1969).

Due to the influence of the side wall and free surface, there is a spiral flow near the water surface that points to the center. The secondary flow brings the low-speed flow near the side wall to the center along the water surface, reducing the surface velocity (Wang et al., 1998). Coles (1956) found that velocity near the water surface deviated from the logarithmic function, and then proposed wake function and wake strength parameter Π to modify the velocity near the water surface. The influence of the wake term on the velocity can be presented using a trigonometric function (Monin and Yaglom, 1971):

$$U_w = U_{*m}\frac{2\prod}{\kappa} sin^2\left(\frac{\pi z}{2H}\right) \quad (5)$$

where Π is Coles's wake strength parameter. For a channel with $B/H < 5.20$, in which B is the channel width, the maximum velocity point is generally below the flow surface, and for $B/H > 5.20$, the maximum velocity point is on the flow surface (Fu et al., 2013).

Raupach et al. (1996) stated that the slip velocity $U_s = (U_2\text{-}U_v)/2$. White and Nepf (2008) also obtained the formula of slip velocity: $U_s = U_i\text{-}U_v$ through experiments in a channel, which was partially covered by the emergent vegetation. Owing to the different experiment condition, the parameter β is introduced in this paper, i.e., $U_i - U_v = \beta (U_2 - U_v)/2$, so that U_i can be obtained iteratively with Eqs. (1) – (5). The verification of the calculated values of U_i and β is discussed in Section 6.2.

3 Parameter determination

The parameters, such as water depth H, vegetated height H_v, the amount of vegetation per unit area m, and the bed slope S can be known easily. To obtain the analytical solution of the velocity distribution, the remaining parameters need to be determined, namely inflection point z_i, velocity U_i at z_i, mixing layer width $\delta_o + \delta_I$, frontal vegetation area per unit volume α, drag coefficient C_D, scale of turbulent momentum transport U_{*m}, and Coles's wake strength parameter Π.

3.1 Velocity U_i at inflection point z_i

The position of the inflection point z_i in the velocity profile is commonly near the vegetation top. Nikora et al. (2013) showed that the inflection point was slightly lower than the top of the vegetation. In Section 4 illustrating the experimental data, it can be seen that z_i/H_v is taken as 0.75. For cases 4 – 5, $z_i/H_v = 0.80$. The vegetation density of cases 4 – 5 is smaller than that of cases 1 – 3 (detailed in Section 4), and the scale of vortices is larger in cases 4 – 5. We suspect that this may be a factor influencing the location of the inflection point. U_i is the velocity at the inflection point z_i, which cannot be measured in advance, so $U_i - U_v = \beta(U_2 - U_v)/2$ mentioned in Section 2 is solved iteratively to obtain the velocity U_i.

3.2 δ_o and δ_I in mixing layer

White and Nepf (2008) studied the transverse distribution of the velocity in the submerged vegetated channels and gave the width of the mixing layer above the inflection point z_i, which was

FIGURE 2
Plastic aquatic grass model.

expressed as:

$$\delta_O = \frac{U_2 - U_i}{\frac{dU}{dz}|_{z=z_i}} \tag{6}$$

where U_2 is the velocity within the water surface layer.

The width of the mixing layer below the inflection point z_i is the maximum of the drag length scale and the blade width constraint:

$$\delta_I = max[0.5(C_D a)^{-1}, 1.8D] \tag{7}$$

Liu et al. (2013) believed that C_D for the rigid cylindrical vegetation could be taken as 1.00. In cases 1 – 3, based on the mean momentum equation of the vegetated flow for completely developed stage, the effective drag coefficient of the vegetation C_D can be obtained from the study of Huai et al. (2019), which is the relation between measured C_D and z/H_v. In cases 4 – 5, C_D is determined from the experiment of Hui et al. (2009), which is 1.50.

3.3 Model parameter β

The β is introduced in U_i - $U_v = \beta(U_2$ - $U_v)/2$. The value of β is likely to be related to the invasion depth of vortices. In cases 1 – 3, the depth of invasion is smaller, which is about 55%, and β is taken as 0.20. In cases 4 – 5, that is about 65%, and β is considered 0.55.

3.4 Shear velocities U_{*m} and U_{*b}

U_{*m} is a velocity scale of the turbulent momentum transport, which is generally equal to the square root of the maximum Reynolds stress, and U_{*b} is the wall shear stress. In vegetated flow, the shear stress is not constant due to the effects of gravity and the momentum sink within the vegetation (the effects of secondary currents can also be potentially significant), that is, $U_{*m} \neq U_{*b}$ (Järvelä, 2002; Pokrajac et al., 2006; Nikora et al., 2007). U_{*b} can be expressed as (Nikora et al., 2001):

$$U_{*b} = \sqrt{gS(H_f + \alpha H_v)} \tag{8}$$

where $H_f = H$ - H_v and α is porosity. Based on Nikora et al. (2013)'s study, $U_{*b} \approx 1.6U_{*m}$.

3.5 Coles's wake strength parameter Π

The Coles's wake strength parameter Π has been extensively studied in the literature. For boundary layers and nonuniform open-channel flows, Π depends on the pressure gradient (Coles, 1956; Kironoto and Graf, 1994). For open-channel flows with vegetation, the value of Π needs to be further investigated considering the influence of turbulence which is caused by the vegetation resistance. Fu et al. (2013) summarized the previous experiments on Π and concluded that it had a range of -0.27 – 0.65. A negative value of Π means that after introducing this parameter in the logarithmic layer, the velocity in this layer is smaller than without consideration of it. In the text for cases 1 – 3: Π = 0.30 – 0.40; cases 4 – 5: Π = 0.10.

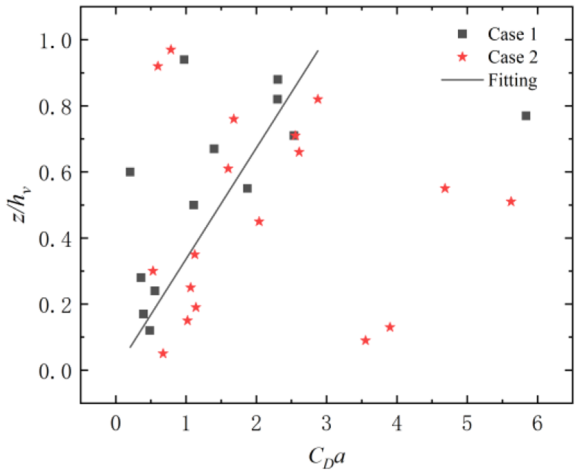

FIGURE 3
C_Da varies in the vertical direction, where the squares represent case 1, the stars represent case 2, and the straight line indicates the general trend of C_Da along the vertical direction.

4 Experiments

4.1 Experiment I

The experiment was conducted in two glass flumes of the State Key Laboratory of Wuhan University by Huai et al. (2019). The tailgate could be used at the end of channels to adjust the water level. Artificial plastic grass was used to simulate natural vegetation, resembling sedges with staggered arrangements, as shown in Figure 2. The measured points were placed at the mid-perpendicular line of two vegetation rows using Acoustic Doppler Velocimetry (ADV) in the section of x = 4.64 m. One measurement point is measured multiple times to get the average value, which is a dual average velocity in time and space.

Referring to the distribution of C_D and a along the vertical direction given by Huai et al. (2019) in the measurement section, the C_Da could be obtained for cases 1 and 2 in Figure 3. It can be seen from Figure 3 that C_Da increased vertically with the increase of z. The model vegetation leaves used in this experiment cause a to reach its peak at the middle of the vegetation and then gradually decrease. The deviation of C_Da from the fitting line near the bed and in the middle of the vegetation increased maybe resulting from the sway of vegetation under the influence of flow.

4.2 Experiment II

Hui et al. (2009) conducted experiments on shrub-like vegetation in the Hydraulics Laboratory of Tsinghua University to measure the vertical distribution of velocity under various flow conditions. In the experiment, the selected vegetation had an average height of 27.50 cm and an average longitudinal maximum diameter of 20.00 cm. The vegetation was staggered and arranged with two different densities: 15.71/m^2 and 7.85/m^2. The velocity distributions in different cross-sections were measured using Acoustic Doppler Velocimetry (ADV). To minimize the influence of spatial heterogeneity on velocity measurement, the velocity at the same depth has been averaged along lateral and longitudinal directions. The ratio of the roots-to-crown diameter was k = 0. 25, that is, the diameter of the vegetation root was 5.00 cm (Figure 4). The drag coefficient of vegetation C_D was 1.50. The corresponding information for the experimental setup is shown in Table 1.

5 Model verification

The comparison between the analytical solution of the proposed model and the measured data along the vertical direction in flow with submerged flexible vegetation is shown in Figure 5. The analytical solution of the velocity distribution in the vertical direction agrees well with the measured data. The area between the two solid black lines is the mixing layer, the area below is the uniform velocity layer, and the area above is the logarithmic layer. The dotted line in the mixing layer represents the vegetation top. In Figure 5, we can see that the velocity in the logarithmic layer ($z_i + \delta_o < z < H$) is much larger than that in the uniform layer ($0 < z < z_i - \delta_I$) for all subplots. Due to the vertical variance of the vegetation frontal area, the velocity in the vegetated layer ($0 < z < z_i$) showed the "S" shape distinctly in Figures 5A–C. The closest velocity to the channel bed is much smaller than that in the uniform velocity layer, which is due to the friction of the channel bed. *Specifically, the velocity near the vegetation bottom is larger than that near the upper of the* vegetation in Figure 5, resulting from the C_Da at the top of the vegetation is greater than C_Da near the root. The velocities in the vegetated layer ($0 < z < z_i$) in Figures 5D, E do not show distinct change along the vertical direction due to the relatively uniform value of C_Da. Due to the vortices formed in the mixing layer, the velocity gradient in the region of $z_i - \delta_I < z < z_i$ gradually decreases as it approaches the inflection point, followed by a gradual increase of the velocity gradient when $z > z_i$. The predicted velocity in the logarithmic layer for Figure 5A appears obvious

FIGURE 4
Schematic diagram of a shrub vegetation model.

deviations from the measured data, maybe the error of parameter calculation in this case. Overall, the proposed model can be applied in the submerged vegetated channel with different flexibilities and vegetation densities.

6 Discussion

6.1 Error analysis

To quantitatively describe the difference between the results of the model and the experimental data, an error analysis from two perspectives: the average values of the absolute error $\bar{\epsilon}$ and the relative error $\overline{\epsilon'}$ is performed. The absolute error ϵ is expressed as follows:

$$\epsilon = | U_{measured} - U_{calculated} | \tag{9}$$

where the subscripts "measured" and "calculated" represent the measured values and the calculated data from the presented model, respectively. The average value of the absolute error $\bar{\epsilon}$ can be expressed as follows:

$$\bar{\epsilon} = \frac{1}{N_m} \sum_{i=1}^{N_m} |\epsilon_i| \tag{10}$$

where N_m represents the number of experimental points. The relative error ϵ' is expressed as follows:

$$\epsilon' = \frac{\epsilon}{U_{measured}} \tag{11}$$

The average value of the relative error $\overline{\epsilon'}$ is expressed as follows:

$$\overline{\epsilon'} = \frac{1}{N_m} \sum_{i=1}^{N_m} |\epsilon_i'| \times 100\,\% \tag{12}$$

Table 2 lists the average values of the absolute and relative errors for cases 1 – 5. The average absolute errors of the five cases are less than 0.015 m/s, and the average relative errors of cases 1 – 5 are less than 10%, which reaches the maximum for case 1. The error analysis indicates that the proposed model is reliable in predicting the velocity in the flows with submerged flexible vegetation.

6.2 Wake strength parameter Π related to U_l

The measured velocities in the logarithmic layer are compared with the predicted data with/without the wake effect for all the cases, which are shown in Figure 6. It can be seen from Figure 6 that the predicted velocity considering the wake effect better agrees well with the measured data than the predicted velocity ignoring the wake effect does. Hence, it is reasonable to conclude that the influence of the wake term on the velocity profile in the logarithmic layer cannot be neglected, which is consistent with the conclusion obtained by Zhang et al. (2021). The Coles's wake strength parameter Π in the wake function ranges from 0.3 – 0.4 for cases 1 – 3 with the relative submergence $H_v/H \approx 0.7$. In cases 4 – 5, Π = 0.1 with the H_v/H = 0.57. The values of Π are all within the range of previous research results (Fu et al., 2013). The relative submergence for cases 1 – 3 is larger than that for cases 4 – 5. We guess that the parameter value of wake strength Π may be inversely correlated with the relative submergence of vegetation. The results show that the Π value has a non-negligible influence on the wake effect, which then influences

TABLE 1 Summary of experimental conditions, where *H* is water depth, *m* is the amount of vegetation per unit area, *S* is bed slope, and *Hv* is deflected vegetation height.

Source	Cases	H(m)	m(m^{-2})	S	H_v(m)
Huai et al. (2019)	1	0.27	43.30	0.01%	0.185
	2	0.27	108.30	0.04%	0.195
	3	0.33	108.30	0.04%	0.210
Hui et al. (2009)	4	0.45	15.71	0.67%	0.255
	5	0.45	7.85	0.67%	0.255

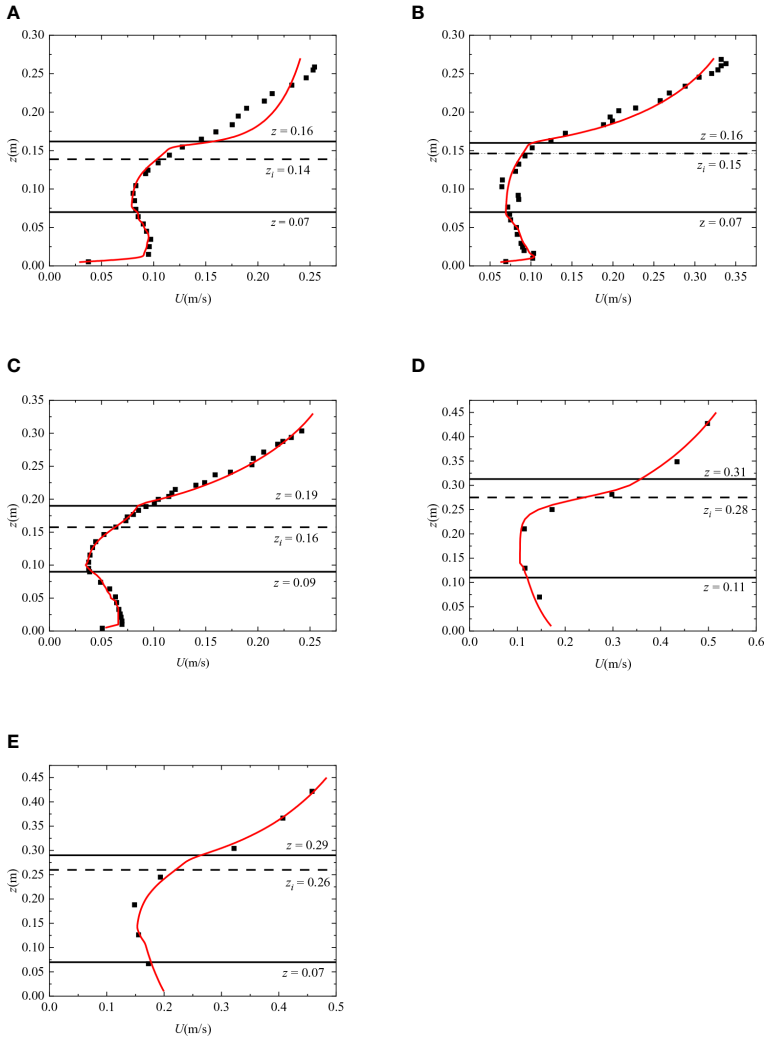

FIGURE 5
Comparison between the measured velocities and the predicted ones for cases 1 – 5. **(A–C)** Are the cases from Huai et al. (2019). **(D, E)** Are the cases of Hui et al. (2019). The solid red lines are predicted data and the points are the measured data. The horizontal dashed lines represent the inflection point, and the region between solid black lines represents the mixing layer.

the velocity profile. Therefore, further experiments for Π are required to refine its application range and to provide better parameter selection for predicting velocity profiles.

6.3 Model extension

The proposed model has good application results in flexible vegetated flows, and the following discussion is made to explore its applicability in rigid vegetated flows. We refer to measured data from two different experiments of the rigid vegetated flow. (i) First set of experimental data for rigid vegetated flow was obtained in the Nepf lab at the Massachusetts Institute of Technology (Zhang et al., 2020), where the experimental flume was 24.00 m long and 0.38 m wide, and the water depth H was 0.36 m. The submerged vegetation was constructed from rigid circular rods, the height H_v of which is 0.07 ± 0.002 m, and the diameter was D = 0.64 ± 0.02 cm, where C_D = 1.30, a = 9.60. (ii) Second set of experimental data was conducted by Shi et al. (2023) at the State Key Laboratory of Water Resources and Hydropower Engineering Science. The open channel was partially covered by rigid cylindrical vegetation, the height of which was 0.25 m with a diameter of 8 mm. The water depth was set

TABLE 2 Error statistics for measured and predicted velocity.

Cases	1	2	3	4	5
$\bar{\epsilon}(m/s)$	0.01	0.009	0.004	0.015	0.008
$\overline{\epsilon'}(\%)$	7.12	6.62	4.69	6.97	3.79

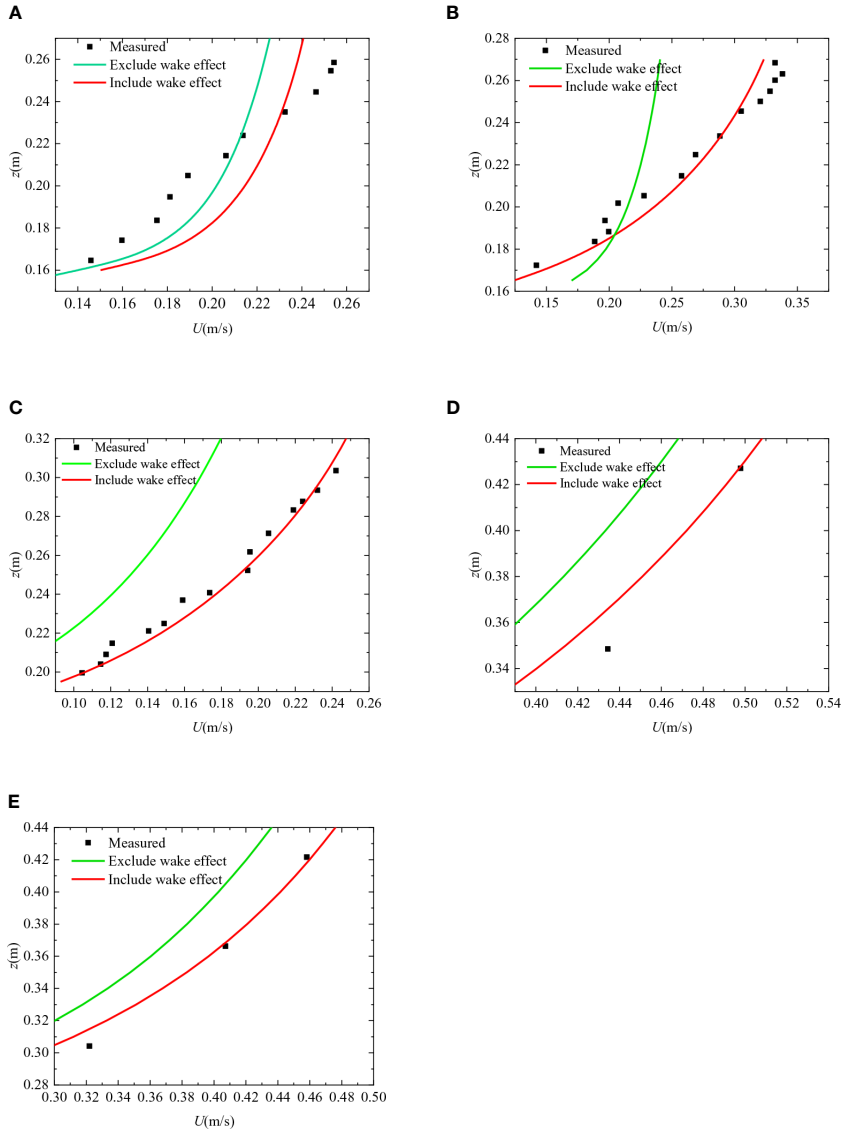

FIGURE 6
Comparison of the analytical solution and measured values for predicted velocity in the logarithmic layer for cases 1-5. **(A–C)** Are the cases from Huai et al. (2019). **(D, E)** Are the cases of Hui et al. (2009). Where the solid green line indicates the model that does not consider the wake effect, and the solid red line indicates that the wake effect is considered.

to 0.35 m. The parameters in the above two cases with rigid vegetation are shown in Table 3.

A comparison between the predicted and measured data is shown in Figure 7. The measured data is represented by the dots and the predicted data is represented by the blue lines. Although the vegetation densities, vegetation arrangements, and vegetation submergences varied, the predicted velocity from the proposed model could capture the velocity profile in the rigid vegetated flows, showing that this model is also applicable to rigid vegetated flows.

6.4 Sensitivity analysis

The influence of β on the prediction of the proposed model is described below. Case 3 is taken as an example. When the target parameter β is adjusted, the other parameters are fixed.

In case 3, the approximate value of β is 0.2 (defined as β_3), and the red solid line in Figure 8 represents the predicted velocity distribution obtained by using β_3. Thus, we considered a wider range of β (= $0.8\beta_3$ – $1.2\beta_3$) to examine the sensitivity of the proposed model. The sensitivity analysis of parameter β is shown in Figure 8. When $\beta < \beta_3$ (e.g., $\beta = 0.8\ \beta_3$, the navy blue line), β produces lower velocities in the non-vegetated layer. In contrast, a larger β (e.g., $\beta = 1.1\ \beta_3$, the light blue line) corresponds to higher velocities in the non-vegetated layer. According to Figure 8, the predicted velocities are sensitive to the parameter β only in the non-vegetated layer and are insensitive to that in the submerged vegetated layer.

β determines the velocity U_i at the inflection point according to Eq. (2). The velocity U_i at the inflection point z_i of cases 1 – 5 is calculated iteratively. The comparison between the measured and calculated U_i is shown in Table 4, demonstrating that they are

TABLE 3 Summary of experimental conditions.

Source	Cases	H(m)	C_D	a(m^{-1})	D(m)	H_v(m)
Zhang et al. (2020)	1	0.36	1.30	9.60	0.0064 ± 0.0002	0.07 ± 0.002
Shi et al. (2023)	2	0.35	1.40	3.20	0.008	0.25

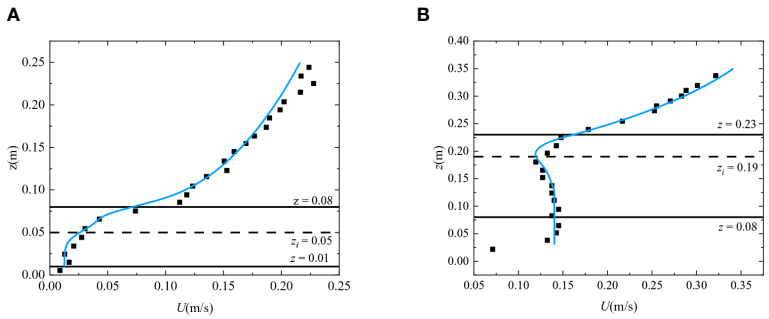

FIGURE 7
Comparison between the measured and predicted velocities for the rigid vegetation cases, where the solid blue line is the predicted velocity and the points are the measured data. **(A)** Zhang et al. (2020); **(B)** Shi et al. (2023). The horizontal lines are the same as those in Figure 5.

basically consistent. The β in cases 1 – 3 is 0.20, which is smaller than 0.55 in cases 4 – 5 with flexible vegetation. It is assumed that the parameter β is related to δ_I, which is the width of the mixing layer below the inflection point z_i. To ensure dimensional homogeneity, the width δ_I is nondimensionalized by the vegetation height H_v. Then, it becomes easy to establish the relationship between the δ and δ_I/H_v, which is $\frac{\delta_I}{H_v} = (1.63 \pm 0.31)$ β for cases 1 – 5 with flexible vegetation and $\frac{\delta_I}{H_v} = (4.10 \pm 0.30)$ β for cases 6 – 7 with rigid vegetation. The averaged velocity $\bar{U} = ((U_v + U_2)/2)$ in Table 4. Nikora et al. (2013) noted that $\bar{U} = U_i$ is only applicable to certain cases and has limited application scope. According to Table 4, with the exception of case 1, there are significant differences between the averaged velocity $\bar{U}$ and the measured U_i except case 1. In this study, we introduce a parameter β to obtain the U_i and give explicit expression for β. After introducing β, the calculated U_i agrees well with the measured U_i.

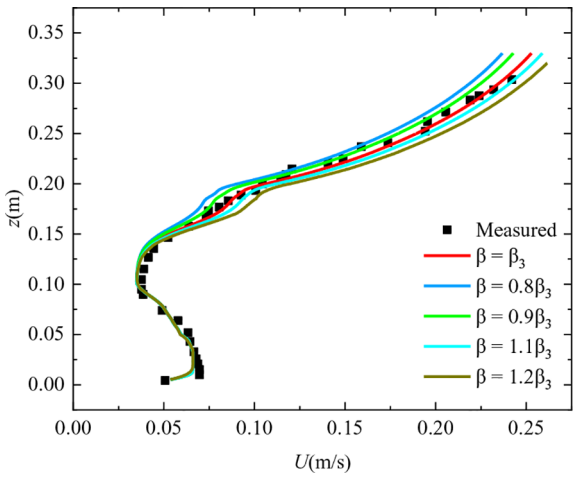

FIGURE 8
Sensitivity analysis of the parameter β for case 3. β_3 indicates the value of β in case 3. Lines of different colors represent velocity distribution obtained with different β in case 3.

6.5 Model limitations

It has been proven that the proposed model can be applied to predict the velocity profile in an open channel with submerged flexible/rigid vegetation. The relative submergence of the vegetation and vegetation density leads to the distinct flow structure and then the flow can be vertically divided into separate sublayers. However, for submerged vegetation existing in a river with larger relative submergence and small vegetation density, the width of the uniform layer can be ignored due to the penetration of the mixing layer. For vegetation with smaller relative submergence, the width of the logarithmic layer may decrease and even disappear due to the mixing layer, that is, the mixing layer may be close to the water surface. Given these two above conditions, the flow structure cannot be divided into three layers. More research is needed to explore the influence of relative submergence on the flow structure and velocity profile and then the theoretical model can be improved and applied in more complex cases.

7 Conclusion

The paper presents a model to study the vertical distribution of the velocity in an open channel with submerged flexible vegetation. The model divides the vegetated flow vertically into three layers: uniform velocity layer, mixing layer, and logarithmic layer. In the uniform velocity layer, the influence of vegetation resistance in the prediction of velocity is mainly considered. The vertical distribution of the longitudinal velocity in the mixing layer is similar to the hyperbolic

TABLE 4 Comparison between the calculated and measured velocity U_i.

Cases	1	2	3	4	5	6	7
Measured U_i(m/s)	0.110	0.090	0.063	0.260	0.250	0.030	0.125
Calculated U_i(m/s)	0.099	0.096	0.055	0.229	0.271	0.028	0.15
$\bar{U}$(m/s)	0.099	0.142	0.099	0.154	0.175	0.114	0.24
β	0.20	0.20	0.20	0.55	0.55	0.15	0.10

tangent profile, and the conventional logarithmic profile concept is applied in the free surface layer. To obtain the width of the mixing layer divided by the inflection point, a parameter is introduced and iteratively applied to determine the velocity at the inflection point. Due to the influence of momentum transport on the total flow depth, the method of velocity superposition is applied in the mixing layer and logarithmic layer, and then the analytical solution of the longitudinal velocity in the vertical direction can be obtained. According to the error analysis by comparing the predicted velocity with the experimental data, the maximum relative error is 7.12%, indicating that the predicted velocity is reliable. Aquatic vegetation in nature is usually distributed in random patches. Future research can put the focus on the vegetation arrangement, density, and relative submergence to enrich the application range of the presented model, which can be of assistance for ecological understanding such as sediment and pollutant transport.

Data availability statement

The original contributions presented in the study are included in the article/supplementary material. Further inquiries can be directed to the corresponding authors.

Author contributions

All authors made contributions to the conception and design of the study. Material preparation and data collection and analysis were performed by JZ, ZM, HW, WW, ZL, and MG. The first draft of the paper was completed by JZ, ZM, and HW, and all authors commented on previous versions of the manuscript and read and approved the final version.

Funding

The authors declare that this study received funding from the National Natural Science Foundation of China [grant numbers U2040208; 52109100; U2243222], the Joint Open Research Fund Program of State key Laboratory of Hydroscience and Engineering, and Tsinghua – Ningxia Yinchuan Joint Institute of Internet of Waters on Digital Water Governance [grant number sklhse-2023-Iow06], the Postdoctoral Research Foundation of China [grant number 2021M702643], and by Anhui Water Resources Development Co., Ltd. [grant number KY-2021-13]. The funder was not involved in the study design, collection, analysis, interpretation of data, the writing of this article or the decision to submit it for publication.

Conflict of interest

Author MG was employed by Anhui Water Resources Development Co., Ltd.

The remaining authors declare that the research was conducted in the absence of any commercial or financial relationships that could be construed as a potential conflict of interest.

Publisher's note

References

Bai, R., Bai, Z., Wang, H., and Liu, S. (2022a). Air-water mixing in vegetated supercritical flow: effects of vegetation roughness and water temperature on flow self-aeration. *Water Resour. Res.* 58, e2021WR031692. doi: 10.1029/2021WR031692

Bai, R., Ning, R., Liu, S., and Wang, H. (2022b). Hydraulic jump on a partially vegetated bed. *Water Resour. Res.* 58, e2022WR032013. doi: 10.1029/2022WR032013

Bai, G., Xu, D., Zou, Y., Liu, Y., Liu, Z., Luo, F., et al. (2022). Impact of submerged vegetation, water flow field and season changes on sediment phosphorus distribution in a typical subtropical shallow urban lake: water nutrients state determines its retention and release mechanism. *J. Environ. Chem. Eng* 10, 107982. doi: 10.1016/j.jece.2022.107982

Baptist, M. J., Babovic, V., Rodríguez Uthurburu, J., Keijzer, M., Uittenbogaard, R. E., Mynett, A., et al. (2007). On inducing equations for vegetation resistance. *J. Hydraul Res.* 45, 435–450. doi: 10.1080/00221686.2007.9521778

Baruah, A., Sarma, A. K., and Hinge, G. (2022). A semicoupled shallow-water model for vertical velocity distribution in an open channel with submerged flexible vegetation. *J. Irrig Drain Eng* 148, 06022005. doi: 10.1061/(ASCE)IR.1943-4774.0001704

Cheng, N. (2011). Representative roughness height of submerged vegetation. *Water Resour. Res.* 47, W08517. doi: 10.1029/2011WR010590

Cheng, N. (2015). Single-layer model for average flow velocity with submerged rigid cylinders. *J. Hydraul Eng* 141, 06015012. doi: 10.1061/(ASCE)HY.1943-7900.0001037

Coles, D. (1956). The law of the wake in the turbulent boundary layer. *J. Fluid Mech.* 1, 191–226. doi: 10.1017/S0022112056000135

Fu, H., Yang, K. L., Wang, T., and Guo, X. (2013). Analysis of parameter sensitivity and value for logarithmic velocity distribution formula. *J. Hydraul Eng* 44, 489–494. doi: 10.13243/j.cnki.slxb.2013.04.014

Huai, W., Han, J., Zeng, Y., An, X., and Qian, Z. (2009a). Velocity distribution of flow with submerged flexible vegetations based on mixing-length approach. *Appl. Math Mech-Engl* 30, 343–351. doi: 10.1007/s10483-009-0308-1

Huai, W., Zeng, Y., Xu, Z., and Yang, Z. (2009b). Three-layer model for vertical velocity distribution in open channel flow with submerged rigid vegetation. *Adv. Water Resour.* 32, 487–492. doi: 10.1016/j.advwatres.2008.11.014

Huai, W., Zhang, J., Katul, G. G., Cheng, Y., Tang, X., and Wang, W. (2019). The structure of turbulent flow through submerged flexible vegetation. *J. Hydrol* 31, 274–292. doi: 10.1007/S42241-019-0023-3

Hui, E., Jiang, C., and Pan, Y. (2009). Vertical velocity distribution of longitudinal flow in a vegetated channel. j. tsinghua univ. *Sci. Technol.* 49, 834–837. doi: 10.16511/j.cnki.qhdxxb.2009.06.017

Huthoff, F., Augustijn, D. C. M., and Hulscher, S. J. M. H. (2007). Analytical solution of the depth-averaged flow velocity in case of submerged rigid cylindrical vegetation. *Water Resour. Res.* 43, W06413. doi: 10.1029/2006WR005625

Järvelä, J. (2002). Flow resistance of flexible and stiff vegetation: a flume study with natural plants. *J. Hydrol* 269, 44–54. doi: 10.1016/S0022-1694(02)00193-2

Kironoto, B., and Graf, W. H. (1994). "Turbulence characteristics in rough uniform open-channel flow," in *Proceedings of the Institution of Civil Engineers - Water Maritime and Energy* 112(4), 336-348. doi: 10.1680/iwtme.1995.28114

Klopstra, D., Barneveld, H., Noortwijk, J., and Velzen, E. (1997). Analytical model for hydraulic roughness of submerged vegetation, American Society of Civil Engineers (ASCE), New-York. 775-780.

Kouwen, N., Unny, T. E., and Hill, H. M. (1969). Flow retardance in vegetated channels. *J. Irrig Drain Div.* 95, 329–342. doi: 10.1061/JRCEA4.0000652

Kowalski, J., and Torrilhon, M. (2017). Moment approximations and model cascades for shallow flow. *Commun. Comput. Phys.* 25, 669–702. doi: 10.4208/cicp.OA-2017-0263

Liu, C., Luo, X., Liu, X., and Yang, K. (2013). Modeling depth-averaged velocity and bed shear stress in compound channels with emergent and submerged vegetation. *Adv. Water Resour.* 60, 148–159. doi: 10.1016/j.advwatres.2013.08.002

Lou, S., Chen, M., Ma, G., Liu, S., and Wang, H. (2022). Sediment suspension affected by submerged rigid vegetation under waves, currents and combined wave–current flows. *Coast. Eng* 173, 104082. doi: 10.1016/j.coastaleng.2022.104082

Monin, A. S., and Yaglom, A. M. (1971). Statistical fluid mechanics: Mechanics of turbulence, Vol. 1, MIT Press, Boston.

Nepf, H. M. (1999). Drag, turbulence, and diffusion in flow through emergent vegetation. *Water Resour. Res.* 35, 479–489. doi: 10.1029/1998WR900069

Nepf, H. M. (2012). Hydrodynamics of vegetated channels. *J. Hydraul Res.* 50, 262–279. doi: 10.1080/00221686.2012.696559

Nepf, H., and Ghisalberti, M. (2008). Flow and transport in channels with submerged vegetation. *Acta Geophysica* 56, 753–777. doi: 10.2478/s11600-008-0017-y

Nepf, H. M., and Vivoni, E. R. (2000). Flow structure in depth-limited, vegetated flow. *J. Geophys. Res.* 105, 28547–28557. doi: 10.1029/2000JC900145

Nikora, V., Goring, D., McEwan, I., and Griffiths, G. (2001). Spatially averaged open-channel flow over rough bed. *J. Hydraul Eng* 127, 123–133. doi: 10.1061/(ASCE)0733-9429(2001)127:2(123

Nikora, V., McLean, S., Coleman, S., Pokrajac, D., McEwan, I., Campbell, L., et al. (2007). Double-averaging concept for rough-bed open-channel and overland flows: applications. *J. Hydraul Eng.* 133, 884–895. doi: 10.1061/(ASCE)0733-9429(2007)133:8(884

Nikora, N., Nikora, V., and O'Donoghue, T. (2013). Velocity profiles in vegetated open-channel flows: combined effects of multiple mechanisms. *J. Hydraul Eng* 139, 1021–1032. doi: 10.1061/(ASCE)HY.1943-7900.0000779

Pokrajac, D., Finnigan, J. J., Manes, C., McEwan, I., and Nikora, V. (2006). "On the definition of the shear velocity in rough bed open channel flows," in *River Flow 2006 (ed. by R. M. L. Ferreira, E. C. T. L. Alves, J. G. A. B. Leal and A. H. Cardoso), 89–98. Taylor & Francis Group, London, UK.*

Raupach, M., Finnigan, J., and Brunet, Y. (1996). Coherent eddies and turbulence in vegetation canopies: the mixing-layer analogy. *Boundary Layer Meteorol.* 78, 351–382. doi: 10.1007/978-94-017-0944-6_15

Ren, S., and Feng, M. (2020). Experimental study on hydraulic characteristics of open channel with flexible vegetation. *J. Water Resour. Water Eng.* 31, 186–192.

Righetti, M., and Armanini, A. (2002). Flow resistance in open channel flows with sparsely distributed bushes. *J. Hydrol* 269, 55–64. doi: 10.1016/S0022-1694(02)00194-4

Shi, H., Liang, X., Huai, W., and Wang, Y. (2019). Predicting the bulk average velocity of open-channel flow with submerged rigid vegetation. *J. Hydrol* 572, 213–225. doi: 10.1016/j.jhydrol.2019.02.045

Shi, Z., Pethick, J. S., and Pye, K. (1995). Flow structure in and above the various heights of a saltmarsh canopy: a laboratory flume study. *J. Coast. Res.* 11, 1204–1209.

Shi, H., Zhang, J., and Huai, W. (2023). Experimental study on velocity distributions, secondary currents, and coherent structures in open channel flow with submerged riparian vegetation. *Adv. Water Res* 173, 104406. doi: 10.1016/j.advwatres.2023.104406

Stone, B. M., and Shen, H. (2002). Hydraulic resistance of flow in channels with cylindrical roughness. *J. Hydraul Eng* 128, 500–506. doi: 10.1061/(ASCE)0733-9429(2002)128:5(500

Sun, X., and Shiono, K. (2009). Flow resistance of one-line emergent vegetation along the floodplain edge of a compound open channel. *Adv. Water Resour.* 32, 430–438. doi: 10.1016/j.advwatres.2008.12.004

Wang, H., Bai, Z., Bai, R., and Liu, S. (2022). Self-aeration of supercritical water flow rushing down artificial vegetated stepped chutes. *Water Resour. Res.* 58, e2021WR031719. doi: 10.1029/2021WR031719

Wang, D., Wang, X., and Li, D. (1998). Comparison of the distribution formula of mean flow velocity in open channel and analysis of influencing factors. (in Chinese) *J. Sediment Res.*, 3, 88–92. doi: 10.16239/j.cnki.0468-155x.1998.03.015

White, B. L., and Nepf, H. M. (2008). A vortex-based model of velocity and shear stress in a partially vegetated shallow channel. *Water Resour. Res.* 44, W01412. doi: 10.1029/2006WR005651

Wu, F., Shen, H. W., and Chou, Y. (1999). Variation of roughness coefficients for unsubmerged and submerged vegetation. *J. Hydraul Eng* 125, 934–942. doi: 10.1061/(ASCE)0733-9429(1999)125:9(934

Yang, K., Cao, S., and Knight, D. W. (2007). Flow patterns in compound channels with vegetated floodplains. *J. Hydraul Eng* 133, 148–159. doi: 10.1061/(ASCE)0733-9429(2007)133:2(148

Yang, W., and Choi, S. U. (2010). A two-layer approach for depth-limited open-channel flows with submerged vegetation. *J. Hydraul Res.* 48, 466 –475. doi: 10.1080/00221686.2010.491649

Yang, Z., Guo, M., and Li, D. (2022). Theoretical model of suspended sediment transport capacity in submerged vegetation flow. *J. Hydrol* 609, 127761. doi: 10.1016/j.jhydrol.2022.127761

Zhang, J., Lei, J., Huai, W., and Nepf, H. (2020). Turbulence and particle deposition under steady flow along a submerged seagrass meadow. *J. Geophysical Res: Oceans* 125, e2019JC015985. doi: 10.1029/2019JC015985

Zhang, J., Wang, W., Shi, H., Wang, W., Li, Z., Tang, X., et al. (2021). An analytical two-layer model for velocity distribution in open-channel flows with submerged flexible canopies considering multiply fluids mechanics. *J. Hydrol* 603, 127102. doi: 10.1016/j.jhydrol.2021.127102

frontiers | Frontiers in Marine Science

TYPE Original Research
PUBLISHED 09 June 2023
DOI 10.3389/fmars.2023.1211981

OPEN ACCESS

EDITED BY
Senlin Zhu,
Yangzhou University, China

REVIEWED BY
Hoang Tran,
Pacific Northwest National Laboratory (DOE), United States
Zhengjian Yang,
China Three Gorges University, China
Shaowei Wang,
Shandong University, China

*CORRESPONDENCE
Zhaowei Liu
liuzhw@tsinghua.edu.cn

RECEIVED 25 April 2023
ACCEPTED 30 May 2023
PUBLISHED 09 June 2023

CITATION
Duan Y, Liu Z and Li M (2023) Super-resolution reconstruction of sea surface pollutant diffusion images based on deep learning models: a case study of thermal discharge from a coastal power plant. *Front. Mar. Sci.* 10:1211981. doi: 10.3389/fmars.2023.1211981

Super-resolution reconstruction of sea surface pollutant diffusion images based on deep learning models: a case study of thermal discharge from a coastal power plant

Yafei Duan[1,2,3], Zhaowei Liu[1,2,3]* and Manjie Li[4]

[1]State Key Laboratory of Hydroscience and Engineering, Tsinghua University, Beijing, China, [2]Key Laboratory of Hydrosphere Sciences of the Ministry of Water Resources, Tsinghua University, Beijing, China, [3]Department of Hydraulic Engineering, Tsinghua University, Beijing, China, [4]Shenzhen International Graduate School, Tsinghua University, Shenzhen, China

While remote sensing images could convey essential information of surface water environment, the low spatial resolution limits their application. This study carried out a series of experiment tests of thermal discharge from a coastal power plant and constructed an image dataset HY_IRS, representing the transport and diffusion of discharged heated water in tidal waters. Two image super-resolution (SR) reconstruction models based on deep learning (DL), ESPCN and ESRGAN, were trained based on this dataset and then used to reconstruct high-resolution remote sensing images. It shows that the two DL models can markedly improve the spatial resolution of the surface diffusion image of thermal discharging, with the PSNR improved by 8.3% on average. The trained two models were successfully used to improve the spatial resolution of thermal infrared remote sensing SST images from Landsat8 TIRS, indicating that the SR model based on DL has a good effect and a crucial application prospect in the field of improving the resolution of pollutant diffusion remote sensing images.

KEYWORDS

super resolution (SR), deep learning, thermal discharge, transport and diffusion field, thermal infrared remote sensing

1 Introduction

Remote sensing images are an essential data source for surface environmental monitoring. However, their spatial resolution is generally low due to the long distance between sensor and observation object as well as the technical limitation of photosensitive device in camera. Table 1 summarizes the current thermal infrared d satellite remote

TABLE 1 Current thermal infrared satellite remote sensing images and their spatial resolutions.

Sensor	Satellite Platform	Number of Thermal Infrared Bands	Swath Width/km	Spatial Resolution/m
ASTER	EOS (USA)	5	60	90
TEM+/TM/LDCM TIRS	Landsat (USA)	1/1/2	185	60/120/100
IRMSS	CBERS-1/02 (China)	1	120	156
IRS	HJ-1A/B (China)	2	720	150 300
AVHRR	NOAA(USA)	3	2800	1100
MODIS	EOS(USA)	16	2330	1000
VIRR/MERSI	FY-3(China)	2	2800/2800	1100/250

sensing techniques, which involve surface temperature information. It can be found that their spatial resolution is around 0.1~1km (Hu et al., 2017). This low spatial resolution makes it unsatisfactory to meet the needs both in scientific research and engineering management. Specifically, the satellite remote sensing is supposed to assist in assessing the impact of thermal discharge by coastal power plants, but in reality the temperature rise area cannot be accurately determined due to the low spatial resolution of sensing images. In the case of near-surface field monitoring and indoor tests, industrial thermal infrared cameras are often used to photograph the thermal effluent dispersion patterns. However, due to the large size of the lens imaging unit of the uncooled thermal infrared imager, the low imaging pixels of the camera (currently, the number of pixels per side of the images produced by state-of-the-art industrial thermal infrared cameras at most 640). In most cases, it is often necessary to carry the camera on a platform far away from the test object (such as low-flying unmanned aerial vehicles) to capture the full-field patterns, resulting in failure to capture a clear and detailed thermal pollutant diffusion field from the sensing inversion images.

Super-resolution (SR) reconstruction refers to the technology focusing on constructing high-resolution (HR) images from low-resolution (LR) ones. SR techniques can be classified into three categories: reconstruction-based, sample learning-based, and deep learning (DL)-based (Tang et al., 2020; Xia et al., 2021). Among them, the f data-driven DL-based image super-resolution algorithms have been significantly improved since 2014, and subsequently applied in computer vision and image processing, which becomes the hotspot in SR research (Wang et al., 2020). The first DL-based SR model is the Super-Resolution Convolutional Neural Network (SRCNN) model based on a pure convolutional neural network proposed by Dong et al. (2014). In 2016, Shi et al. (2016) improved the SRCNN by introducing sub-pixel convolution layers and proposed the Efficient Sub-Pixel Convolutional Neural Network (ESPCN) model. The ESPCN model offers a computationally efficient solution by leveraging sub-pixel convolution layers, which perform upscaling in the feature space rather than the image space. This design significantly reduces computational complexity and memory requirements, allowing the model to perform super-resolution tasks at a much faster rate compared to the traditional methods. Subsequently, the Super-Resolution Generative Adversarial Network (SRGAN) model, combining residual networks and generative adversarial networks (GANs), has been developed with a more satisfactory performance. In 2018, Wang et al. (2018) proposed the Enhanced Super-Resolution GAN (ESRGAN) model, an extension of the SRGAN introducing several significant improvements, which includes a generator, a discriminator, and a feature extraction network. Recently, the application of a transformer-based approach was presented in (Lu et al., 2022), named the Efficient Super-Resolution Transformer, and it has also been successfully applied to image super-resolution reconstruction. Deep learning techniques continue to outperform traditional based algorithms in terms of efficiency and effectiveness due to end to end training (Bashir et al., 2021). Deep learning algorithms carry flexibility which could handle super resolution issue with different scale factors, blur kernels and noise levels inside a unified maximum a posteriori framework (Dawa et al., 2023). Overall, the ESPCN and ESRGAN models are currently the most advanced and widely-used SR models.

The fates of pollutants in water are dominated by the dynamic flow and the turbulent field, resulting in the chaotic but organized distribution patterns and boundaries (Figure 1A). However, the current ESPCN and ESRGAN SR models are usually developed for universal use and thus trained by diverse categories data (Figure 1B), consequently they cannot specifically address SR for pollutant diffusion images in natural waters. In recent years, DL has been applied to SR research on geographic remote sensing images (Dong et al., 2020; Li et al., 2020; Shen et al., 2020; Zhang et al., 2020; Guo et al., 2021). Nevertheless, the satellite images used for model training generally have a low resolution, resulting in an insufficient capture of the details of pollutant diffusion field such as the turbulent diffusion driven by small-scale vortices.

Taking the thermal discharge in cooling water from a coastal power plant as an example, this study aims to establish a thermal infrared imaging dataset for surface temperature measurement. The ESPCN and ESRGAN models were trained and tested to conduct SR research on the images of surface-water pollutants diffusion, and then applied to the satellite remote sensing images of thermal discharge from a coastal power plant to evaluate the effectiveness of image quality improvement by DL models.

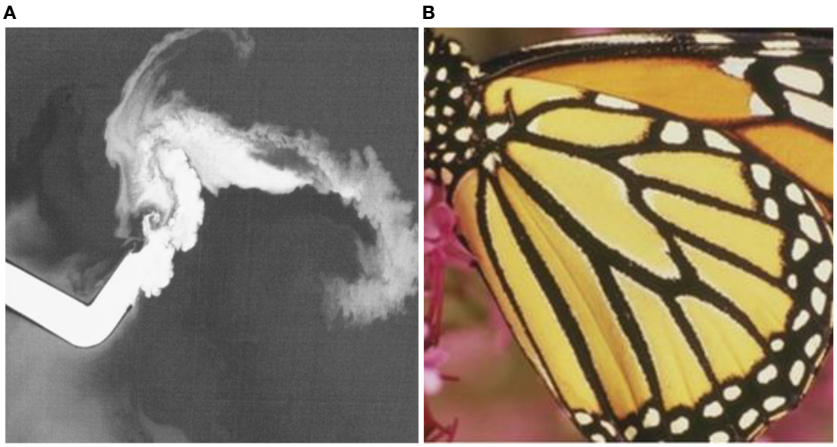

FIGURE 1
Typical distribution patterns of pollutant transport in natural waters **(A)** and a typical image (a butterfly image from the DIV2K dataset) used in DL SR model training **(B)**.

2 Thermal infrared image dataset of cooling water discharged from coastal power plants

The dataset used in this study consists of continuously-observed thermal infrared images in a physical test for the cooling water discharged from a coastal power plant. The power plant uses raw seawater for cooling, which is drawn vis a channel on the southeast side of the plant and discharged through another channel on the west side. The layout of the water intake and discharge can be found in Figure 2A. The study area locates in a typical irregular semi-diurnal tidal zone, with tidal durations of 346 minutes and 397 minutes for the flooding tide and ebbing tide periods, respectively.

A series of physical model experiments were conducted to study the thermal discharge. Experiment scenarios include two types of heat discharge, three types of tides (typical spring, moderate, and neap tides) in two seasons (winter and summer), and two types of open channel discharge schemes. The experiments were designed based on gravity and buoyancy similarity, with the detailed parameters shown in Table 2. The surface thermal diffusion field was obtained by the TVS-500EX thermal infrared camera (Produced by NEC Corporation of Japan), with a temperature detection sensitivity of 0.1 °C and an imaging size of 320×240 pixels. The camera was installed at a height of 7 meters above the water surface, and the shooting interval was 3 seconds in the experiment, corresponding to 1.64 minutes in the prototype. Some images captured by the camera are listed in Figure 2B. During the experiment, the ambient temperature in the lab was 4.1 °C, and the emissivity of water body was 0.97.

The experimentally acquired images were organized into a dataset named HY_IRS dataset including 10736 thermal infrared images of cooling water discharge under different experiment conditions was obtained. These images were converted into grayscale images with a resolution of 320×240 pixels and randomly divided into a training set (8701 images), a validation set (1535 images), and a test set (500 images). The training set samples were generated by down-sampling the original images with a 1/4 scaling factor (i.e., r=4).

During the summer of 2020, prototype monitoring of the sea surface temperature (SST) in the vicinity of the power plant was conducted using ship-based measurements, unmanned aerial

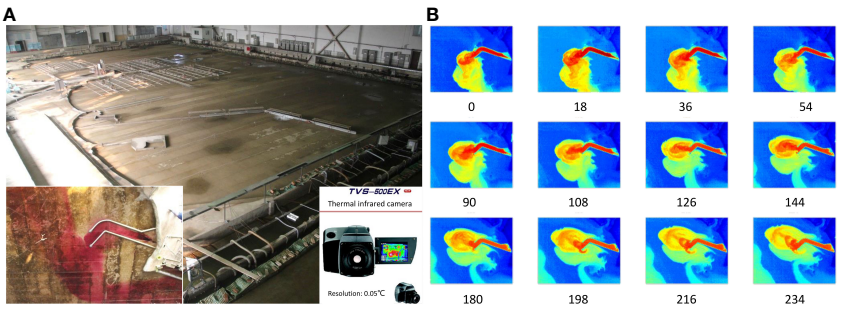

FIGURE 2
Physical model test of the thermal discharge from a coastal power plant **(A)**, and the thermal infrared images captured by TVB-500EX infrared thermal imager **(B)**.

TABLE 2 Design parameters of the physical test for thermal discharge from a coastal power plant.

Flow scale Q_r	Horizontal scale L_r	Vertical scale H_r	Time scale	Discharge temperature rise
4.732×10^5	360	120	32.863	8.1 °C
Prototype flow: 134/268 m^3/s	Prototype length and width: 21.6×14.5 km^2	Prototype maximum water depth: 12 m		
Model flow: 0.283/0.566 L/s	Model length and width: 40.4×60 m^2	Model maximum water depth: 10 cm		

vehicles, and satellite remote sensing. Seventeen cloudless satellite images (since the nuclear power plant has been in operation since October 2018) were obtained from Landsat8 TIRS. The C1 Level1 data products of thermal infrared bands 10 and 11 of the TIRS sensor were selected. The SST of the TIRS data was retrieved using the atmospheric correction method based on the radiative transfer equation and the atmospheric correction parameter calculator provided by National Oceanic and Atmospheric Administration of United States (NOAA) (Barsi et al., 2003), making use of the meteorological data collected from the local meteorological tower. The spatial resolution of the SST retrieval images from Landsat8 TIRS was 100 meters per pixel.

3 Model establishment and training

Through improving the ESPCN and ESRGAN architectures, SR models for thermal infrared diffusion images of cooling water discharge from the power plant were established.

3.1 ESPCN model

The DL-based ESPCN model proposed by Shi et al. (2016) was specifically designed for single-image SR tasks, with the primary objective of upscaling LR images to HR ones while retaining or even enhancing the perceptual quality. In its architecture, the feature maps are extracted in the LR space, and an efficient sub-pixel convolution layer which learns an array of upscaling filters to upscale the final LR feature maps into the HR output is introduced. The handcrafted bicubic filter in the SR pipeline is replaced with more complex upscaling filters specifically trained for each feature map, whilst reducing the computational complexity of the overall SR operation.

The underlying architecture of ESPCN comprises three key components: a convolutional feature extraction layer, a non-linear mapping layer, and a sub-pixel convolution layer.

Convolutional Feature Extraction Layer: The initial layer in the ESPCN model is dedicated to extracting essential features from the LR input image. This layer employs a set of convolutional filters, which are convolved with the input image to generate feature maps. The purpose of this process is to capture both local and global structures present in the image which are crucial for reconstructing the HR output.

Non-linear Mapping Layer: Following the feature extraction layer, the second layer aims to establish a non-linear mapping between the extracted features and the HR image representations. This layer consists of multiple convolutional filters which are applied to the previously generated feature maps. These filters are responsible for learning the complex relationships between the LR input and the HR output, enabling the model to effectively upscale the image.

Sub-pixel Convolution Layer: The final component of the ESPCN architecture is the sub-pixel convolution layer, also known as the upscaling or deconvolution layer. This layer performs a pixel-shuffle operation to rearrange the feature maps produced by the non-linear mapping layer into a HR output. The sub-pixel convolution layer ensures that the reconstructed image retains the spatial characteristics of the input image while minimizing computational complexity and memory usage.

In this study, MeanSquaredError was used as the loss function and the Adam was adopted as the optimizer with 0.001 learning rate. The architecture of the ESPCN model consists of three convolution layers for feature maps extraction, and a sub-pixel convolution layer that aggregates the feature maps from LR space and builds the SR image in a single step. The last layer is processed to convert the LR feature maps to a HR image. r=4 is referred to the upscaling ratio when downsample the image; n_l is the number of features at layer l, (where $l \in (1, L-1)$ for a network with L layers, L=5 in this model); $n_0 = 3$ is equal to the color channels of the image in this work. The output shapes of layer 1 to 5 are 1, 64, 64, 32, 16, 1, with 0, 1664, 36928, 18464, 4624, 0 parameters respectively. This architecture avoids upscaling LR image before feeding it into the network. It first applied a l layer convolutional neural network directly to the LR image, and then applied a sub-pixel convolution layer that upscaled the LR feature maps to produce SR image. After the input layer, one convolutional layer was added in accordance with Shi et al. (2016). The channel numbers of the three conventional 2D convolutional layers were 64, 64, and 32, respectively, with convolution kernel sizes of 5, 3, and 3, and finally follows a 2D convolutional layer with $r^2 = 42$ channels, with a kernel size of 3×3. The network was trained with input training images of size (320/4) × (240/4). The total number of network parameters was 61680.

3.2 ESRGAN model

ESRGAN introduces several enhancements to the original SRGAN model, such as the incorporation of the Residual-in-Residual Dense Block (RRDB) architecture, a relativistic discriminator, and an improved loss function that combines

perceptual, adversarial, and content losses. These innovations result in superior performance and the ability to generate HR images with enhanced perceptual quality, finer details, and fewer artifacts. The ESRGAN model consists of a generator, a discriminator, and a feature extraction network.

Generator: The generator in ESRGAN is responsible for producing HR images from the given LR inputs. The architecture of the generator is based on the RRDB design, which is an enhanced version of the residual dense block in the original SRGAN. RRDB incorporates a hierarchical residual learning mechanism to facilitate efficient information flow and gradient propagation, allowing the generator to capture both global and local features effectively. The generator consists of multiple RRDBs, followed by an upscaling layer that employs sub-pixel convolution to upscale the generated feature maps into an HR image.

Discriminator: The discriminator in ESRGAN is designed to distinguish the HR images generated by the generator from the ground truth HR images. The architecture of the discriminator is based on a deep convolutional neural network, which includes several convolutional, batch normalization, and Leaky ReLU activation layers. The primary objective of the discriminator is to guide the generator towards producing more realistic and perceptually convincing HR images.

Feature Extraction Network: In addition to the generator and discriminator, ESRGAN employs a feature extraction network to compute the perceptual loss during the training process. The perceptual loss is calculated as the difference between these extracted features, encouraging the generator to produce images with similar high-level structures and characteristics as the ground truth.

The ESRGAN model selects the optimal parameters trained on the bicubically down-sampled DIV2K dataset (https://tfhub.dev/captain-pool/esrgan-tf2/1). The network architecture used in this study is shown in Figure 3. Compared with the traditional SRGAN, this network removes all batch norm (BN) layers from residual block (RB) and replaces the original basic block with RRDB, which combines a multi-layer residual network and dense connection, and introduces a residual scaling factor β.

3.3 Loss function and evaluation metrics

As for the loss function design, the following three image training effect evaluation indicators are combined in the standard ESPCN model and ESRGAN model:

(1) Mean squared error (MSE) of image interpolation;

(2) Peak signal-to-noise ratio (PSNR),

$$PSNR = 10 \times log_{10}(\frac{(2n-1)^2}{MSE})$$

where n represents the bit depth of each pixel in the image, which is 8 in this study.

SR algorithms are typically evaluated by several widely-used distortion measures, such as *PSNR*. Compared with the subjective evaluation of images by human observers, *PSNR* is more objective in evaluating the effect of image signal processing (Ledig et al., 2017). Human visual quality is more sensitive to the low spatial frequencies and more sensitive to brightness compared to chromaticity. Besides, visual judgment could be easily affected by neighbouring pixels. Generally, for image reconstruction, a *PSNR* > 40 dB represents good quality, *PSNR* = 30~40 dB represents moderate quality, *PSNR* = 20~30 dB represents poor quality, and *PSNR*< 20 represents unacceptable quality.

(3) Hash fingerprint comparison between images

The hash fingerprints of the images are calculated using mean hash algorithm and difference hash algorithm. The main process is as follows: first, the image is converted to grayscale. In the mean algorithm, the mean value of grayscale within the whole image is calculated first; then traverse the gray value of each pixel, set it to 1 if it is greater than the mean value, and set it to 0 if it is less than the mean value, to form a fingerprint; finally, the similarities of corresponding pixels between the two images are compared, by calculating the proportion of the same number of pixels to the total number of pixels. In the difference algorithm, the pixel value is compared with the next pixel value in the order of rows and columns, and the greater is recorded as 1, and the smaller is recorded as 0, forming a fingerprint; finally, compare the similarities of the corresponding pixels of the two images, and

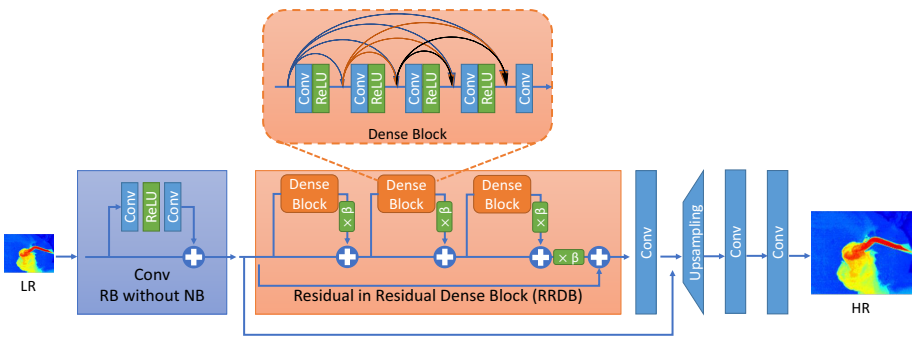

FIGURE 3
The network architecture of ESRGAN model in this work redrawn based on the model proposed by Wang et al. (2018). Residual in Residual Network consisting of convolution layers, residual in residual block (RB) as the trunk of the model, pixel shuffler layers, and the upscaling convolutional layers. All BN layers in RB are removed compared the standard SRGAN model, the RRDB block is added to replace the original basic block, and β is the residual scaling parameter.

count the proportion of the mean value of the same number to the total number of pixels.

3.4 Model training

The model was built using the DL framework TensorFlow 2.3.0. Model training and evaluation were conducted on an HP Z4G4 GPU workstation. The GPU parameters were NVIDIA Quadro RTX 4000, Cudnn 7.6.5 cuda10.1_0, RAM: 32.0GB, and Python 3.8.10.

During model training, the batch size was from 8 to 64, and EarlyStopping technique was used for regularization. The model was tested by training 20-100 epochs, and the model with the best performance in the last 100 batches was selected. The results showed that after 20 batches, the loss gradually stabilized, and the *PSNR* gradually increased to above 37, as shown in Figure 4A.

Fifty thermal infrared images, representing temperature fields on different tidal state, were selected from 500 images of temperature distribution under cooling water discharge. The ESPCN model was used to test the SR effect, and the traditional Bicubic method was used as the comparative baseline. The image quality of the model prediction was evaluated, as shown in Figure 5. The results showed that the average *PSNR* of the LR images obtained by Bicubic was 33.6, while the *PSNR* of the images reconstructed by the ESPCN model increased to 36.4, with an improvement in image resolution of 8.3%, as shown in Figure 4B. Although there is still some difference between "HR" and "ESPCN", it is clear that the reconstructed HR images are significantly closer to the original HR images. The transport-diffusion patterns shaped by tidal flow and turbulence, as well as the irregular edge of the heated water could be better restored.

4 SR of thermal infrared satellite remote sensing images

The optimal ESPCN model trained on the HY_IRS dataset and the ESRGAN model trained on the DIV2K dataset were used to reconstruct 4x super-resolution Landsat8 SST inversion images (for the selected 18 views from Oct. 2018 to Dec. 2022). Since no original high-resolution image is available for satellite remote sensing images, the bicubic interpolation method was used as a baseline for comparison. The PSNR of the ESPCN predicted images and Bicubic is 33.96 on average (with maximum value 34.64 and minimum value 33.39), while that of the ESRGAN predicted images and Bicubic is 28.96 on average. Figure 6A shows the SR effect of remote sensing images at 2:30 GMT on December 24, 2018. It shows that both the two DL models improve the spatial resolution of remote sensing images and ensure coherence with the original images and the bicubic reconstructed images.

The quantitative comparison and detailed analysis of the water surface temperature (SST) area, obtained by remote sensing before

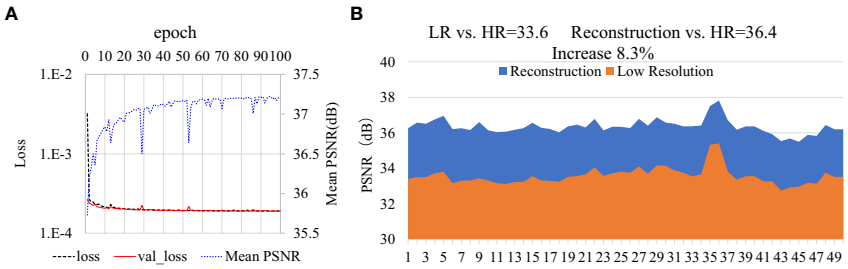

FIGURE 4
The training process of ESPCN model **(A)** and its result evaluation of *PSNR* for 50 selected test images **(B)**. The model was tested by training 100 epochs, and the model with the best performance in the last 100 batches was selected. The results showed that after 20 batches, the loss gradually stabilized, and the *PSNR* gradually increased to above 37, as shown in subfigure **(A)**. The val_loss (red line) is the value of cost function for the cross-validation data, and the loss (black dashed line) is the value of cost function for the training data. The mean *PSNR* for epoch is shown in blue dotted line. In subfigure **(B)**, the orange results represent *PSNR* of LR image and HR image, and the blue results represent *PSNR* of ESPCN reconstruction and HR.

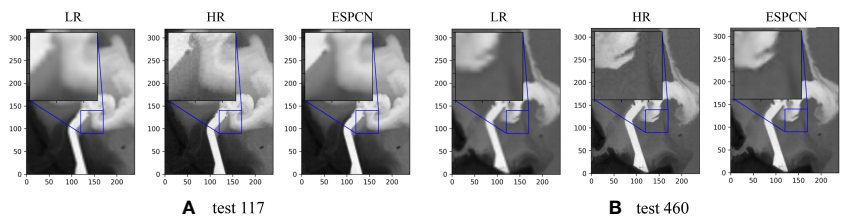

FIGURE 5
Two super-resolution reconstructed image samples by ESPCN model. As for the ebbing tidal image shown in **(A)**, the PSNR increase by 8.1% from 33.26 (LR vs. HR) to 35.95 (ESPCN vs. HR). As for the flooding tidal image shown in **(B)**, the PSNR increase by 10.6% from 32.91 (LR vs. HR) to 36.37 (ESPCN vs. HR).

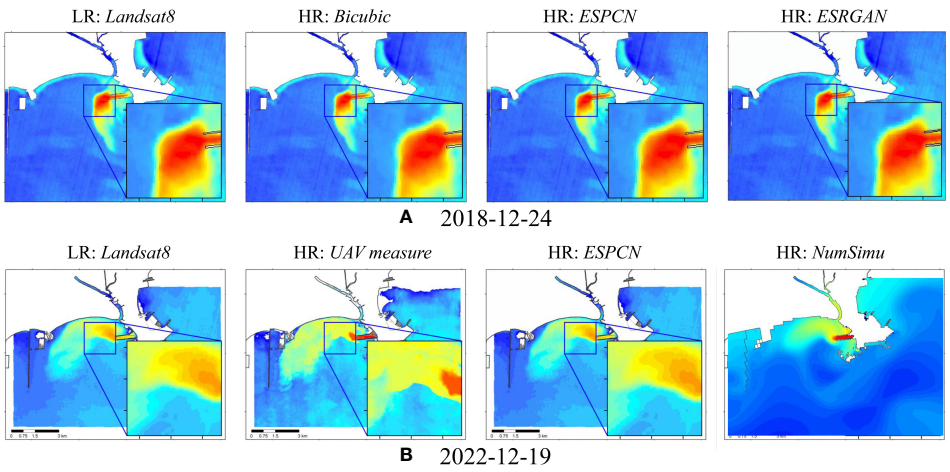

FIGURE 6
SR of Landsat8 TIRS thermal infrared satellite images based on DL models. Subfigure **(A)** shows the SR effect of remote sensing images at 2:30 GMT on December 24, 2018 based on ESPCN and ESRGAN; subfigure **(B)** compares the results obtained by all three methods, i.e., Landsat8 satellite remote sensing inversion, UAV remote sensing inversion, and numerical simulation.

and after SR, as well as by the *In-situ* observation and numerical simulation, were conducted. Take the results of SST field near the coastal power plant on December 19, 2022 as an example. At 2:30 am GMT, a low-spatial-resolution (100m) image of the SST field was obtained using Landsat8 satellite remote sensing inversion, and we refer to it as the LR *: Landsat8* Image. The image was inverted from the single-channel thermal infrared data on the satellite, through the atmospheric impact correction by method of MODTRAN atmospheric radiative transfer model. Simultaneously, we carried out thermal infrared remote sensing survey using a low-altitude UAV (with the Optris PI640 thermal infrared imager on board) and obtained a HR (1.2m) image of the SST field, and we refer to it as the *UAV measure* image. Both the inversion SST results obtained by satellite and UAV remote sensing were calibrated using a large number of direct measurements at the sea surface. Also, a SST three-dimensional numerical simulation was carried out using the Delft3D model (Deltares, FLOW2D3D Version 6.03.00.64634). In the simulation, meteorological data were obtained from the monitoring data at the power plant site and the reanalysis data CFSv2 of the National Centers for Environmental Prediction (NCEP). The corresponding simulation result is denoted as *NumSimu*. Finally, we reconstructed the 4x high-resolution image from the input of LR *: Landsat8* Image by the trained ESPCN model that discussed above.

The results obtained by all the above methods are compared in Figure 6B. These areas of different temperature ranges (within the 134 km^2 observation area) of all the methods are quantitatively analyzed for comparison, shown in Figure 7. Statistically, there are some visible differences between the statistical results of temperature areas obtained by low-resolution satellite remote sensing and that by the high-resolution UAV remote sensing. The mean relative error of temperature areas (from ≥0 to ≥015 °C) is -28.4%. At the same time, it can be found that the statistical area values of different temperature intervals of the images after SR reconstruction by DL model are closer to the high-resolution UAV real-world results. The mean relative error of temperature areas reduced to -11.4%. In contrast, the errors of temperature areas in the result of the numerical simulation are significantly larger, with an average relative error of 50.2%. Even some obviously difference in distribution shape of the temperature rise can be seen. It is understandable that the numerical simulations yielded poor results, since the numerical simulation of coastal water temperature is always a difficult task. There are many sources of errors in the simulation, such as numerical errors, inaccurate input meteorological conditions, errors in the calculation for tidal flow and surface heat exchange, etc. The use of DL models to improve image resolution has proven to be a very effective and fast way to achieve the goal of improving the statistical accuracy of SST remote sensing data.

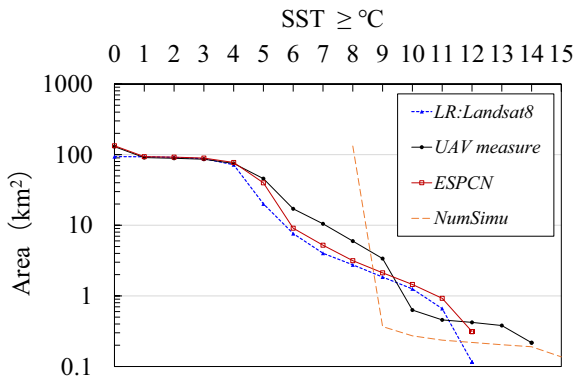

FIGURE 7
Quantitatively comparison in areas of different temperature ranges on 2022-12-19, acquired by different methods. LR *: Landsat8* Image: the low-spatial-resolution (100m) image of the SST field from Landsat8 satellite remote sensing inversion; the *UAV measure* image: a high-spatial-resolution (1.2m) image of the SST field acquired by the thermal infrared remote sensing survey using a low-altitude UAV; *NumSimu*: a SST three-dimensional numerical simulation was carried out using the Delft3D model; HR *: ESPCN:* the 4x reconstructed HR image from the input of LR *: Landsat8* Image by the trained ESPCN model.

5 Conclusion

In conclusion, the study carried out a series of physical tests of thermal discharge from a coastal power plant and built an image dataset HY_IRS, representing the pollutant transport and diffusion in tidal waters. Two SR models based on deep learning, ESPCN and ESRGAN, were trained based on this dataset. Dataset HY_IRS is designed to facilitate the development of SR models for thermal infrared images of cooling water discharge, which is of great significance for improving the accuracy of water pollution surveys and providing effective support for water environmental management.

Targeted training of deep learning-based image SR models using thermal infrared images of wastewater discharge experiments can effectively capture the distribution morphology of pollutant transport and diffusion in tidal waters and enhance spatial resolution for images of such substance diffusion fields. The average improvement of the spatial resolution of images is up to 8.3%. Quantitatively comparison in areas of different temperature ranges given by satellite and UAV remote sensing inversion, as well as a numerical model indicates that the use of DL models to improve image resolution has proven to be a very effective and fast way to achieve the goal of improving the statistical accuracy of SST remote sensing data. Deep learning models trained on thermal infrared images of thermal discharge experiments can be used for spatial resolution enhancement of satellite remote sensing inversed images of the surface water environment.

Data availability statement

The original contributions presented in the study are included in the article/supplementary materials, further inquiries can be directed to the corresponding author/s.

Author contributions

YD and ZL contributed to conception and design of the study. YD organized the database, performed the statistical analysis, and wrote the first draft of the manuscript. ML improved the English writing. All authors contributed to the article and approved the submitted version.

Funding

This study was supported by the National Key Research and Development Program of China under grant No. 2022YFC3203903, the National Natural Science Foundation of China under grant No. 42206214 and No. 52179083.

Conflict of interest

The authors declare that the research was conducted in the absence of any commercial or financial relationships that could be construed as a potential conflict of interest.

Publisher's note

References

Barsi, J. A., Barker, J. L., and Schott, J. R. (2003). "An atmospheric correction parameter calculator for a single thermal band earth-sensing instrument," in *IGARSS 2003. 2003 IEEE International Geoscience and Remote Sensing Symposium. Proceedings (IEEE Cat. No. 03CH37477)*, Vol. 5. 3014–3016 (Denver, Colorado, USA: IEEE).

Bashir, S. M. A., Wang, Y., and Khan, M. (2021). A comprehensive review of deep learning-based single image super-resolution. *PeerJ Computer Sci.* 7, e621. doi: 10.7717/peerj-cs.621

Dawa, C. L., Bhawna, G., Ayush, D., and Goyal, V. (2023). Image super-resolution: a comprehensive review, recent trends, challenges and applications. *Inf. Fusion* 91, 230–260. doi: 10.1016/j.inffus.2022.10.007

Dong, C., Loy, C. C., He, K., and Tang, X. (2014). "Learning a deep convolutional network for image super-resolution," in *Computer vision–ECCV 2014: 13th European conference, Zurich, Switzerland, September 6-12, 2014, proceedings, part IV 13* (Zurich, Switzerland: Springer International Publishing), 184–199.

Dong, X., Sun, X., Jia, X., Xi, Z., Gao, L., and Zhang, B. (2020). Remote sensing image super-resolution using novel dense-sampling networks. *IEEE Trans. Geosci. Remote Sens.* 59 (2), 1618–1633. doi: 10.1109/TGRS.2020.3041211

ESRGAN *Enhanced super-resolution generative adversarial networks [2] TF 2.0 implementation of ESRGAN*. Available at: https://tfhub.dev/captain-pool/esrgan-tf2/1.

Guo, D., Xia, Y., Xu, L., Li, W., and Luo, X. (2021). Remote sensing image super-resolution using cascade generative adversarial nets. *Neurocomputing* 443, 117–130. doi: 10.1016/j.neucom.2021.02.026

Hu, D., Kun, Q., Xingling, W., Limin, Z., and Guohua., Ji (2017). Comparison of three single-window algorithms for retrieving land-surface temperature with landsat 8 TIRS data. *Geomatics Inf. Sci. Wuhan Univ.* 42 (7), 869–876. doi: 10.13203/j.whugis20150164

Ledig, C., Theis, L., Huszár, F., Caballero, J., Cunningham, A., Acosta, A., et al. (2017). "Photo-realistic single image super-resolution using a generative adversarial network," in *Proceedings of the IEEE conference on computer vision and pattern recognition*. (Honolulu, Hawaii, USA: IEEE), 4681–4690.

Li, J., Cui, R., Li, B., Song, R., Li, Y., Dai, Y., et al. (2020). Hyperspectral image super-resolution by band attention through adversarial learning. *IEEE Trans. Geosci. Remote Sens.* 58 (6), 4304–4318. doi: 10.1109/TGRS.2019.2962713

Lu, Z., Li, J., Liu, H., Huang, C., Zhang, L., Zeng, T., et al. (2022) in *Proceedings of the IEEE Conference on Computer Vision and Pattern Recognition Workshops (CVPRW 2022)*. (New Orleans, LA, USA: IEEE)

Shen, H., Lin, L., Li, J., Yuan, Q., and Zhao, L. (2020). A residual convolutional neural network for polarimetric SAR image super-resolution. *ISPRS J. Photogrammetry Remote Sens.* 161, 90–108. doi: 10.1016/j.isprsjprs.2020.01.006

Shi, W., Caballero, J., Huszár, F., Totz, J., Aitken, A. P., Bishop, R., et al. (2016). "Real-time single image and video super-resolution using an efficient sub-pixel convolutional neural network," in *Proceedings of the IEEE conference on computer vision and pattern recognition*. (Las Vegas, NV, USA: IEEE), 1874–1883.

Tang, Y.-Q., Hong, P., Ya-Ping, Z., and Xin-De., Li (2020). A survey of image super-resolution reconstruction. *Acta Electronica Sin.* 48 (7), 1407–1420. doi: 10.3969/j.issn.0372-2112.2020.07.002

Wang, Z., Chen, J., and Hoi, S. (2020). Deep learning for image super-resolution: a survey. *IEEE Trans. Pattern Anal. Mach. Intell.* PP (99), 1–1. doi: 10.1109/TPAMI.2020.3015213

Wang, X., Yu, K., Wu, S., Gu, J., Liu, Y., Dong, C., et al. (2018). "Esrgan: enhanced super-resolution generative adversarial networks," in *Proceedings of the European conference on computer vision (ECCV) workshops*. (Munich, Germany: Springer International Publishing), 0–0.

Xia, H., Hongfeng, L., Jun, L., and Nian., C. (2021). Survey on deep learning based image super-resolution. *Comput. Eng. Appl.* 57 (24), 51–60. doi: 10.3778/j.issn.1002-8331.2105-0418

Zhang, D., Shao, J., Li, X., and Shen, H. T. (2020). Remote sensing image super-resolution via mixed high-order attention network. *IEEE Trans. Geosci. Remote Sens.* 59 (6), 5183–5196. doi: 10.1109/TGRS.2020.2969764

frontiers | Frontiers in Marine Science

TYPE Original Research
PUBLISHED 16 June 2023
DOI 10.3389/fmars.2023.1182823

OPEN ACCESS

EDITED BY
Alberto Basset,
University of Salento, Italy

REVIEWED BY
Jiancai Deng,
Chinese Academy of Sciences (CAS), China
Arda Özen,
Cankiri Karatekin University, Türkiye

*CORRESPONDENCE
Qingchuan Chou
chouqc@ihb.ac.cn

RECEIVED 09 March 2023
ACCEPTED 15 May 2023
PUBLISHED 16 June 2023

CITATION
Tian Y, Lv C, Huang L, Shan H, Wang H, Wen Z, Yin C, Chou Q, Zhang X, Ni L and Cao T (2023) Seasonal variation and nutrient jointly drive the community structure of macrophytes in lakes with different trophic states.
Front. Mar. Sci. 10:1182823.
doi: 10.3389/fmars.2023.1182823

Seasonal variation and nutrient jointly drive the community structure of macrophytes in lakes with different trophic states

Yuqing Tian[1,2], Chaochao Lv[1,2], Liangliang Huang[3], Hang Shan[1,2], Hao Wang[1,2], Zihao Wen[1], Chengjie Yin[1], Qingchuan Chou[1]*, Xiaolin Zhang[1], Leyi Ni[1] and Te Cao[1]

[1]State Key Laboratory of Freshwater Ecology and Biotechnology, Institute of Hydrobiology, Chinese Academy of Sciences, Wuhan, China, [2]University of Chinese Academy of Sciences, Beijing, China, [3]The Guangxi Key Laboratory of Theory and Technology for Environmental Pollution Control, Guilin University of Technology, Guilin, China

Introduction: Macrophytes are essential for maintaining the health of shallow lake ecosystems, however, the driving and responsive relationship between ecological factors (such as seasonal changes and nutrition, etc.) and plant communities is not yet clear.

Methods: In this study, we conducted seasonal surveys of macrophyte community composition in lakes with different nutrient states, aiming to understand the incidence relation between macrophyte community diversity, seasonal changes and environmental factors.

Results: According to the classification criteria of comprehensive nutritional index, there were significant differences in the trophic status of the three lakes. Among them, the Xihu Lake has reached mild eutrophication with a *TLI* value of 56.33, both Cibi Lake and Haixihai Lake are mesotrophic with *TLI* value of 36.03 and 33.48, respectively. The results of diversity analysis showed a significant negative correlation between α-diversity (include Species richness, Shannon-Wiener index, Simpson index and Pielou index) and lake nutrient status. Among them, Xihu Lake showed the lowest α-diversity in all seasons, Haixihai Lake exhibited the middle α-diversity, Cibi Lake indicated the highest α-diversity. Non-metric multidimensional ordination showed that there were obvious spatial structures differences among the macrophyte communities in the three lakes. Macrophyte community composition in the three lakes was more similar in summer and autumn, but there was a wider gap in spring and winter. The redundancy analysis indicated distinct differences between diversity index and ecological factors, the eigenvalues of Axis 1 and Axis 2 being, respectively, 36.13% and 8.15%. Environmental factors could explain 44.8% of the total variation in macrophyte communities structure. Among these, nitrogen, phosphorus, water

transparency and water temperature contributed 50.2%, 3.5%, 3.8% and 27.5%, respectively.

Conclusions: In summary, the community structure of macrophytes in plateau shallow lakes is co-regulated by seasons and nutrients.

KEYWORDS

macrophyte community, trophic state, environmental factors, plateau shallow lakes, α-diversity

1 Introduction

The composition of macrophyte communities has a great impact on lake ecosystems, especially in shallow lakes (Carpenter and Lodge, 1986; Blindow et al., 1998; Sondergaard et al., 2013), as they not only limit sediment resuspension (Zuccarini et al., 2011), and also play a crucial role in sediment flow, accumulation and stability (Carpenter, 1980). They are responsible for an important part of the primary productivity of the lakeshore zone, providing complex habitats and food for aquatic organisms, ranging from macroinvertebrates to mammals (Schneider, 2007; Liu et al., 2014). In shallow lakes, they are particularly important as they can contribute to transparency (Mjelde and Faafeng, 1997; Zuccarini et al., 2011). Macrophyte communities can also contribute to a clear lake state through various self-reinforcing feedback mechanisms (Scheffer and Carpenter, 2003), as they can control phytoplankton growth (Scheffer, 1998). Its occurrence and structure depend on environmental factors such as light conditions and nutrient availability (Mjelde and Faafeng, 1997; Nagengast and Kuczynska-Kippen, 2015) and the economic development of lakes and their use of catchments (Kissoon et al., 2013). Degradation of macrophytes due to water quality decline is a typical result of eutrophication and degradation of shallow lakes in all climatic regions, usually from a clear-water state dominated by macrophytes to a stable turbid water state (Moss, 1990; Jin et al., 2006; Klimaszyk et al., 2015). In particular, the change in water nutrition has been proven to significantly alter the species richness and diversity of plants and animals (Thiebaut and Muller, 1998). This means that lake eutrophication will lead to changes in the structure of macrophyte communities.

The reality is that the degradation of macrophyte communities in shallow lakes has been accelerating globally in response to an increasing anthropogenically-driven eutrophication in recent decades (Jeppesen et al., 1998; Scheffer, 1998; Zhang et al., 2017). In China, the majority of lakes have been affected by eutrophication and water quality degradation as a result of social development and other human activities (Cheng and Li, 2006; Qin et al., 2013). Consequently, the diversity of macrophyte communities in lakes has been negatively affected, leading to a disruption in the ecological balance of the lake (Sand-Jensen et al., 2000; Hilt and Gross, 2008; Bornette and Puijalon, 2011; Alahuhta et al., 2013; Qin et al., 2013). In order to restore the health of lakes and promote their beneficial effects on human survival, the restoration of aquatic ecosystems, especially the restoration of macrophytes, has become a top priority (Zhang et al., 2012; Wang et al., 2016). However, the changes in macrophyte communities are affected by both biological and abiotic factors in nature, such as nutritional constraints, seasonal changes, light availability, and the relationship with fish and algae (Irfanullah and Moss, 2004; Bornette and Puijalon, 2011; Alahuhta et al., 2013; Li et al., 2015; Wang et al., 2016). Therefore, it is essential to adopt sustainable management and effective recovery for macrophytes (Peretyatko et al., 2009).

Substantial studies have investigated the differences in macrophyte communities with varying nutrient levels, such as long term monitoring in Europe has found that species richness in moderately eutrophic lakes is higher than that in low or high eutrophic waters, eutrophic lakes support more species than malnourished or nutrient poor waters (Rorslett, 1991). However, it has also been reported that the submerged flora in eutrophic lakes decreased (Rorslett, 1991). In Finnish naturally oligotrophic lakes, eutrophication typically increases the species richness of aquatic flora (Leka et al., 2008). Among the environmental driving factors, nutrient enrichment is the main factor affecting the composition of macrophyte communities in lakes (Wang et al., 2014; Phillips et al., 2016; Gerdol et al., 2018; Salgado et al., 2018a; Wang et al., 2020). Coupled with water transparency and competition from phytoplankton, eutrophication not only filters out species that are not well adapted to stress, but may also exclude functionally similar species (Arthaud et al., 2012; Fu et al., 2017; Salgado et al., 2018b). At the same time, it has been found that indirect facilitation can prevent the decline of aquatic plant diversity in freshwater ecosystems threatened by eutrophication (Le Bagousse-Pinguet et al., 2012). In eutrophic lakes in China, nitrogen content and water transparency are important factors affecting aquatic plants. Restoring submerged vegetation is a feasible method to improve water environment and enhance ecological function (Ye et al., 2018). However, few studies have tested the macrophyte communities of shallow lakes on the plateau, especially those with different nutrients in the same basin. An enhanced understanding of these response mechanisms of macrophytes under eutrophication will provide useful information for the management of macrophytes.

To examine the diversity and driving factors of macrophyte communities in plateau water bodies of different trophic states, we conducted field surveys on three lakes located in Yunnan Province,

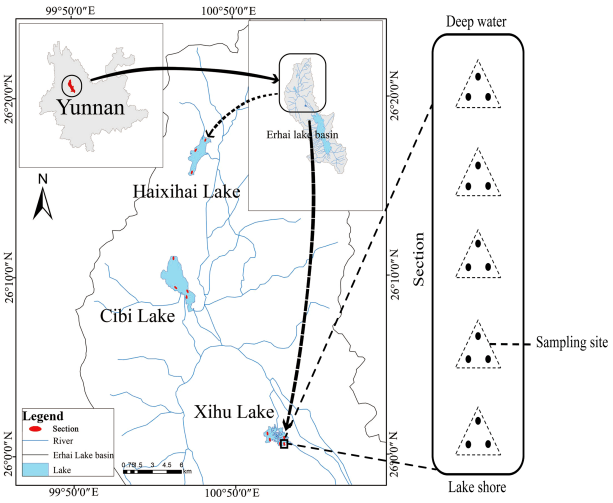

FIGURE 1
Location of sample distribution.

China. We main concern: (1)What is the nutritional status of the three lakes? And what impact will it have on the diversity and community structure of macrophyte? (2)Which ecological factors play an important role in regulating the structure of macrophyte community?

2 Materials and methods

2.1 Study area

The three studied lakes (Xihu Lake, Cibi Lake and Haixihai Lake; 25°25′-26°16′N, 99°32′-100°27′E) are located in Dali Bai Autonomous Prefecture, the northwest of Yunnan Province, China (Figure 1, Table 1). They are located in the Lancang River Basin, which is located in mid-subtropical southwest monsoon climate zone. (Chen and Wu, 2020; Li et al., 2020). These three lakes are all connected to Erhai Lake through rivers, which making them an important water source for the Erhai Lake. As the upstream lake, Xihu Lake flows into the Erhai Lake through the Luoshi River, while Cibi Lake and Haixihai Lake flow into the Erhai Lake through the Miju River. It is affected by the Indian Ocean climate. Rainfall is unevenly distributed throughout the year, with approximately 80% occurring from May to October, and the annual average rainfall is 994.2 mm. The multiyear average temperature is 14.6 °C (Zheng et al., 2021).

2.2 Macrophyte community

Macrophytes were sampled in three lakes, with 5 (Xihu Lake), 4 (Cibi Lake) and 3 (Haixihai Lake) sections. For each section we start at a depth of 1 m with a depth gradient of 0.5m, until no plants were present by using a rotatable reaping hook with a diameter 0.5m and area of 0.2m^2. Each Sampling, three times at per water depth site (Figure 1). All collected samples were washed before identified. Then the plants were dried, and weighed to determine the biomass. Every three months of sampling were conducted from June 2020 to March 2022, corresponding to spring, summer, autumn, and winter, respectively. In order to ensure that as many plants as possible were present in our survey, the cross section of each lake was evenly distributed along the shoreline. A total of 33 macrophyte species were recorded during the survey period (Appendix 1).

2.3 Environmental factor

We collected water samples at each sampling section. They were collected from a mixture of subsamples taken from the surface (below 0.2m of water surface), middle (the middle of the water depth at that site), and bottom layers (0.5 m above sediment surface) of the water column. The water transparency (SD) was used by Secchi disk to determine onsite. At the same time, water temperature (T), dissolved oxygen (DO), Salinity (SAL), and pH were measured at a water depth of 0.5 m using a YSI Professional Plus Water Quality Monitor (YSI Inc., Yellow Springs, Ohio, USA). Water samples were placed in a cooler and sent to a laboratory for testing as soon as possible. Analysis indicators included total nitrogen (TN), total phosphorus (TP), ammonium (NH_4-N), and phytoplankton chlorophyll a (Chl.a) according to relevant detection methods (Huang et al., 1999). A total of 9 environmental driver variables were included.

2.4 Data analysis

The comprehensive nutrient index method was used to evaluate lake eutrophication (Jin, 1995). The formula for calculating the comprehensive nutritional status index is as follows:

$$TLI(Chl.a) = 10\,(2.5 + 1.086\,ln\,\mathrm{Chl.a})$$

$$TLI(TP) = 10\,(9.436 + 1.624\,ln\,\mathrm{TP})$$

$$TLI(TN) = 10\,(5.453 + 1.694\,ln\,\mathrm{TN})$$

$$TLI(SD) = 10\,(5.118 - 1.94\,ln\,\mathrm{SD})$$

$$TLI(\Sigma) = W(\mathrm{Chl.a}) \times TLI(\mathrm{Chl.a}) + W(\mathrm{TP}) \times TLI(\mathrm{TP}) + W(\mathrm{TN}) \times TLI(\mathrm{TN}) + W(\mathrm{SD}) \times TLI(\mathrm{SD})$$

TABLE 1 Basic condition of the three lakes.

	Elevation(m)	Area(m^2)	Maximum depth(m)	Mean depth(m)	Volume(m^3)
Xihu Lake	1967.8	4.66	8.3	2-3	1.8×10^7
Cibi Lake	2055.7	8.5	32	11	9.3×10^7
Haixihai Lake	2015.0	2.6	16	10	2.2×10^7

In the formula, *W* (Chl.a), *W* (TP), *W* (TN), *W* (SD) are 0.3260, 0.2300, 0.2192, 0.2246, respectively. Lake nutrient status is graded from 0 to 100: *TLI* (Σ)≤30, poor nutrition; 30≤*TLI* (Σ)≤50, medium nutrition; 50≤*TLI* (Σ)≤60, mild eutrophication; 60≤*TLI* (Σ)≤70, moderate eutrophication; 70≤*TLI* (Σ)≤100, highly eutrophication.

The α-diversity index was used to measure the taxonomic diversity attributed to each lake, while the diversity was measured by the Species richness (*S*), Shannon-Wiener index (*H'*), Simpson index (*D*) and Pielou index (*J'*). To examine the α-diversity index of the macrophyte community in different lakes, the one-way ANOVA was used to test the differences of macrophyte community diversity between the three lakes.

To test the similarity of macrophyte communities in different lakes, the non-metric multidimensional scaling (NMDS) was used to visualize the overall differences using the "vegan" package.

The relationships between the diversity indices and the environmental parameters were defined using direct gradient analysis, with the CANOCO 5 program. And the redundancy analysis (RDA) was chosen to further test the potential effects of the environmental parameters on the diversity indices. Forward selection of variables was used to provide a ranking of the relative importance of specific variables and to avoid colinearity.

All data were tested for normality and homogeneity before analysis, and log (x+1) or log (1/x) conversion was performed on data that did not meet the above conditions. The significance levels were all set to $p<0.05$. All the statistical analyses were completed by R statistical package (vegan), SPSS 22.0 software and Origin 2021.

3 Results

3.1 Water environmental factors and nutrient levels of different lakes

The one-way ANOVA showed that except for NH_4-N and T indicators, there was strong heterogeneity among the physicochemical factors of water in different lakes (Table 2). The mean values have little difference. The average concentrations of TN and TP in the three lakes were between 0.25-1.10 mg/L and 0.02-0.09 mg/L, respectively. One-way ANOVA showed that there were significant differences in TN and TP between the Xihu Lake and other lakes. The Chl.a concentration was significantly different among the three lakes, with Cibi Lakes and Haixihai Lake had 4.23 ug/L and 4.36 ug/L, respectively, while Xihu Lake had a much higher concentration of 34.83 ug/L. Regarding SD, there were also significant differences between the Xihu Lake and the other two lakes, with Xihu Lake having a much lower SD of only 1.21 m compared to the other two lakes with SD values of 3.72 m and 3.59 m, respectively. In addition to the above indicators, all three lakes had higher DO and the mean values ranged form 7.78-8.64 mg/L. And there were significant differences between the Xihu Lake and the Cibi Lake. In terms of SAL, the highest of 0.22 belongs to the Xihu Lake, and the Cibi Lake had 0.18. The Haixihai Lake had the lowest of 0.11. The three studied lakes were all alkaline with a mean pH range of 8.34-8.73.

The comprehensive nutrient index method showed that the three lakes had different nutrition level (Table 3). Among them, the Xihu Lake of eutrophic index is between 50-60, of the mean value of the nutrient index was 56.33. As a result, it has reached the standard of a mildly entrophication lake. The eutrophication index of the other two lakes ranges from 30 to 40, of which the mean value of the nutrient index of the Cibi lake and the Haixihai lake was 36.03 and 33.48, respectively. These two lakes are classified as medium nutrition lakes.

3.2 Change of α-diversity index of different lakes

This study showed that the α-diversity index of different lakes had hump-shape relationships with seasons (Figure 2), and there were significant differences among lakes ($p<0.05$). For the three lakes, the α-diversity index of Xihu Lake was the lowest and that of Cibi Lake was the highest in each of the four seasons. Both showed a lower trend in spring and winter, and a higher trend in summer and autumn.

TABLE 2 Environmental factors of the three lakes.

Variables	Xihu Lake (Mean ± SD)	Cibi Lake (Mean ± SD)	Haixihai Lake (Mean ± SD)
NH_4-N(mg/L)	0.06 ± 0.03^{a}	0.06 ± 0.04^{a}	0.05 ± 0.03^{a}
TN(mg/L)	1.10 ± 0.30^{a}	0.34 ± 0.13^{b}	0.25 ± 0.11^{b}
TP(mg/L)	0.09 ± 0.03^{a}	0.03 ± 0.02^{b}	0.02 ± 0.01^{b}
Chl.a(ug/L)	34.83 ± 20.88^{a}	4.23 ± 2.35^{b}	4.36 ± 2.19^{b}
SD(m)	1.21 ± 0.70^{b}	3.72 ± 1.21^{a}	3.59 ± 0.89^{a}
T(°C)	18.53 ± 4.15^{a}	19.58 ± 4.00^{a}	18.42 ± 3.79^{a}
DO(mg/L)	8.64 ± 1.83^{a}	7.78 ± 1.20^{b}	8.06 ± 1.39^{ab}
SAL	0.22 ± 0.03^{a}	0.18 ± 0.02^{b}	0.11 ± 0.01^{c}
pH	8.43 ± 0.43^{ab}	8.34 ± 0.66^{b}	8.73 ± 0.76^{a}

Different letters in horizontal direction indicate that the value has significant difference among different of lakes ($p< 0.05$)

10.3389/fmars.2023.1182823

TABLE 3 Nutrient levels in three lakes during different seasons.

	March *TLI*(Σ)	June *TLI*(Σ)	September *TLI*(Σ)	December *TLI*(Σ)	Nutrition level
Xihu Lake	50.44	56.91	61.24	56.74	mild eutrophication
Cibi Lake	38.59	38.39	33.81	33.31	medium nutrition
Haixihai Lake	35.24	30.86	35.04	32.76	medium nutrition

For the mean species richness, the minimum value of Xihu Lake was 3 in winter and the maximum value was 6 in summer. The minimum value of Haixihai Lake appeared in spring, which was 6, and the maximum value appeared in autumn, which was 9. The minimum value of Cibi Lake was 9 in spring and autumn, and the maximum value was 11 in autumn (Figure 2A). The maximum value of Cibi Lake was about 2 times higher than that of Xihu Lake.

Simpson index mean resulted that the lowest value of Xihu Lake was 0.13 in winter and the highest value was 0.38 in summer. The lowest value of Haixihai Lake was 0.32 in spring, and the highest value was 0.53 in summer. The lowest value of Cibi Lake was 0.58 in spring, and the highest value was 0.78 in autumn (Figure 2B).

The research on the Shannon-Wiener index mean showed that Xihu Lake was the minimum of the three lakes. Its lowest value was 0.26 in winter, and its highest value was 0.72 in summer. The lowest value of Haixihai Lake was 0.63 in spring and the highest value was 1.07 in summer. And Cibi Lake was the largest of the three lakes, the lowest value was 1.25 in spring, and the highest value was 1.70 in autumn (Figure 2C).

The Pielou index indicated that the minimum value of Xihu Lake was 0.22, which appeared in autumn, and the maximum value was 0.41, which appeared in summer. The minimum value of Haixihai Lake was 0.36, which appeared in spring, and the maximum value was 0.54, which appeared in summer. The minimum value of Cibi Lake was 0.58, which appeared in spring, and the maximum value was 0.73, which appeared in autumn (Figure 2D).

The results of diversity analysis showed a significant negative correlation between α-diversity and lake nutrient status (Appendix 2). The difference of the three lakes in that although the change trend was the same, the seasonal differences of the maximum value of different diversity indexes were different. In terms of the mean species richness, the Xihu Lake reached its maximum in summer, while Haixihai Lake and Cibi Lake reached their maximum in autumn. For Simpson index, Shannon-Wiener index and Pielou index, the Xihu Lake and Haixihai Lake reached the maximum in summer, while the Cibi Lake reached the maximum in autumn.

3.3 Macrophyte communities in functional space of different lakes

Non-metric multidimensional ordination (NMDS) showed that there were obvious spatial structures differences among the macrophyte communities in the three lakes (Figure 3).

In terms of seasons, the community samples of the three lakes in spring and winter were far away from each other, indicating that the macrophyte communities structure were quite different in these two seasons. The stress coefficients of the spatial structures of macrophyte communities in the two seasons were 0.1299 and 0.1398, respectively. The results of NMDS analysis were basically reliable. In summer and autumn, the spatial structures of macrophyte communities in the three lakes were more similar, especially in Haixihai Lake and Cibi Lake, indicating that there was little difference in the structure of

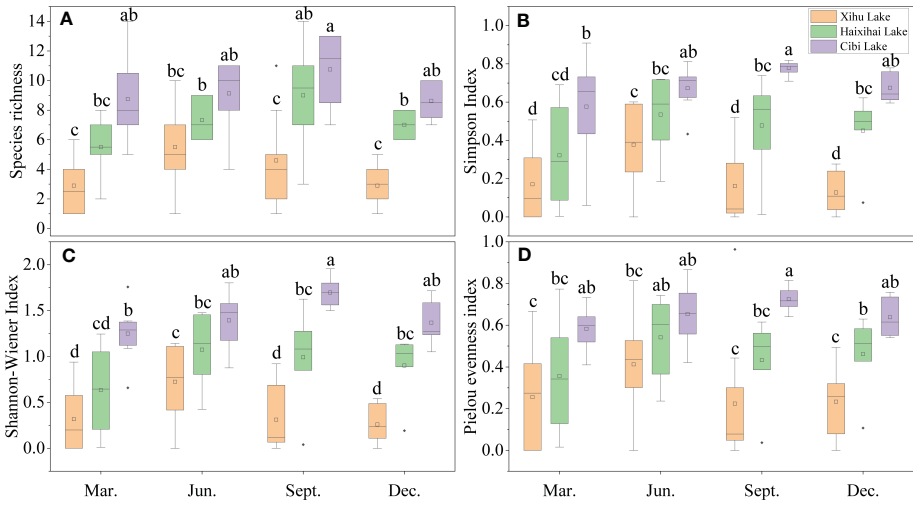

FIGURE 2
Seasonal variation of macrophytes aquatic plant a-diversity index in the three lakes. Different lowercase letters indicate a significant difference ($p<0.05$). **(A)** (Species richness), **(B)** (Simpson index), **(C)** (Shannon-Wiener index), **(D)** (Pielou index). Spring (March), Summer (June), Autumn (September), Winter (December), the same in Figure 3.

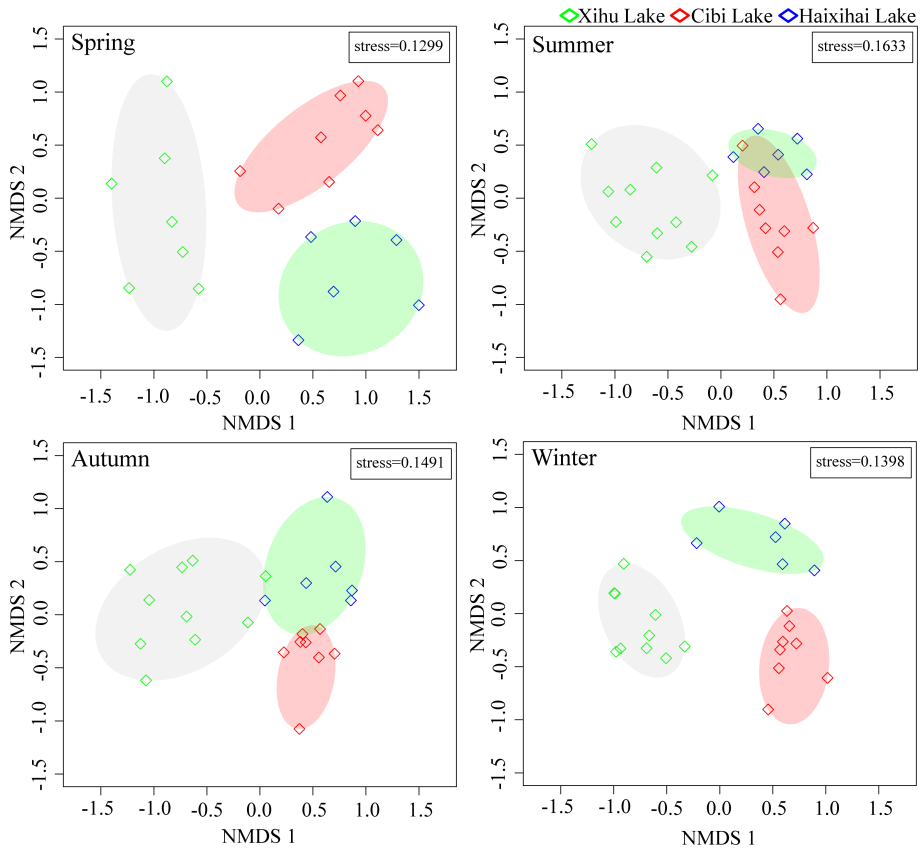

FIGURE 3
Non-metric multidimensional scaling results of three lakes in different seasons.

macrophyte communities between the two seasons. The stress coefficients of the spatial structures of macrophyte communities in the two seasons were 0.1633 and 0.1491, respectively. The results of NMDS analysis were also reliable.

3.4 Macrophyte communities and environmental drivers

RDA results showed that the environmental driving factors of the three lakes vary significantly across seasons, as well as between lakes (Figure 4). Throughout the year, the RDA indicated distinct differences between diversity index and ecological factors, the eigenvalues of Axis 1 and Axis 2 being, respectively, 36.13% and 8.15%. Environmental factors could explain 44.8% of the total variation in macrophyte communities structure. Among these, nitrogen, phosphorus, water transparency and water temperature contributed 50.2%, 3.5%, 3.8% and 27.5%, respectively.

The RDA analysis results in spring showed that the eigenvalues of the first two axis were 52.16% and 7.68%, respectively. Environmental factors could explain 60.7% of the total variation in macrophyte communities structure. Among these, nitrogen, phosphorus, water transparency and water temperature contributed 32.7%, 3.4%, 0.2% and 13.3%, respectively.

The eigenvalues of the first two axis of RDA analysis in summer were 42.29% and 8.17%, respectively. Environmental factors could explain 54.6% of the total variation in macrophyte communities structure. Among these, nitrogen, phosphorus, water transparency and water temperature contributed 6.3%, 54.6%, 0.4% and 4.0%, respectively.

The eigenvalues of the first two axis of RDA analysis in autumn were 47.32% and 5.68%, respectively. Environmental factors could explain 55.0% of the total variation in macrophyte communities structure. Among these, nitrogen, phosphorus, water transparency and water temperature contributed 64.4%, 1.1%, 7.3% and 4.2%, respectively.

The eigenvalues of the first two axis of RDA analysis in winter were 70.5% and 4.81%, respectively. Environmental factors could explain 77.2% of the total variation in macrophyte community structure. Among these, nitrogen, phosphorus, water transparency and water temperature contributed 74.6%, 2.6%, 5.4% and 9.3%, respectively.

These results indicated that the ranking could better reflect the relationship between environmental factors and macrophyte communities indicators. Based on the RDA analysis of macrophyte communities and environmental factors in the three lakes during the four seasons, our research showed that for the three lakes, TN and TP had a positive correlation effect on the macrophyte communities in the Xihu Lake, while a negative correlation effect on the Haixihai Lake

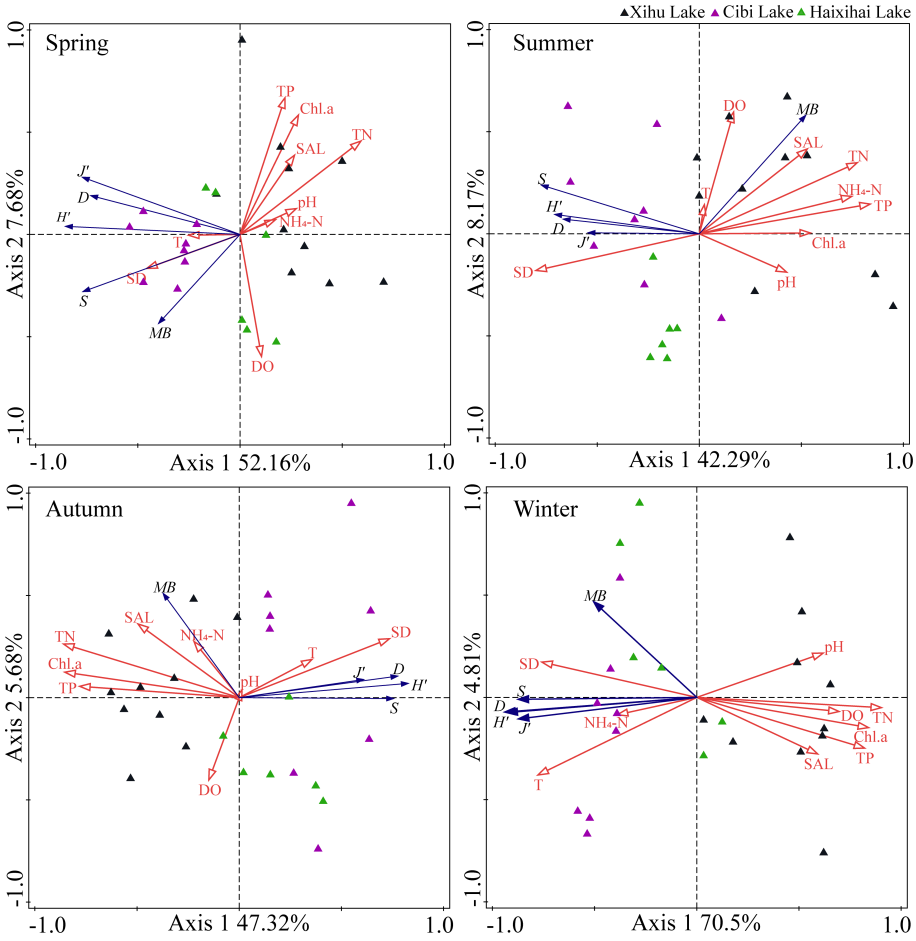

FIGURE 4
Redundancy analysis (RDA) for macrophyte communities and environmental factors in different seasons. *S* (Species richness), *H'* (Shannon-Wiener index), *D* (Simpson index), *J'* (Pielou index), *MB* (Mean biomass), SD (water transparency), pH (hydrogen ion concentration), T (water temperature), DO (dissolved oxygen), SAL (Salinity), TN (total nitrogen), TP (total phosphorus), NH_4-N (ammonium), Chl.a (phytoplankton chlorophyll a).

and Cibi lake. In different seasons, SD and T were not the key factors affecting community biomass in summer and autumn (June and September), but the key factors affecting community biomass were various nutrients. In winter and spring (December and March), SD and T were the key factors affecting community biomass, and the effect of nutrients on community biomass was not the main factor.

4 Discussion

Previous studies have shown that transparency and lake nutrient status significantly affect the species diversity and biomass of submerged plants (Ye et al., 2018; Wang et al., 2022). It is well known that the relationship between water quality and macrophytes is mutually beneficial (Bornette and Puijalon, 2011). Macrophytes are strongly influenced by a variety of water quality parameters and sediment characteristics (Alahuhta et al., 2013). In addition, macrophytes can help improve water quality by absorbing nutrients from water and sediment and by preventing sediment suspension (Jeppesen et al., 1998). Owing to lake eutrophication, phytoplankton biomass will increase and water transparency will decrease. This also leads to the species richness of habitats from mesotrophic to eutrophic is higher, while the species richness of oligotrophic, malnourished and eutrophic ultra eutrophic water bodies is lower (Rorslett, 1991; Toivonen and Huttunen, 1995; Murphy, 2002). In fact, ultra eutrophic lakes that are heavily shaded by phytoplankton may lack submerged vegetation, even almost none in the coastal zone (Morris et al., 2003; RodrÃGuez-Gallego et al., 2010). The transparency of 13 eutrophic lakes in Denmark decreases with the increasing total phosphorus concentration. In the eutrophication process of Taihu lake, the richness and area of large plant species decreased (Qin et al., 2013). A study of 60 lakes in the United Kingdom and Poland found that macrophyte diversities with increasing nitrogen concentration, particularly nitrate nitrogen concentration in winter, followed by phosphorus concentration (James et al., 2005). These studies have demonstrated that eutrophication in lakes can lead to a series of changes in the physical and chemical properties of water bodies, which in turn affect the diversity of macrophytes. The evidence produced by this study suggested that the three lakes, Xihu Lake, Haixihai Lake and

Cibi Lake, which belong to the same watershed, exhibit obvious heterogeneity in their nutrient composition, such as nitrogen, phosphorus contents and chlorophyll concentration, etc. In general, the contents of TN, TP and Chl.a in the Xihu Lake were higher than those in the other two lakes. And the SD was significantly lower than that of the other two lakes. As a mildly eutrophication lake, the α-diversity index of Xihu Lake were the lowest compared with the other two medium nutrition lakes. It also proved that eutrophication and water transparency had a significant effect on the diversity of aquatic plants. In this study, we found that the seasons in which the same α-diversity index reached its highest value were different in different lakes. This may be due to the different trophic states of different lakes. Chla, SD, etc. vary with the seasons. And due to the differences in nutrient status of lakes, the composition of macrophytes varies, the different growth requirements of different species, and the differences in competition among species. Therefore, in order to maintain the health of lake ecosystem, it is necessary to ensure the diversity of macrophyte. It is important to restore the health of lake and slow down or even eliminate the process of eutrophication in lakes.

NMDS analysis revealed that the characteristics of macrophyte communities in the three lakes were more similar in summer and autumn. Moreover, among the four seasons, the Haixihai Lake and the Cibi lake had closer similarities. Community structure is also affected by variations of ambient temperature (Lacoul and Freedman, 2006). In the plateau area of the northern hemisphere, there are obvious seasonal changes. For a long time, people have a clear understanding of the existence of their own living habits of macrophytes. The growth of macrophytes requires sufficient light and temperature conditions. Due to insufficient light and low water temperature in winter and spring, only a few macrophytes with low survival threshold survive in the lake, with low biomass and richness. Conversely, in summer and autumn, enhanced light and increased water temperature create favorable conditions for the rapid growth of large aquatic plants. Therefore, the species richness of the three lakes increases, and the community characteristics are similar. Based on the results of this study, the Haixihai Lake and the Cibi Lake were mesotrophic lakes with similar hydrological conditions and physical and chemical properties, resulting in similar in the community characteristics of macrophytes.

Studies have shown that the macrophyte communities in lakes are mainly affected by eutrophication parameters, and the species richness of lakes with low nutrient levels is higher than that of lakes with high nutrient levels, which is mainly related to TN, TP (Szoszkiewicz et al., 2014). *Littorella uniflora* is restricted to low phosphorus habitats, while *Lemna minor*, *Spirodela polyrhiza* and *Zanichellia palustris* require medium to high phosphorus concentrations (Heegaard et al., 2001; Trei and Pall, 2004). However, the distribution of *Isoetes lacustris*, *Lemna minor*, and *Myriophyllum alterniflorum* is influenced by integrated gradients of nitrogen, phosphorus, and sometimes other nutrients (Heegaard et al., 2001; Rubio et al., 2003; Paal and Trei, 2004). Studies have also revealed that N has a significantly adverse effect on the growth of submerged plants when TP concentration is not high (Olsen et al., 2015). Our research showed that increased nitrogen and phosphorus in mesotrophic lakes like the Haixihai Lake and the Cibi Lake decreases the abundance of macrophytes, resulting in changes in ecosystem structure. This is consistent with the results of previous studies. However, the relationship between N, P and macrophytes in the Xihu Lake was opposite to that in the other two lakes. This may be because Xihu Lake has an average water depth of only 2-3m, whereas the other two lakes have an average water depth of approximately 10m. Therefore, under the conditions of water eutrophication and high transparency, the large aquatic plants in the Xihu Lake allow different submerged plant species to replace each other along the environmental gradient of water temperature, light availability and wave exposure from shallow to deep water (Vestergaard and Sand-Jensen, 2000). Among lakes, macrophytes are not only limited by nutrients, but their biomass and distribution often change with the variations of water physical properties, such as transparency and temperature (Chambers and Kalff, 1985; Dale, 1986; Royle and King, 1991). The RDA results showed that in summer and autumn, SD and T were not the key factors affecting biomass, and nutrients played a decisive role in biomass. In winter and spring, on the contrary, SD and T become the key factors determining biomass, while nutrients are not the key factors. Some studies have found that in lakes after submerged vegetation restoration, the SD of water bodies with vegetation in summer is higher than that of water bodies without vegetation (Ye et al., 2018), and the water temperature in summer and autumn reaches the growth threshold suitable for large aquatic plants. This indicates that during summer and autumn, SD and T are not limiting factors. At this time, macrophytes grow rapidly and need ample nutrient support. Water nutrients have become a limiting factor. In winter and spring, due to seasonal fluctuations, changes in climatic and hydrological characteristics, the development of macrophytes basically stagnates in winter. In spring, the temperature and water temperature rise, the days grow longer, and when the light is sufficient, the biomass of macrophytes increases (Champion and Tanner, 2000; Riis et al., 2003). Therefore, the biomass is limited by SD and T during this time. Seasonal changes bring about changes in environmental factors (SD, T, etc.). In the process of change, macrophyte growth still needs to obtain sufficient nutrients. Therefore, throughout the year, although nutrients and seasons alternations play a major role, they also jointly drive the community structure of macrophytes.

In addition to the above environmental factors, those not covered in this paper, such as lake area, lake shoreline length, shoreline morphology, water flow rate and physical characteristics of sediment, etc., may also have an impact on large plant community. Generally speaking, the longer length of lake shoreline, the more complex morphology of lake shoreline and the larger lake area, the higher diversity of macrophytes plants and the higher biomass (Kent et al., 1982). At the same time, the water flow rate may affect the growth of aquatic plant, thus affecting the reproduction and growth of macrophytes plant, leading to a decline in species diversity and biomass (Biggs, 1996). The physical characteristics of sediment usually affect the growth of macrophytes plant by influencing their

rooting. These factors increase the heterogeneity of habitats, so they can provide more suitable habitats for macrophytes plant and affect large plant community.

5 Conclusion

In conclusion, we have conducted a study on the changes in diversity and environmental drivers of aquatic macrophyte communities in shallow eutrophic lakes on the plateau. It was found that the α-diversity of lakes with different nutrient types differs significantly, and the macrophyte communities of lakes with the changes of seasons makes more similar. Additionally, RDA analysis was employed to investigate the effects of environmental factors on macrophyte communities, which confirmed that nutrients were still the key factors affecting macrophytes in eutrophic plateau lakes, and SD and T also proved to play a key role in eutrophic plateau lakes. Seasons and nutrients jointly drive changes in the structure of macrophyte community. Therefore, more attention needs to be paid to the eutrophication of plateau lakes in the future, and adopt various measures to reduce pollution output and slow down the eutrophication rate of lakes. The research results can provide reference for the ecological restoration and lake health management of eutrophic plateau lakes in the future.

Data availability statement

The original contributions presented in the study are included in the article/supplementary material. Further inquiries can be directed to the corresponding author.

Author contributions

YT is the primary author who analyzed the datasets, generated results, and wrote the draft. CL is mainly responsible for data collection. LH and HS contributed to the data collection. WH provided critical technique support. ZW and CY helped interpret the results. QC contributed to the manuscript review and editing and provided comments for the data analyses. XZ and LN provided constructive suggestions in the manuscript. TC was responsible for the overall design of the work and provided constructive suggestions in the discussion section. All authors provided comments and suggestions for the manuscript revision. All authors contributed to the article and approved the submitted version.

Funding

This work was supported by the National Natural Science Foundation of China (32101319, 31930074, 32071574), and the Research funds of The Guangxi Key Laboratory of Theory and Technology for Environmental Pollution Control (Guikeneng2001K007).

Conflict of interest

The authors declare that the research was conducted in the absence of any commercial or financial relationships that could be construed as a potential conflict of interest.

Publisher's note

All claims expressed in this article are solely those of the authors and do not necessarily represent those of their affiliated organizations, or those of the publisher, the editors and the reviewers. Any product that may be evaluated in this article, or claim that may be made by its manufacturer, is not guaranteed or endorsed by the publisher.

References

Alahuhta, J., Kanninen, A., Hellsten, S., Vuori, K.-M., Kuoppala, M., and Hamalainen, H. (2013). Environmental and spatial correlates of community composition, richness and status of boreal lake macrophytes. *Ecol. Indic.* 32, 172–181. doi: 10.1016/j.ecolind.2013.03.031

Arthaud, F., Vallod, D., Robin, J., and Bornette, G. (2012). Eutrophication and drought disturbance shape functional diversity and life-history traits of aquatic plants in shallow lakes. *Aquat. Sci.* 74, 471–481. doi: 10.1007/s00027-011-0241-4

Biggs, B. (1996). Hydraulic habitat of plants in streams. *Regulated. Rivers. Res. Manage.* 12, 131–144. doi: 10.1002/(SICI)1099-1646(199603)12:2/3<131::AID-RRR385>3.0.CO;2-X

Blindow, I., Hargeby, A., and Andersson, G. (1998). *Alternative stable states in shallow lakes: what causes a shift?* (New York: Springer).

Bornette, G., and Puijalon, S. (2011). Response of aquatic plants to abiotic factors: a review. *Aquat. Sci.* 73, 1–14. doi: 10.1007/s00027-010-0162-7

Carpenter, S. R. (1980). The decline of *Myriophyllum spicatum* in a eutrophic Wisconsin lake. *Can. J. Botany-Revue. Can. Botanique.* 58, 527–535. doi: 10.1139/b80-064

Carpenter, S. R., and Lodge, D. M. (1986). Effects of submersed macrophytes on ecosystem processes. *Aquat. Bot.* 26, 341–370. doi: 10.1016/0304-3770(86)90031-8

Chambers, P. A., and Kalff, J. (1985). Depth distribution and biomass of submersed aquatic macrophyte communities in relation to secchi depth. *Can. J. Fisheries. Aquat. Sci.* 42, 701–709. doi: 10.1139/f85-090

Champion, P. D., and Tanner, C. C. (2000). Seasonality of macrophytes and interaction with flow in a new Zealand lowland stream. *Hydrobiologia* 441, 1–12. doi: 10.1023/A:1017517303221

Chen, J., and Wu, C. (2020). Evaluation of ecological sensitivity in erhai lake basin, southwest China. *IOP. Conf. Series.: Earth Environ. Sci.* 612 (1), 012072. doi: 10.1088/1755-1315/612/1/012072

Cheng, X., and Li, S. (2006). An analysis on the evolvement processes of lake eutrophication and their characteristics of the typical lakes in the middle and lower reaches of Yangtze river. *Chin. Sci. Bull.* 51 (013), 1603–1613. doi: 10.1007/s11434-006-2005-4

Dale, H. M. (1986). Temperature and light-the determining factors in maximum depth distribution of aquatic macrophytes in Ontario, Canada. *Hydrobiologia* 133, 73–77. doi: 10.1007/BF00010804

Fu, H., Zhong, J., Fang, S., Hu, J., Guo, C., Lou, Q., et al. (2017). Scale-dependent changes in the functional diversity of macrophytes in subtropical freshwater lakes in south China. *Sci. Rep.* 7 (1), 8294. doi: 10.1038/s41598-017-08844-8

Gerdol, R., Brancaleoni, L., Lastrucci, L., Nobili, G., Pellizzari, M., Ravaglioli, M., et al. (2018). Wetland plant diversity in a coastal nature reserve in Italy: relationships with salinization and eutrophication and implications for nature conservation. *Estuaries. Coasts.* 41, 2079–2091. doi: 10.1007/s12237-018-0396-5

Heegaard, E., Birks, H. H., Gibson, C. E., Smith, S. J., and Wolfe-Murphy, S. (2001). Species-environmental relationships of aquatic macrophytes in northern Ireland. *Aquat. Bot.* 70, 175–223. doi: 10.1016/S0304-3770(01)00161-9

Hilt, S., and Gross, E. M. (2008). Can allelopathically active submerged macrophytes stabilise clear-water states in shallow lakes? *Basic. Appl. Ecol.* 9, 422–432. doi: 10.1016/j.baae.2007.04.003

Huang, X. ,. F., Chen, W. M., and Cai, Q. M. (1999). *Survey, observation and analysis of lake ecology.Standard methods for observation and analysis in Chinese ecosystem research network, series V* (Beijing: Standards Press of China).

Irfanullah, H. M., and Moss, B. (2004). Factors influencing the return of submerged plants to a clear-water, shallow temperate lake. *Aquat. Bot.* 80, 177–191. doi: 10.1016/j.aquabot.2004.07.010

James, C., Fisher, J., Russell, V., Collings, S., and Moss, B. (2005). Nitrate availability and hydrophyte species richness in shallow lakes. *Freshw. Biol.* 50, 1049–1063. doi: 10.1111/j.1365-2427.2005.01375.x

Jeppesen, E. S., Sondergaard, M., Sondergaard, M., and Christoffersen, K. (1998). "The structuring role of submerged macrophytes in lakes," in *Ecological studies* (New York: Springer), 1–423.

Jin, X. (1995). *Lake environment in China* (Beijing (in Chinese): Ocean Press).

Jin, X., Xu, Q., and Yan, C. (2006). Restoration scheme for macrophytes in a hypertrophic water body, wuli lake, China. *Lakes. Reservoirs.: Res. Manage.* 11, 21–27.

Kent, C., Wong, J.J.C.J.O.F., and Sciences, A. (1982). An index of littoral zone complexity and its measurement. *Can J Fish Aquat Sci.* 39, 847–853. doi: 10.1139/f82-115

Kissoon, L. T. T., Jacob, D. L., Hanson, M. A., Herwig, B. R., Bowe, S. E., and Otte, M. L. (2013). Macrophytes in shallow lakes: relationships with water, sediment and watershed characteristics. *Aquat. Bot.* 109, 39–48. doi: 10.1016/j.aquabot.2013.04.001

Klimaszyk, P., Piotrowicz, R., and Rzymski, P. (2015). Changes in physico-chemical conditions and macrophyte abundance in a shallow soft-water lake mediated by a great cormorant roosting colony. *J. Limnol.* 74, 114–122. doi: 10.1111/j.1440-1770.2006.00291.x

Lacoul, P., and Freedman, B. (2006). Environmental influences on aquatic plants in freshwater ecosystems. *Environ. Rev.* 14, 89–136. doi: 10.1139/a06-001

Le Bagousse-Pinguet, Y., Liancourt, P., Gross, N., and Straile, D. (2012). Indirect facilitation promotes macrophyte survival and growth in freshwater ecosystems threatened by eutrophication. *J. Ecol.* 100, 530–538. doi: 10.1111/j.1365-2745.2011.01931.x

Leka, J., Toivonen, H., Leikola, N., and Hellsten, S. (2008). *Vesikasvit Suomen Järvien Tilan Ilmentäjinä Ekologisen Tilaluokittelun Kehittäminen (Macrophytes as Indicators of the Ecological Quality of Finnish Lakes. Development of Ecological Classification) The Finnish Environment 18/2008, Finnish Environment Institute (SYKE).* Available at: www.ymparisto.fifi/julkaisut (in Finnish with English summary)..

Li, J., Bai, Y., and Alatalo, J. M. (2020). Impacts of rural tourism-driven land use change on ecosystems services provision in erhai lake basin, China. *Ecosyst. Serv.* 42, 101081. doi: 10.1016/j.ecoser.2020.101081

Li, H.-L., Xu, Y.-S., Wang, Y.-Y., Yu, N.-Q., Zhang, M.-X., Lei, G.-C., et al. (2015). Does clonal fragmentation of the floating plant *Eichhornia crassipes* affect the growth of submerged macrophyte communities? *Folia Geobot.* 50, 283–291. doi: 10.1007/s12224-015-9226-8

Liu, G., Liu, Z., Gu, B., Smoak, J. M., and Zhang, Z. (2014). How important are trophic state, macrophyte and fish population effects on cladoceran community? a study in lake erhai. *Hydrobiologia* 736, 189–204. doi: 10.1007/s10750-014-1906-5

Mjelde, M., and Faafeng, B. A. (1997). *Ceratophyllum demersum* hampers phytoplankton development in some small Norwegian lakes over a wide range of phosphorus concentrations and geographical latitude. *Freshw. Biol.* 37, 355–365. doi: 10.1046/j.1365-2427.1997.00159.x

Morris, K., Bailey, P. C., Boon, P. I., and Hughes, L. (2003). Alternative stable states in the aquatic vegetation of shallow urban lakes. II. catastrophic loss of aquatic plants consequent to nutrient enrichment. *Mar. Freshw. Res.* 54, 201–215. doi: 10.1071/MF02003

Moss, B. (1990). Engineering and biological approaches to the restoration from eutrophication of shallow lakes in which aquatic plant communities are important components. *Hydrobiologia* 200, 367–377. doi: 10.1007/BF02530354

Murphy, K. J. (2002). Plant communities and plant diversity in softwater lakes of northern Europe. *Aquat. Bot.* 73, 287–324. doi: 10.1016/S0304-3770(02)00028-1

Nagengast, B., and Kuczynska-Kippen, N. (2015). Macrophyte biometric features as an indicator of the trophic status of small water bodies. *Oceanol. Hydrobiol. Stud.* 44, 38–50. doi: 10.1515/ohs-2015-0005

Olsen, S., Chan, F., Li, W., Zhao, S., Sondergaard, M., and Jeppesen, E. (2015). Strong impact of nitrogen loading on submerged macrophytes and algae: a long-term mesocosm experiment in a shallow Chinese lake. *Freshw. Biol.* 60, 1525–1536. doi: 10.1111/fwb.12585

Paal, J., and Trei, T. (2004). Vegetation of Estonian watercourses; the drainage basin of the southern coast of the gulf of Finland. *Annales. Bot. Fennici.* 41, 157–177.

Peretyatko, A., Teissier, S., De Backer, S., and Triest, L. (2009). Restoration potential of biomanipulation for eutrophic peri-urban ponds: the role of zooplankton size and submerged macrophyte cover. *Hydrobiologia* 634, 125–135. doi: 10.1007/s10750-009-9888-4

Phillips, G., Willby, N., and Moss, B. (2016). Submerged macrophyte decline in shallow lakes: what have we learnt in the last forty years? *Aquat. Bot.* 135, 37–45. doi: 10.1016/j.aquabot.2016.04.004

Qin, B., Gao, G., Zhu, G., Zhang, Y., Song, Y., Tang, X., et al. (2013). Lake eutrophication and its ecosystem response. *Chin. Sci. Bull.* 58, 961–970. doi: 10.1007/s11434-012-5560-x

Riis, T., Biggs, B. J. F., and Flanagan, M. (2003). Seasonal changes in macrophyte biomass in south island lowland streams, new Zealand. *New Z. J. Mar. Freshw. Res.* 37, 381–388. doi: 10.1080/00288330.2003.9517174

RodrÃGuez-Gallego, L. R., Mazzeo, N., Gorga, J., Meerhoff, M., Clemente, J., Kruk, C., et al. (2010). The effects of an artificial wetland dominated by free-floating plants on the restoration of a subtropical, hypertrophic lake. *Lakes Reserv. Res. Manag.* 9, 203–215. doi: 10.1111/j.1440-1770.2004.00245.x

Rorslett, B. (1991). Principal determinants of aquatic macrophyte richness in northern European lakes. *Aquat. Bot.* 39, 173–193. doi: 10.1016/0304-3770(91)90031-Y

Royle, R. N., and King, R. J. (1991). Aquatic macrophytes in lake Liddell, new south Wales biomass, nitrogen and phosphorus status, and changing distribution from 1981 to 1987. *Aquat. Bot.* 41, 281–298. doi: 10.1016/0304-3770(91)90048-A

Rubio, G., Zhu, J. M., and Lynch, J. P. (2003). A critical test of the two prevailing theories of plant response to nutrient availability. *Am. J. Bot.* 90, 143–152. doi: 10.3732/ajb.90.1.143

Salgado, J., Sayer, C. D., Brooks, S. J., Davidson, T. A., Goldsmith, B., Patmore, I. R., et al. (2018a). Eutrophication homogenizes shallow lake macrophyte assemblages over space and time. *Ecosphere* 9, e02406. doi: 10.1002/ecs2.2406

Salgado, J., Sayer, C. D., Brooks, S. J., Davidson, T. A., and Okamura, B. (2018b). Eutrophication erodes inter-basin variation in macrophytes and co-occurring invertebrates in a shallow lake: combining ecology and palaeoecology. *J. Paleolimnol.* 60, 311–328. doi: 10.1007/s10933-017-9950-6

Sand-Jensen, K., Riis, T., Vestergaard, O., and Larsen, S. E. (2000). Macrophyte decline in Danish lakes and streams over the past 100 years. *J. Ecol.* 88, 1030–1040. doi: 10.1046/j.1365-2745.2000.00519.x

Scheffer, M. (1998). *Ecology of shallow lakes* (London(in English): Chapman & Hall).

Scheffer, M., and Carpenter, S. R. (2003). Catastrophic regime shifts in ecosystems: linking theory to observation. *Trends Ecol. Evol.* 18, 648–656. doi: 10.1016/j.tree.2003.09.002

Schneider, S. (2007). Macrophyte trophic indicator values from a European perspective. *Limnologica* 37, 281–289. doi: 10.1016/j.limno.2007.05.001

Sondergaard, M., Phillips, G., Hellsten, S., Kolada, A., Ecke, F., Maeemets, H., et al. (2013). Maximum growing depth of submerged macrophytes in European lakes. *Hydrobiologia* 704, 165–177. doi: 10.1007/s10750-012-1389-1

Szoszkiewicz, K., Ciecierska, H., Kolada, A., Schneider, S. C., Szwabinska, M., and Ruszczynska, J. (2014). Parameters structuring macrophyte communities in rivers and lakes - results from a case study in north-central Poland. *Knowledge. Manage. Aquat. Ecosyst.* 145 (415), 08. doi: 10.1051/kmae/2014034

Thiebaut, G., and Muller, S. (1998). The impact of eutrophication on aquatic macrophyte diversity in weakly mineralized streams in the northern vosges mountains (NE France). *Biodivers. Conserv.* 7, 1051–1068. doi: 10.1023/A:1008809131487

Toivonen, H., and Huttunen, P. (1995). Aquatic macrophytes and ecological gradients in 57 small lakes in southern Finland. *Aquat. Bot.* 51, 197–221. doi: 10.1016/0304-3770(95)00458-C

Trei, T., and Pall, P. (2004). Macroflora in the watercourses of saaremaa island (Estonia). *Boreal. Environ. Res.* 9, 25–35.

Vestergaard, O., and Sand-Jensen, K. (2000). Aquatic macrophyte richness in Danish lakes in relation to alkalinity, transparency, and lake area. *Can. J. Fisheries. Aquat. Sci.* 57, 2022–2031. doi: 10.1139/f00-156

Wang, H.-J., Wang, H.-Z., Liang, X.-M., and Wu, S.-K. (2014). Total phosphorus thresholds for regime shifts are nearly equal in subtropical and temperate shallow lakes with moderate depths and areas. *Freshw. Biol.* 59, 1659–1671. doi: 10.1111/fwb.12372

Wang, H., Wen, Z., Ren, W., Ni, L., Zhang, X., Li, K., et al. (2022). What is the mechanism of submerged macrophyte biodiversity affecting biomass productivity along water depth: niche complementarity or selection effect? *Ecol. Indic.* 138, 108858. doi: 10.1016/j.ecolind.2022.108858

Wang, H., Wen, Z., Zhang, Z., Zhang, X., Fu, H., Cao, Y., et al. (2020). Environmental vs. spatial drivers of submerged macrophyte community assembly in different seasons and water depths in a mesotrophic bay of erhai lake, China. *Ecol. Indic.* 117, 106696. doi: 10.1016/j.ecolind.2020.106696

Wang, P., Zhang, Q., Xu, Y.-S., and Yu, F.-H. (2016). Effects of water level fluctuation on the growth of submerged macrophyte communities. *Flora* 223, 83–89. doi: 10.1016/j.flora.2016.05.005

Ye, C., Yao, L., Deng, A., Liu, G., and Liu, W. (2018). Spatial and seasonal dynamics of water quality, sediment properties and submerged vegetation in a eutrophic lake after ten years of ecological restoration. *Wetlands* 38, 1147–1157. doi: 10.1007/s13157-018-1021-x

Zhang, Q., Dong, B.-C., Li, H.-L., Liu, R.-H., Luo, F.-L., Zhang, M.-X., et al. (2012). Does light heterogeneity affect structure and biomass of submerged macrophyte communities? *Bot. Stud.* 53, 377–385. doi: 10.1105/tpc.112.099994

Zhang, Y., Jeppesen, E., Liu, X., Qin, B., Shi, K., Zhou, Y., et al. (2017). Global loss of aquatic vegetation in lakes. *Earth-Sci. Rev.* 173, 259–265. doi: 10.1016/j.earscirev.2017.08.013

Zheng, L., An, Z., Chen, X., and Liu, H. (2021). Changes in water environment in erhai lake and its influencing factors. *Water* 13 (10), 1362. doi: 10.3390/w13101362

Zuccarini, P., Ciurli, A., and Alpi, A. (2011). Implications for shallow lake manipulation: results of aquaria and enclosure experiments manipulating macrophytes, zooplankton and fish. *Appl. Ecol. Environ. Res.* 9, 123–140. doi: 10.15666/aeer/0902_123140

Appendix 1 List of the three lakes species.

Family	Genus	Species	Xihu Lake				Cibi Lake				Haixihai Lake				Life Form
			Spr.	Sum.	Aut.	Win.	Spr.	Sum.	Aut.	Win.	Spr.	Sum.	Aut.	Win.	
Salviniaceae	*Azolla*	*Azolla pinnata*					+								F
Characeae	*Chara*		+	+	+	+	+	+	+	+	+	+	+	+	S
Potamogetonaceae	*Stuckenia*	*Stuckenia pectinata*	+	+	+	+	+	+		+	+	+	+	+	S
	Potamogeton	*Potamogeton perfoliatus*		+	+		+	+	+	+	+	+	+	+	S
		Potamogeton acutifolius	+	+	+								+		S
		Potamogeton lucens		+	+	+	+	+	+	+	+		+	+	S
		Potamogeton oxyphyllus					+					+			S
		Potamogeton wrightii			+			+	+	+	+	+	+	+	S
		Potamogeton maackianus	+	+	+	+	+	+	+	+	+	+	+	+	S
		Potamogeton crispus	+	+			+								S
		Potamogeton pusillus	+	+								+	+		S
Hydrocharitaceae	*Najas*	*Najas marina*						+	+			+	+	+	S
		Najas minor			+								+		S
	Hydrilla	*Hydrilla verticillata*		+	+	+	+	+	+	+	+	+	+	+	S
	Ottelia	*Ottelia acuminata*			+										S
	Hydrocharis	*Hydrocharis dubia*			+			+	+						FL
	Vallisneria	*Vallisneria natans*	+	+	+	+	+	+	+	+			+		S
Ceratophyllaceae	*Ceratophyllum*	*Ceratophyllum demersum*	+	+	+	+	+	+	+	+	+	+	+	+	S
Haloragaceae	*Myriophyllum*	*Myriophyllum verticillatum*	+	+	+	+	+	+	+	+	+	+	+	+	S
		Myriophyllum aquaticum					+	+		+					S
Poaceae	*Cynodon*	*Cynodon dactylon*											+	+	H
Nelumbonaceae	*Nelumbo*	*Nelumbo nucifera*							+						E
Lentibulariaceae	*Utricularia*	*Utricularia vulgaris*					+	+	+	+					S
Polygonaceae	*Persicaria*	*Persicaria amphibia*					+								E
		Persicaria hydropiper											+	+	FL

(Continued)

10.3389/fmars.2023.1182823

Continued

Family	Genus	Species	Xihu Lake				Cibi Lake				Haixihai Lake				Life Form
			Spr.	Sum.	Aut.	Win.	Spr.	Sum.	Aut.	Win.	Spr.	Sum.	Aut.	Win.	
Lythraceae	*Trapa*	*Trapa natans*			+			+	+						E
Plantaginaceae	*Limnophila*	*Limnophila sessiliflora*							+						S
Cabombaceae	*Cabomba*	*Cabomba caroliniana*								+					F
Pontederiaceae	*Eichhornia*	*Eichhornia crassipes*	+		+										H
Amaranthaceae	*Alternanthera*	*Alternanthera philoxeroides*			+		+			+	+				E
Ranunculaceae	*Batrachium*	*Batrachium bungei*									+		+		S
Nymphaeaceae	*Nymphaea*	*Nymphaea tetragona*						+							FL
Menyanthaceae	*Nymphoides*	*Nymphoides peltata*					+	+	+	+					FL

H, hygrophyte; E, Emergent plant; S, Submerged plant; F, Floating plant; FL, Floating leaf plant.

Appendix 2 Correlation between nutrient status and α-diversity in lakes.

	TLI(Σ)	Species richness	Shannon-Wiener index	Simpson index
Species richness	-0.633**			
Shannon-Wiener index	-0.519**	0.838**		
Simpson index	-0.615**	0.723**	0.955**	
Pielou index	-0.519**	0.606**	0.909**	0.925**

*, significant difference ($p<0.05$); **, significant difference ($p<0.01$).

10.3389/fmars.2023.1182823

frontiers | Frontiers in Environmental Science

TYPE Original Research
PUBLISHED 11 September 2023
DOI 10.3389/fenvs.2023.1098993

OPEN ACCESS

EDITED BY
Jaan H. Pu,
University of Bradford, United Kingdom

REVIEWED BY
Amir Ghaderi,
Urmia University, Iran
Manish Pandey,
National Institute of Technology
Warangal, India

*CORRESPONDENCE
Weijie Wang,
wjwang@whu.edu.cn

RECEIVED 06 January 2023
ACCEPTED 18 April 2023
PUBLISHED 11 September 2023

CITATION
Zhao H, Wang W, Jia F, Wang H, Liu Z and Xu Y (2023), Numerical and analytical flow models in ecological channels with interaction of vegetation and freshwater. *Front. Environ. Sci.* 11:1098993. doi: 10.3389/fenvs.2023.1098993

Numerical and analytical flow models in ecological channels with interaction of vegetation and freshwater

Hanqing Zhao[1,2], Weijie Wang[3]*, Fengcong Jia[4], Huilin Wang[5], Zhiwu Liu[1] and Yuxuan Xu[3,6]

[1]China Three Gorges Corporation, Wuhan, China, [2]National Engineering Research Center of Water Resources Efficient Utilization and Engineering Safety, Nanjing, China, [3]State Key Laboratory of Simulation and Regulation of Water Cycle in River Basin, China Institute of Water Resources and Hydropower Research, Beijing, China, [4]College of Water Resources and Civil Engineering, China Agricultural University, Beijing, China, [5]School of Water Conservancy and Civil Engineering, South China Agricultural University, Guangzhou, China, [6]School of Water Conservancy, North China University of Water Resources and Electric Power, Zhengzhou, China

Aquatic vegetation interferes with river hydrodynamics, thus affecting the mass transport and energy transfer in an ecosystem. The flow over submerged vegetation is characterized by a complex velocity profile and multiple turbulence structures, which have been usually simulated using cylinders or strips in previous studies. Because the simplified vegetation configuration may hide or amplify some physical processes found in natural conditions, we investigate the velocity distribution and turbulence structure in foliaged vegetation flows using both analytical and numerical approaches. The main innovations and findings can be summarized as follows: 1) numerical and analytical models adopted in this paper accurately simulate the flow velocity profile in vegetated channel; 2) the Karman constant is found to be unsuitable for complex vegetation morphologies, so we proposed adjusted coefficient; 3) an image processing method is adopted to quantify the vegetation morphology accurately; 4) the existing mixing-layer thickness formula is found to be unsuitable for vegetation with leaves, an improved formula is proposed showing high correlation coefficient (0.9562) between measured and predicted data; 5) to ensure applicability to larger-scale hydrodynamic simulations, an analytical expression of Manning's coefficient is proposed based on an analytical multi-layer flow velocity model. These research findings can provide theoretical support for the design of vegetated river and ecological restoration.

KEYWORDS

numerical model, analytical model, vegetated flow, velocity profile, Manning's coefficient

1 Introduction

Water flow and associated material, microorganism transport is one of the research hotspots in ecological hydraulics (Wu et al., 2021a; Jiang et al., 2022; Li et al., 2023). The vegetation that is ubiquitous in rivers changes the flow structure, thereby affecting flood conveyance (Katul et al., 2011; Konings et al., 2012), sediment and pollutant transport (Huai et al., 2009; Shucksmith et al., 2010; Huai et al., 2019a; Huai et al., 2019b; Shan et al., 2020; Afzal et al., 2021; Wu et al., 2021b; Zhao and Nepf, 2021), channel evolution (Rominger et al.,

2010; Zhao et al., 2021), and creature activity (Kemp et al., 2000; Bornette and Puijalon, 2011). Ecological channels usually grow a large number of aquatic vegetation. Under the given flow conditions, the velocity distribution characteristics in the river are affected by the vegetation and the shape of the river, and the distribution of vegetation affects the shape of the river. The flow blocking mechanism of vegetation and the turbulent characteristics of flow are related to the river boundary, water level, flow and the type, density and shape of vegetation, and the water quality and ecology along the river were directly improved by vegetation (Huai et al., 2018). Studies on the flow characteristics of ecological channels with vegetation help to clarify the physical and ecological functions of river systems.

Analytical method is the application of analytical formula to solve mathematical models. The analytical model has advantages over the actual laboratory experiment in terms of cost, time and limitations of field collection conditions. Therefore, the further study and improvement of the analytical model has always been the focus of attention of scientists. Owing to the drag exerted by plants, the flow passes over submerged vegetation, the velocity distribution becomes vertically discontinuous and an inflection point occurs at the canopy top (Nepf and Vivoni, 2000). Thus, the profile of the velocity U is S-shaped and no longer follows a logarithmic law (Carollo et al., 2002). Some researchers have simulated vegetated flows numerically by modifying the momentum equation with the canopy drag force formula. For example, Fischer-Antze et al. (2001) solved the three-dimensional Navier–Stokes (3D N-S) equations using the SIMPLE method and the k-ε turbulence model, while Erduran and Kutija (2003) proposed a quasi-3D numerical solution that couples the finite volume solution of the shallow water equations with a finite difference solution of the N-S equations. Zeng and Li (2014) incorporated the Spalart–Allmaras turbulence closure into the 3D N-S model, whereas Pu et al. (2020) combined the improved Shiono-Knight model (SKM) with a Multi-Zonal (MZ) method (proposed by Pu et al., 2020) and applied the proposed analytical model to the flow of rectangular channels. These numerical models can capture the hydrodynamic characteristics of the flow at any point (Lu and Dai, 2016; Yan et al., 2017), Pourshahbaz et al. (2022) compared the numerical model with the experimental results in literature, and found that the overall results of the model better reproduced the measured data,.But their accuracy depends on the parameter settings of the model, which are semi-empirical and suffer from a shortage of suitable guidelines. Other scholars have explored the U profile in an analytical manner by directly solving the N-S equations. This approach represents the kinetic viscosity ν through some turbulence characteristic terms, such as the mixing-length, turbulent kinetic energy, or turbulent kinetic energy dissipation rate (Katul et al., 2004; Poggi et al., 2009; Wang et al., 2018). For example, Katul et al. (2011) found that U exhibits exponential and logarithmic profiles within and above the canopy, respectively; and Cheng et al. (2012) showed that the U profile is exponential above the canopy in a depth-limited flow where the submergence degree is less than 2.

Scientists have not only analyzed the influence of canopy resistance formulas on the U profile of submerged vegetation velocity, but several studies have also explored the profile of U by analyzing motions of turbulent vortices. Vegetated flows are generally characterized by the Kelvin–Helmholtz (KH) vortex, which is driven by the KH instability and billows around the canopy top (Nepf, 2012). Ghisalberti and Nepf (2004) defined the waving region of the KH vortex as the vegetal shear layer (VSL), and observed a hyperbolic tangent profile for U in the exact region. Because the flow below and above the VSL is characterized by wake turbulence and boundary shear turbulence, U is assumed to display constant and logarithmic profiles, respectively (Nezu and Sanjou, 2008). Nikora et al. (2013) proposed a general velocity distribution formula that incorporates multiple turbulent mechanisms to depict the profile of U throughout the water depth. The proposed formula is efficient and accurate, but the VSL boundaries must be provided beforehand. The VSL lower boundary Z_l can be evaluated according to the Reynolds shear stress profile, canopy density, or zero-plane displacement height (Nepf and Vivoni, 2000; Luhar et al., 2008; Nepf and Ghisalberti, 2008). The VSL upper boundary Z_u is assumed to be the critical point at which the U profile deviates downwards from the logarithmic law near the free surface (Nezu and Sanjou, 2008), and can be assessed indirectly by the VSL thickness, which is proportional to the momentum thickness θ. The value of θ is calculated using the flow velocities U_l, U_u at the VSL boundaries and the frequency of the KH vortex f_{KH}, i.e., $\theta = \int_{-\infty}^{+\infty}\{1/4 - [(U - (U_l + U_u)/2)/(U_u - U_l)]^2\} \cdot dz$ or $\theta = 0.016 \cdot (U_l + U_u)/f_{KH}$ (Ho and Huerre, 1984; Ghisalberti and Nepf, 2002). Nepf and Ghisalberti (2008) estimated f_{KH} by analyzing the distribution of the spectral density, which attains its peak at f_{KH}, and showed that f_{KH} is fixed throughout the VSL. In the upper canopy region, where both the KH and wake vortices exist, the spectral distribution is characterized with peaks at both f_{KH} and the wake vortex frequency f_W (Poggi et al., 2004). The spectral density at f_W reflects the coupled actions of both the wake turbulence and the stem scale turbulence (Konings et al., 2012). According to studies on terrestrial canopy flows, the stem scale turbulence is caused by a "spectral shortcut", which interferes with the eddy cascading process by directly breaking up the vegetal shear turbulence (Fathi-Maghadam, 1997). Further studies have shown that the spectral shortcut consumes 58%–71% of the shear turbulent energy, and this action becomes fiercer as the vegetation density increases or the relative submergence decreases (Zhao et al., 2020).

Previous hydrodynamic studies of submerged vegetation have been based on reducing vegetation to cylindrical rods. Finnigan, 2000 pointed out that vegetation cannot be simply considered as a rigid cylinder, because vegetation tends to have complex structural and biomechanical properties, which will produce great deviations in the study of flow resistance and velocity. Recent studies have tended to study vegetated flows with natural-like plant morphologies, because any simplification of the vegetation configuration hides or amplifies some of the physical processes found in natural conditions (Tinoco, 2020). Li et al. (2020) presented the vertical distributions of velocity, Reynolds shear stress, and turbulence intensities in foliaged vegetation flow. Wang et al. (2019) and Zhang et al. (2021) derived analytical solutions for the profile of U in flows over submerged flexible vegetation with variable frontal widths. Tschisgale et al. (2021) explored the interaction between coherent flow structures and vegetation reconfiguration, and discussed the mechanism that drives the wavy motion of the canopy in the Monami regime. Wilson et al. (2003) found that vegetation with foliage increases the canopy drag

force and inhibits vertical momentum exchange, thereby inhibiting the vegetal shear turbulence. Chembolu et al. (2019) showed that a mixed arrangement of different morphologies of vegetation reduces the flow velocity and vegetal shear turbulence, and this shifts the peak Reynolds stress distribution upwards from the canopy top.

In summary, the vegetation morphology affects the motion of the KH and wake vortices and changes the U profile by redistributing the canopy drag (Caroppi and Järvelä, 2022). This study investigates hydrodynamic features such as the turbulence motion and velocity distribution law in an open-channel flow with different types of submerged vegetation. Specifically, we explore the profile velocity using both analytical solutions of the N-S equations and turbulence investigations of the vortex structures, different from existing studies on turbulence structures or analytical solutions of the velocity profile.

2 Theory

2.1 Numerical model

By introducing the resistance term of vegetation into the Reynolds-averaged N-S equations, the momentum equation in the flow direction can be obtained as follows (Luhar et al., 2008; Nepf, 2012):

$$\frac{Du}{Dt} = gS_o - \frac{1}{\rho}\frac{\partial p}{\partial x} - \frac{\partial \overline{u'w'}}{\partial z} + \nu\frac{\partial^2 u}{\partial z^2} - \delta F_d \tag{1}$$

where ν is the kinematic viscosity of water and z is the vertical distance calculated from the bottom of the riverbed.

The critical items in the above equation are

$$K_1 = \frac{\partial \overline{u'w'}}{\partial z} \tag{2}$$

which is the spatially averaged Reynolds stress term,

$$K_2 = \frac{\nu\partial^2 u}{\partial z^2} \tag{3}$$

which is the viscous shear stress, and

$$F_d = \frac{1}{2}C_d m D u^2 \tag{4}$$

which is the vegetation resistance term, i.e., the drag force term. Where $\delta = 1$ in the vegetation layer ($z/h_v < 1$) and $\delta = 0$ above vegetation ($z/h_v > 1$).

Further studies have been carried out for vegetated water flows in the case of a constant uniform flow, and the pressure term expression is as follows:

$$\partial p/\partial x = 0 \tag{5}$$

Subsequently, the flow control equation for constant uniform flow conditions is simplified as

$$gS_o - \frac{\partial \overline{u'w'}}{\partial z} - \delta F_d = 0 \tag{6}$$

For Reynolds stress, the standard K-equation is

$$\overline{u'w'} = -K_m\frac{d\bar{u}}{dz} \tag{7}$$

where K_m is the vortex viscosity coefficient. Substituting the above equation into the control equation gives

$$gS_o + K_m\frac{d^2u}{dz^2} + \frac{dK_m}{dz}\frac{du}{dz} - \frac{\delta}{2}C_d m D u^2 = 0 \tag{8}$$

where C_d is the drag force coefficient. D is water retention width that changes along the vegetation stem, and the variation can be derived in a photography-mathematical method in this article.

To resolve the flow velocity using this equation, the distribution law of the vortex viscosity coefficient needs to be tackled. By means of the Prandtl mixing-length model, we can write

$$K_m = l_{eff}^2\left|\frac{du}{dz}\right| \tag{9}$$

where l_{eff} is the effective mixing-length scale, which is a function of the dominant vortex size.

For the boundary layer on top of the vegetation, the mixing length is

$$l_{eff} = \kappa L_{CBL} = \kappa(z - d) \tag{10}$$

where d is the zero-plane, which can be determined by the following equation:

$$d = \frac{\int_0^{h_v} zF_d(z)dz}{\int_0^{h_v} F_d(z)dz} \tag{11}$$

The vegetation layer contains the entire Karman vortex zone (lower part of the vegetation layer) as well as part of the mixing layer. Under a simplified approach, the mixing length of the vegetation layer can be written as

$$l_{eff} = \psi h_v \tag{12}$$

where ψ is a constant that can be derived from the assumption of continuity of the mixing length over the entire water depth:

$$\psi = \kappa\left(1 - \frac{d}{h_v}\right) \tag{13}$$

2.2 Analytical model

The methods currently used to describe velocity profiles can be divided into three main categories: 1) methods based on the concept of a single profile; 2) methods based on segmented velocity profiles, where the velocity profile is represented by a set of relationships defined for non-overlapping flow zones or segments; and 3) a (linear) superposition based on several traditional concepts applied to the entire flow depth. In contrast to the segment-based model, this paper uses a flow superposition model based on traditional concepts proposed by Nikora et al. (2013), with the innovation that the superposition model is applied to vegetation with a realistic morphology, i.e., the velocity profile can be represented as a superposition of individual profiles formed by specific momentum transport mechanisms. The proposed approach combines these concepts simulatively over the entire

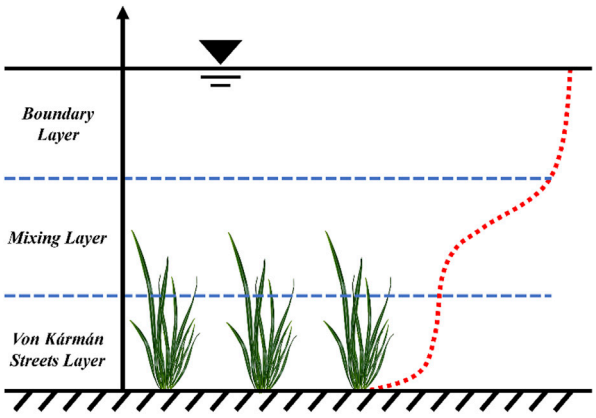

FIGURE 1
Typical diagram of flow velocity distribution in three zones.

flow depth, allowing significant overlaps of momentum transport and turbulence production mechanisms. On this basis, the analysis focuses on the Kármán vortex street zone, the mixing-layer zone, and the boundary layer zone (Figure 1).

2.2.1 Kármán vortex street zone

The vertical variation of the Reynolds stress can be neglected near the bottom, and the vegetation drag force is balanced by the gravity component, so Eq. 6 can be simplified as

$$gS_o - F_d = 0 \tag{14}$$

Furthermore, following Nikora et al. (2013) and Nepf (2012), we can write

$$U_{karman} = \left(\frac{gS_0}{0.5C_d a}\right)^{1/2} \tag{15}$$

where a is the total frontal vegetation area per unit volume, and U_{karman} is flow velocity in the Kármán vortex street zone where the velocity is vertically constant.

2.2.2 Mixing-layer zone

Ei-Hakim and Salama, 1992 argued that Mixing-layer turbulence, formed around the inflectional mean velocity profile which develops between two coflowing streams of different velocities. Ghisalberti and Nepf (2002) implemented this analogy and showed that there is good agreement between velocity profiles measured in their experiments and the hyperbolic tangent law of the mixing layer theory. Nepf and Ghisalberti (2008) proposed two equations to describe the velocity profile gravity. To obtain the complete velocity profile, the submodels proposed for the different layers and zones were combined by imposing various matching conditions (e.g., the velocities and velocity gradients at the boundaries between the different zones should match). Coles (1956) studied the flow velocity distribution by showing that only the logarithmic law occurring in the inner region of the boundary layer is valid and proposed a wake function. Thus, he proposed that the overall velocity profile should be represented "by a linear combination of two universal functions," the law of the wall and the law of the wake. Later, several researchers demonstrated the applicability of this concept to open channel flow [Zhao et al., 2019 and Stoesser et al., 2009].

$$U_{\mathrm{ML}} = U_i + (U_i - U_{\mathrm{Karman}})\tanh\left(\frac{z - z_i}{L_e}\right) \tag{16}$$

where U_i is velocity at the inflection point z_i; and L_e is characteristic length scale of the mixing layer.

2.2.3 Logarithmic rate zone

The logarithmic component of velocity U_{LL} is mainly caused by the proportional variation of turbulence with distance from the bed, and can be represented by the well-known logarithmic law. Kouwen et al. (1969) use the boundary layer concept and the associated logarithmic formula (or logarithmic law) to calculate the velocity distribution above the canopy as

$$\frac{U_{LL}}{u_*} = \frac{1}{\kappa}\ln\left(\frac{z}{h_v}\right) + C \tag{17}$$

where U_{LL} is the time-averaged velocity, z is the vertical distance from the canopy top, κ is the von Kármán constant, u_* is the frictional flow velocity, and $C = u_{h_v}/u_*$.

Ghisalberti and Nepf, 2006 studied the velocity distribution, used the logarithmic section to model, and tried to use the zero plane displacement to move the inflection point. The equation proposed by Kouwen et al. (1969) suffers from the defect that the zero plane, which is the horizontal asymptote of the logarithmic equation, is located at the channel bed. Considering the effect of zero-plane displacement, the logarithmic flow velocity profile of flow above the vegetation should be described as

$$\frac{U_{LL}}{u_*} = \frac{1}{\kappa}\ln\left(\frac{z - d}{z_o}\right) \tag{18}$$

where z_0 is the hydrodynamic roughness length.

2.3 Turbulent energy spectrum analysis

Spectral analysis of the flow velocity data involves transforming the time domain signal into a frequency domain signal. This enables analysis of the oscillation frequency of the instantaneous flow velocity sequence. The power spectral density is mainly based on the squared value of the flow velocity signal, and the frequency corresponding to the peak power spectral density is the dominant frequency of the vortex. The experimental data are first smoothed and then the power spectral function curve is obtained by applying a Fourier transform to the autocorrelation function of the pulsating flow velocity.

The fast Fourier transform (FFT) is a common method for analyzing the spectral characteristics of turbulent pulsation energy by converting the time-domain flow pulsation signal into a frequency-domain signal. The fluctuating velocity is generally divided into two types: the high frequency and small amplitude fluctuation caused by the small vortex in the turbulence, and the low frequency and large amplitude fluctuation caused by the large vortex. The FFT is applied to the instantaneous flow velocity

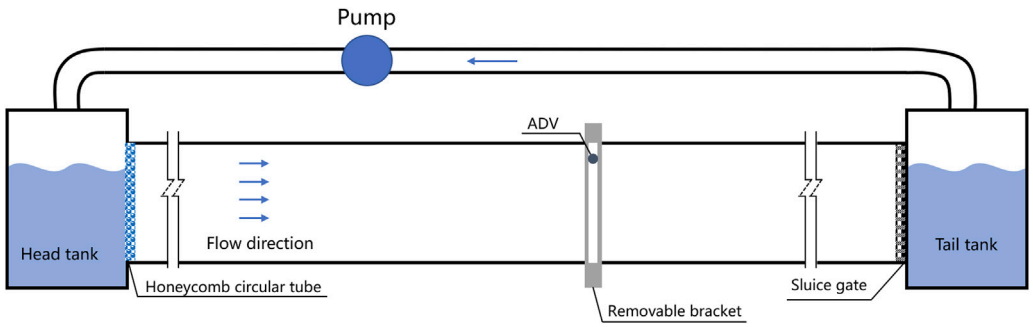

FIGURE 2
Schematic diagram of the submerged vegetation flume test setup.

sequence V, which contains $n = 2^m$ samples. The resulting vector F contains $j = 1\text{-}2^{m-1}$ elements, and satisfies the following equation:

$$F_j = \frac{1}{n}\sum_{k=1}^{n=1} V_k e^{2\pi (j/n)ki} \tag{19}$$

where the amplitude of F is related to the sampling epoch and the number of samples.

3 Experimental setup and program

3.1 Experimental equipment and measurement devices

3.1.1 Experimental equipment

Experiments were completed at the State Key Laboratory of China Institute of Water Resources and Hydropower Research. The experimental set consists of a tank-flume system, simulated vegetation, water ruler, Doppler flow velocity measurement instruments, and related auxiliary facilities. The laboratory has constant heating measures and good ventilation, which ensures stabilities of water temperature and the surrounding environment during the experiment measurement. Figure 2 shows a schematic diagram of the tank-flume system that can be divided into four parts, i.e., an inlet head tank, glass flume, tail tank, and circulation pipe. The glass flume is rectangular and 12 m long, 1 m wide, and 1 m high. A honeycomb structure is installed at the flume entrance to make incoming flow uniform. The flume bed is made of PVC board with magnetic suction bases to locate vegetation elements, and a sluice gate is set at the flume end to maintain the flow depth. The head tank and tail tank is connected by a circulation pipe that is equipped with pump-electromagnetic flowmeter to control the inflow discharge of the flume.

3.1.2 Acoustic Doppler velocity meter

In the experiment, the Acoustic Doppler Velocimeter (ADV) was 200 Hz to measure the velocity field under vegetation flow conditions. The working principle of ADV is based on Doppler Effect, which is mainly composed of signal processing equipment and probe. The probe consists of one transmitter and three receivers. The transmitter generates acoustic waves. If there is a particle movement in the measurement area, the frequency of the acoustic wave reflected by the particles will be different from the original frequency. The three receivers will receive acoustic signals of different frequencies reflected by the particles. The signal processing equipment processes these signals according to the frequency shift principle of Doppler and calculates the instantaneous velocity and movement direction of the particles. The velocity distribution on the whole measuring line is obtained by superimposing the data measured by the probe. The highest sampling frequency is 200 Hz, and the sampling volume is less than 0.09 cm^3. In this experiment, ADV uses a lateral probe, the sampling frequency is 200 Hz, and the sampling time of each point is 120 s. The vertical line spacing is 1cm, and the maximum height measured is 3 cm below the water depth because of the lateral probe. The ADV device is fixed on a customized bracket to ensure the measurement stability during the experiment (Figure 3). The bracket is spatially movable, so the flow velocity at any point can be measured.

3.1.3 Experimental materials

According to the experimental requirements, the vegetation covered bed area of 9 m in length and 1 m in width, and distributed 1 m downstream of the flume inlet. The vegetation type and arrangement were designed to be adjustable. Following research on mudflat areas, the simulated vegetation consisted of dwarf grass with 6 cm height and sedge with 13.5 cm height, and specific parameters of the experimental vegetation are shown in Figure 3.

3.2 Experimental process

3.2.1 Experimental working conditions

To study hydrodynamic characteristics and turbulence development in the rectangular flume, tests were carried out under different vegetation densities and submergence degree conditions. Specific parameters of the tests are listed in Table 1.

3.2.2 Measurement point cross-section

To ensure a relatively complete and in-depth study of the vegetation flow, the onset of turbulence was examined in a preliminary analysis. Turbulent flow was found to be fully developed in the longitude region of x = 400–900 cm.

FIGURE 3
Simulated vegetation experimental area.

TABLE 1 Multi-vegetation pattern test conditions.

Run	Vegetation type	Vegetation height (cm)	Vegetation spacing	Flow depth/cm	Bulk velocity/(cm s^{-1})
1	dwarf grass	6	20 cm × 15 cm (sparse)	30	10
2	dwarf grass	6	20 cm × 15 cm (sparse)	40	7.5
3	dwarf grass	6	10 cm × 7.5 cm (Dense)	30	10
4	Sedge	13.5	20 cm × 15 cm (sparse)	30	10
5	Sedge	13.5	20 cm × 15 cm (sparse)	40	7.5
6	Sedge	13.5	10 cm × 7.5 cm (Dense)	30	10

The measurement points include the vegetated and surrounding areas, and the vegetation was arranged symmetrically along the centerline of the flume. The average values of the flow velocity at $y = 40$ cm and $y = 50$ cm were taken as the plane mean flow velocity for the vegetation spacing of 20 cm × 15 cm; the average values of the flow velocity at $y = 45$ cm and $y = 50$ cm were taken as the plane mean flow velocity for the vegetation spacing of 10 cm × 7.5 cm. The vertical measurement step was set to be 0.05 times the water depth.

3.3 Data processing

When ADV is used to measure turbulent flow, some invalid signals may be collected because of various environmental factors. Therefore, we take some post-processing methods to remove noise signals before calculating velocity values. When removing the interference values from the sample data, four times the standard deviation of the sample was taken as the interval for filtering. The processing method was performed as follows.

First, the overall flow velocity data were processed to remove the interference values in the sample data, i.e., those greater than four times the sample standard deviation. The flow rate sequence obtained with a sampling time of 2 min and sampling frequency of 200 Hz was taken as the data sample, and mean and variance of the data sequence were calculated. When the absolute value of difference between the flow rate signal value $u_i(t)$ and the sample mean was greater than 5 times of the variance, i.e., σ_1, the signal value was considered to be interference, and the two adjacent correct signal values were interpolated to replace the interference signal value.

$$\sigma_1 = \sqrt{\frac{\sum_{i=1}^{N}(u-U)^2}{N}}, \cdots i = 1, 2, 3 \cdots, N \tag{20}$$

where u(t) is the instantaneous velocity in the direction corresponding to the data, U is the time-averaged value of u(t), and N is the total number of samples.

For smaller disturbance values, it is difficult to distinguish them from turbulent pulsations within the flow velocity time series, mainly in the form of large abrupt changes from the preceding and following adjacent flow velocity values. To reflect the nature of continuous variations in the flow velocity, a subtle correction was made to the local abrupt flow velocity data according to the adjacent flow velocity data. The mean and standard deviation of the five flow velocity values before and after the flow velocity at a given point were used to determine whether the flow velocity value at that point was an interference peak.

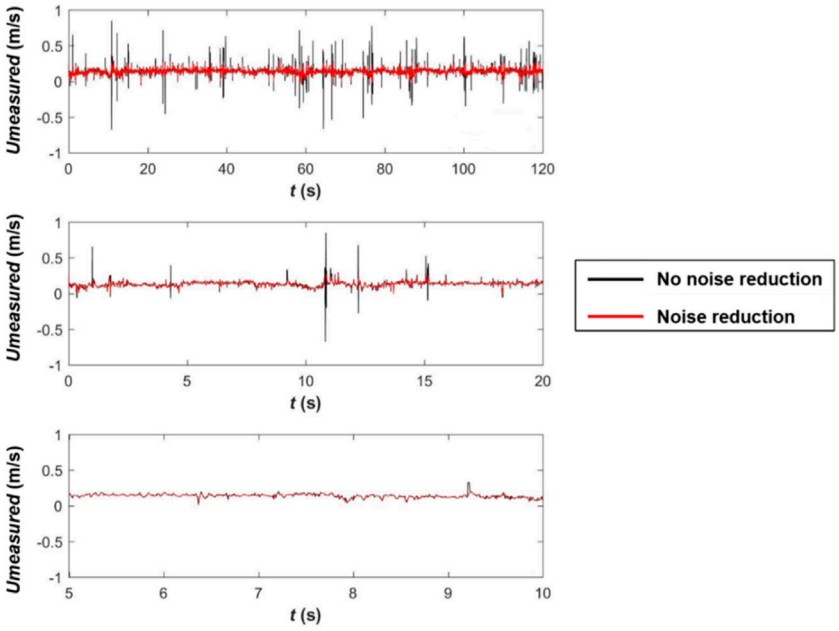

FIGURE 4
Comparison of data before and after noise reduction.

$$\sigma_2 = \sqrt{\frac{\sum_{j=1}^{N}(u - U')^2}{n}}, \cdots i = 1, 2, 3 \cdots, N \tag{21}$$

where $n = 10$ is the number of local data. If the flow velocity at the intermediate point was not within $2\sigma_2$ of the average value, it was regarded as an interference peak.

The noise reduction process effectively removes the interference signal caused by environmental factors, while retaining the true form of the water flow signal. A comparison of the data before and after noise reduction is shown in Figure 4.

4 Results and discussion

4.1 Morphological characteristics of submerged vegetation

In this study, a simulation method was used to measure the diameter of the plant stems. First, the distance between the shooting point and the plant was measured using laser distance measurement technology, and an image of the plant was collected at the shooting point.

$$Gray = 0.299\mathrm{R} + 0.587\mathrm{G} + 0.114\mathrm{B} \tag{22}$$

Where, R represents red pixel, G represents green pixel, and B represents blue pixel. Grayscale image is gray and black and white with different depths, which describes the overall and local chroma and brightness of the image and color image.

The column averages of the recorded data were calculated and divided into a predetermined number of consecutive recognition zones. The demarcation points of the recognition zones were calculated, and the length of the pixel corresponding to the diameter of the plant stem was computed using the pixel coordinates of the two adjacent demarcation points. Finally, the diameter of the plant stem was determined using the length of the pixel, the distance between the shooting point and the plant, and the orientation of the image.

The length of the pixel correspond”ng t’ the diameter of the plant stem is given by

$$L = \sqrt{(\Delta u)^2 + (\Delta v)^2} \tag{23}$$

The plant stem diameter calculation determines the diameter of the plant stem using the following formula:

$$D = L \times S / f \tag{24}$$

This method overcomes the problems of measuring the diameter of plant stems, namely, the low efficiency, poor accuracy, and time-consuming procedure. It also removes the influence of the topography and planting density on the results, and ensures a higher measurement accuracy. Through image processing, the submerged vegetation height h_v corresponding to the two groups of working conditions and the vegetation retaining width D along the vertical variation were obtained. On this basis, the “adaptive” characteristics of vegetation morphology under the water flow environment can be qualitatively determined for dwarf grass and sedge. The vegetation water retention width D along the vertical direction is calculated separately for each working condition. The treatment images are shown in Figure 5A.

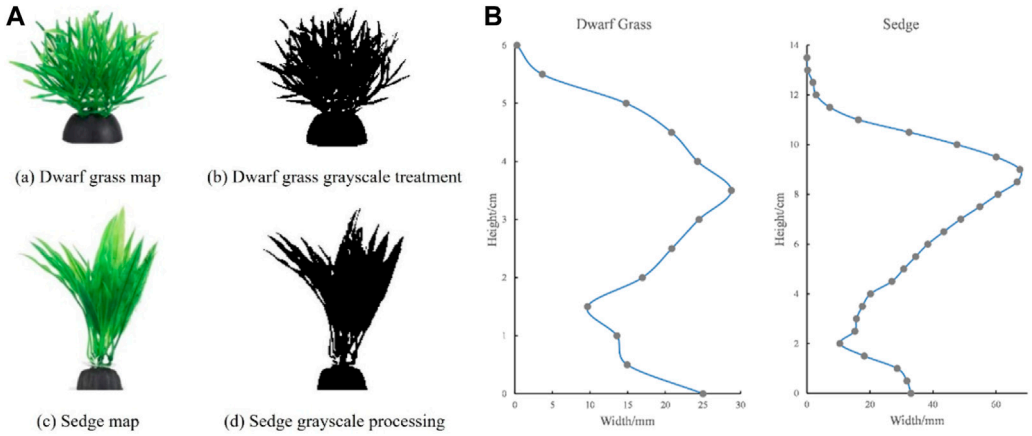

FIGURE 5
(A) Vegetation prototype and grayscale processing; **(B)** Vertical width of underwater morphology of different vegetation.

The underwater morphology of the vegetation and the vegetation water retention width along the vertical direction corresponding to each working condition are shown in Figure 5B. The equivalent widths of the two types of vegetation are found to be 2.73 cm for dwarf grass and 2.97 cm for sedge.

4.2 First-order closure model validation

The results of these spatial analyses of canopy flow are reflected in the traditional vertical profiles of velocity moments. As is readily apparent from a statistical examination of the data, the results are highly dependent on the proximity to the canopy, leading to the generation of very large vertical heterogeneity, especially in vegetated environments with variable vertical orientation. The changes in curvature of the velocity profile, from a logarithmic form in the high-momentum layer above the top of the canopy to an exponential form in the resistance layer below, leads to an inflection point near $z = h_v$. The results indicate that an increase in canopy density leads to enhanced flow characteristics, as shown in Figure 6 for various working conditions, where the flow velocity in the canopy decreases and the shear at the top of the canopy increases. The vertical variation in leaf diameter moderates these effects, which tend to be stronger when more leaves are concentrated in the upper layer. This is especially true in the case of denser vegetation, where the turbulent state in the canopy seems to be mainly determined by the upper canopy elements and is minimally influenced by the lower part of the vegetation.

The specific parameters selected for the numerical calculation of the flow velocity distribution using first-order closure are presented in Table 2. C_d is calculated by adopting method of Cheng and Nguyen (2011):

$$C_d = \frac{130}{r_{v^*}^{0.85}} + 0.8\left[1 - \exp\left(-\frac{r_{v^*}}{400}\right)\right]; r_{v^*} = \left(\frac{gS}{\nu^2}\right)^{1/3}\left(\frac{4 - \pi m D^2}{4mD}\right) \quad (25)$$

As can be seen from Table 2, there is a high correlation between k_v and the vegetation attributes and inundation degree. When the vegetation is relatively short, the value of k_v is large, and when the vegetation height is relatively high, the value of k_v remains basically unchanged. In the environment where the vegetation is short, an increase in the inundation degree enhances the value of k_v, which explains why the vegetation height produces a difference in diameters. Specific simulation results are shown in Figure 6.

4.3 Flow rate superposition model validation

4.3.1 Turbulent energy spectrum analysis

This subsection investigates the turbulent structure of the shear layer formed at the interface between the vegetated and non-vegetated zones. The KH instability leads to the formation of vortex structures within the shear layer. These vortex structures dominate the lateral transport of energy as well as momentum, which is reflected at the interfacial interface, where periodic fluctuations in velocity and Reynolds stress occur. The longitudinal and transverse flow velocities are inversely correlated, indicating that there is a strong momentum exchange at the intersection, and the strong sweep is accompanied by weak promotion. The approximate periodicity of velocity and Reynolds stress proves that there is a dominant frequency of the vortex structures at the intersection, and energy spectrum density analysis can be used to determine this dominant frequency.

The vegetation morphology affects the vortices generated by the water flow when passing through the submerged vegetation. In general, the turbulence intensity of the water flow increases with increasing flow velocity, whereupon the vortex propagation frequency becomes faster. Therefore, the flow velocity sequence on top of the vegetation is analyzed using the energy spectrum, and then the propagation frequency and energy dissipation law of turbulence are determined.

Spectrum analysis indicates that, under the influence of the vegetation properties and the distribution method, the water flow produces large and small vortices near the lower edge of the vegetation cover. These vortices cause strong periodic oscillations and momentum transport in the flow, specifically the periodic oscillation of the longitudinal flow velocity and vertical Reynolds

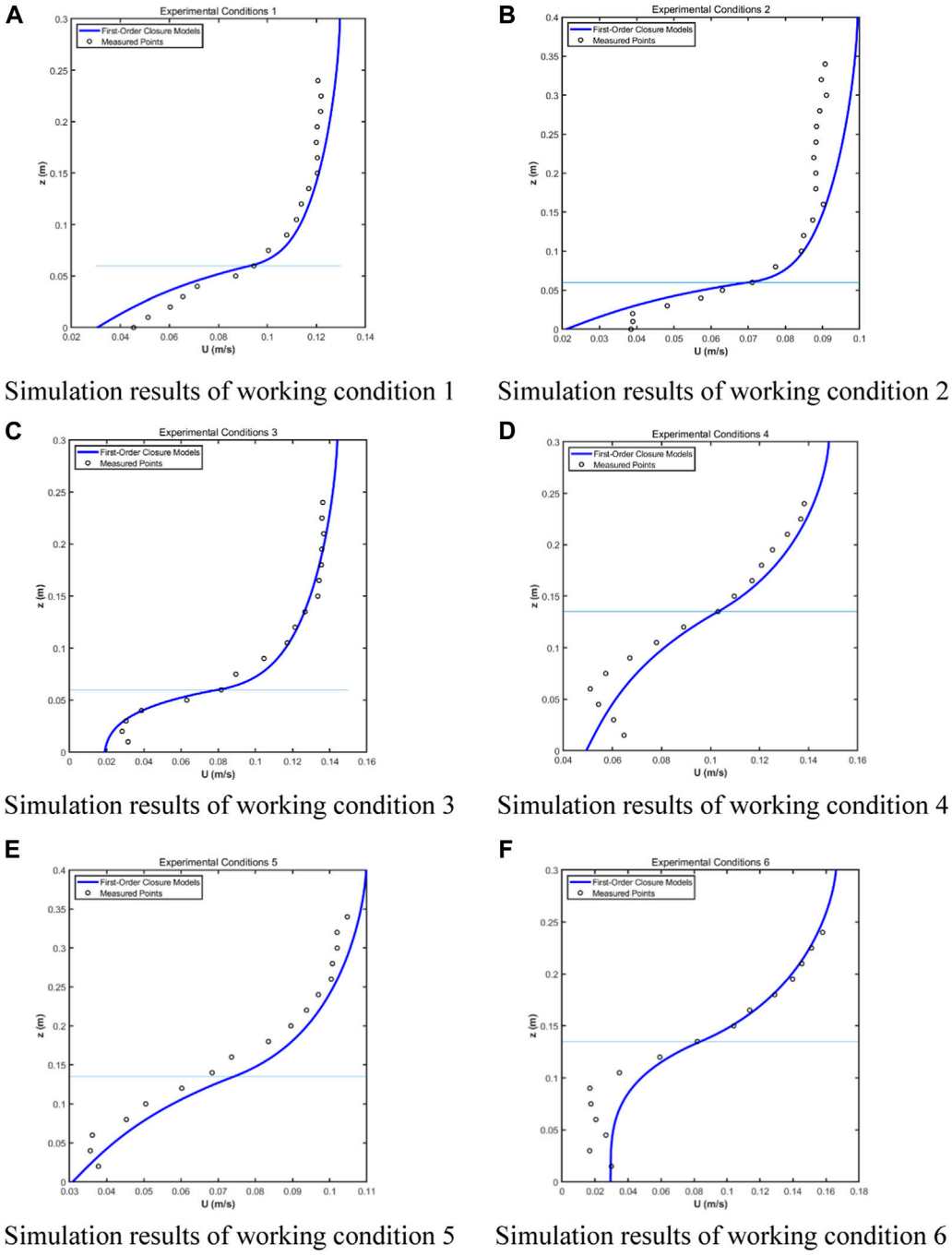

FIGURE 6
Simulation of the first-order closed model for working condition 1–6 **(A–F)**.

stress. Analysis of the peak frequency of the energy spectrum (Figure 7) shows that the distribution of the energy spectrum satisfies the −5/3 power law.

Further analysis of the water flow in the fully developed region (x/l_{veg} = 0.61) indicates that the dominant frequency of the eddies varies considerably at the vegetation intersections. The dimensionless Strouhal number (S_t) describes the relationship between the frequency of eddy shedding and the characteristic length of the obstacle, and is widely used in conditions where the Karman vortex street or the stem turbulence generating term P_w is dominant. S_t is calculated as

$$S_t = \frac{fL}{U} \tag{26}$$

where f is the vortex frequency, i.e., the dominant frequency in the energy spectrum analysis, L is the characteristic length of the vortex size, and U is the characteristic flow velocity (usually the traveling flow velocity near the obstacle). For a large range of Reynolds

TABLE 2 First-order closure model parameters.

Conditions	h_w (m)	h_v (m)	m (Stem/m^2)	S	k_v	D (m)	C_d	RMSE	R
1	0.3	0.06	33.3	0.0001	1.81	0.052	1.2146	0.007645784	0.9968
2	0.4	0.06	33.3	0.00005	2.3	0.052	1.2836	0.007438259	0.9942
3	0.3	0.06	133.3	0.00019	1.3	0.042	1.8689	0.005133355	0.994
4	0.3	0.135	33.3	0.00015	0.41	0.033	1.1001	0.007070949	0.9821
5	0.4	0.135	33.3	0.000045	0.59	0.025	1.1166	0.005625299	0.9929
6	0.3	0.135	133.3	0.0004	0.41	0.042	1.629	0.010235187	0.9935

numbers, Huai et al., 2021 noted that $S_t = 0.21$. Poggi et al. (2004) found that *St* tends to remain constant as the rigid vegetation density varies.

Using Nepf's formula, which differs significantly from our measured values, we have

$$f_{KH} = 0.032\left(\frac{\bar{U}}{\theta}\right) \tag{27}$$

whereas Ho et al. (1991) suggested that

$$\theta = \int_{-\infty}^{\infty}\left[\frac{1}{4} - \left(\frac{U-\bar{U}}{\Delta U}\right)^2\right]dz \tag{28}$$

The presence of vegetation strongly changes the cross-sectional distribution of mean streamwise velocity. This parameter is obtained by separating the average velocity and instantaneous velocity fluctuation of each velocity component (Hopkinson and Wynn, 2009). Compared with non-vegetated flow, the change of vegetation-driven turbulence is a function of physical parameters such as vegetation type (flexibility and rigidity), relative submergence (submergence and outflow) and density (sparse and dense). In the case of complete submergence, the vegetation changes the velocity and turbulence intensity profiles, forming a vertical mixing layer near the top of the S-shaped velocity profile at the inflection point (Ghisalberti and Nepf, 2002). This mixing layer is a large-scale coherent vortex with properties, which convections the high momentum fluid to the low momentum fluid region in the canopy. This mechanism can be further modified. The energy spectrum density analysis method is used to process the interface velocity, and the peak energy spectrum density corresponds to the dominant frequency of the continuous vortex structure.

4.3.2 Flow rate superposition model

Most studies on the hydrodynamic characteristics of aquatic plant canopies under inundation have recognized that their time-averaged flow velocity distributions have inflection points near top of the canopy. Several studies have also recognized hyperbolic-type distributions. Shi et al., 2023 derived hyperbolic sine and hyperbolic cosine distribution patterns above the canopy through an analytical approach. By adjusting each parameter in them, these functional expressions were able to obtain better agreement with the measured values. Researchers believe that the logarithmic distribution of the time-averaged flow velocity is the result of turbulent motion in the boundary layer, while the inverse tangent or hyperbolic distribution with an inflection point is the result of turbulent vertical mixing in the mixed layer. The essence of the former is the submerged aquatic plant canopy forming a rough boundary layer in the flow. The boundary layer above the canopy turbulent vortices does not penetrate the interior of the canopy, and is thus unaffected by the mixing of the two layers of water inside and outside the canopy. The essence of the latter is the plant canopy providing a rough pore medium for water flow through the canopy, whereby the two layers of different velocities inside and outside the canopy mix with each other to produce mixed-layer turbulent vortices, thus causing momentum exchange in the upper region. Nikora et al. (2013) derived a third type of distribution, namely, segmental superposition, which replicates the characteristics of interconnectedness and smoothness between the segments by superposition. A flow velocity superposition diagram is shown in Figure 8.

The analytical model was applied to solve the model using the parameters presented in Table 3.

For experimental conditions including flexible vegetation, a genetic algorithm gives

$$f_{KH} = 0.113\left(\frac{\bar{U}}{\theta}\right) \tag{29}$$

Compared with Eq. 30, Nepf formula and Eq. 30 were used to calculate f_{KH}. The correlation coefficient of Nepf formula was −0.5015, and that of Eq. 30 was 0.9562, indicating a great improvement in simulation accuracy (see Figure 9).

4.4 Manning's coefficient: Theoretical formula to solution

Manning's formula is used to calculate the resistance coefficient of water flow in rivers and wetlands, such as in river flow calculations, flood control analysis, and watershed water transfer. The complexity of actual river flow states requires extended and modified versions of Manning's formula. However, the specific expression of Manning's formula for vegetated rivers under nonuniform hook flow conditions remains unclear. As the core parameter in Manning's formula, this paper presents an equation for calculating Manning's coefficient for vegetated rivers. Using

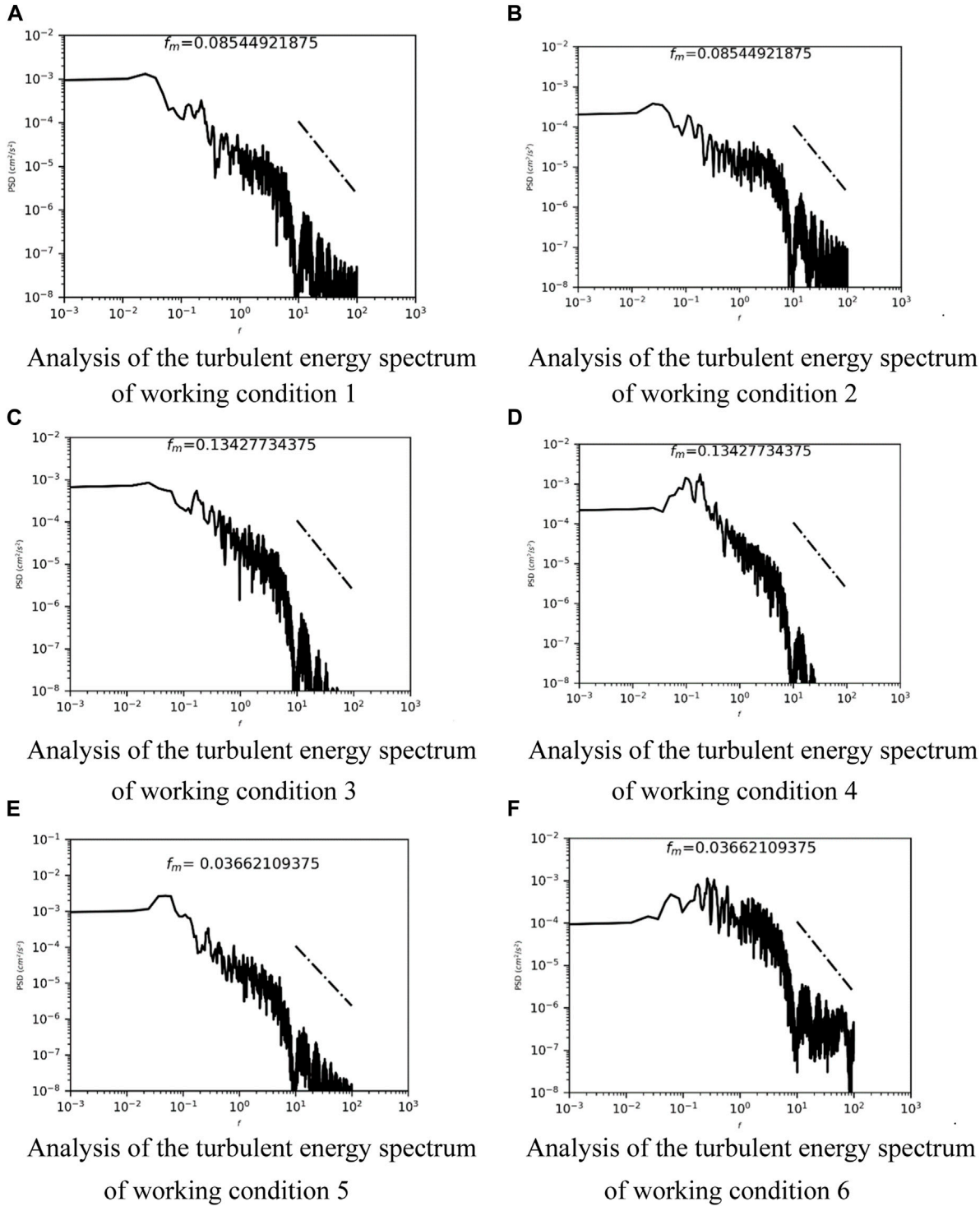

FIGURE 7
Analysis of turbulent energy spectrum for working condition 1–6 **(A–F)**.

this coefficient, we can then derive Manning's formula in nonuniform flow conditions. Manning's coefficient can be expressed as

$$U = \frac{1}{n} R^{2/3} S^{1/2} \tag{30}$$

The analytical solution for the flow velocity is averaged in the water depth direction to obtain the section average flow velocity, which is substituted into Eq. 30 to obtain the Manning's coefficient equation for the reference flow velocity superposition model. The linear superposition model equation can be expressed as

10.3389/fenvs.2023.1098993

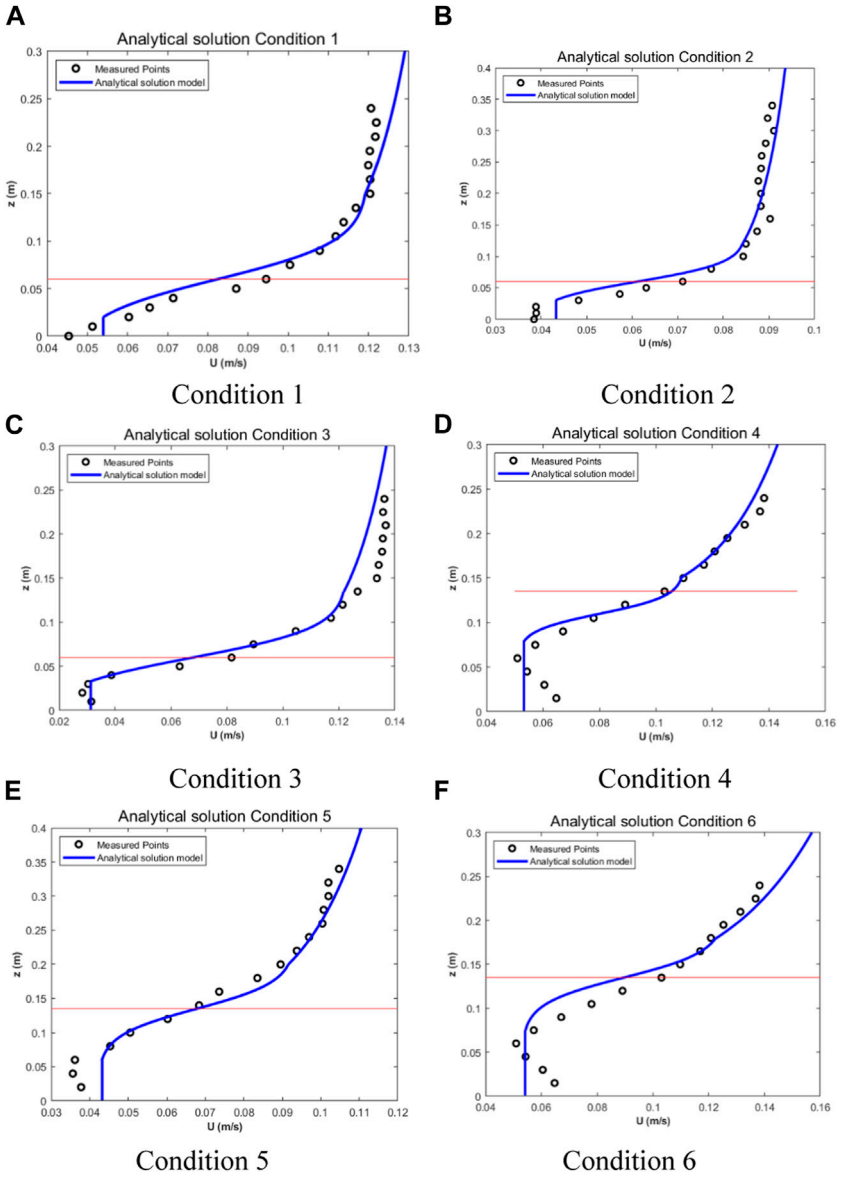

FIGURE 8
Analytical solutions of the flow velocity distribution for working condition 1–6 **(A–F)**.

TABLE 3 Parameters of superposition model.

Run	Shear vortex frequency (Hz)	U_1 (m/s)	U_2 (m/s)	d (m)	Z_0 (m)	θ (m)	*RMSE*	*R*
1	0.085449219	0.12	0.045	0.048	0.00000175	0.020	0.005774345	0.9801
2	0.085449219	0.085	0.0375	0.048	0.0000000495	0.015	0.004464172	0.9745
3	0.134277344	0.123	0.0125	0.048	0.000017	0.017	0.006171732	0.994
4	0.134277344	0.11	0.0507	0.108	0.000345	0.01	0.004990359	0.9918
5	0.036621094	0.0935	0.042	0.108	0.00035	0.02	0.003981397	0.9934
6	0.036621094	0.126	0.053	0.108	0.002118	0.015	0.008239536	0.9821

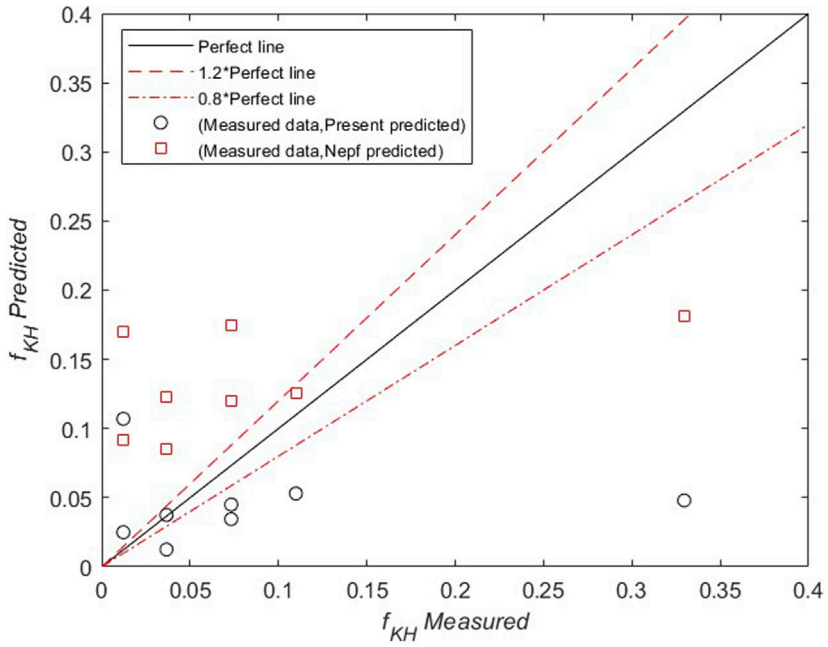

FIGURE 9
Comparison of measurements with f_{KH} of Nepf (2012) and predicted f_{KH} of present study.

$$\frac{U_f}{u_{*b}} = \underbrace{\frac{1}{u_{*b}}\left(\frac{gS_b}{0.5C_D a}\right)^{1/2}}_{\text{Unifrom Distribution}} + \underbrace{\frac{(U_i - U_{karman})}{u_{*b}}\left[1+\tanh\left(\frac{z-z_i}{L_e}\right)\right]}_{\text{Mixing Layer}} \times \underbrace{+\frac{u_{*m}}{u_{*b}}\frac{1}{\kappa}\ln\left(\frac{z-z_i-d_i}{z_o}\right)}_{\text{Log Layer}} \tag{31}$$

The expression for Manning's coefficient can be solved by performing a segmental integration of the following terms.

(1) U_{karman}

$$U_1 = \frac{1}{Z_1}\int_0^{Z_1} U_{karman}dZ = \left(\frac{gS_b}{0.5C_d a}\right)^{1/2} \tag{32}$$

Where 0~Z_1 is the zone of Karman vortex.

(2) U_{ML}

$$U_2 = \frac{1}{Z_2 - Z_1}\int_{Z1}^{Z2} U_{ML}dZ = \frac{\left\{\bar{u} + \frac{\Delta u \cdot m}{2}\cdot \ln\left[\cosh\left(\frac{z-\bar{z}}{Lm}\right)\right]\right\}\Big|_{z=z_2} - \left\{\bar{u} + \frac{\Delta u \cdot Lm}{2}\ln\left[\cosh\left(\frac{z-\bar{z}}{\mathrm{Lm}}\right)\right]\right\} \mid z = z_1}{Z_2 - Z_1} \tag{33}$$

Where Z_1~Z_2 is the zone of Mixing layer.

(3) U_{LL}

$$U_3 = \frac{1}{h_w - Z_2}\int_{Z_2}^{h_w} U_{ML}dZ = \frac{1}{h_w - Z_2}\left\{\frac{u_*}{k}\left[-Z + (Z-d)\ln\left(\frac{Z-d}{Z_0}\right)\right]\Big|_{Z=h_w} - \frac{u_*}{k}\left[-Z + (Z-d)\ln\left(\frac{Z-d}{Z_0}\right)\right]\Big|_{Z=Z_2}\right\} \tag{34}$$

Where Z_2~h_w is the Logarithmic rate region.

The resistance of water flow in a river channel directly affects the water level and water distribution in the basin. Simulations of the hydraulic process in a river channel using a mathematical model require the relevant resistance characteristics. The resistance of a vegetated river channel under nonuniform flow conditions mainly consists of two parts: the resistance caused by the rough form of the river itself and the resistance caused by the vegetation blocking water. The presence of vegetation causes the water depth and flow velocity to vary along the course, forming a constant nonuniform flow. In this case, we must consider both along-range energy loss and local resistance energy loss, which leads to the calculation formula for Manning's coefficient.

$$U_b = \frac{U_1 Z_1 + U_2 (Z_2 - Z_1) + U_3 (h_w - Z_2)}{h_w} \tag{35}$$

Combining Eqs. 30, 35, we obtain

$$n = R^{2/3}S^{1/2}\Big/ \times \left\{\begin{array}{c} Z_1^{\,2}\left(\frac{gS_b}{0.5C_D a}\right)^{1/2} + \left\{\bar{u} + \frac{\Delta u \cdot m}{2}\cdot \ln\left[\cosh\left(\frac{z_2 - \bar{z}}{L_m}\right)\right]\right\} \\ -\left\{\bar{u} + \frac{\Delta u \cdot Lm}{2}\ln\left[\cosh\left(\frac{z_1 - \bar{z}}{L_m}\right)\right]\right\} + \left[\left(\frac{-u_* d}{k}\ln\left(\frac{h_w - d}{Z_0}\right) + \frac{u_* d}{k}\ln\left(\frac{Z_2 - d}{Z_0}\right)\right)\left(\frac{h_w - Z_2}{h_w}\right)\right] \end{array}\right\} \tag{36}$$

5 Conclusion

The first-order closure model and analytical models were used to calculate and analyze the flow velocity distribution in a vegetated rectangular channel. Using experimental data from actual measurements and correlation coefficients gives results that are in good agreement with the actual measurements. This confirms that the application of both models to vegetated river channels is feasible.

The conclusions from this study can be summarized as follows: 1) Both the numerical model and the analytical model proposed in this paper can accurately simulate the water flow movement under the influence of vegetation. 2) In scenarios where Karman's constant is not applicable to complex vegetation morphologies, we have proposed a new Karman coefficient. 3) We adopted an image processing method to quantify the vegetation morphology accurately. 4) As the existing mixed-layer thickness formula is not applicable to vegetation with leaves, we have derived an improved approach. 5) To ensure applicability to larger-scale hydrodynamic simulations, we proposed an expression for Manning's coefficient based on the multi-layer flow velocity analytical solution model. Finally, we demonstrated the variation characteristics of Manning's coefficient with respect to the inundation degree, which provides theoretical support for vegetated river design and ecological restoration.

Data availability statement

The original contributions presented in the study are included in the article/supplementary material, further inquiries can be directed to the corresponding author.

Author contributions

Conceptualization: WW and HZ, methodology: WW and HZ, data analysis and modelling: WW, FJ, HW, and ZL, writing-original draft: FJ, HZ, and WW, writing-review and editing: WW, HZ, and YX. All authors contributed to the article and approved the submitted version.

Funding

This work was financially supported by a Scientific Research Project of the China Three Gorges Corporation (202103399), and Talent Program of China Institute of Water Resources and Hydropower Research (WE0199A052021), National Natural Science Foundation of China (52209083, 51809286).

Conflict of interest

HZ and ZL were employed by China Three Gorges Corporation.

The remaining authors declare that the research was conducted in the absence of any commercial or financial relationships that could be construed as a potential conflict of interest.

Publisher's note

References

Afzal, M. S., Holmedal, L. E., and Myrhaug, D. (2021). Sediment transport in combined wave–current seabed boundary layers due to streaming. *J. Hydraulic Eng.* 147 (4), 04021007. doi:10.1061/(asce)hy.1943-7900.0001862

Bornette, G., and Puijalon, S. (2011). Response of aquatic plants to abiotic factors: A review. *Aquat. Sci.* 73, 1–14. doi:10.1007/s00027-010-0162-7

Carollo, F. G., Ferro, V., and Termini, D. (2002). Flow velocity measurements in vegetated channels. *J. Hydraulic Eng.* 128 (7), 664–673. doi:10.1061/(asce)0733-9429(2002)128:7(664)

Caroppi, G., and Järvelä, J. (2022). Shear layer over floodplain vegetation with a view on bending and streamlining effects. *Environ. Fluid Mech.* 22, 587–618.

Chembolu, V., Kakati, R., and Dutta, S. (2019). A laboratory study of flow characteristics in natural heterogeneous vegetation patches under submerged conditions. *Adv. Water Resour.* 133, 103418. doi:10.1016/j.advwatres.2019.103418

Cheng, N. S., and Nguyen, H. T. (2011). Hydraulic radius for evaluating resistance induced by simulated emergent vegetation in open-channel flows. *J. hydraulic Eng.* 137 (9), 995–1004. doi:10.1061/(asce)hy.1943-7900.0000377

Cheng, N. S., Nguyen, H. T., Tan, S. K., and Shao, S. (2012). Scaling of velocity profiles for depth-limited open channel flows over simulated rigid vegetation. *J. Hydraulic Eng.* 138 (8), 673–683. doi:10.1061/(asce)hy.1943-7900.0000562

Ei-Hakim, O., and Salama, M. M. (1992). Velocity distribution inside and above branched flexible roughness. *J. Irrigation Drainage Eng.* 118 (6), 914–927. doi:10.1061/(asce)0733-9437(1992)118:6(914)

Erduran, K. S., and Kutija, V. (2003). Quasi-three- dimensional numerical model for flow through flexible, rigid, submerged and non-submerged vegetation. *J. Hydroinformatics* 5, 189–202. doi:10.2166/hydro.2003.0015

Fathi-Maghadam, M. N Kouwen. Nonrigid nonsubmerged Vegetative roughness on floodplains.*Jounral Hydraulic Eng.*, 1997,1 23(1):51–57.

Finnigan, J. Turbulence in plant canopies. *Annu. Rev. Fluid Mech.*, 2000, 32: 519–571.

Fischer- Antze, T., Stoesser, T., Bates, P., and Olsen, N. (2001). 3D numerical modelling of open-channel flow with submerged vegetation. *J. Hydraulic Res.* 39 (3), 303–310. doi:10.1080/00221680109499833

Ghisalberti, M., and Nepf, H. M. (2002). Mixing layers and coherent structures in vegetated aquatic flows. *J. Geophys. Res.* 107 (C2), 3011. doi:10.1029/2001jc000871

Ghisalberti, M., and Nepf, H. M. (2004). The limited growth of vegetated shear layers. *Water Resour. Res.* 40, W07502. doi:10.1029/2003wr002776

Ghisalberti, M., and Nepf, H. M. (2006). The structure of the shear layer in flows over rigid and flexible canopies. *Environ. Fluid Mech.* 6, 277–301. doi:10.1007/s10652-006-0002-4

Ho, C. M., and Huerre, P. (1984). Perturbed free shear layers. *Annu. Rev. Fluid Mech.* 16, 365–422. doi:10.1146/annurev.fl.16.010184.002053

Hopkinson, L., and Wynn, T. (2009). Vegetation impacts on near bank flow[J]. Ecohydrology: Ecosystems, land and water process interactions. *Ecohydrogeomorphology* 2 (4), 404–418. doi:10.1002/eco.87

Huai, W. X., Shi, H. R., Song, S. W., and Ni, S. (2018). A simplified method for estimating the longitudinal dispersion coefficient in ecological channels with vegetation. *Ecol. Indic.* 92, 91–98. doi:10.1016/j.ecolind.2017.05.015

Huai, W. X., Li, S., Katul, G. G., Liu, M. y., and Yang, Z. h. (2021). Flow dynamics and sediment transport in vegetated rivers: A review. *J. Hydrodynamics* 33 (3), 400–420. doi:10.1007/s42241-021-0043-7

Huai, W. X., Yang, L., Wang, W. J., Guo, Y. K., Wang, T., and Cheng, Y. G. (2019a). Predicting the vertical low suspended sediment concentration in vegetated flow using a random displacement model. *J. Hydrology* 578, 124101. doi:10.1016/j.jhydrol.2019.124101

Huai, W. X., Zeng, Y. H., Xu, Z. G., and Yang, Z. (2009). Three-layer model for vertical velocity distribution in open channel flow with submerged rigid vegetation. *Adv. Water Resour.* 32, 487–492. doi:10.1016/j.advwatres.2008.11.014

Huai, W. X., Zhang, J., Katul, G. G., Cheng, Y. g., Tang, X., and Wang, W. j. (2019b). The structure of turbulent flow through submerged flexible vegetation. *J. Hydrodynamics* 31 (2), 274–292. doi:10.1007/s42241-019-0023-3

Jiang, W., Zeng, L., Fu, X., and Wu, Z. (2022). Analytical solutions for reactive shear dispersion with boundary adsorption and desorption. *J. Fluid Mech.* 947, A37. doi:10.1017/jfm.2022.656

Katul, G. G., Mahrt, L., Poggi, D., and Sanz, C. (2004). One- and two-equation models for canopy turbulence. *Boundary- Layer. Meteorol.* 113, 81–109. doi:10.1023/b:boun.0000037333.48760.e5

Katul, G. G., Poggi, D., and Ridolfi, L. (2011). A flow resistance model for assessing the impact of vegetation on flood routing mechanics. *Water Resour. Res.* 47 (8), W08533. doi:10.1029/2010wr010278

Kemp, J. L., Harper, D. M., and Crosa, G. A. (2000). The habitat-scale ecohydraulics of rivers. *Ecol. Eng.* 16, 17–29. doi:10.1016/s0925-8574(00)00073-2

Konings, A. G., Katul, G. G., and Thompson, S. E. (2012). A phenomenological model for the flow resistance over submerged vegetation. *Water Resour. Res.* 48 (2), W02522. doi:10.1029/2011wr011000

Li, G., Gong, Z., Jiang, W., Zhan, J., Wang, B., Fu, X., et al. (2023). Environmental transport of gyrotactic microorganisms in an open-channel flow. *Water Resour. Res.* 59, e2022WR033229. doi:10.1029/2022WR033229

Li, Y., Xie, L., and Su, T. C. (2020). Profile of suspended sediment concentration in submerged vegetated shallow water flow. *Water Resour. Res.* 56 (4), e2019WR025551. doi:10.1029/2019wr025551

Lu, J., and Dai, H. C. (2016). Large eddy simulation of flow and mass exchange in an embayment with or without vegetation. *Appl. Math. Model.* 40 (17-18), 7751–7767. doi:10.1016/j.apm.2016.03.026

Luhar, M., Rominger, J., and Nepf, H. M. (2008). Interaction between flow, transport and vegetation spatial structure. *Environ. Fluid Mech.* 8, 423–439. doi:10.1007/s10652-008-9080-9

Nepf, H. M. (2012). Flow and transport in regions with aquatic vegetation. *Annu. Rev. Fluid Mech.* 44, 123–142. doi:10.1146/annurev-fluid-120710-101048

Nepf, H. M., and Ghisalberti, M. (2008). Flow and transport in channels with submerged vegetation. *Acta Geophys.* 56 (3), 753–777. doi:10.2478/s11600-008-0017-y

Nepf, H. M., and Vivoni, E. R. (2000). Flow structure in depth-limited, vegetated flow. *J. Geophys. Res.* 105 (C12), 28547–28557. doi:10.1029/2000jc900145

Nezu, I., and Sanjou, M. (2008). Turburence structure and coherent motion in vegetated canopy open-channel flows. *J. Hydro-environment Res.* 2, 62–90. doi:10.1016/j.jher.2008.05.003

Nikora, N., Nikora, V., and O'Donoghue, T. (2013). Velocity profiles in vegetated open-channel flows: Combined effects of multiple mechanisms. *J. Hydraulic Eng.* 139, 1021–1032. doi:10.1061/(asce)hy.1943-7900.0000779

Poggi, D., Krug, C., and Katul, G. G. (2009). Hydraulic resistance of submerged rigid vegetation derived from first-order closure models. *Water Resour. Res.* 45, W10442. doi:10.1029/2008wr007373

Poggi, D., Porporato, A., Ridolfi, L., Albertson, J. D., and Katul, G. G. (2004). The effect of vegetation density on canopy sub-layer turbulence. *Boundary-Layer Meteorol.* 111, 565–587. doi:10.1023/b:boun.0000016576.05621.73

Pourshahbaz, H., Abbasi, S., Pandey, M., Pu, J. H., Taghvaei, P., and Tofangdar, N. (2022). Morphology and hydrodynamics numerical simulation around groynes. *ISH J. Hydraulic Eng.* 28 (1), 53–61. doi:10.1080/09715010.2020.1830000

Pu, J. H., Pandey, M., and Hanmaiahgari, P. R. (2020). Analytical modelling of sidewall turbulence effect on streamwise velocity profile using 2D approach: A comparison of rectangular and trapezoidal open channel flows. *J. Hydro-Environment Res.* 32, 17–25. doi:10.1016/j.jher.2020.06.002

Rominger, J. T., Lightbody, A. F., and Nepf, H. M. (2010). Effects of added vegetation on sand bar stability and stream hydrodynamics. *J. Hydraulic Eng.* 136 (12), 994–1002. doi:10.1061/(asce)hy.1943-7900.0000215

Shan, Y. Q., Zhao, T., and Liu, C. (2020). Turbulence and bed-load transport in channels with randomly distributed emergent patches of model vegetation. *Geophys. Res. Lett.* 47 (12), e2020GL087055.

Shi, J. Z., Li, Y. H., Hughes, J. M. R., and Zhao, M. (2013). Hydrological characteristics of vegetated river flows: A laboratory flume study. *Hydrological Sci. J.* 58 (5), 1047–1058. doi:10.1080/02626667.2013.797580

Shucksmith, J. D., Boxall, J. B., and Guymer, I. (2010). Effects of emergent and submerged natural vegetation on longitudinal mixing in open channel flow. *Water Resour. Res.* 46 (4), W04504. doi:10.1029/2008wr007657

Stoesser, T., Salvador, G. P., Rodi, W., and Diplas, P. (2009). Large eddy simulation of turbulent flow through submerged vegetation. *Transp. Porous Media* 78 (3), 347–365. doi:10.1007/s11242-009-9371-8

Tinoco, R. O. (2020). Simplification bias: Lessons from laboratory and field experiments on flow through aquatic vegetation. *Earth Surf. Process. Landforms* 45 (1), 121–143. doi:10.1002/esp.4743

Tschisgale, S., Löhrer, B., Meller, R., and Fröhlich, J. (2021). Large eddy simulation of the fluid-structure interaction in an abstracted aquatic canopy consisting of flexible blades. *J. Fluid Mech.* 916 (A43), A43–A37. doi:10.1017/jfm.2020.858

Wang, W. J., Huai, W. X., Li, S. L., Wang, P., Wang, Y. F., and Zhang, J. (2019). Analytical solutions of velocity profile in flow through submerged vegetation with variable frontal width. *J. Hydrology* 578, 124088. doi:10.1016/j.jhydrol.2019.124088

Wang, W. J., Peng, W. Q., Huai, W. X., Katul, G., Liu, X. B., Dong, F., et al. (2018). Derivation of canopy resistance in turbulent flow from first- order closure models. *Water* 10, 1782. doi:10.3390/w10121782

Wilson, C. A. M. E., Stoesser, T., Bates, P. D., and Pinzen, A. B. (2003). Open channel flow through different forms of submerged flexible vegetation. *J. Hydraulic Eng.* 129, 847–853. doi:10.1061/(asce)0733-9429(2003)129:11(847)

Wu, H. L., Cheng, N. S., and Chiew, Y. M. (2021a). Bed-load transport in vegetated flows: Phenomena, parametrization, and prediction. *Water Resour. Res.* 57 (4), e2020WR028143. doi:10.1029/2020wr028143

Wu, H. L., Singh, A., Foufoula-Georgiou, E., Guala, M., Fu, X., and Wang, G. (2021b). A velocity-variation-based formulation for bedload particle hops in rivers. *J. Fluid Mech.* 912, A33. doi:10.1017/jfm.2020.1126

Yan, C., Nepf, H. M., Huang, W. X., and Cui, G. X. (2017). Large eddy simulation of flow and scalar transport in a vegetated channel. *Environ. Fluid Mech.* 17 (3), 497–519. doi:10.1007/s10652-016-9503-y

Zeng, C., and Li, C. W. (2014). Measurements and modeling of open-channel flows with finite semi-rigid vegetation patches. *Environ. Fluid Mech.* 14 (1), 113–134. doi:10.1007/s10652-013-9298-z

Zhang, J., Wang, W. J., Shi, H. R., Li, Z., Tang, X., and Xia, Z. H. (2021). An analytical two-layer model for velocity distribution in open-channel flows with submerged flexible canopies considering multiply fluids mechanics. *J. Hydrology* 603, 127102. doi:10.1016/j.jhydrol.2021.127102

Zhao, H. Q., Tang, H. W., Yan, J., Dai, H. C., and Liu, Z. W. (2021). Interactions between bedforms and open channel flows through submerged vegetation. *Adv. Water Sci.* 32 (2), 250–258. (In Chinese).

Zhao, H. Q., Tang, H. W., Yan, J., Liang, D. F., and Zheng, J. Y. (2020). Spectral shortcut in turbulence energy transfer in open channel flow over submerged vegetation. *J. Hydro-environment Res.* 33, 10–18. doi:10.1016/j.jher.2020.10.002

Zhao, H. Q., Yan, J., Yuan, S. Y., Liu, J. F., and Zheng, J. Y. (2019). Effects of submerged vegetation density on turbulent flow characteristics in an open channel. *Water* 11, 2154. doi:10.3390/w11102154

Zhao, T., and Nepf, H. (2021). Turbulence dictates bedload transport in vegetated channels without dependence on stem diameter and arrangement. *Geophys. Res. Lett.* 48, e2021GL095316. doi:10.1029/2021gl095316

Nomenclature

a	the total frontal vegetation area per unit volume
C_d	the drag force coefficient
D	water retention width
d	the zero-plane
F_d	the vegetation resistance term
f	the vortex frequency
K_m	the vortex viscosity coefficient
κ	the von Kármán constant
L	the characteristic length of the vortex size
L_e	characteristic length scale of the mixing layer
l_{eff}	the effective mixing-length scale
N	the total number of samples
S_t	the dimensionless Strouhal number
U	the characteristic flow velocity
U_i	velocity at the inflection point zi
U_{karman}	flow velocity in the Kármán vortex street zone
U_{LL}	the time-averaged velocity
u(t)	the instantaneous velocity in the direction corresponding to the data
u_*	the frictional flow velocity
ν	the kinematic viscosity of water
z_0	the hydrodynamic roughness length
z	the vertical distance calculated from the bottom of the riverbed
δ	Shear layer thickness

frontiers | Frontiers in Marine Science

TYPE Original Research
PUBLISHED 27 September 2023
DOI 10.3389/fmars.2023.1251469

OPEN ACCESS

EDITED BY
Weijie Wang,
China Institute of Water Resources and Hydropower Research, China

REVIEWED BY
Bo-Ping Han,
Jinan University, China
Liang Peng,
Jinan University, China

*CORRESPONDENCE
Ming Duan
duanming@ihb.ac.cn

RECEIVED 01 July 2023
ACCEPTED 11 September 2023
PUBLISHED 27 September 2023

CITATION
Zhang C, Mei F, Luo B, Zhang D, Cheng X, Xiong Y, Bao J, Duan R, Jiang H, Jeppesen E and Duan M (2023) Phytoplankton control by stocking of filter-feeding fish in a subtropical plateau reservoir, southwest China. *Front. Mar. Sci.* 10:1251469. doi: 10.3389/fmars.2023.1251469

Phytoplankton control by stocking of filter-feeding fish in a subtropical plateau reservoir, southwest China

Chaoshuo Zhang[1,2,3], Feng Mei[1,4], Bin Luo[1,5], Dongxu Zhang[1,2], Xinyu Cheng[6], Yongying Xiong[7], Jianghui Bao[1], Rui Duan[8], Hao Jiang[9], Erik Jeppesen[3,10,11,12,13] and Ming Duan[1]*

[1]State Key Laboratory of Freshwater Ecology and Biotechnology, Institute of Hydrobiology, Chinese Academy of Sciences, Wuhan, China, [2]University of Chinese Academy of Sciences, Beijing, China, [3]Limnology Laboratory, Department of Biological Sciences and Centre for Ecosystem Research and Implementation, Middle East Technical University, Ankara, Türkiye, [4]School of Life Sciences, Nanchang University, Nanchang, China, [5]College of Animal Science, Guizhou University, Guiyang, China, [6]Agronomy and Life Science Department, Zhaotong University, Zhaotong, China, [7]Zhaotong Yudong Reservoir Administration, Zhaotong, China, [8]Wuhan Sino-Hiking Technology Company Limited, Wuhan, China, [9]China Renewable Energy Engineering Institute, Beijing, China, [10]Department of Ecoscience, Aarhus University, Aarhus, Denmark, [11]Sino-Danish Centre for Education and Research, Beijing, China, [12]Institute of Marine Sciences, Middle East Technical University, Mersin, Türkiye, [13]Institute for Ecological Research and Pollution Control of Plateau Lakes, School of Ecology and Environmental Science, Yunnan University, Kunming, China

Stocking of filter-feeding fish (mainly *Hypophthalmichthys molitrix* and *Aristichthys nobilis*) is a common method used in lakes and reservoirs in (sub) tropical China to control phytoplankton, but the results are ambiguous and lack long-term data to support. We analysed a decade (2010-2020) of monitoring data from a subtropical plateau reservoir, southwest China, to which filter-feeding fish were stocked annually. We found that the total phytoplankton biomass, cyanobacteria biomass and average individual mass of phytoplankton decreased significantly during the study period despite absence of nutrient concentration reduction. However, the grazing pressure of zooplankton on phytoplankton also decreased markedly as judged from changes in the ratio of zooplankton biomass to phytoplankton biomass and *Daphnia* proportion of total zooplankton biomass. This is likely a response to increasing predation on zooplankton by the stocked fish. Our results also indicated that water temperature, total phosphorus and water level promoted phytoplankton growth. Our results revealed that filter-feeding fish contributed to the decline in the biomass of phytoplankton but that it also had a strong negative effect on the grazing pressure of zooplankton on phytoplankton, even in this deep reservoir where zooplankton may have a better chance of survival through vertical migration. The particular strong effect on zooplankton is most likely due to imbalance of stocking and harvesting of fish. In the management of eutrophic reservoirs, the reduction of external nutrient loading should have highest priority. In highland (low temperature) deep-water eutrophic reservoirs, stocking of filter-feeding fish may help to control filamentous phytoplankton provided that the fish stocking is properly managed. The optimal stocking intensity of filter-feeding fish that can help control

phytoplankton in such reservoirs without excessive impact on large-bodied zooplankton is a topic for further elucidation, however.

KEYWORDS

phytoplankton, filter-feeding fish, trophic cascade, highland reservoir, fish stocking

1 Introduction

Cyanobacteria blooms caused by eutrophication are threatening the health of freshwater ecosystems (Amorim et al., 2017; Zhang et al., 2019). The ecosystem services, aquatic organisms and human beings who depend on freshwater resources are all affected by this environmental problem (Olokotum et al., 2020). Various in-lake techniques have been developed in eutrophic waters to restore water quality and prevent lake deterioration in addition to external nutrient loading reduction. One of these techniques is biomanipulation, which involves controlling phytoplankton with large-bodied zooplankton, achieved by planktivorous fish removal to reduce predation pressure on zooplankton (Shapiro et al., 1975; Jeppesen et al., 2005). Increasing the grazing pressure on phytoplankton, including cyanobacteria directly by stocking of filter-feeding fish (mainly silver carp *Hypophthalmichthys molitrix* and bighead carp *Aristichthys nobilis*) is another technique. Filter-feeding fish influence phytoplankton through trophic cascades, (Attayde and Hansson, 2001; Jeppesen et al., 2012; Lemmens et al., 2018) and have been widely used in (sub)tropical regions in China (Xie and Liu, 2001; Guo et al., 2015; Lin et al., 2020; Lin et al., 2021). However, the effectiveness of phytoplankton control by filter-feeding fish remains controversial.Some studies have suggested that filter-feeding fish is a useful method to suppress phytoplankton and enhance water quality in shallow lakes (Starling, 1993; Guo et al., 2015), while other results demonstrated that filter-feeding fish cannot control phytoplankton instead increase the biomass or density of phytoplankton, b ecause grazing pressure of zooplankton is reduced by indiscriminate filter feeding from fish (Lin et al., 2020; Mao et al., 2020; Lin et al., 2021). Others again have argued that in the cases of large individual phytoplankton as the dominant species, filter-feeding fish are able to suppress these effectively (Domaizon and Devaux, 1999; Guo et al., 2015).

There may also be variations in the outcome of filter-feeding fish stocking with lake depth. In most experiments conducted in shallow lakes and mesocosms in the subtropics, filter-feeding fish were not able to control the phytoplankton despite massive stocking (Mao et al., 2020; Shen et al., 2021). In fact, they may even stimulate the growth of nanoplankton by preying on zooplankton and by sediment disturbance, potentially bringing nutrients to the water (Jeppesen et al., 2012; Zhang et al., 2016a). Compared with shallow lakes, it may be easier for filter-feeding fish to control phytoplankton in highland reservoirs as studies have shown that zooplankton gets lower predation pressure form fish in deep lakes and reservoirs than in shallow lakes (Jeppesen et al., 1997), and cladocerans in deep reservoirs may have more opportunity to avoid predation by vertical migration (Jeppesen et al., 1997; Hart, 2011). There may also be better chances for zooplankton population recovery when fish predation is released (Lin et al., 2014). These zooplankton may contribute to the control of nanoplankton that filter-feeding fish cannot feed on. The low mean annual temperature in deep and highland subtropical lakes may also make phytoplankton control less challenging than in lowland, shallow, subtropical lakes (Jeppesen et al., 2012; Mao et al., 2020), where high temperatures stimulate growth of phytoplankton.

To reveal how the silver carp and bighead carp affect phytoplankton and zooplankton, we conducted a decade-long study (from January 2010 to December 2020) in Yudong Reservoir, a highland eutrophic reservoir. We hypothesised that the continuous filter-feeding fish stockings would alleviate the cyanobacteria blooms and reduce the biomass of phytoplankton in this deep highland (low temperature) subtropical reservoir, although it might also lead to reduction in zooplankton biomass and their grazing on phytoplankton, though this effect would be less than in shallow lakes, as zooplankton may have a better chance of survival through vertical migration (Jeppesen et al., 1997).

2 Materials and methods

2.1 Study area

The Yudong Reservoir, located at the upper stream of Hengjiang River (a tributary of the lower Jinsha River) in Zhaotong City, is one of eight large reservoirs (capacity > 10^8 m^3) in Yunnan Province, China (Figure 1). As a comprehensive water conservancy project, Yudong Reservoir supplies water for 800,000 people and irrigates 250 km^2 of farmland. It is a typical deep valley plateau reservoir with an average elevation of almost 2000 m. The maximum and average water depths are 84.4 m and about 30.3 m, respectively. The area of the Yudong Reservoir is 13.6 km^2, and its total storage capacity is 3.64×10^8 m^3, with an annual exchange coefficient of 0.8-1.0. In its 709 km^2 watershed, mainly consisting of high mountains and small valley plains, agriculture is the major economic activity. The area has distinct dry and rainy seasons. The annual precipitation is 700-800 mm, and precipitation in the rainy season (May to October) is about 90% of the whole year's rainfall.

The Yudong Reservoir was fully filled in 2000, followed by fish stocking and fishery activities. At first, the purpose of stocking was to enhance the local economic income. However, the water quality

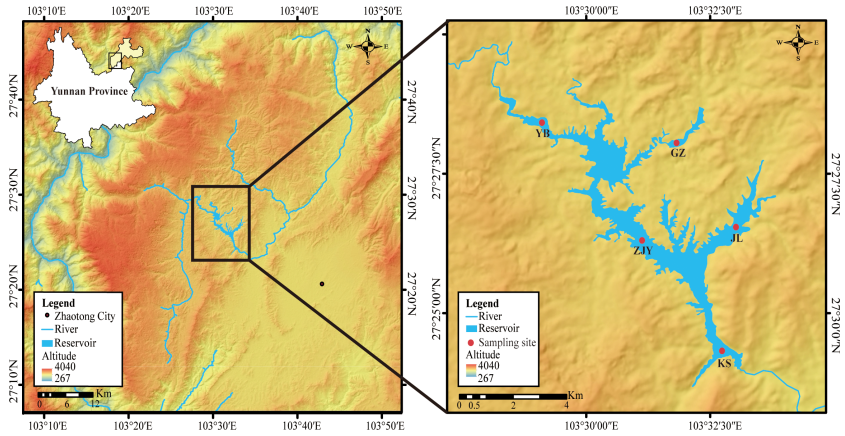

FIGURE 1
Location of sampling sites in the Yudong Reservoir, Yunnan Province, China, 2010-2020.

deteriorated, affected by the ecological deterioration and rural non-point source pollution in the watershed. Since 2008, cyanobacteria blooms have often occurred, causing serious threats to the safety of the drinking water supply. Therefore, the management strategy was adjusted to control phytoplankton by stocking filter-feeding fish. The quantities of stocking were determined by the local management department based on the year's phytoplankton density and water transparency. And these stocking were completed in the late spring of each year, normally in April, before the rainy season. The average weight of the stocked silver carp was 6.2 ± 0.8g, average total length was 3.0 ± 0.5cm and the average weight of the bighead carp was 48.5 ± 5.8g, average total length was 15 ± 2.5cm. The fishing of silver carp and bighead carp was mainly carried out by net trawling, supplemented by gillnet fishing. Individuals with a body weight < 5kg were released back.

2.2 Sampling and processing

2.2.1 Water parameters and fish

The data about Yudong Reservoir water quality were obtained from the Zhaotong Yudong Reservoir Administration. Water samples were collected at 5 fixed long-term monitoring sites monthly (Figure 1) from January 2010 to December 2020 by the department's professional monitoring team following the *Environmental Quality Standards for Surface Water* (China, 2002a) and the standard of the *Guidance on Sampling Techniques* (China, 2009). Chemistry analyses were completed according to the *Standard Methods for the Examination of Water and Wastewater* (China, 2002b). The water quality parameters included 10 variables, including pH, water temperature (WT, °C), conductivity (Cond, μs/cm), total phosphorus (TP, mg/L), total nitrogen (TN, mg/L), ammonia (NH_4-N, mg/L), nitrate (NO_3-N, mg/L), water transparency (SD, m), water level (WL, m) and chlorophyll a (Chl-a, μg/L). The monthly sampling dates were selected based on weather conditions to ensure that the water samples were not affected by rainfall, strong winds and runoff. The analytical quality control was carried out in accordance with APHA (2005), with reference to previous studies (Table S1; Wu et al., 2018; Qu et al., 2020).

Filter-feeding fish data on Yudong Reservoir from 2010 to 2020 were provided by the Zhaotong Yudong Reservoir Administration. The annual stocking and harvesting weights, as well as CPUE of filter-feeding fish, were recorded in detail.

2.2.2 Plankton community

We collected 1 L depth-integrated water from each site once a month. After treated with 10 mL Lugol's iodine solution and sedimentation more than 48 h, the residue was collected and examined under ×100 to ×400 magnification to enumerate phytoplankton. The phytoplankton species were identified following the taxonomic classification of Hu (2006). The biomass of common phytoplankton taxa was calculated based on cell size measurements using formulae from Zhang and Huang (1991). The approximation dry weight of phytoplankton was obtained from corresponding biological volume multiplied by 0.29 (Reynolds, 1984).

We also collected zooplankton samples every month in some years (2011, 2013, 2015, 2018, 2019 and 2020). At each sampling, we filtered 10 L depth-integrated water with 64 mm net and preserved the samples in 4% formaldehyde. Crustacean zooplankton (cladocerans, copepodites and adult copepods) were counted at microscope with an ocular micrometer. Species represented by more than 100 individuals were identified according to Chiang and Du (1979). Crustacean zooplankton biomass (wet weight) was calculated by formulas from Dumont et al. (1975) and Huang (1999) based on length measurements of 30 individuals of each taxon. Rotifers were counted at ×100 magnification, and the biomass was calculated according to the standard weights obtained from several lakes in the Yangtze River (He et al., 2018).

2.3 Statistical analyses

2.3.1 Generalized additive model

We used generalized additive models (GAMs) on monthly data to uncover the temporal trend in variables using the "gam" function and cubic regression spline from the R-package "mgcv" (Wood, 2020). All parameters besides pH and water level were log-transformed [log10(X+1)] to reduce distributional skewness. Spearman rank correlation coefficient (ρ) with year was calculated, when the temporal change of parameter was not linear.

2.3.2 Piecewise structural equation model

Piecewise structural equation modelling (pSEM) was used to elucidate the influences of filter-feeding fish and environmental variables on the phytoplankton and zooplankton communities through different pathways. Different from SEM, piecewise SEM has a more flexible mathematical framework and a wider range of use (less restrictions on the original dataset). We assumed that filter-feeding fish could not only directly reduce phytoplankton biomass through grazing effects but also indirectly by changing the predation pressure of zooplankton. Environmental variables can also directly affect the phytoplankton biomass through bottom-up effects. All response variables were transformed to achieve normal distributions, as for the GAMs. During the model building process, factors that affect the degree of fit were removed. The model fit was assessed by Fisher's C statistics (Shipley, 2013).

2.3.3 Top-down control

We calculated several indicators to assess the trophic cascade effects of filter-feeding fish stocking via predation on zooplankton. The proportion of large-bodied cladocerans (species sensitive to fish grazing) within the total zooplankton biomass, zooplankton and cladoceran body mass were used to indicate the predation pressure on the zooplankton community (Jackson et al., 2007; Jeppesen et al., 2011). In addition, the ratio of zooplankton biomass to phytoplankton biomass was calculated to reflect the grazing pressure of zooplankton on phytoplankton (Jeppesen et al., 2003; Jeppesen et al., 2011). The average individual mass of phytoplankton was calculated using total phytoplankton biomass divided by total phytoplankton abundance (Yvon-Durocher et al., 2011; Zhang et al., 2016b).

2.4 Data analysis strategy

We first used GAMs to analyse the trend of environmental variables, zooplankton, phytoplankton and top-down strength (zooplankton biomass to phytoplankton, Zoop : Phty) over time. Second, Spearman correlation analyses and redundancy analysis (RDA) were conducted to analysis the relationships between filter-feeding fish stocking, environmental variables and phytoplankton and zooplankton taxonomic groups. Hierarchical partitioning (HP) was conducted to estimate the contributions of environmental factors to the variance in the phytoplankton biomass and several indicators of top-down control (Walsh and Mac Nally, 2013). Finally, piecewise SEM analyses were performed to show the influence of filter-feeding fish on the phytoplankton community in deep reservoirs represented by the Yudong Reservoir. We used the Friedman test to check the condition of phytoplankton average individual biomass and cyanobacteria biomass. All graphs and statistical analysis were performed by the RStudio software. The results were considered to be significant when $p < 0.05$ or $p < 0.01$. As zooplankton data were partially missing, the only data from the years for which zooplankton data were available were used in the Spearman correlation analysis, the redundancy analysis, the hierarchical partitioning and the construction of the piecewise structural model.

3 Results

3.1 Dynamics of the environmental variables and fish

From 2010 to 2020, the average TP in Yudong Reservoir was 0.13 mg/L and remained high (Figure 2; Table S2). TN, NH_4-N and NO_3-N showed a significant upward trend ($\rho = 0.27$, $\rho = 0.13$ and $\rho = 0.25$, respectively). The mean concentration of TN was 1.14 mg/L. Chl-a decreased significantly ($\rho = -0.68$) but remained high, with an annual average value of 34 μg/L in 2020. Cond and SD increased ($\rho = 0.41$ and $\rho = 0.13$), while WT, pH and WL did not change significantly during the study period (Figures 2; S1). The contribution of each variable to principal components is displayed in Figure S2.

Fishing was organised annually with the primary aim of nutrient removal. However, the annual average catches of fish were far lower than the amount stocked (Figure 3).

3.2 Dynamics of the plankton community

The biomass of phytoplankton decreased significantly ($\rho = -0.206$), from 14.6 mg/L in 2010 to 3.6 mg/L in 2020 (24% of that in 2010) (Figure 4A). Meanwhile, the cyanobacteria biomass decreased significantly (Friedman test, $p<0.01$). the average individual biomass of phytoplankton decreased, from 5.3×10^{-6} μg/ind to 0.3×10^{-6} μg/ind (Friedman test, $p<0.01$) (Figure S3). The zooplankton biomass ($\rho = -0.938$) decreased significantly to an average of 0.04 mg/L in 2020, which was 1% of the level in 2011 (Figure 4B). Coinciding with this, the ratio of zooplankton biomass: phytoplankton biomass decreased markedly from 1.79 to 0.01 ($\rho = -0.865$, Figure 4C). *Daphnia*% in terms of biomass, zooplankton body mass and cladoceran body mass showed similar decreasing trends ($\rho = -0.589$, $\rho = -0.178$ and $\rho = -0.329$, Figure 4).

3.3 Environmental factors driving plankton resource

The effects of environmental variables on phytoplankton biomass were evaluated by redundancy analysis. The first and

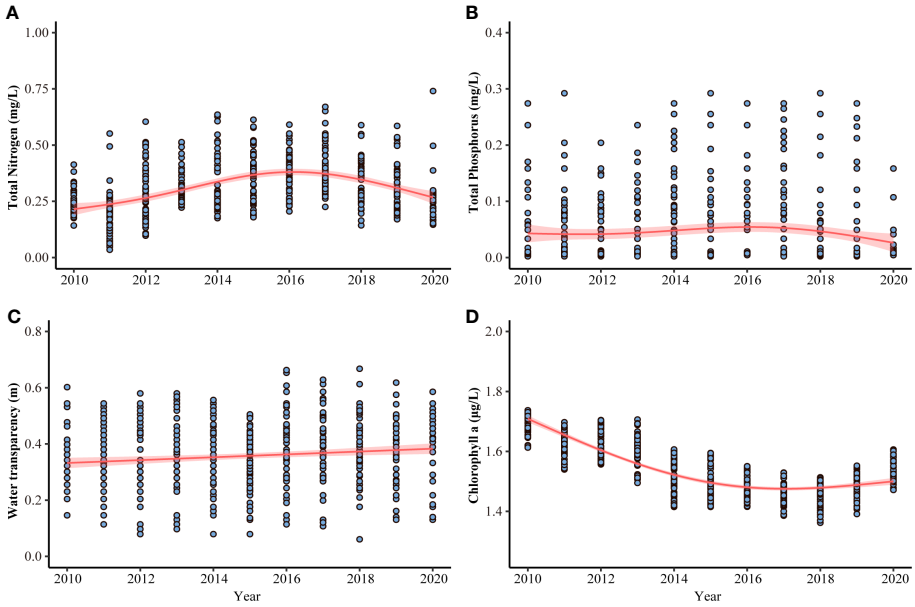

FIGURE 2
Time series of monthly total nitrogen **(A)**, total phosphorus **(B)**, water transparency **(C)** and chlorophyll-a **(D)** in Yudong reservoir. The solid line represents the regression line fitted with monthly data using generalized additive models (GAMs). The 95% confidence intervals from the GAM model are shaded.

second ordinal axes of RDA explained a total of 98.8%. The results indicated that the biomass and average individual biomass of phytoplankton were mainly affected by fish, TN, TP and WT (Figure 5A).

Both silver carp CPUE and bighead carp CPUE and thus total fish stocking had significant negative correlations with the cyanobacteria biomass and the average individual biomass of phytoplankton. TP and WT promoted the phytoplankton biomass, including cyanobacteria, and the water level increasing also can promote the phytoplankton biomass. However, there was a negative correlation between TN and phytoplankton, including cyanobacteria (Figure 5B).

For all three response variables (phytoplankton biomass, cyanobacteria biomass and average individual mass of phytoplankton), hierarchical partitioning revealed WT (2.5 to 36.4%) and silver carp CPUE (2.4% to 37.2%) to be the most important influencing variables (Figure 6A), showing the largest independent effects on variance. For the zooplankton variables, phytoplankton biomass (16.3 to 19.7%), cyanobacteria biomass (12.9 to 19.3%) and silver carp CPUE (14.2 to 17.1) were the most important influencing variables (Figure 6B). The results of RDA and HP revealed that phytoplankton and cyanobacteria in the reservoir were mainly affected by silver carp CPUE and WT. Phytoplankton and cyanobacteria were affected more by silver carp than zooplankton, and zooplankton was affected by both top-down and bottom-up factors.

The results of the piecewise SEM overall concur with the other analyses. The filter-feeding effects on zooplankton and phytoplankton were significant, indicating that filter-feeding fish contributed importantly to the reduction of zooplankton and phytoplankton

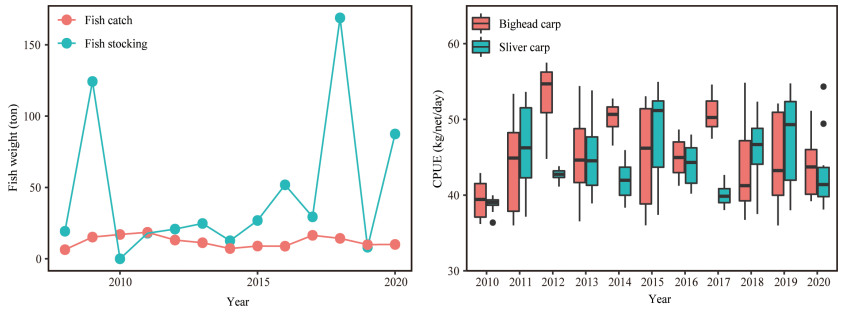

FIGURE 3
Time series of fish stocking, fish harvesting and CPUE obtained from the Zhaotong Yudong Reservoir Administration (2010–2020).

10.3389/fmars.2023.1251469

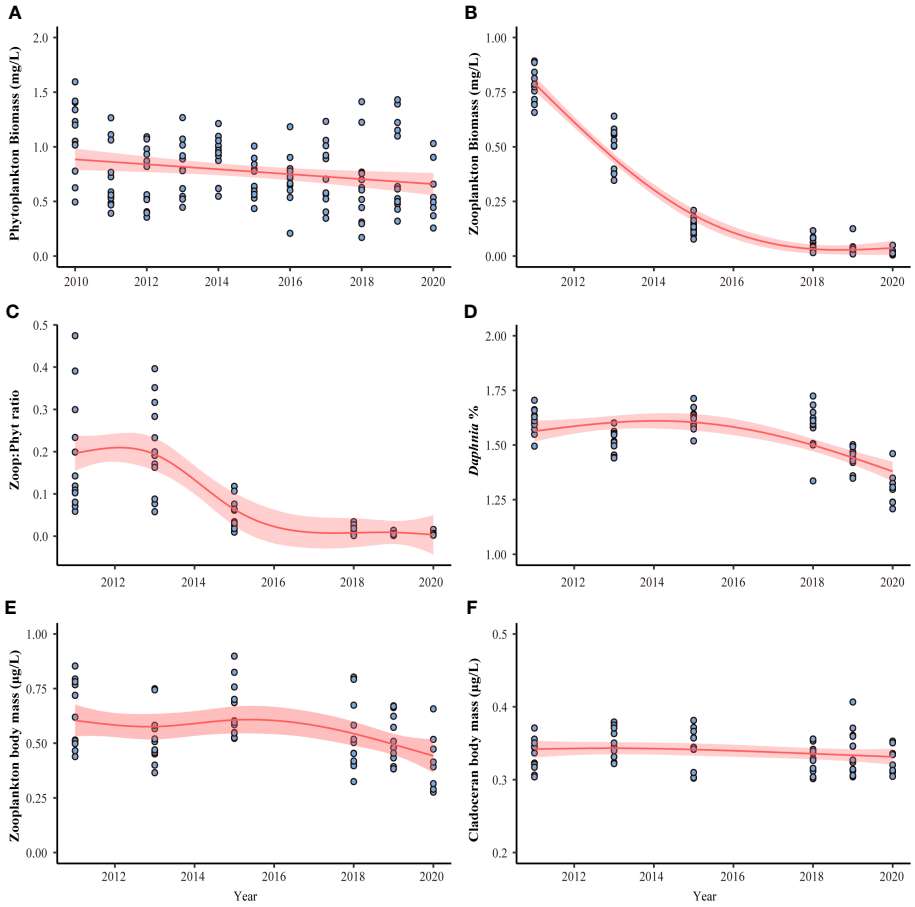

FIGURE 4
Time-series of phytoplankton biomass **(A)**, zooplankton biomass **(B)**, the ratio of zooplankton biomass to phytoplankton biomass ratio (Zoop: Phyt, **(C)**, *Daphnia* biomass percentage (*Daphnia* %, **(D)**, zooplankton body mass **(E)** and cladoceran body mass **(F)** in Yudong Reservoir.

biomass. The grazing pressure of zooplankton was weak, and the negative correlation between zooplankton and phytoplankton was not obvious. By contrast, TP and WT promoted the growth of phytoplankton, while bighead carp CPUE and total fish stocking also had negative correlations with cyanobacteria biomass and the average individual biomass of phytoplankton. Higher phytoplankton biomass may decrease water transparency. TN also had a negative relationship with phytoplankton (Figure 7).

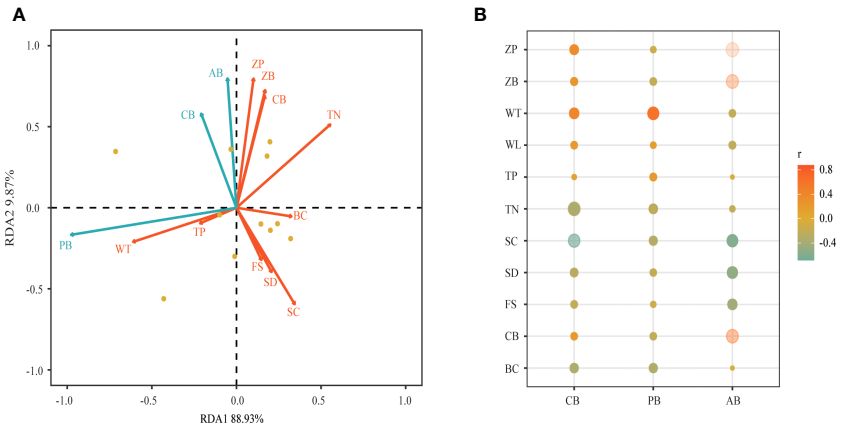

FIGURE 5
Redundancy analysis **(A)** and Spearman correlation analysis **(B)** of phytoplankton between several environmental indicators and top-down effect indicators. FS, fish stocking; BC, bighead carp CPUE; SC, silver carp CPUE; PB, phytoplankton biomass; AB, average individual mass of phytoplankton; PB, phytoplankton biomass; CB, cyanobacteria biomass; TP, total phosphorus; TN, total nitrogen; WT, water temperature; WL, water level; SD, water transparency; ZP, zooplankton biomass, phytoplankton biomass; ZB, zooplankton biomass.

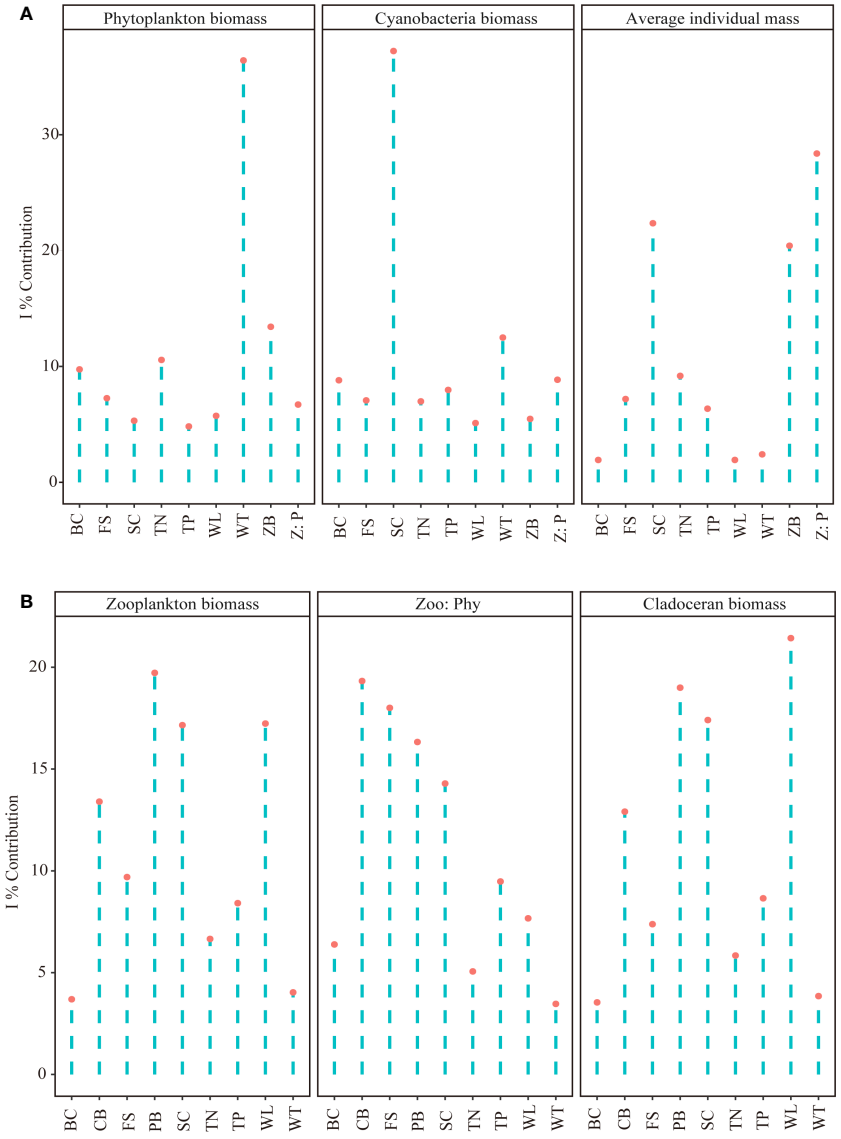

FIGURE 6
Comparison of predictors explaining variance of zooplankton **(A)** and phytoplankton **(B)** in Yudong Reservoir with % independent contribution by hierarchical partitioning. (% I). FS, fish stocking; BC, bighead carp CPUE; SC, silver carp CPUE; PB, phytoplankton biomass; CB, cyanobacteria biomass; TP, total phosphorus; TN, total nitrogen; WT, water temperature; WL, water level; ZP, zooplankton biomass, phytoplankton biomass; ZB, zooplankton biomass.

4 Discussion

Using Yudong Reservoir as a case study, we discussed the effects of environment parameters and filter-feeding fish as well as the contribution difference of trophic cascades on phytoplankton in deep highland reservoirs. Coinciding with the continuous introduction of filter-feeding fish into Yudong Reservoir, we found that the phytoplankton biomass and average individual mass of phytoplankton decreased significantly despite no reduction in nutrient level. Moreover, the biomass of zooplankton, including cladocerans, has declined significantly in recent years. The body size of zooplankton and cladocerans decreased as well, indicating strong top-down control on zooplankton by the fish.

4.1 Effects of environmental factors on phytoplankton

Even though the Yudong Reservoir is located in a subtropical climate, its high-altitude level and its large depth leads to a lower average WT than typically found in lowland subtropical lakes (e, g., Lake Qiandao and Lake Taihu) (Mao et al., 2020; Su et al., 2021), and this may dampen the growth of cyanobacteria (Li et al., 2020; Nwankwegu et al., 2020). Supporting this view, our correlation analysis indicated that, under the current eutrophic conditions (high TN and TP), increased WT promoted phytoplankton growth (Figure 6).

The RDA results illustrated that the phytoplankton biomass was negatively correlated with TN (Figure 5). pSEM also

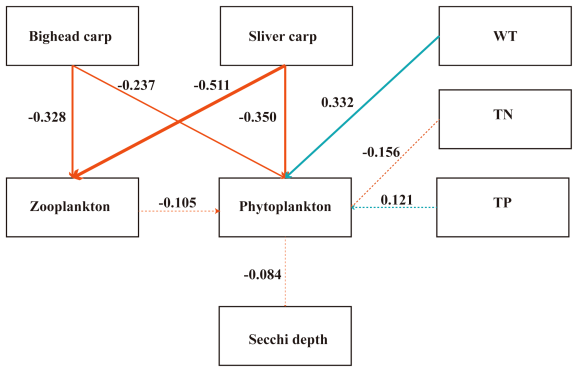

FIGURE 7
Piecewise structural equation model (pSEM) of the direct and indirect effects of bighead carp and silver carp stocking on phytoplankton in Yudong Reservoir. Fisher's C = 48.739; df = 18; P = 0.185; AIC = 50.53. Orange, blue and dashed arrows represent negative, positive and non-significant paths, respectively. The thickness of paths represents the magnitude of the standardised regression coefficient or effect sizes given on the arrows.

indicated that high TN concentrations do not promote phytoplankton biomass (Figure 7). This phenomenon has also been found in other eutrophication lakes and considered due to N subsidy-stress effects (Mao et al., 2020). Filstrup et al. (2018) suggested when TN concentration is more than 2 mg/L, it might negatively influence phytoplankton (Chla) concentrations. Mao et al. (2020) demonstrated the same trend in Lake Taihu where the mean TN value was 3.4 mg/L. However, whether high TN is of importance for the decrease in phytoplankton biomass in our study or not is an open question as it coincides with the increase in the net stocking (stocking minus harvesting) of bigheaded carp (Figure 3). We also found that water level fluctuation can affect the phytoplankton biomass (Figure 5B). Rising water levels due to excessive precipitation may result in higher input of nutrients from the catchment to the reservoir, promoting phytoplankton growth. The precipitation season of Yudong reservoir is concentrated, mainly from May to October. High nutrient concentrations made Yudong Reservoir unable to meet the standards of an ideal water source indicating the original management strategy is not sufficient (Table S2; China, 2002a). To reduce pollution from catchments, local legislation like rational use of phosphorus fertilizer and establish more sewage treatment plants have been introduced to strengthen watershed management. Restricted areas have also been established to reduce nutrient runoff generated by dispersed waste disposal and to prevent soil erosion (Wu et al., 2012; Lian et al., 2018). However, the complex residential and farming conditions in the catchment of the reservoir make it challenging to obtain high water quality, and until target loadings are reached, other methods must be applied of which stocking of filter feeding fish is one possibility (Lin et al., 2014; Han et al., 2020; Xiang et al., 2021).

4.2 Effects of filter-feeding fish and zooplankton on phytoplankton

Our results from Yudong Reservoir indicate that filter-feeding fish, especially silver carp, contributed to the reduction of phytoplankton, especially the larger specimens (Figures 5, 7). Thus, an increase in CPUE of silver carp significantly reduces the biomass of phytoplankton and cyanobacteria (Figure 5), and the average individual size of the phytoplankton declined despite no reduction in nutrient concentrations (Figure S3). The results are consistent with previous research showing that silver carp can feed on large-bodied phytoplankton and decrease the average body size of phytoplankton. However, nanoplankton cannot be effectively controlled, especially if zooplankton grazing is also reduced (Zhao et al., 2013; Shen et al., 2021). Since the filtering efficiency of silver carp depends on the interval of gill rakers and on the size of phytoplankton, silver carp cannot filter phytoplankton whose size is less than 10 µm (Vörös et al., 1997; Radke and Kahl, 2002). The higher density of gill rakers makes silver carp more efficient to filter phytoplankton than bighead carp, silver carp might feed more phytoplankton even in the same scenario (Xie and Liu, 2001). Accordingly, we found that the effect of bighead carp on phytoplankton in Yudong Reservoir was weaker than that of silver carp at similar CPUEs (Figures 5B, 7).

In addition to fish, zooplankton can effectively control phytoplankton provided that they are not too heavily predated upon by fish as evidenced in numerous biomanipulation experiments involving fish removal in temperate lakes (Shapiro et al., 1975; Søndergaard et al., 2007). Filter-feeding fish, however, decreased biomass of large-bodied zooplankton (Shen et al., 2021; Mao et al., 2023) as seen in Yudong Reservoir after years of filter fish stocking (Figure 4). Thus, we found a substantial decrease in large-bodied zooplankton, a smaller cladoceran body weight and a decreased ratio of zooplankton biomass to phytoplankton biomass, all indicated a higher grazing pressure on zooplankton and weaker pressure on phytoplankton in the reservoir (Figure 4; Jeppesen et al., 2011). Such results are not unexpected given the imbalance between stocking and harvesting of filter-feeding fish in Yudong Reservoir (Figure 3), especially at the end of the research phase, where the changes in the zooplankton metrics were largest (Figure 4). A lower stocking of carp or a larger harvest would, therefore, be required to better exert zooplankton control over phytoplankton (Lin et al., 2021; Mao et al., 2023). The top-down effect of phytoplankton in the Yudong Reservoir mainly came from filter-feeding fish, and the effect from zooplankton was weak.

5 Conclusions

Our results revealed that stocking of filter feeding fish (mainly silver carp and bighead carp) most likely were the key drivers of the observed reduction of the biomass of phytoplankton and cyanobacteria and the

decrease in phytoplankton average size in Yudong Reservoir. Stocking also led to a major reduction of large-bodied zooplankton, which, if abundant, are the most efficient grazers on phytoplankton. Imbalance in stocking and harvesting over the years likely contributed to the loss of effective grazers. Furthermore, the fish stocking did not solve the eutrophication problem as chlorophyll-a and phytoplankton biomass remained high. In the management of the Yudong and other eutrophic reservoirs, a reduction of external nutrient loading should, therefore, be given top priority. Our results indicate that in highland (low temperature) deep-water eutrophic reservoirs, unlike observations from lowland shallow lakes, stocking of filter-feeding fish may contribute to the control of filamentous phytoplankton provided that the fish stocking is properly managed. The optimal stocking intensity of filter-feeding fish that can help control phytoplankton without excessive impact on large-bodied zooplankton in highland reservoirs is a topic for further investigation, however.

Data availability statement

The original contributions presented in the study are included in the article/Supplementary Materials, further inquiries can be directed to the corresponding author.

Ethics statement

The animal study was approved by Research Ethics Committee of Institute of Hydrobiology, Chinese Academy of Sciences. The study was conducted in accordance with the local legislation and institutional requirements.

Author contributions

CZ: conceptualization, methodology, form analysis, investigation, data curation, validation, writing–original draft. FM: methodology, investigation, data curation, validation, writing-review and editing. BL: methodology, investigation and data curation. DZ: methodology, investigation and data curation. XC: form analysis and investigation. YX: form analysis and investigation. JB: writing-review and editing. RD: writing-review and editing. HJ: writing-review and editing. EJ: conceptualization, writing-review and editing. MD: conceptualization, funding acquisition, writing-review and editing. All authors contributed to the article and approved the submitted version.

Funding

This work was financially supported by the National Key R & D Program of China (2022YFB3206903), the National Natural Science Foundation of China (32172955), the Science and Technology Poverty Alleviation Program of the Chinese Academy of Sciences (KFJ-FP-201905 and KFJ-FP-202102), and the Guizhou Province Science and Technology Support Plan (Qiankehe Support [2022] General 129). EJ was supported by the TÜBITAK program BIDEB2232 (Project 118C250). CZ was supported by the China Scholarship Council (CSC 202204910443).

Acknowledgments

We would like to thank the staff of Zhaotong Yudong Reservoir Administration for their help. We also would like to thank Anne Mette Poulsen for linguistic assistance.

Conflict of interest

Author RD is employed by Wuhan Sino-Hiking Technology Company Limited, Wuhan, China.

The remaining authors declare that the research was conducted in the absence of any commercial or financial relationships that could be construed as a potential conflict of interest.

Publisher's note

Supplementary material

The Supplementary Material for this article can be found online at: https://www.frontiersin.org/articles/10.3389/fmars.2023.1251469/full#supplementary-material

References

Amorim, C. A., Ulisses, C., and Moura, A. N. (2017). Biometric and physiological responses of Egeria densa Planch. cultivated with toxic and non-toxic strains of Microcystis. *Aquat. Toxicol.* 191, 201–208. doi: 10.1016/j.aquatox.2017.08.012

APHA (2005). *Standard Methods for the Examination of Water and Wastewater. 21st edition* (Washington, DC, USA: American Public Health Association, American Water Works Association, Water Environment Federation).

Attayde, J. L., and Hansson, L. A. (2001). Fish-mediated nutrient recycling and the trophic cascade in lakes. *Can. J. Fish. Aquat. Sci.* 58, 1924–1931. doi: 10.1139/f01-12

Chiang, S. C., and Du, N. S. (1979). *Fauna Sinica, Crustacea, Freshwater Cladocera* (Beijing: Science press).

China, M. (2002a) *Environmental Quality Standards for Surface Water*. Available at: https://english.mee.gov.cn/Resources/standards/water_environment/quality_standard/200710/t20071024_111792.shtml (Accessed June 1, 2002).

China, M. (2002b). *Standard Methods for the Examination of Water and Wastewater (Version 4) China* (Beijing: Environmental Science Press).

China, M. (2009) *Water Quality Guidance on Sampling Techniques*. Available at: https://www.mee.gov.cn/ywgz/fgbz/bz/bzwb/jcffbz/200910/t20091010_162158.shtml (Accessed November 1, 2009).

Dumont, H. J., Van de Velde, I., and Dumont, S. (1975). The dry weight estimate of biomass in a selection of Cladocera, Copepoda and Rotifera from the plankton, periphyton and benthos of continental waters. *Oecologia* 19, 75–97. doi: 10.1007/BF00377592

Domaizon, I., and Devaux, J. (1999). Experimental study of the impacts of silver carp on plankton communities of eutrophic Villerest reservoir. *Aquat. Ecol.* 33, 193–204. doi: 10.1023/A:1009984713183

Filstrup, C. T., Wagner, T., Oliver, S. K., Stow, C. A., Webster, K. E., Stanley, E. H., et al. (2018). Evidence for regional nitrogen stress on chlorophyll a in lakes across large landscape and climate gradients. *Limnol. Oceanogr.* 63, 324–339. doi: 10.1002/lno.10742

Guo, L., Wang, Q., Xie, P., Tao, M., Zhang, J., Niu, Y., et al. (2015). A non-classical biomanipulation experiment in Gonghu Bay of Lake Taihu: control of Microcystis blooms using silver and bighead carp. *Aquac. Res.* 46, 2211–2224. doi: 10.1111/are.12375

Han, Q., Tong, R., Sun, W., Zhao, Y., Yu, J., Wang, G., et al. (2020). Anthropogenic influences on the water quality of the Baiyangdian Lake in North China over the last decade. *Sci. Total Environ.* 701, 134929. doi: 10.1016/j.scitotenv.2019.134929

Hart, R. C. (2011). Zooplankton biomass to chlorophyll ratios in relation to trophic status within and between ten South African reservoirs: Causal inferences, and implications for biomanipulation. *Water SA* 37, 513–522. doi: 10.4314/wsa.v37i4.9

He, H., Jin, H., Jeppesen, E., Li, K., Liu, Z., and Zhang, Y. (2018). Fish-mediated plankton responses to increased temperature in subtropical aquatic mesocosm ecosystems: implications for lake management. *Water Res.* 144, 304–311. doi: 10.1016/j.watres.2018.07.055

Hu, H. J. (2006). *The Freshwater Algae of China: Systematics, Taxonomy and Ecology* (Beijing: Science Press).

Huang, X. F. (1999). *Survey Observation and Analysis of Lake Ecology* (Beijing: Standards Press of China).

Jackson, L. J., Lauridsen, T. L., Søndergaard, M., and Jeppesen, E. (2007). A comparison of shallow Danish and Canadian lakes and implications of climate change. *Freshw. Biol.* 52, 1782–1792. doi: 10.1111/j.1365-2427.2007.01809.x

Jeppesen, E., Jensen, J. P., Jensen, C., Faafeng, B., Hessen, D. O., Søndergaard, M., et al. (2003). The impact of nutrient state and lake depth on top-down control in the pelagic zone of lakes: a study of 466 lakes from the temperate zone to the Arctic. *Ecosystems* 6, 313–325. doi: 10.1007/PL00021503

Jeppesen, E., Jensen, J. P., Søndergaard, M., Lauridsen, T., Pedersen, L. J., and Jensen, L. (1997). Top-down control in freshwater lakes: the role of nutrient state, submerged macrophytes and water depth. *Hydrobiologia* 342, 151–164. doi: 10.1023/A:1017046130329

Jeppesen, E., Noges, P., Davidson, T. A., Haberman, J., Noges, T., Blank, K., et al. (2011). Zooplankton as indicators in lakes: a scientific-based plea for including zooplankton in the ecological quality assessment of lakes according to the European Water Framework Directive (WFD). *Hydrobiologia* 676, 279–297. doi: 10.1007/s10750-011-0831-0

Jeppesen, E., Søndergaard, M., Lauridsen, T. L., Davidson, T. A., Liu, Z., Mazzeo, N., et al. (2012). Biomanipulation as a restoration tool to combat eutrophication: recent advances and future challenges. *Adv. Ecol. Res.* 47, 411–488. doi: 10.1016/B978-0-12-398315-2.00006-5

Jeppesen, E., Søndergaard, M., Mazzeo, N., Meerhoff, M., Branco, C., and Huszar, V. (2005). *Lake restoration and biomanipulation in temperate lakes: relevance for subtropical and tropical lakes* (Enfield: Science Publisher).

Lemmens, P., Declerck, S. A., Tuytens, K., Vanderstukken, M., and De Meester, L. (2018). Bottom-up effects on biomass versus top-down effects on identity: a multiple-lake fish community manipulation experiment. *Ecosystems* 21, 166–177. doi: 10.1007/s10021-017-0144-x

Li, Y., Nwankwegu, A. S., Huang, Y., Norgbey, E., Paerl, H. W., and Acharya, K. (2020). Evaluating the phytoplankton, nitrate, and ammonium interactions during summer bloom in tributary of a subtropical reservoir. *J. Environ. Manage.* 271, 110971. doi: 10.1016/j.jenvman.2020.110971

Lian, Y., Li, C., Ye, S., Li, W., Liu, J., and Li, Z. (2018). Fish spatial distribution patterns and controlling factors in Yudong Reservoir, Yunnan Plateau. *J. Lake Sci.* 30 1755–1765. doi: 10.18307/2018.0626

Lin, Q., Chen, Q., Peng, L., Xiao, L., Lei, L., and Jeppesen, E. (2020). Do bigheaded carp act as a phosphorus source for phytoplankton in (sub) tropical Chinese reservoirs? *Water Res.* 180, 115841. doi: 10.1016/j.watres.2020.115841

Lin, Q., Jiang, X., Han, B. P., and Jeppesen, E. (2014). Does stocking of filter-feeding fish for production have a cascading effect on zooplankton and ecological state? A study of fourteen (sub) tropical Chinese reservoirs with contrasting nutrient concentrations. *Hydrobiologia* 736, 115–125. doi: 10.1007/s10750-014-1896-3

Lin, Q., Zeng, D., Guo, T., and Peng, L. (2021). Filter-feeding fish (*Hypophthalmichthys molitrix*) mediated phosphorus recycling versus grazing pressure as drivers of the trophic cascade in large enclosures subsidized by allochthonous detritus. *Water Res.* 204, 117579. doi: 10.1016/j.watres.2021.117579

Mao, Z., Cao, Y., Gu, X., Zeng, Q., Chen, H., and Jeppesen, E. (2023). Response of zooplankton to nutrient reduction and enhanced fish predation in a shallow eutrophic lake. *Ecol. Appl.* 33, e2750. doi: 10.1002/eap.2750

Mao, Z., Gu, X., Cao, Y., Zhang, M., Zeng, Q., Chen, H., et al. (2020). The role of top-down and bottom-up control for phytoplankton in a subtropical shallow eutrophic lake: evidence based on long-term monitoring and modeling. *Ecosystems* 23, 1449–1463. doi: 10.1007/s10021-020-00480-0

Nwankwegu, A. S., Li, Y., Huang, Y., Wei, J., Norgbey, E., Lai, Q., et al. (2020). Nutrient addition bioassay and phytoplankton community structure monitored during autumn in Xiangxi Bay of Three Gorges Reservoir, China. *Chemosphere* 247, 125960. doi: 10.1016/j.chemosphere.2020.125960

Olokotum, M., Mitroi, V., Troussellier, M., Semyalo, R., Bernard, C., Montuelle, B., et al. (2020). A review of the socioecological causes and consequences of cyanobacterial blooms in Lake Victoria. *Harmful Algae* 96, 101829. doi: 10.1016/j.hal.2020.101829

Qu, X., Chen, Y., Liu, H., Xia, W., Lu, Y., Gang, D. D., et al. (2020). A holistic assessment of water quality condition and spatiotemporal patterns in impounded lakes along the eastern route of China's South-to-North water diversion project. *Water Res.* 185, 116275. doi: 10.1016/j.watres.2020.116275

Radke, R. J., and Kahl, U. (2002). Effects of a filter-feeding fish [silver carp, *Hypophthalmichthys molitrix* (Val.)] on phyto-and zooplankton in a mesotrophic reservoir: results from an enclosure experiment. *Freshw. Biol.* 47, 2337–2344. doi: 10.1046/j.1365-2427.2002.00993.x

Reynolds, C. F. (1984). *The Ecology of Freshwater Phytoplankton* (Cambridge: Cambridge University Press).

Shapiro, J., Lamarra, V., and Lynch, M. (1975). "Biomanipulation: an ecosystem approach to lake restoration," in *Proc. Symp. on water quality management through biological control* (Florida: Univ. Florida and US Environ. Prot. Agency), 85–95.

Shen, R., Gu, X., Chen, H., Mao, Z., Zeng, Q., and Jeppesen, E. (2021). Silver carp (*Hypophthalmichthys molitrix*) stocking promotes phytoplankton growth by suppression of zooplankton rather than through nutrient recycling: An outdoor mesocosm study. *Freshw. Biol.* 66, 1074–1088. doi: 10.1111/fwb.13700

Shipley, B. (2013). The AIC model selection method applied to path analytic models compared using ad-separation test. *Ecology* 94, 560–564. doi: 10.1890/12-0976.1

Søndergaard, M., Jeppesen, E., Lauridsen, T. L., Skov, C., Van Nes, E. H., Roijackers, R., et al. (2007). Lake restoration: successes, failures and long-term effects. *J. Appl. Ecol.* 44, 1095–1105. doi: 10.1111/j.1365-2664.2007.01363.x

Starling, F. L. D. R. M. (1993). Control of eutrophication by silver carp *(Hypophthalmichthys molitrix*) in the tropical Paranoa Reservoir (Brasília, Brazil): a mesocosm experiment. *Hydrobiologia* 257, 143–152. doi: 10.1007/BF00765007

Su, H., Pan, J., Feng, Y., Yu, J., Liu, J., Wang, L., et al. (2021). Stocking alien carp leads to regime shifts in native fish populations: Evidence from long-term observation and ecological modeling of a Chinese reservoir. *Ecol. Indic.* 132, 108327. doi: 10.1016/j.ecolind.2021.108327

Vörös, L., Oldal, I., Présing, M., and Balogh, K. (1997). Size-selective filtration and taxon-specific digestion of plankton algae by silver carp (*Hypophthalmichthys molitrix* Val.). *Hydrobiologia* 342, 223–228. doi: 10.1023/A:1017039423485

Walsh, C., and Mac Nally, R. (2013). *hier.part: hierarchical partitioning* (Vienna: R package version 1.0-4. R Project for Statistical Computing).

Wood, S. N. (2020). *Package "mgcv"*. Available at:https://cran.r-project.org/web/packages/mgcv/index.html.

Wu, Z., Wang, X., Chen, Y., Cai, Y., and Deng, J. (2018). Assessing river water quality using water quality index in Lake Taihu Basin, China. *Sci. Total Environ.* 612, 914–922. doi: 10.1016/j.scitotenv.2017.08.293

Wu, W., Yang, K., Wang, Z., Li, B., and Liu, Y. (2012). Community structure and seasonal succession of phytoplankton in Yudong Reservoir of Yungui-plateau. *J. Hydroecol.* 33, 69–75.

Xiang, R., Wang, L., Li, H., Tian, Z., and Zheng, B. (2021). Water quality variation in tributaries of the Three Gorges Reservoir from 2000 to 2015. *Water Res.* 195, 116993. doi: 10.1016/j.watres.2021.116993

Xie, P., and Liu, J. (2001). Practical success of biomanipulation using filter-feeding fish to control cyanobacteria blooms: a synthesis of decades of research and application in a subtropical hypereutrophic lake. *Sci. World J.* 1, 337–356. doi: 10.1100/tsw.2001.67

Yvon-Durocher, G., Montoya, J. M., Trimmer, M., and Woodward, G. U. Y. (2011). Warming alters the size spectrum and shifts the distribution of biomass in freshwater ecosystems. *Glob. Change Biol.* 17, 1681–1694. doi: 10.1111/j.1365-2486.2010.02321.x

Zhang, Z., Cao, Y., Jeppesen, E., and Li, W. (2016b). The response of Vallisneria spinulosa (*Hydrocharitaceae*) and plankton to pulse addition of inorganic nitrogen with different loading patterns. *Hydrobiologia* 767, 175–184. doi: 10.1007/s10750-015-2494-8

Zhang, Y., Cheng, L., Li, K., Zhang, L., Cai, Y., Wang, X., et al. (2019). Nutrient enrichment homogenizes taxonomic and functional diversity of benthic macroinvertebrate assemblages in shallow lakes. *Limnol. Oceanogr.* 64, 1047–1058. doi: 10.1002/lno.11096

Zhang, Z. S., and Huang, X. F. (1991). *Methods in Freshwater Plankton Study* (Beijing: Science Press).

Zhang, X., Liu, Z., Jeppesen, E., Taylor, W. D., and Rudstam, L. G. (2016a). Effects of benthic-feeding common carp and filter-feeding silver carp on benthic-pelagic coupling: implications for shallow lake management. *Ecol. Eng.* 88, 256–264. doi: 10.1016/j.ecoleng.2015.12.039

Zhao, S., Sun, Y., Lin, Q., and Han, B. (2013). Effects of silver carp (*Hypophthalmichthys molitrix*) and nutrients on the plankton community of a deep, tropical reservoir: an enclosure experiment. *Freshw. Biol.* 58, 100–113. doi: 10.1111/fwb.12042

frontiers | Frontiers in Marine Science

TYPE Original Research
PUBLISHED 11 October 2023
DOI 10.3389/fmars.2023.1226379

OPEN ACCESS

EDITED BY
Weijie Wang,
China Institute of Water Resources and Hydropower Research, China

REVIEWED BY
Dehai Song,
Ocean University of China, China
Busnur Rachotappa Manjunatha,
Mangalore University, India

*CORRESPONDENCE
Barak Herut
barak@ocean.org.il
Simona Avnaim-Katav
simonaav@ocean.org.il

†These authors jointly supervised this work

‡Retired

RECEIVED 21 May 2023
ACCEPTED 18 September 2023
PUBLISHED 11 October 2023

CITATION
Herut B, Guy-Haim T, Almogi-Labin A, Fischer HW, Ransby D, Sandler A, Katz T and Avnaim-Katav S (2023) Marine oligotrophication due to fine sediments and nutrient starvation caused by anthropogenic sediment and water retention in large rivers: the Nile damming case.
Front. Mar. Sci. 10:1226379.
doi: 10.3389/fmars.2023.1226379

Marine oligotrophication due to fine sediments and nutrient starvation caused by anthropogenic sediment and water retention in large rivers: the Nile damming case

Barak Herut[1*†], Tamar Guy-Haim[1], Ahuva Almogi-Labin[2†], Helmut W. Fischer[3‡], Daniela Ransby[4], Amir Sandler[2], Timor Katz[1] and Simona Avnaim-Katav[1*]

[1]Israel Oceanographic and Limnological Research, National Institute of Oceanography, Haifa, Israel, [2]Geological Survey of Israel, Jerusalem, Israel, [3]Institute of Environmental Physics, University of Bremen, Bremen, Germany, [4]Alfred Wegener Institute, Helmholtz Centre for Polar and Marine Research, Bremerhaven, Germany

In the last two centuries, human activities have radically reduced the transport of suspended sediment and water to marine systems, mainly in the northern hemisphere, while complete sediment retention has been reported for the Nile River after the construction of the Aswan High Dam (AHD). Here, we focused on changes in the inner-shelf sediments most exposed to the pre-AHD flood plume in the distal part of its littoral cell as a predictor of the ecological response to large river fragmentation. Substantial reductions in fine (15-40%) and increases in coarse (~8 fold) sediment accumulation rates, increases in $CaCO_3$ (~50%), decreases in autochthonous and total organic carbon (OC), and changes in the benthic foraminiferal assemblage toward more OC-sensitive species suggest an enhanced oligotrophication trend. The reduced nutrient fluxes and OC accumulation, and the coarsening of the shelf sediments inhibit the retention of "blue" carbon. Combined with fast climate warming and salinization, river fragmentation may have essential implications for the Eastern Mediterranean ecosystem via benthic oligotrophication processes.

KEYWORDS

nutrients, sediments, anthropogenic, dams, foraminifera, Mediterranean Sea, oligotrophic radionuclides

1 Introduction

Sediments and water transport by rivers have been dramatically changed by human activities in the last two centuries (Best, 2019), reducing their fluxes to the oceans mainly in the northern hemisphere (Syvitski et al., 2005; Dethier et al., 2022), or accelerating suspended sediment and fluxes in the southern hemisphere (south to 20° N) due to increased erosion resulting from intensive land use change (Dethier et al., 2022) and in high mountain Asia due to a warmer and wetter climate change (Li et al., 2021).

Dams and large reservoirs are responsible for extreme basin-wide sediment trapping in several rivers worldwide (Milliman and Farnsworth, 2013). Recent studies of pre- and post-damming in northern hemisphere rivers present a combined reduction in continental fluxes of 49 ± 25%, while rivers with large dams are often intensively blocked (Milliman and Farnsworth, 2013; Dethier et al., 2022). An almost complete (~100%) trapping is reported for the Nile system (Vörösmarty et al., 2003; Syvitski et al., 2005; Milliman and Farnsworth, 2013). During the last two centuries, a series of dams have been built along the Nile, starting with the Aswan Low Dam (1898-1902), and since the operation of the Aswan High Dam (AHD; 1960-1964), almost all discharge to the southeastern (SE) Mediterranean Sea has been stopped, which includes ~10^7 t y^{-1} of fine sediments (Nixon, 2003), most of which is silty clay trapped in upper lake reservoirs (e.g., Lake Nasser) (Farhat and Salem, 2015). The Nile system shows severe fragmentation as compared to other major rivers in the world (Best, 2019) and has been subject to prolonged damming processes up to the most recent Grand Ethiopian Renaissance Dam (GERD, 2011-2020; Wheeler et al., 2020).

Prior to the AHD, the African monsoon caused extensive Nile River discharge/flooding into the Mediterranean Sea, averaging ~8 × 10^{10} m^3 yr^{-1} (Sharaf El Din, 1977; Halim et al., 1995; Woodward et al., 2007; Rohling et al., 2015). Its reduced surface-water salinities and enhanced turbidity plume have been observed from the Nile Delta northward along the eastern Levantine coast (Hecht, 1964; Hecht and Gertman, 2001; Zviely et al., 2007). In the long past, the development of the East Mediterranean sapropels (sedimentary layers of high organic content) during the last ~13 million years has been linked to monsoon intensification and consequent discharge of the Nile as a major supplier of freshwater and suspended sediments to the basin, in addition to oceanographic pre-conditioning (Rohling et al., 2015). Since damming, Nile water discharge has been dramatically reduced (Sharaf El Din, 1977; Nixon, 2003; Ludwig et al., 2009), and seasonal monsoon-related floods (August-October) have stopped completely.

Sediment retention in reservoirs and the reduction of terrestrial sediment and water supply to coastal areas have a significant influence on coastal erosion, nutrient fluxes, the benthic shelf environment, and other marine resources (Stanley and Warne, 1993; Nixon, 2003; Syvitski et al., 2005; Abd-El Monsef et al., 2015). The area ratio between the Nile River drainage basin (2933 10^3 km^2; Milliman and Farnsworth, 2013; Best, 2019) and the South Levantine marine basin (840 10^3 km^2; Ludwig et al., 2009; Best, 2019) is exceptionally high (>3) compared to other large river-ocean system links, emphasizing its ideal relevance as a natural laboratory for assessing the impacts of fine sediment and nutrient retention by large, fragmented rivers on marine shelf ecosystems.

The combination of geochemical and faunal records can provide clues on benthic ecosystem changes. Benthic foraminifera (BF), living in marine shelf environments, are well-known single-celled eukaryotes highly sensitive to environmental changes. Their wide abundance and potential preservation in sedimentary archives make them ideal bioindicators for reconstructing past ecological, climatic, and anthropogenic changes (Jorissen et al., 1995; Sen Gupta, 1999; Katz et al., 2010; Avnaim-Katav et al., 2019; Schmiedl, 2019; Martínez et al., 2023), and they have recently been adopted as reliable indices for biomonitoring purposes (e.g., Bouchet et al., 2021). Furthermore, changes in BF species composition could be utilized as a reliable indicator of benthic macrofaunal community structure (Bouchet et al., 2018). Such recent (2011) changes in BF biotopes on the inner Mediterranean shelf off Israel, based on dissimilarities between the dead and live BF assemblages, were attributed to the long-term impacts of Nile damming (Avnaim-Katav et al., 2021).

The Nile system shows almost complete retention of fine sediments and nutrients that were transported to the SE Levantine Basin prior to the AHD, mimicking the marine consequences of severe fragmentation of large rivers worldwide. In this study, we focused on the distal part of the Nile littoral cell (Zviely et al., 2007) along the inner Mediterranean shelf off Israel (Figure 1) as a natural laboratory for a fast-responsive sedimentary system that has been affected by the Nile damming. Geochemical and sedimentological properties were analyzed in short sediment cores collected at 40 m water depth (Figure 1), representing the area of the pre-damming sedimentary silt belt (30-50m) (Nir, 1984) derived from past Nile floods that reach the Israeli coast at the end of each summer by wind-induced counterclockwise longshore currents (Hecht, 1964). In addition, to track benthic ecological changes attributed to the AHD, we analyzed BF assemblages in sedimentary layers representing pre- (~1910) and post- (1997; 2011; 2021) AHD conditions. The results show a substantial increase in grain size, a decrease in the organic carbon content and its marine/autochthonous fraction, and BF assemblages trending toward further oligotrophication.

2 Materials and methods

2.1 Field sampling

The presented data consist of a set of sediment samples obtained in this study and data from previous studies, as shown in Table 1. The data originate from short sediment cores and surface sediment samples collected along ~140 km of Israel's inner Mediterranean shelf from off Ashqelon in the south to off Beit Yannay in the north, representing the distal part of the Nile littoral cell at different periods (Figure 1; Table 1). The stations were located within the ~30-50 m water depth silty belt, an area most sensitive to past Nile River discharge/flood dynamics (Hecht, 1964; Nir, 1984).

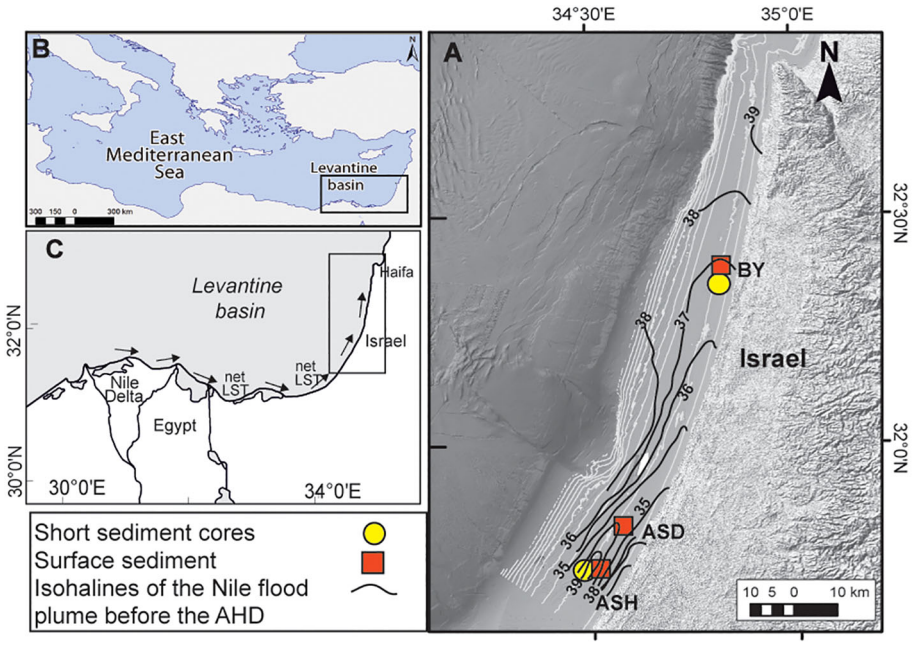

FIGURE 1
Locations of the studied short sediment cores (circles) (BY: 32°22.48N; 34°48.28E; ASH: 31°42.42N; 34°30.84E) and surface sediment box cores (boxes) (ASD: 31°47.86N; 34°32.20E) **(A)**; Black contours are isohalines of the Nile flood plumes based on measurements before the Aswan High Dam (Hecht, 1964) **(A)**. The Nile Delta **(B, C)** and the net long-shore transport (LST) flow northward along the SE Levantine basin coast off Israel (after Zviely et al., 2007) **(C)**.

Short sediment cores were sampled in 2007 by the R/V *Shikmona* off Ashqelon (33 m water depth) and Beit Yannay (40 m water depth), representing the southern and northern zones of the study area. In addition, surface sediment samples were collected in 2021 by the R/V *Bat-Galim* at three stations (Ashkelon, Ashdod, and Beit Yannay) at ~40 m water depth. Surface sediments and the short cores were collected using a box corer (Ocean Instruments BX 700 AL, Ocean Instruments, Fall City, United States) and Perspex tubes.

The sediment cores were sliced onboard into 1 cm slices, frozen, and lyophilized in the laboratory. Sub-samples were analyzed for granulometry, major elements, $CaCO_3$, P speciation, total organic carbon (TOC), and δ^{13}Corg. Chronology was determined in two parallel cores using lead-210 (details are below).

Duplicates of surface sediment (top 0–1 cm) were sampled for micropaleontological analysis from each box core at each station. Because the abundance of living foraminiferal assemblages is low in the study area (Avnaim-Katav et al., 2020), each duplicate included three repeated samples of the top 0–1 cm interval using a 55 mm diameter Perspex mini corer. Micropaleontological analyses followed Schonfeld et al. (Schonfeld et al., 2012). Sediment samples were stained with rose bengal solution (2 g rose bengal/l 95%- ethanol) for two weeks at the time of sampling. Rose bengal confirms the presence of cytoplasm and is widely used to distinguish between dead and presumed live foraminifera (Avnaim-Katav et al., 2020; Avnaim-Katav et al., 2021). The samples for analyses of dead foraminiferal assemblages, representing pre-AHD deposition, were collected from the bottom layer of two short cores off Beit Yannay and Ashkelon.

TABLE 1 Summary of the data set presented in this study.

Period	Sample type	Grain size	Geochemistry	Foraminifera	Locations	Reference
1900-2005	Short cores	+	+	Dead BF Abundance	Beit Yannay (BY); Ashkelon (ASH)	This study
1910 – pre AHD	Sediment bottom layers	+	Al, Si	Dead BF assemblage	Beit Yannay; Ashdod (ASD); Ashkelon	This study
1997	Sediment surface layers	+	+	Dead BF assemblage	Beit Yannay; Ashdod; Ashkelon	Hyams-Kaphzan et al. (2008)
2011	Sediment surface layers	+	+	Dead & Live BF assemblage	Beit Yannay; Ashdod; Ashkelon	Avnaim-Katav et al. (2020; 2021)
2021	Sediment surface layers	+	+	Dead & Live BF assemblage	Beit Yannay; Ashdod; Ashkelon	This study

2.2 Analytical methods

Grain size analysis followed Crouvi et al. (2008) and was performed on sediments <2 mm using a Malvern Mastersizer MS-2000 (Malvern Panalytical, Malvern, United Kingdom). Detailed information on the analysis of the major elements, Total Organic Carbon (TOC), $\delta^{13}C$ of organic matter ($\delta^{13}Corg$), and $CaCO_3$ is presented in Bookman et al. (2021). In general, major elements were analyzed with an inductively coupled plasma-atomic emission spectrophotometer (ICP-OES OPTIMA 3300, Agilent Technologies, Santa Clara, United States) after the fusion of sediment sub-samples with $LiBO_2$. International standards (e.g., USGS SRS T-207, T-209) were used along with the known samples. The accuracy of the analyses of the major elements was better than 2%. Total Organic Carbon (TOC) content and $\delta^{13}Corg$ were determined using the Thermo Flash 2000 Elemental Analyzer (manufactured by Thermo Fisher Scientific, Waltham, United States) that interfaced with a Thermo Finnigan Delta V Isotope Ratio Mass Spectrometer (IRMS) (Thermo Fisher Scientific) at the Geological Survey of Israel. The mass spectrometer measures the $^{13}C/^{12}C$ ratio in the sample and standard and calculates the $\delta^{13}Corg$ in ‰. All analyses have been reported relative to VPDB for $\delta^{13}Corg$ and calibrated against the international standards Urea #2, Acetanilide #1, B2151, and B2153. The $CaCO_3$ content was determined by gasometry.

P speciation was performed following Eckert et al. (2003) by sequential extraction of the solid phase to metal (Fe)-bound P. P bound to Fe hydroxides was released by leaching with NaOH (~0.1M) and measurement of molybdate-reactive P.

2.3 Chronology

The chronology of the two sediment cores was based on a combination of two radiotracers, ^{210}Pb and ^{137}Cs, due to their suitable half-lives of 22.2 and 30.0 years. A total of 38 slices of the sediment cores from ASH (19 upper 1 cm slices) and BY (19 upper 1 cm slices) were subjected to gamma spectroscopy. The dried sediments were sealed in cylindrical plastic dishes with a diameter of 3.5 cm using Rn-tight foil. Before measurement, they were left sealed for a minimum of 3 weeks so that the radioactive equilibrium between ^{226}Ra and ^{222}Rn (and their daughters) could be established.

For gamma spectroscopy, a coaxial HPGe detector with 50% relative efficiency (Canberra Industries/Mirion Technologies, Atlanta, United States) was used, housed in a 10 cm Pb shield with Cu and plastic inner linings, and operated under Genie 2000 software (Canberra Industries/Mirion Technologies). Measurement times varied from 77149 to 426623 seconds (long counting times of up to 5 days had to be used for samples with very low activity). Photopeak efficiencies were calculated using LabSOCS© (Laboratory SOurceless Calibration System), the calibration tool of the Genie 2000 software (Mirion Technologies). The calculation is based on the definitions of sample geometry, composition and density, and sample-detector geometry, and the detector has been factory-characterized for use with LabSOCS. Comparison with measurements of radioactive standard materials revealed deviations of less than 5% between measured and calculated efficiencies in most cases. The activity concentrations of all estimated radioisotopes were recalculated to the date of sampling. For the determination of $^{210}Pb_{xs}$, the excess ^{210}Pb activity and the supported ^{210}Pb activity (determined via the 351.9 keV line of ^{214}Pb) were subtracted from the total ^{210}Pb signal, measured via the 46.5 keV line. Additionally, the artificial isotope ^{137}Cs was analyzed via the 661.6 keV line of the daughter isotope ^{137m}Ba. For several samples, no clear ^{137}Cs signal could be detected at the 95% confidence level. The decision threshold varied for individual samples, mainly depending on their mass and counting time, and mostly reached values between 0.4 and 1.0 Bq kg^{-1}. The chronological models were applied to data expressed in units of activity concentration Bq kg^{-1}. Comparable results (within standard error) were obtained with data recalculated to Bq cm^{-3} using dry densities that do not vary significantly in the profiles. A grain size normalization procedure was applied to the $^{210}Pb_{xs}$ data (Kirchner and Ehlers, 1998). When $^{210}Pb_{xs}$ and ^{137}Cs enter the marine environment, they are removed from the solution by adsorption on inorganic particles or organic matter in suspension, which is later deposited on the bottom. Most of the activity is linked to the finest fraction with the highest effective surface area. The sediment cores were dated by applying a simple exponential model (constant $^{210}Pb_{xs}$ flux, constant sedimentation rate) to normalized data from the profiles (Supplementary Figure 1). Variations in sediment particle size were accounted for using the fine fraction for grain size correction ($^{210}Pb_{xs}$ (Bq kg^{-1})/fraction <63 µm (%) * 100). When alternatively using Al content (Alvarez-Iglesias et al., 2007) for fine material normalization ($^{210}Pb_{xs}$ (Bq kg^{-1})/Al (%) * 100, data not shown), the data look very similar to those after grain size correction. We confirmed this by the appearance of the ^{137}Cs values and the geochemical profiles, which support this sedimentation model and the pre-1950s origin of the deeper layers. The accompanying radionuclide data and age model can be found in the PANGAEA data repository (Ransby et al., 2023).

2.4 Foraminiferal analysis

In total, 55 surface and sub-surface sediment samples were washed through a 63 µm sieve and dried at 50°C, and the >125 µm fraction was used for foraminiferal analyses (Table 1). The living assemblage, which included individuals with bright pink and homogeneous cytoplasm, was studied in the entire duplicate sample according to the protocol of Schonfeld et al. (2012). The living assemblage in all of these samples (except for three samples with <50 specimens) had more than 100 individuals, a sufficient number for multivariate statistical methods, and relatively robust environmental interpretation (Hayward et al., 2019). The time-averaged dead assemblage in recently deposited sediments (2021) and pre-AHD dam samples was examined in samples that were split into aliquots containing generally at least 200 dead specimens (one-quarter of the samples contained 118 to 166 shells, and the remaining contained 217 to 590 shells). Specimens were identified

to species level and counted to determine the total number of benthic foraminiferal individuals per gram of dry sediment (BF/g). Taxonomic identification was based on Loeblich and Tappan (1987; 1994); Cimerman and Langer (1991); Hottinger et al. (1993); Jones (1994), and the World Foraminifera Database, World Register of Marine Species (2023). The state of preservation of the specimens was evaluated and was generally very good in all samples examined.

2.5 Statistical analysis

To measure the differences in community structure between study periods and study sites in the live and dead assemblages, we performed non-metric multidimensional scaling (NMDS) ordinations after computation of a Bray-Curtis dissimilarity matrix based on foraminifera abundances using the "vegan" package (version 2.5-6) (Oksanen et al., 2019) in R v4.2.2 (R Core Team, 2021). Foraminiferal abundance data were log(x+1) transformed prior to analyses to reduce the influence of the most abundant species. As an additional test, we performed Ward.D hierarchical cluster analysis on the Bray-Curtis dissimilarity matrix using the hclust function in the "vegan" package. The Ward.D algorithm is based on minimizing variances in hierarchically identified assemblages and fits aggregated data, for which the Bray-Curtis measure is generally recommended (Singh et al., 2011). Transformed abundances and clustering were visualized using the "pheatmap" package in R (Kolde and Maintainer, 2018). The significance of the differences between live and dead foraminiferal assemblages derived from the Bray-Curtis matrix was assessed with PERMANOVA (permutational multivariate ANOVA) tests, with period and site as fixed factors, followed by *post-hoc* pairwise comparisons. We further calculated the relative contribution of each species to the similarities within each assemblage using a SIMPER (similarity percentage) analysis, which examines the percentage contribution of each species to the similarity within and dissimilarity between assemblages (Clarke, 1993).

Following the classification of benthic foraminifera into five categories based on their ecological quality status (EcoQS) (Alve et al., 2016), we have analyzed the temporal changes in the total relative abundance of category 1 (oligotrophic bioindicators) and category 3 (eutrophic bioindicators) using the Kruskal-Wallis rank sum test in R.

3 Results and discussion

The Israeli inner continental shelf is an integral and distal part of the Nile littoral cell, extending ~700 km from Alexandria, Egypt, in the south, to Akko, Israel, in the north (Inman, 2003; Zviely et al., 2007). Prior to the AHD, the Nile flood events in late summer (between August and November) discharged approximately 50% of the flood volume into the Mediterranean Sea, estimated to be ~84x10^9 m^3 between 1900 and 1959 and ~55x10^9 m^3 between 1959 and 1963 (Halim et al., 1995). These annual floods produced a plume of turbid (brownish) water that transported nutrients and ~117 t/y of fine sediments along the shallow coastal water towards the distal part of the Nile littoral cell off Israel (Oren and Komarovsky, 1961; Hecht, 1964; Oren, 1969; Sharaf El Din, 1977; Halim et al., 1995). Sediments from the Nile River and the submerged delta were transported to the east by the prevailing waves and the wind-induced counterclockwise longshore currents (Inman and Jenkins, 1984; Inman, 2003). The effect of the late summer Nile flood events was dramatic, recording a drop-in in salinity (from 39 to as low as 33 psu), an increase in turbid nutrient-enriched waters and phytoplankton biomass, and a change in the phytoplankton composition of the surface waters (Halim, 1960; Oren and Komarovsky, 1961; Hecht, 1964). Below, we show that the sediment regime of the inner shelf of Israel has indeed recorded the dramatic impact attributed to the prevention of the Nile flood discharge, both of suspended particulate matter and nutrient-induced organic matter, pioneering at the distal part of its littoral cell. This damming process terminates a long climatological Nile-derived geological record of changing flow intensities affecting the SE Levantine sedimentary province (Bookman et al., 2021) and the eastern Mediterranean basin in general (Rohling et al., 2015).

3.1 Impact of the Aswan High Dam on the geochemical properties and organic matter sources of the distal Nile littoral cell

Here, we present the geochemical changes in two short sediment cores, one located at the northernmost edge of the Nile littoral cell (BY) and the other ~100 km to the south (ASH), assuming that they best represent the outcomes of the Nile damming. Indeed, the top ~10 cm, accumulated during the last ~40 years, is significantly coarser than the underlying pre-AHD sediments (Figure 2A).

Applying the exponential model to the grain size normalized data in cores ASH and BY, we obtained sedimentation rates of 2.3 ± 0.5 mm yr^{-1} and 1.8 ± 0.3 mm yr^{-1}, respectively. The occurrence of ^{137}Cs at the depths of 10.5 cm and ~7 cm in cores ASH and BY, respectively, was thus dated to 1962 (± 10 yr) and 1967 (± 7 yr), respectively, in good agreement with the maximum of the ^{137}Cs bomb test fallout in 1963 (Supplementary Figure 1). ^{137}Cs is associated with organic matter and the fine clay mineral fraction in sediments, which makes its detection analytically easier in fine-grained, organically rich sediment types. The fact that no ^{137}Cs could be detected in the deeper, finer layers, while it was detected with the same experimental setup in the coarser sediments in the shallower layers, strongly supports the pre-1950s origin of the deeper layers. Extrapolation of the ^{210}Pb-derived sedimentation rate to depths beyond 10 cm is somewhat uncertain, as the data scatter is very large. On the other hand, for both cores, the ^{210}Pb inventory in the upper 10 cm corresponds to about 75% of the total inventory (1305 of 1756 Bq m^{-2} for ASH, 3350 of 4033 Bq m^{-2} for BC), which also supports the assumption that these sections are not much older than two half-lives of the radioisotope, i.e., approximately 45 years. Although it cannot be excluded from the data that ^{210}Pb is present at depths below 20 cm that are not accessible in this data set, the ratio of inventories above and below

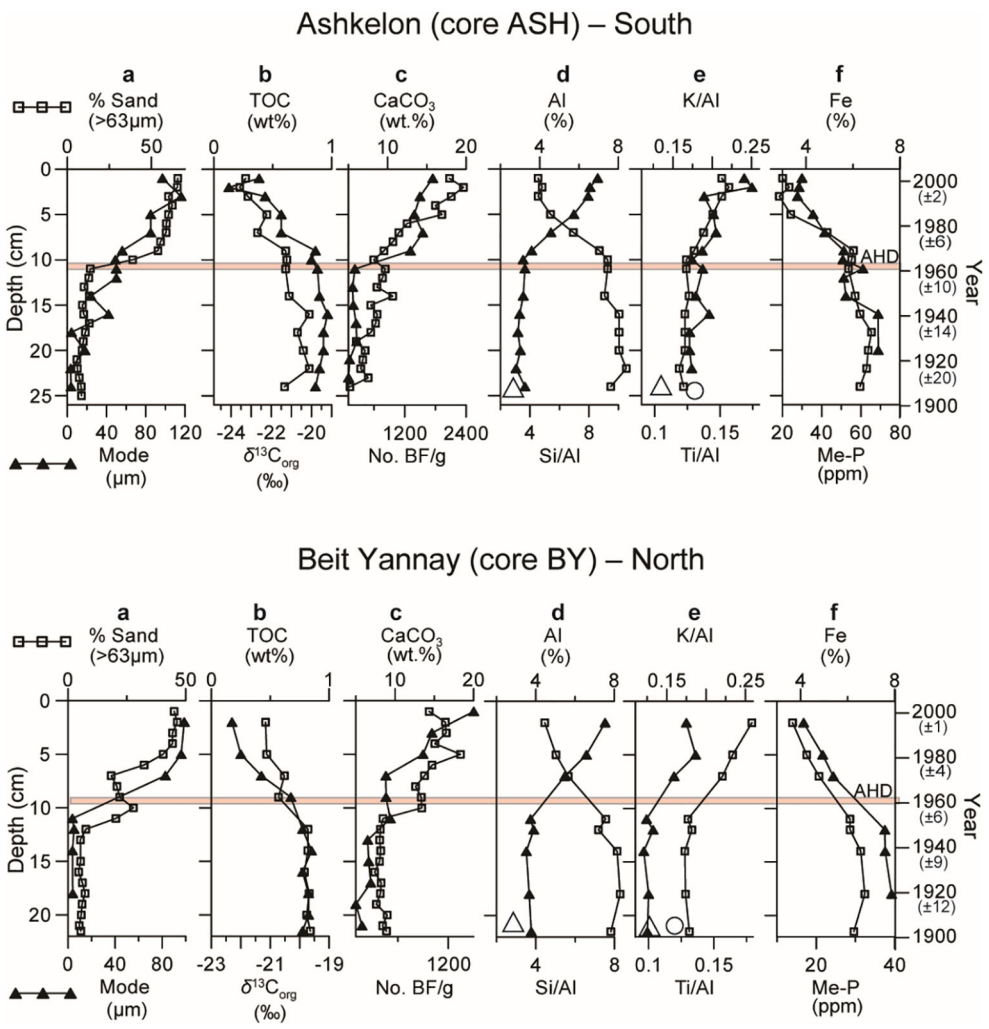

FIGURE 2
Short sediment core profiles representing the last ~100 years in the distal part of the Nile littoral cell (continental shelf of Israel) at a southern (Ashkelon) and northern (Beit Yannay) location: **(A)** % >63µm size fraction and grain size mode (µm); **(B)** TOC (wt.%) content and δ^{13}Corg (‰), vertical bars represent dating error for all profiles; **(C)** % $CaCO_3$ and benthic foraminiferal abundance; **(D)** % Al and Si/Al ratios; **(E)** K/Al and Ti/Al ratios; **(F)** % Fe and metal-bound phosphorus (Me-P). Large empty triangle and circle symbols represent Nile sediment ratios (Krom et al., 1999). It should be noted that the major change in sedimentation pattern coincides with the operation of the Aswan High Dam in the southern core, while earlier damming impacts may explain the earlier change in the northern core. The top and bottom axes refer to black squares and triangles, respectively.

10 cm is a strong argument for the age model and its extrapolation to greater depths.

Analysis of the normalized sand and fines (<63µm) inventories in the two cores (kg m^{-2}; considering the porosity and particle density of 2.65 gr cm^{-3}) shows a shift at depths that correspond to the mid-1960s, post-AHD, according to the ^{210}Pb exponential age model (Figure 3). The sedimentation rates and the slope of the cumulative sands and fines (Figure 3) were used to calculate the mean annual accumulation along the cores. Accordingly, for the BY core, we calculated mean sand and fines accumulation rates of 0.08 and 1.5 kg m^{-2} y^{-1} before the mid-1960s and 0.66 and 1.3 kg m^{-2} y^{-1} thereafter, respectively. For the ASH core, mean sand and fines accumulation rates were 0.2 and 1.9 kg m^{-2} y^{-1} before the mid-1960s and 1.6 and 1.1 kg m^{-2} y^{-1} thereafter, respectively. This would indicate a respective ~15% and ~40% reduction in fines accumulation rates in BY and ASH cores, respectively, and an ~8-fold increase in sand accumulation rates in both stations. A certain increase in the sand fraction (coarsening) in the top layers would occur solely from the decrease in the flux of Nile-derived fine sediments while maintaining the sand flux as in the previous AHD. Nonetheless, these unexpected calculated accumulation rates suggest that sand transport increased from the Nile Delta northward to the inner shelf band of Israel after the AHD. This estimate holds even if, for some unknown reason, our age model grossly (e.g., by a factor of four) overestimated post-AHD sedimentation rates. A possible cause for such a process is probably associated with the accelerated erosion rates of the sandy Nile Delta (tens of meters per year) after the AHD (3-5 times the rates before the AHD) and the northeastward transport and export of these sands along the coast (Frihy, 1988; Smith and Abdel-Kader, 1988; Frihy and Komar, 1991; Inman et al., 1993; Frihy and Lotfy, 1997). It has been proposed that the blockage of the

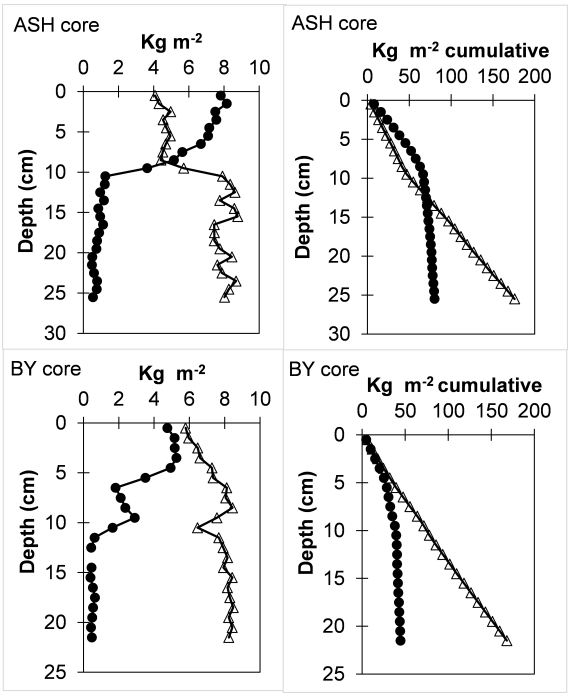

FIGURE 3
Sand (circles) and fines (<63μm; triangles) layer (kg m^{-2}) and cumulative inventories (kg m^{-2} cumulative) profiles in ASH and BY cores. A shift in slope at depths consistent with the operation of the AHD should be noted (Figure 2).

blockage of the Nile sand caused by the AHD forced currents to remove sand from the delta coast, compensating for the reduction and preventing sand shortages further north in the Nile littoral cell (Zviely et al., 2007). Additionally, man-made structures such as breakwaters in ports in Egypt, Gaza, and Israel may have diverted transported sand further offshore. Other factors that may somewhat affect sediment transport and grain size distribution on the shelf may include extreme flooding of the large ephemeral El-Arish River (Klein, 2000), fluctuations in erosion rates of the coastal escarpment (Mushkin et al., 2016), and various physical processes (Van Wellen et al., 2000; Shaeri et al., 2020).

The sand content exceeds ~50% in the post-AHD sediments, compared to <20% in the pre-AHD sediments (Figure 2A). The grain size mode increased gradually from ~5 μm in the pre-AHD sediments to ≥85μm in the post-AHD sediments. The silt fraction, which was ~75% in the pre-AHD sediments, decreased to ~45% in the post-AHD sediments, and the clay content decreased by ~50%, from ~20% to <10%. The latter reduction in fine sediments post-AHD is reflected in the changes in the chemical composition of the sediments, which show significantly higher Al and Fe concentrations and lower Si/Al ratios in the pre-AHD sediments (Figures 2D, F). The significantly lower K/Al, Ti/Al, and Si/Al ratios in the pre-AHD shelf sediments (Figures 2D, E) coincide with these ratios in the Nile sediments (Krom et al., 1999), emphasizing their strong reduction in the post-AHD sediments. Sediment coarsening is also accompanied by a distinct but moderate increase in $CaCO_3$, from less than 10% to 15-20%, mainly attributed to the increase in BF abundance (Figure 2C). The grain size coarsening is more abrupt and rapid in the southern shelf (ASH core), closer to the Nile, than in the northern distal part (BY core; Figure 2). In the latter, the coarsening starts earlier, is more gradual, and increases in two steps, probably in response to an earlier stage of Nile damming (since the Aswan Low Dam in 1898 -1902) that was barely recorded in the southern shelf.

TOC contents of 0.8-1wt.% with δ^{13}Corg of approximately -19.5‰ in pre-AHD sediments decreased to less than 0.5wt.% TOC and approximately -22-23‰ δ^{13}Corg in the overlying younger sediments (Figure 2B). Metal (mainly iron oxides)-bound phosphorus concentrations are lower in the post-AHD sediments, probably reflecting reduced scavenged phosphate in iron oxides as compared to the enhanced discharge of nutrients and iron in the pre-AHD period, especially during the seasonal floods (Figure 2F).

The bulk geochemical data from the two sediment cores are presented in Supplementary Table 1. Processing the geochemical data for principal component analysis (PCA) reveals two principal components that account for approximately 94% of the total variance in both sediment cores. Supplementary Figure 2 shows that the variance in elemental composition corresponds to the relative contribution of two major sources: terrestrial and marine-biogenic. The marine component contributes mainly to Ca or $CaCO_3$ as a major constituent of micro- and macro-faunal shells and to Si as a major constituent of quartz grains, both of which affect the proportion of sand grain size. Al, Fe, Mg, K, and Ti mostly correspond to terrestrial aluminosilicate minerals. Metal (mainly iron oxides)-bound phosphorus (P-metal) concentrations are linked to terrestrial sources of both dissolved phosphate and iron. The variance of TOC and its isotopic composition seem predominantly affected by the change in the terrestrial discharge of dissolved nutrients that trigger the marine-born TOC.

The relationships between δ^{13}Corg and TOC (Figure 4) show a mixing curve between depleted TOC with relatively more negative δ^{13}Corg in the post-AHD period and a more enriched TOC with a marine/algae δ^{13}Corg signature in the pre-AHD sediment. The ~3 ‰ decrease (-19.2 to -22.6 ‰; one measurement of -24.6 ‰; Figure 4) in δ^{13}Corg may reflect a shift in the relative contribution of autochthonous versus allochthonous organic carbon. Marine planktonic δ^{13}C in the eastern Mediterranean and other marine areas at similar latitudes ranges between -18 and -22 ‰ (Goericke and Fry, 1994; Meyers, 1994; Harmelin-Vivien et al., 2008; Li et al., 2016), and terrestrial δ^{13}C ranges from -25 to -28 ‰ (Hedges et al., 1997; Li et al., 2016). The ~50% decrease in TOC may indicate a drastic reduction in dissolved nutrient supply post-AHD. This observation suggests that prior to the AHD, the Nile system supplied significant amounts of dissolved nutrients to its distal cell, which enhanced algal biomass and the sedimentation of autochthonous organic carbon, but only an insignificant amount of allochthonous organic carbon. While the pre-AHD transported significant amounts of silty-clay sediments, it is speculated that the Nile-born detrital organic matter was decomposed or retained in the Nile delta, while the dissolved nutrients, representing a much larger stock, were transported northward along the eastern Levantine coast, fueling the primary producers, especially during the seasonal floods. The floods peaked between August and October/November (Sharaf El Din, 1977) and triggered a large

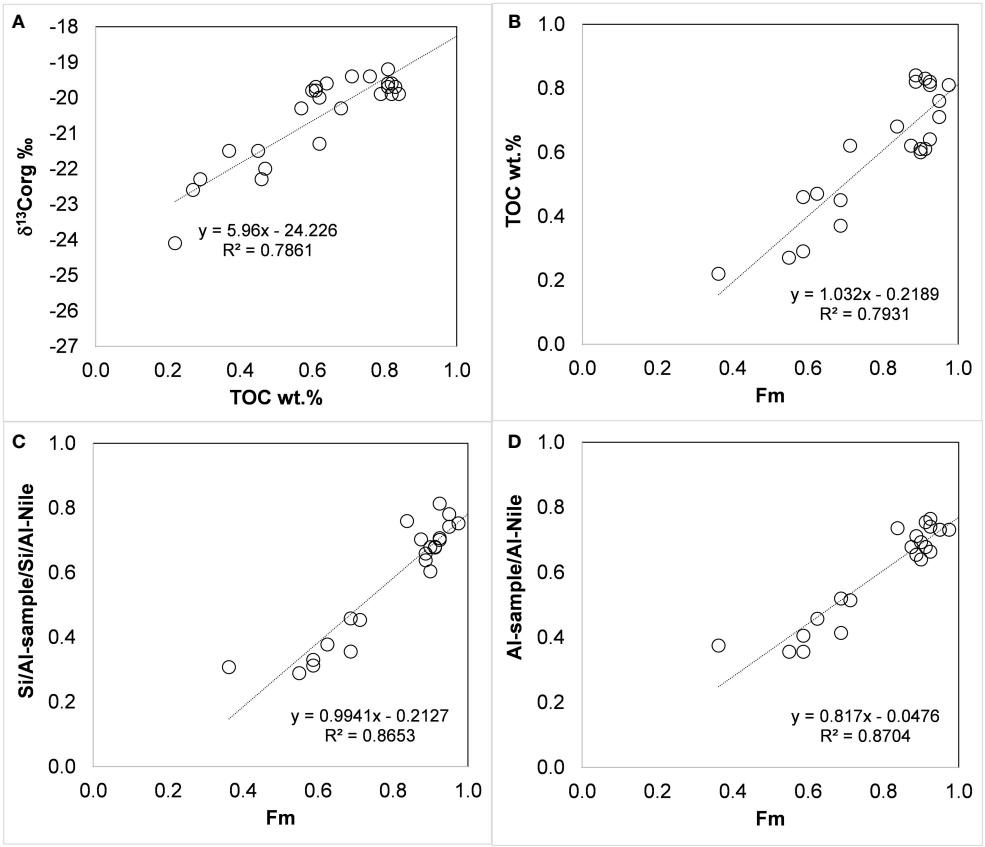

FIGURE 4
δ^{13}Corg ‰ vs. TOC % **(A)**, TOC % vs. marine fraction (Fm, eq. 2) **(B)**, [Si/Al-sample]/[Si/Al-Nile] vs. Fm **(C)**, and [Al-sample/Al-Nile] vs. Fm **(D)**. [Si/Al-Nile] = 2.483 wt./wt. and [Al-Nile] = ~11 wt.% (Krom et al., 1999).

phytoplankton bloom in the nearshore waters off the Egyptian and Israeli coasts (Oren and Komarovsky, 1961; Dowidar, 1984). At present, the southeastern Mediterranean Levantine Basin and coastal waters off Israel display oligotrophic conditions (Herut et al., 2000; Kress et al., 2019). Nonetheless, partial, but probably not dominant, changes in the TOC content can be attributed to the significant increase in grain size after the AHD (Hedges and Oades, 1997; Magill et al., 2018).

The changes in δ^{13}Corg composition in shallow continental shelf sediments are a first-order estimate due to mixing between marine/autochthonous and terrestrial/allochthonous organic carbon (Shultz and Calder, 1976). The isotopic mixing equation then represents a conservative mixing of these two end members (Shultz and Calder, 1976):

$$\delta^{13}\text{Corg}-\text{sample} = \text{Fm} \times \delta^{13}\text{Corg}-\text{m} + \text{Ft} \times \delta^{13}\text{Corg}-\text{t} \quad (1)$$

where Fm and Ft are the fractions of marine and terrestrial organic carbon (Fm + Ft = 1), and δ^{13}Corg-m and δ^{13}Corg-t are the isotopic compositions of the terrestrial and marine source end members.

Rearranging Equation 1,

$$\text{Fm} = \left[\delta^{13}\text{Corg}-\text{sample} - \delta^{13}\text{Corg}-\text{t}\right] / \left[\delta^{13}\text{Corg}-\text{m} - \delta^{13}\text{Corg}-\text{t}\right] \quad (2)$$

Based on the above literature data, we calculated Fm (eq. 2) using a terrestrial δ^{13}C-t of -27 ‰ and δ^{13}Corg-m -19 ‰ as end members. Fm ranges from 0.4 to ~0.9 before the AHD, corresponding to higher TOC concentrations. We assumed that the Si/Al or Al ratios between the sample and the Nile sediment end member (Si/Al ratio of 2.483 wt./wt. and Al concentration of ~11 wt.%; Krom et al., 1999) could serve as a proxy for the intensity of dissolved nutrient supply, as they coincide with the transport of Nile-derived fine sediments. These ratios may represent the fraction of marine-born organic carbon attributable to the supply of Nile-derived nutrients, as they show a similar fractional range and a significant linear correlation with Fm calculated from carbon isotopic composition (Figure 4).

The decline in these variables reflects a major change in the regional nutrient budget and a large decrease in primary production that coincides with the damming of the Nile (Halim et al., 1995). The trend of increasing oligotrophy on the inner shelf of Israel differs from reports of a large anthropogenic contribution of nutrients supporting increasing fisheries in the Mediterranean coastal waters off Egypt (Nixon, 2003). This increase in fertility seems to be on a local scale, mainly restricted to the delta area, unlike the pre-AHD summer floods, which were of significant and large magnitude and affected the Israeli shelf annually. The decrease

in TOC and δ^{13}Corg, indicators of nutrient supply and primary production, predates the sharp sediment coarsening. This may indicate that earlier phases of Nile damming had already contributed to the increasing oligotrophy of the EM, which accelerated after the operation of the AHD and continues at present.

3.2 Changes in the dead and live foraminiferal assemblages as proxies for the ecological evolution attributed to the damming of the Nile

The current study traces the temporal variations in the BF assemblage composition linked to changes in the sedimentary regime in the distal part of the Nile littoral cell following the damming of the Nile. We presented the BF assemblages in sedimentary layers representing pre (~1910) and post (1997; 2011; 2021) AHD conditions. The integrated database of surface and subsurface sediment samples (Table 1) contains a total of 170 taxa, of which 120 were identified at the species level after taxonomic refinement (Supplementary Table 2). The comparison of species accumulation curves of 10 surface sediment samples collected in 2021 between BY and ASH stations (three versus five sites) indicates that the three chosen sites represent 92% of the total species richness (56/61 species) (Supplementary Table 3; Supplementary Figure 3).

Cluster analysis and nonmetric multidimensional scaling (NMDS) ordination revealed a clear separation between dead (cluster A) and live (cluster B) BF assemblages and time periods, as detailed below (Figure 5; Supplementary Figure 4; Supplementary Table 4, Permanova analysis). We focused mainly on the dead BF assemblage, which provides the long-term record since before the AHD and integrates time-averaged information. The dead BF (Cluster A, Supplementary Figure 4) are divided into two major sub-clusters, A1 and A2, which are further subdivided by periods. A1 includes the separation between pre-AHD and 1997 samples, and A2 shows the division between 1997, 2011, and 2021 (Figure 5). Pairwise analysis between periods showed a significant difference ($p<0.02$) between pre-AHD, 2011 and 2021, and between 1997, 2011, and 2021 (Supplementary Table 5). The opportunistic species *Ammonia tepida*, *Porosononion subgranosus*, and *Cribroelphidium poeyanum* are among the most significant species in the pre-AHD samples (in sub-cluster A1), contributing 35% of the similarity between these samples (SIMPER, Supplementary Table 6). Their relative abundances ranged between 21-42%, 4-22%, and 8-18% of the assemblage composition, respectively. While these species may inhibit sediments poor in TOC, their highest abundances are favored by organic carbon enrichment (e.g., Bouchet et al., 2018; Jorissen et al., 2018). These species are also part of the 1997 samples; however, their contribution is relatively much lower, while other species such as *Ammonia parkinsoniana*, *Asterigerinata mamilla*, and *Textularia agglutinans* show increased relative abundances, ranging between 3-7%, 4-14% and 2-3%, respectively. These latter species are known to be sensitive to organic carbon enrichment and occur mainly in natural oligotrophic ecosystems (Alve et al., 2016; Jorissen et al., 2018).

We used the classification of ecological groups following Bouchet et al. (2021) as a proxy for changes in sedimentary total organic carbon levels. Based on the ecological quality status (EcoQS) BF groups, the two most relevant categories for changes in the Nile damming sediments are category 1 (sensitive species - oligotrophic bioindicators) and category 3 (tolerant species to organic carbon enrichment – elevated trophic state bioindicators). EcoQS category 1 showed an increasing trend over time ($p<0.02$; Kruskal-Wallis rank sum test), while category 3 showed significantly lower levels during 1997-2021 than in the pre-AHD (Figure 6; Supplementary Table 7). These trends are consistent with the geochemical observations showing lower TOC and fine sediment post-AHD.

EcoQS category 2 includes "indifferent species" to organic carbon enrichment, which are usually observed at relatively low abundances (Bouchet et al., 2021). It is thus expected that this group will be less responsive to the inferred damming effects and the decrease in TOC, as indeed observed along the periods (Figure 6). They occur in low abundance, with no changes between the different periods.

Additionally, based on pairwise analyses, the similarity between sites within periods showed that in pre-AHD and 1997, the BY station was the most dissimilar to the ASH and ASD stations ($p<0.04$, Permanova, Supplementary Table 8), while in 2011-2021, a greater dissimilarity developed between the two southern stations (ASH and AHD). This spatial dissimilarity trend suggests a further ongoing process from the northernmost distal part of the Nile cell southward.

Although live BF populations represent a snapshot of seasonal distribution that may record taphonomic processes compared to the subsurface assemblages, they are also responsive to anthropogenic impacts (e.g., Kidwell, 2007; Goineau et al., 2015). Indications for the ongoing changes in the BF composition associated with the damming of the Nile are also recorded in the live BF communities collected in 2011 and 2021. *Eggerelloides scaber, Paratrochammina madeira*, and the sensitive species *Bolivina striatula*, *Cycloforina quinquecarinata*, and *Textularia agglutinans* are among the living BF that contribute most (60% contribution) to the similarity between the samples of cluster B, based on SIMPER (Figure 5; Supplementary Table 6). EcoQS category 1 showed a slight decrease (of about 10%) in their abundance compared to their appearance in the dead assemblages of 2020 (Figure 6), while category 3 of opportunistic species continued to decrease in their density, representing 4% of the assemblage. The ongoing changes in sediment properties demonstrate the continuous impact of the Nile damming and the subsequent enhanced benthic oligotrophication process. Changes in the composition of the live BF assemblage have been observed over the last two decades on the southeastern Mediterranean shelf, where the Nilotic biotope has retreated southward (Avnaim-Katav et al., 2020; Avnaim-Katav et al., 2021). We speculate that the ongoing environmental changes in this unique ecosystem will continue to affect the distribution of benthic communities along the shelves of the Nile domain and thus require further study.

10.3389/fmars.2023.1226379

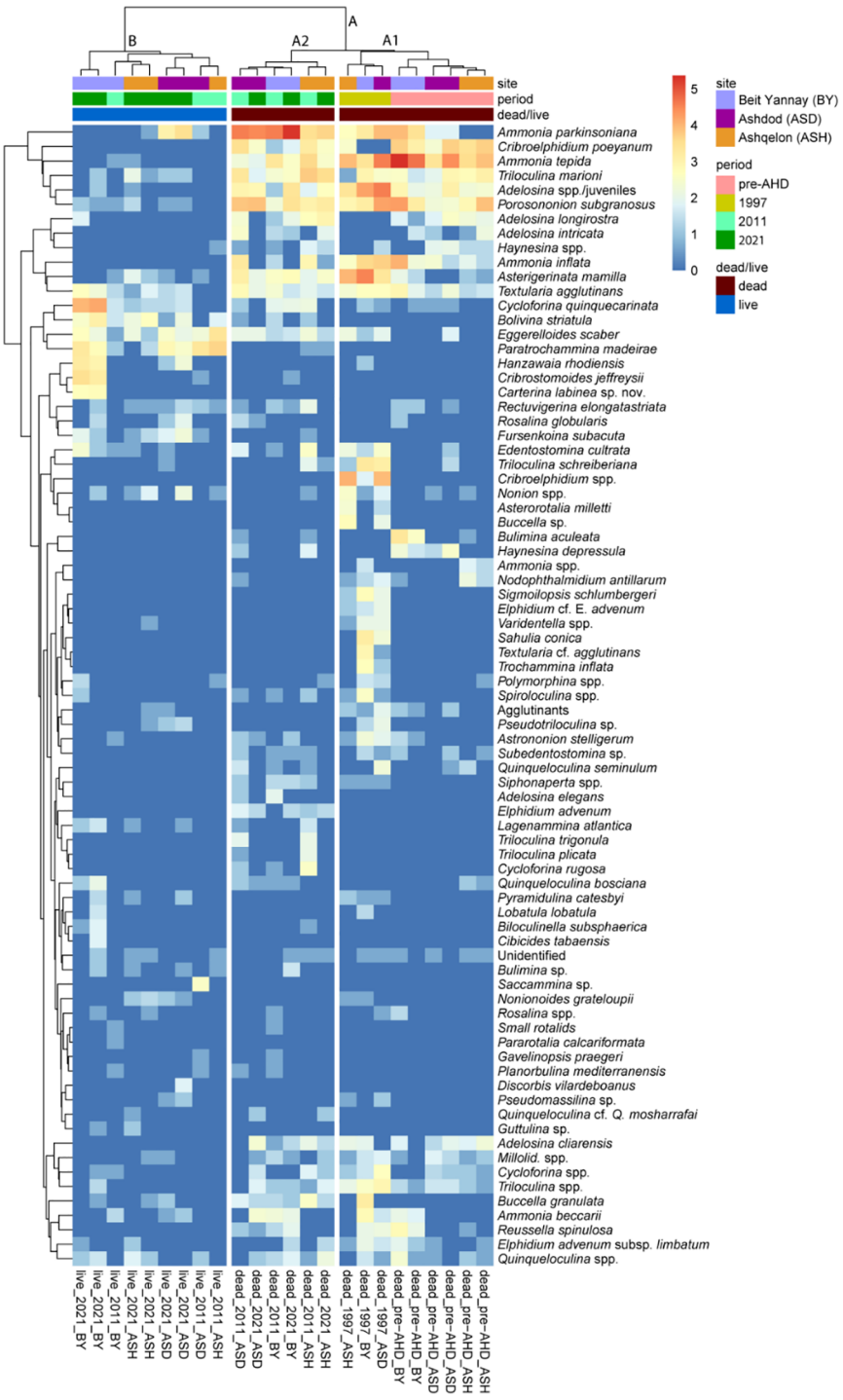

FIGURE 5
Q-mode Ward.D hierarchical cluster analysis of the surface and subsurface samples from stations BY, ASH, and ASD on the southeastern Mediterranean shelf (40 m water depth), representing the pre-AHD, 1997, 2011, and 2021 periods. The figure presents a visualization of the relative proportions of the 101 major taxa (>2% of the total assemblage) contributing to the clusters. The cluster analysis and the heat map of the full dataset of 170 taxa are shown in Supplementary Figure 4. A clear separation between dead (cluster A) and live (cluster B) BF assemblages and time periods (sub-clusters A1 and A2) is highlighted.

4 Conclusion

In this work, we followed the benthic sedimentological changes during the last approximately 100 years, which were significantly influenced by the damming of the Nile River, resulting in an almost complete retention of fine sediments and a decrease of dissolved nutrients previously exported to its distal domain in the southeastern Mediterranean basin. The substantial change in

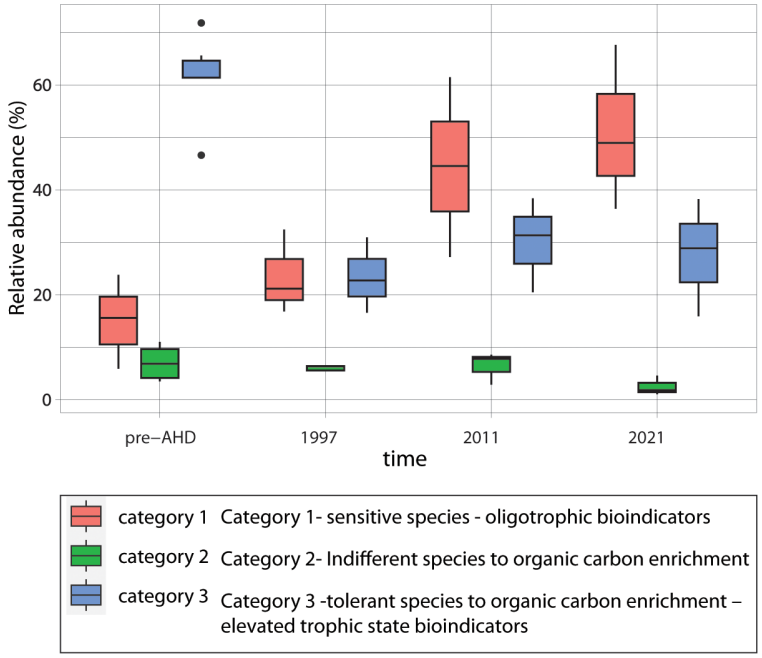

FIGURE 6
Box plots of BF ecological groups following Bouchet et al. (2021) as a proxy for changes in the sedimentary total organic carbon levels. Three BF ecological quality status (EcoQS) groups are presented for the different time periods: category 1 - sensitive species (oligotrophic bioindicators), category 2 - "indifferent species", and category 3 - tolerant species to organic carbon enrichment (elevated trophic state bioindicators).

grain size, organic carbon, and BF assemblages, tending toward further oligotrophication, combined with fast warming and salinization in the Levantine basin (Ozer et al., 2022), mainly attributed to climate change, may have essential implications for the southeastern Mediterranean ecosystem. The assessment of the effects of climate change on the nutrient dynamics and the planktonic ecosystem in the western and eastern basins of the Mediterranean Sea is mostly based on the analysis of simulations under different Representative Concentration Pathways (RCPs) 4.5 and 8.5, as presented by Reale et al. (2022) and references therein. While different projections have been reported, Reale et al. (2022) show stable nutrient concentrations in the euphotic layer until 2030 and a significant decrease thereafter for the worst-case scenario (RCP8.5). Nevertheless, the projection of the biogeochemical/nutrient responses to river loading and Gibraltar exchange associated with climate change is highly important and requires further investigation (Richon et al., 2019). While in this study the damming of the Nile is evident by the turnover observed in the foraminiferal species composition shifting from EcoQS category 3 to EcoQS category 1 (Figure 6), the global warming trend is likely to alter the BF assemblages on the continental shelf, but further research is needed to follow this effect.

Both the reduced nutrient fluxes and the coarsening of the shelf sediments may reduce the preservation of organic matter and the retention of "blue" carbon in the shelf sediments. The severe fragmentation of the Nile and other coastal river systems may also interrupt the past periodic formation of sapropels (rich organic layers) over the last 13.5 million years, known from sedimentary sequences in the eastern Mediterranean basin, corresponding to monsoon runoff/intensification and other oceanographic preconditions (Rohling et al., 2015). The Nile system may serve as a predictor of ecological marine responses in other large, fragmented rivers worldwide where human activities have significantly reduced their sediment and water fluxes (Syvitski et al., 2005; Best, 2019; Dethier et al., 2022).

Data availability statement

The original contributions presented in the study are included in the article/Supplementary Material, further inquiries can be directed to the corresponding author/s.

Author contributions

Conceptualization: BH and AA-L; Sampling: BH, AA-L, and TK; Methodology: AA-L, BH, TK, TG-H, AS, and SA-K; Chronology: HF and DR; Statistics: TG-H; Writing-original draft: BH and SA-K; Writing and editing: All authors participated in discussion and writing; Resources: BH and AA-L. All authors contributed to the article and approved the submitted version.

Funding

This study was carried out with the support of the Israeli Ministry of Energy (grant no. 28-17-006), partially by the Israel Science Foundation (grant 145/02-13.0) to AA-L and BH, and partially by the National Monitoring Program of Israel's Mediterranean Waters.

Acknowledgments

We would like to thank the team of the geochemical and sedimentological units of the Geological Survey of Israel for their help in sampling and analysis; we thank the chemistry laboratory of the Kinneret Limnological Laboratory of the IOLR for the phosphorus analyses; we thank the captain and crew of the R.V. Shikmona and R.V. Bat Galim for their dedicated work during the sampling campaigns.

Conflict of interest

The authors declare that the research was conducted in the absence of any commercial or financial relationships that could be construed as a potential conflict of interest.

Publisher's note

Supplementary material

The Supplementary Material for this article can be found online at: https://www.frontiersin.org/articles/10.3389/fmars.2023.1226379/full#supplementary-material

References

Abd-El Monsef, H., Smith, S. E., and Darwish, K. (2015). Impacts of the Aswan high dam after 50 years. *Water Resour. Manage.* 29, 1873–1885. doi: 10.1007/s11269-015-0916-z

Alvarez-Iglesias, P., Quintana, B., Rubio, B., and Pérez-Arlucca, M. (2007). Sedimentation rates and trace metal input history in intertidal sediments from San Simón Bay (Ría de Vigo, NW Spain) derived from ^{210}Pb and ^{137}Cs chronology. *J. Environ. Radioactivity* 98, 3 229–3 250. doi: 10.1016/j.jenvrad.2007.05.001

Alve, E., Korsun, S., Sch€onfeld, J., Dijkstra, N., Golikova, E., Hess, S., et al. (2016). Foram-AMBI: a sensitivity index based on benthic foraminiferal faunas from North-East Atlantic and Arctic fjords, continental shelves and slopes. *Mar. Micropaleontology* 122, 1–12. doi: 10.1016/j.marmicro.2015.11.001

Avnaim-Katav, S., Almogi-Labin, A., Herut, B., Kanari, M., and Guy-Haim, T. (2021). Benthic foraminifera from the Southeastern Mediterranean shelf: Dead assemblages and living-dead comparisons recording consequences of Nile River damming. *Mar. Micropaleontology* 164, 101977. doi: 10.1016/j.marmicro.2021.101977

Avnaim-Katav, S., Almogi-Labin, A., Kanari, M., and Herut, B. (2020). Living benthic foraminifera of southeastern Mediterranean ultra-oligotrophic shelf habitats: implications for ecological studies. *Estuarine Coast. Shelf Sci.* 234, 106633. doi: 10.1016/j.ecss.2020.106633

Avnaim-Katav, S., Almogi-Labin, A., Schneider-Mor, A., Crouvi, O., Burke, A. A., Kremenetski, K. V., et al. (2019). A multi-proxy shallow marine record for mid-to-late holocene climate variability, thera eruptions and cultural change in the Eastern Mediterranean. *J. Quaternary Sci. Rev.* 204, 133–148. doi: 10.1016/j.quascirev.2018.12.001

Best, J. (2019). Anthropogenic stresses on the world's big rivers. *Nat. Geosci.* 12 (1), 7–21. doi: 10.1038/s41561-018-0262-x

Bookman, R., Mor-Federman, T., Herut, B., Harlavan, Y., Taha, N., Stein, M., et al. (2021). Development of the Nile Littoral Cell during the past 8.2 kyr. *Quaternary Sci. Rev.* 274, 107262. doi: 10.1016/j.quascirev.2021.107262

Bouchet, V. M.P, Frontalini, F., Francescangeli, F., Sauriau, P-G., Geslin, E., Martins, M. V.A., et al. (2021). Indicative value of benthic foraminifera for biomonitoring: Assignment to ecological groups of sensitivity to total organic carbon of species from European intertidal areas and transitional waters. *Mar. pollut. Bull.* 164, 112071. doi: 10.1016/j.marpolbul.2021.112071

Bouchet, V. M. P., Goberville, E., and Frontalini, F. (2018). Benthic foraminifera to assess the Ecological Quality Status of Italian transitional waters. *Ecol. Indic.* 84, 130–139. doi: 10.1016/j.ecolind.2017.07.055

Cimerman, F., and Langer, M. R. (1991). Mediterranean foraminifera. Academia scientarium et aritium slovenica, dela, opera 30, classis IV. *Hist. Nat.*, 118 p., 93 pl.

Clarke, K. R. (1993). Non-parametric multivariate analyses of changes in community structure. *Aust. J. Ecol.* 18 (1), 117–143. doi: 10.1111/j.1442-9993.1993.tb00438.x

Crouvi, O., Amit, R., Enzel, Y., Porat, N., and Sandler, A. (2008). Sand dunes as a major proximal dust source for late Pleistocene loess in the Negev desert, Israel. *Quaternary Res.* 70, 275–282. doi: 10.1016/j.yqres.2008.04.011

Dethier, E. N., Renshaw, C. E., and Magilligan, F. J. (2022). Rapid changes to global river suspended sediment flux by humans. *Science* 376 (6600), 1447–1452.

Dowidar, N. M. (1984). Phytoplankton biomass and primary productivity of the south-eastern Mediterranean. *Deep Sea Res. Part A. Oceanographic Res. Papers* 31 (6-8), 983–1000. doi: 10.1016/0198-0149(84)90052-9

Eckert, W., Didenko, J., Uri, E., et al. (2003). Spatial and temporal variability of particulate phosphorus fractions in seston and sediments of Lake Kinneret under changing loading scenario. In: Kronvang, B. (eds) The Interactions between Sediments and Water. Developments in Hydrobiology, vol 169. Springer, Dordrecht. doi: 10.1007/978-94-017-3366-3_30

Farhat, H. I., and Salem, S. G. (2015). Effect of flooding on distribution and mode of transportation of Lake Nasser sediments, Egypt. *Egyptian J. Aquat. Res.* 41 (2), 165–176. doi: 10.1016/j.ejar.2015.03.009

Frihy, O. E. (1988). Nile Delta shoreline changes: aerial photographic study of a 28-year period. *J. Coast. Res.*, 597–606.

Frihy, O. E., and Komar, P. D. (1991). Patterns of beach-sand sorting and shoreline erosion on the Nile Delta. *J. Sedimentary Res.* 61 (4), 544–550.

Frihy, O. E., and Lotfy, M. F. (1997). Shoreline changes and beach-sand sorting along the northern Sinai coast of Egypt. *Geo-Marine Lett.* 17, 140–146. doi: 10.1007/s003670050019

Goericke, R., and Fry, B. (1994). Variations of marine plankton δ^{13}C with latitude, temperature, and dissolved CO2 in the world ocean. *Global Biogeochemical Cycles* 8 (1), 85–90. doi: 10.1029/93GB03272

Goineau, A., Fontanier, C., Mojtahid, M., Fanget, A. S., Bassetti, M. A., and Jorissen, F. J. (2015). Live–dead comparison of benthic foraminiferal faunas from the Rhˆone prodelta (Gulf of Lions, NW Mediterranean): Development of a proxy for palaeoenvironmental reconstructions. *Mar. Micropaleontology* 119, 17–33. doi: 10.1016/j.marmicro.2015.07.002

Halim, Y. (1960). Observations on the nile bloom of phytoplankton in the Mediterranean. *ICES Journal of Marine Science* 26, 1, 57–67. doi: 10.1093/icesjms/26.1.57

Halim, Y., Morcos, S. A., Rizkalla, S., and El-Sayed, M. K. (1995). "The impact of the Nile and the Suez Canal on the living marine resources of the Egyptian Mediterranean waters, (1958–1986)," in *Effects of riverine inputs on coastal ecosystems and fisheries resources*, vol. 349. , 19–56.

Harmelin-Vivien, M., Loizeau, V., Mellon, C., Beker, B., Arlhac, D., Bodiguel, X., Bodiguel, X., et al. (2008). Comparison of C and N stable isotope ratios between surface particulate organic matter and microphytoplankton in the Gulf of Lions (NW Mediterranean). *Continental Shelf Res.* 28 (15), 1911–1919. doi: 10.1016/j.csr.2008.03.002

Hayward, B. W., Sabaa, A. T., and Triggs, C. M. (2019). Using foraminiferal test-size distribution and other methods to recognize Quaternary bathyal turbidites and taphonomically-modified faunas. *Mar. Micropaleontology* 148, 65–77. doi: 10.1016/j.marmicro.2019.03.008

Hecht, A. (1964). *On the turbulent diffusion of the water of the Nile floods in the Mediterranean Sea* Vol. 36 (Haifa, Israel: Sea Fisheries Research Station, Bulletin), 1–24.

Hecht, A., and Gertman, I. (2001). Physical features of the eastern Mediterranean resulting from the integration of POEM data with Russian Mediterranean cruises. *Deep Sea Res. Part I: Oceanographic Res. Papers* 48 (8), 1847–1876. doi: 10.1016/S0967-0637(00)00113-8

Hedges, J. I., Keil, R. G., and Benner, R. (1997). What happens to terrestrial organic matter in the ocean? *Organic geochemistry* 27 (5-6), 195–212. doi: 10.1016/S0146-6380(97)00066-1

Hedges, J. I., and Oades, J. M. (1997). Comparative organic geochemistries of soils and marine sediments. *Organic geochemistry* 27 (7-8), 319–361. doi: 10.1016/S0146-6380(97)00056-9

Herut, B., Almogi-Labin, A., Jannink, N., and Gertman, I. (2000). The seasonal dynamics of nutrient and chlorophyll a concentrations on the SE Mediterranean shelf-slope. *Oceanologica Acta* 23 (7), 771–782. doi: 10.1016/S0399-1784(00)01118-X

Hottinger, L., Halicz, E., and Reiss, Z. (1993). *Recent foraminiferida from the gulf of aqaba, red sea, 33* (Ljubljana: Opera Sazu), 179 p., 230 pls.

Hyams-Kaphzan, O., Almogi-Labin, A., Sivan, D., and Benjamini, C. (2008). Benthic foraminifera assemblage change along the southeastern Mediterranean inner shelf due to fall-off of Nile-derived siliciclastics. *Neues Jahrbuch für Geologie und Paläontologie-Abhandlungen* 248, 315–344. doi: 10.1127/0077-7749/2008/0248-0315

Inman, D. L. (2003). Littoral cells.

Inman, D. L., Elwany, M. H. S., Khafagy, A. A., and Golik, A. (1993). "Nile Delta profiles and migrating sand blankets," in *Coastal engineering 1992*, 3273–3284.

Inman, D. L., and Jenkins, S. A. (1984). "The Nile littoral cell and man's impact on the coastal littoral zone in the SE Mediterranean," in *Proceedings of the 17th International Coastal Engineering Conference*. 1600–1617 (Australia: ASCE, Sydney).

Jones, R. W. (1994). *The challenger foraminifera* (London: Oxford University Press. Natural History Museum Pub.), 149 pp.,115 pls.

Jorissen, F. J., de Stigter, H. C., and Widmark, J. G. V. (1995). A conceptual model explaining benthic foraminiferal microhabitats. *Mar. micropaleontology* 26 (1-4), 3–15. doi: 10.1016/0377-8398(95)00047-X

Jorissen, F., Nardelli, M. P., Almogi-Labin, A., Barras, C., Bergamin, L., Bicchi, E., et al. (2018). Developing Foram-AMBI for biomonitoring in the Mediterranen: species assignments to ecological categories. *Mar. Micropaleontology* 140, 33–45. doi: 10.1016/j.marmicro.2017.12.006

Katz, M. E., Cramer, B. S., Franzese, A., Hönisch, B., Miller, K. G., Rosenthal, Y., et al. (2010). Traditional and emerging geochemical proxies in foraminifera. *J. Foraminiferal Res.* 40 (2), 165–192. doi: 10.2113/gsjfr.40.2.165

Kidwell, S. M. (2007). Discordance between living and death assemblages as evidence for anthropogenic ecological change. *PNAS* 104, 17701–17706. doi: 10.1073/pnas.0707194104

Kirchner, G., and Ehlers, H. (1998). Sediment geochronology in changing coastal environments: potentials and limitations of the ^{137}Cs and ^{210}Pb methods. *J. Coast. Res.* 14 (2), 483–492.

Klein, M. (2000). The formation and disappearance of a delta at the El-Arish river mouth. IAHS PUBLICATION, 303–310.

Kolde, R., and Maintainer, R. K. (2018). *Package 'pheatmap*, Vol. 1. 10, *R package*.

Kress, N., Rahav, E., Silverman, J., and Herut, B. (2019). Environmental status of Israel's Mediterranean coastal waters: Setting reference conditions and thresholds for nutrients, chlorophyll-a and suspended particulate matter. *Mar. pollut. Bull.* 141, 612–620. doi: 10.1016/j.marpolbul.2019.02.070

Krom, M. D., Cliff, R. A., Eijsink, L. M., Herut, B., and Chester, R. (1999). The characterisation of Saharan dusts and Nile particulate matter in surface sediments from the Levantine basin using Sr isotopes. *Mar. Geology* 155 (3-4), 319–330. doi: 10.1016/S0025-3227(98)00130-3

Li, D., Lu, X., Overeem, I., Walling, D. E., Syvitski, J., Kettner, A. J., et al. (2021). Exceptional increases in fluvial sediment fluxes in a warmer and wetter High Mountain Asia. *Science* 374 (6567), 599–603.

Li, Y., Zhang, H., Tu, C., Fu, C., Xue, Y., and Luo, Y. (2016). Sources and fate of organic carbon and nitrogen from land to ocean: Identified by coupling stable isotopes with C/N ratio. *Estuarine Coast. Shelf Sci.* 181, 114–122. doi: 10.1016/j.ecss.2016.08.024

Loeblich, A. R., and Tappan, H. (1987). *Foraminiferal genera and their classification, 2* (New York: Van Nostrand Reinhold Company), 970 pp. 847 pls.

Loeblich, A. R., and Tappan, H. (1994). *Foraminifera of the sahul shelf and timor sea* (Cushman Foundation for Foraminiferal Research), 661 pp. 393 pls. Special Publication No. 31.

Ludwig, W., Dumont, E., Meybeck, M., and Heussner, S. (2009). River discharges of water and nutrients to the Mediterranean and Black Sea: major drivers for ecosystem changes during past and future decades? *Prog. oceanography* 80 (3-4), 199–217. doi: 10.1016/j.pocean.2009.02.001

Magill, C. R., Ausín, B., Wenk, P., McIntyre, C., Skinner, L., Martínez-García, A., et al. (2018). Transient hydrodynamic effects influence organic carbon signatures in marine sediments. *Nat. Commun.* 9 (1), 4690. doi: 10.1038/s41467-018-06973-w

Martínez, T., Marchant, M., and Urbina, M. (2023). Are physiological responses in foraminifera reliable environmental stress bioindicators? *A systematic review. Environ. Res.* 216 (Part 2), 114515. doi: 10.1016/j.envres.2022.114515

Meyers, P. A. (1994). Preservation of elemental and isotopic source identification of sedimentary organic matter. *Chem. geology* 114 (3-4), 289–302. doi: 10.1016/0009-2541(94)90059-0

Milliman, J. D., and Farnsworth, K. L. (2013). *River discharge to the coastal ocean: a global synthesis* (Cambridge University Press).

Mushkin, A., Katz, O., Crouvi, O., Alter, S. R., and Shemesh, R. (2016). Sediment contribution from Israel's coastal cliffs into the Nile's littoral cell and its significance to cliff-retreat mitigation efforts. *Eng. Geology* 215, 91–94. doi: 10.1016/j.enggeo.2016.11.005

Nir, Y. (1984). Recent sediments of the Israel Mediterranean continental shelf and slope (Sweden: Göteborg University), 149 pp. (PhD Dissertation).

Nixon, S. W. (2003). Replacing the Nile: are anthropogenic nutrients providing the fertility once brought to the Mediterranean by a great river? *AMBIO: A J. Hum. Environ.* 32 (1), 30–39. doi: 10.1579/0044-7447-32.1.30

Oksanen, J. F., et al. (2019) *vegan: Community ecology package*. Available at: https://CRAN.R-project.org/package=vegan.

Oren, O. H. (1969). Oceanographic and biological influence of the Suez Canal, the Nile and the Aswan Dam on the Levant Basin. *Prog. Oceanography* 5, 161–167. doi: 10.1016/0079-6611(69)90038-X

Oren, O. H., and Komarovsky, B. (1961). The influence of the Nile flood on the shore waters of Israel. *Rapports et Proces-Verbaux des Reunions, Conseil International pour l'Exploration Scientifique de la Mer Medeterranee. Monaco* 16, 655–659.

Ozer, T., Gertman, I., and Gildor H and Herut, B. (2022). Thermohaline temporal variability of the SE mediterranean coastal waters (Israel) – long-term trends, seasonality, and connectivity. *Front. Mar. Sci.* 8. doi: 10.3389/fmars.2021.799457

Ransby, D., Fischer, H. W., Herut, B., and Almogi-Labin, A. Radionuclides and chronology of short sediment cores BY and ASH from the Israel inner Mediterranean shelf. *PANGAEA*. doi: 10.1594/PANGAEA.956901

Reale, M., Cossarini, G., Lazzari, P., Lovato, T., Bolzon, G., Masina, ,. S., et al. (2022). Acidification, deoxygenation, and nutrient and biomass declines in a warming Mediterranean Sea. *Biogeosciences* 19 (17), 4035–4065. doi: 10.5194/bg-19-4035-2022

Richon, C., Dutay, J. C., Bopp, L., Le Vu, B., Orr, J. C., Somot, S., et al. (2019). Biogeochemical response of the Mediterranean Sea to the transient SRES-A2 climate change scenario. *Biogeosciences* 16 (1), 135–165. doi: 10.5194/bg-16-135-2019

Rohling, E. J., Marino, G., and Grant, K. M. (2015). Mediterranean climate and oceanography, and the periodic development of anoxic events (sapropels). *Earth-Science Rev.* 143, 62–97. doi: 10.1016/j.earscirev.2015.01.008

Schmiedl, G. (2019). "Use of foraminifera in climate science," in *Oxford research encyclopedia of climate science* (Oxford University Press). doi: 10.1093/acrefore/9780190228620.013.735

Schonfeld, J., Alve, E., Geslin, E., Jorissen, F., Korsun, S., Spezzaferri, S., et al. (2012). The FOBIMO (FOraminiferal BIo-MOnitoring) initiative—towards a standardized protocol for soft-bottom benthic foraminiferal monitoring studies. *Mar. Micropaleontology* 94, 1–13. doi: 10.1016/j.marmicro.2012.06.001

Sen Gupta, B. K. (Ed.) (1999). *Modern foraminifera* (Dordrecht, the Netherlands: Kluwer Academic Publishers).

Shaeri, S., Etemad-Shahidi, A., and Tomlinson, R. (2020). Revisiting longshore sediment transport formulas. *J. Waterway Port Coastal Ocean Eng.* 146 (4), 04020009. doi: 10.1061/(ASCE)WW.1943-5460.0000557

Sharaf El Din, S. H. (1977). Effect of the Aswan High Dam on the Nile flood and on the estuarine and coastal circulation pattern along the Mediterranean Egyptian coast. *Limnology Oceanography* 22 (2), 194–207. doi: 10.4319/lo.1977.22.2.0194

Shultz, D. J., and Calder, J. A. (1976). Organic carbon $^{13}C^{12}C$ variations in estuarine sediments. *Geochimica Cosmochimica Acta* 40 (4), 381–385. doi: 10.1016/0016-7037(76)90002-8

Singh, W., Hjorleifsson, E., and Stefansson, G. (2011). Robustness of fish assemblages derived from three hierarchical agglomerative clustering algorithms performed on Icelandic groundfish survey data. *ICES J. Mar. Sci.* 68 (1), 189–200. doi: 10.1093/icesjms/fsq144

Smith, S. E., and Abdel-Kader, A. (1988). Coastal erosion along the Egyptian delta. *J. Coast. Res.*, 245–255.

Stanley, D. J., and Warne, A. G. (1993). Nile Delta: recent geological evolution and human impact. *Science* 260 (5108), 628–634.

Syvitski, J. P. M., Vörösmarty, C. J., Kettner, A. J., and Green, P. (2005). Impact of humans on the flux of terrestrial sediment to the global coastal ocean. *Science* 308 (5720), 376–380. doi: 10.1126/science.1109454.

Van Wellen, E., Chadwick, A. J., and Mason, T. (2000). A review and assessment of longshore sediment transport equations for coarse-grained beaches. *Coast. Eng.* 40 (3), 243–275. doi: 10.1016/S0378-3839(00)00031-4

Vörösmarty, C. J., Meybeck, M., Fekete, B., Sharma, K., Green, P., and Syvitski, J. P. (2003). Anthropogenic sediment retention: major global impact from registered river impoundments. *Global Planetary Change* 39 (1-2), 169–190. doi: 10.1016/S0921-8181(03)00023-7

Wheeler, K. G., Jeuland, M., Hall, J. W., Zagona, E., and Whittington, D. (2020). Understanding and managing new risks on the Nile with the Grand Ethiopian Renaissance Dam. *Nat. Commun.* 11 (1), 5222. doi: 10.1038/s41467-020-19089-x

Woodward, J. C., Macklin, M. G., Krom, M. D., Williams, M. A., and Gupta, A. (2007). The Nile: evolution, Quaternary river environments and material fluxes. *Large rivers: geomorphology Manage.* 13, 712.

WoRMS Editorial Board (2023) *WoRMS editorial board world register of marine species*. Available at: https://www.marinespecies.org (Accessed 2023-02-09). at VLIZ.

Zviely, D., Kit, E., and Klein, M. (2007). Longshore sand transport estimates along the Mediterranean coast of Israel in the Holocene. *Mar. Geology* 238 (1-4), 61–73. doi: 10.1016/j.margeo.2006.12.003

Frontiers in Marine Science

Explores ocean-based solutions for emerging global challenges

The third most-cited marine and freshwater biology journal, advancing our understanding of marine systems and addressing global challenges including overfishing, pollution, and climate change.

Discover the latest Research Topics

See more →

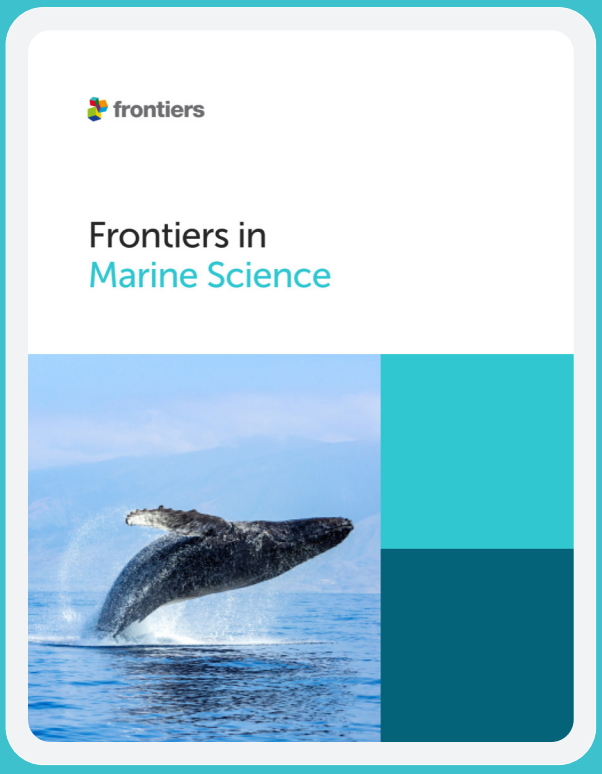

Frontiers

Avenue du Tribunal-Fédéral 34
1005 Lausanne, Switzerland
frontiersin.org

Contact us

+41 (0)21 510 17 00
frontiersin.org/about/contact